(13)

Selective Cell Separation Utilizing Porous Immunoaffinity Membranes

by

Michael J. Pomianek

B.S., Chemical Engineering
Drexel University (1988)

M.S., Chemical Engineering Practice
Massachusetts Institute of Technology (1990)

Submitted to the Department of Chemical Engineering in Partial Fulfillment of the Requirements for the Degree of
Doctor of Philosophy in Chemical Engineering

at the

MASSACHUSETTS INSTITUTE OF TECHNOLOGY

February, 1998

Author .....
Department of Chemical Engineering
November 12, 1997

Certified by .....
Clark K. Colton
Professor of Chemical Engineering
Thesis Supervisor

Accepted by .....
Robert E. Cohen
St. Laurent Professor of Chemical Engineering
Chairman, Committee for Graduate Students

Selective Cell Separation Utilizing Porous Immunoaffinity Membranes

by
Michael J. Pomianek

Submitted to the Department of Chemical Engineering on November 12, 1997 in partial fulfillment of the requirements for the degree of Doctor of Philosophy in Chemical Engineering

Abstract

In this thesis, a novel method for performing positive, selective immunoaffinity cell separations was developed, analyzed and tested. The concept utilizes a porous substrate, such as a membrane, and takes advantage of physical forces, generated by shear flow and permeation through the substrate, for cell deposition and detachment. The procedure for performing cell separations proceeds as follows. A cell mixture containing a defined target cell population is introduced into a device containing one or more porous membranes which have been chemically modified to have specific affinity for target cells. Cells are deposited onto the surface by gravity settling or by filtration. Cells are allowed to incubate on the membrane under static conditions to enable specific attachments to form between the substrate and the target cells. Non-target cells are removed from the substrate with shear flow, and target cells are eluted by pressurizing the side of the membrane opposite that to which the cells are adsorbed (back-pressure) causing back-filtration which generates physical removal forces on the cell-surface contact area. Back-pressure elution may be supplemented by shear flow or the use of exogenous specific-bond disruption agents.

A mathematical analysis of the cell attachment and detachment steps was performed assuming deterministic reversible binding kinetics between receptors on target cells and ligands on porous substrates. The analysis predicted the number of bonds formed at equilibrium for cells with both fixed and freely diffusible receptors, the force necessary to remove cells with uniformly stressed bonds, and the critical shear stress and transmembrane pressure drop required for cell removal. Back-pressure was found to be most effective for cells which form relatively large, flattened contact areas (with size on the order of the cell radius or greater), while shear was most effective for fully rounded cells with small contact areas. The analysis also indicated that membranes where flow cannot occur or is restricted within the plane of the membrane (anisotropic membranes), or membranes whose pressure drop determining region comprises a very thin layer adjacent to the surface to which cells are attached ("skinned" membranes), were most efficient at transmitting back-pressure to the cell contact area. The analysis was used to investigate the required features of cells and membranes for feasible cell detachment with shear and back pressure.

Cell separation experiments were performed using chemically modified polyethersulfone/polyethylene oxide hollow-fiber membranes to which specific ligands, such as monoclonal antibodies or Protein A, were attached. The transformed cell lines HL-60 and Namalwa were used as a model system. We found that when cells were loaded onto the

membranes by gravity settling, that binding selectivity was greater than 90 % and often greater than 99 %, and that up to 86 % of attached target cells could be removed during elution with back-filtration, or 96 % with back-filtration combined with a bond disruption agent. Electron microscopic observation of target cells indicated that the target cells formed large flattened contact areas during attachment (on the order of the cell diameter), and that minimum separation distances were on the order of the length of molecular cross-bridges. Experiments where cells were loaded onto membranes by filtration failed to replicate the results observed with gravity settled cells. When cells were loaded by filtration, both target and non-target cells strongly attached to the membranes and were not effectively removed by shear stress or back-pressure. Transmission electron microscopic images of cells attached to membranes after loading by filtration indicated that cells were able to infiltrate into the internal porous structure of the membranes. Since cell loading by filtration has many practical advantages over gravity settling, the mechanism of cell infiltration was investigated. Additional experiments with similar hollow-fiber membranes indicated that infiltration was a passive process which did not require active metabolism or cytoskeletal motility. The degree of infiltration was related to the pore size of the membrane and the filtration pressure. In order to understand the process of cell infiltration more thoroughly, we performed cell loading experiments using polycarbonate track-etched membranes with uniform, well-defined pore diameters of 0.05, 0.1, and 0.2 μm. An apparatus was constructed to apply controlled, uniform pressures to HL-60 cells on membranes, and to chemically fix the cells under pressure. Fixed cells were observed by scanning and transmission electron microscopy. Results indicated that the cells were able to infiltrate into pores at pressures far below those predicted by existing theory for small-curvature cell deformation, and even below those pressures predicted by the law of Laplace. Cells readily deformed into 0.2 μm pores at pressures as low as 2 mmHg and into 0.1 μm pores at pressures as low as 5 to 10 mmHg. Results for 0.05 μm membranes was less conclusive, but no convincing evidence of infiltration was observed for pressures up to 200 mmHg. Based on microscopic evidence, we speculate that the mechanism of initial infiltration may be the result of the aspiration and elongation of pre-formed cell surface features such as microvilli. These results have important implications for design of membrane-based cell separation devices, indicating, for example, that a homogeneous pore-size distribution is desirable for cell loading by filtration. The results also have important implications for the study of cell mechanical properties and procedures involving filtration of cell suspensions.

The first chapter describes results from an unrelated project. In this project, we investigated the effects of exposure whole blood to shear stress on cytokine production by mononuclear cells. We employed a Couette flow device to shear blood at shear stresses of 50, 200, and 500 dynes/cm^2 for exposure times of 30 sec or 5 min. We found that shear exposure alone did not stimulate synthesis of any of the cytokines measured, but that exposure to the highest shear stress for 5 min increased synthesis of TNFα and IL-1Ra in response to certain secondary stimulants. Il-1 synthesis was not significantly affected by shear exposure for any of the conditions tested. These results have important implications for the biocompatibility of extracorporeal blood-handling devices such as hemodialyzers and plasmapheresis devices.

Thesis Supervisor: Clark K. Colton
Title: Professor of Chemical Engineering

Acknowledgements

I give thanks to God for the strength, perseverance, and stamina to complete this work. I also thank my wife Debbie for unfailing and continuous support. So many people have given me inspiration and hope throughout the course of my thesis work that it is impossible to list them all. Especially helpful have been the crew of the Colton Lab: Chase Orsello, Sujatha Karoor, Yoshiaki Takemoto, Stathis Avgoustinatos, Abdul Barakat, Brian Laffey, Haiyan Wu, and Susan Lessner. Very special thanks to Ms. Patricia Reilly at the MIT Biological Electron Microscopy facility for help and kindness beyond the call of duty. Also special thanks to Dr. Laurie Miller for expert guidance and assistance in my early years. I am greatly indebted to the Sepracor company (Marlborough, MA) for providing materials, assistance and expertise (special thanks to Dr. Sam Williams, Dr. Abdul Azad, Dr. O.D. Holton, Dr. Eric Lee, and Dr. Ja-young Koo). From a professional perspective, I would like to express my thanks and appreciation to my thesis advisor Professor Clark Colton for having the confidence in me to let me be independent, and for providing demanding standards, constructive criticism, and challenge. From a personal perspective, I will always remember his accessibility, and the ease and informality of our many discussions over these years. Finally, I thank my thesis committee for assistance, guidance direction, focus and space. Individually, and as a group, they have provided a level of support and structure indispensable to the completion of this work. For that I express my deepest gratitude.

Table of Contents

List of Figures

List of Tables

Chapter 1: The Effect of Exposure of Whole Blood to Shear Stress on Synthesis of TNFα, IL-1, and IL-1 Receptor Antagonist by Human Peripheral Blood Mononuclear Cells

1.1 Abstract

Extracorporeal circulation exposes blood to shear stress. Many studies have reported effects of shear stress on morphology and function of various blood cells, but effects on cytokine synthesis have not been studied. We investigated the effect of shear stress on the synthesis of IL-1β, IL-1α, TNFα, and IL-1Ra by human peripheral blood mononuclear cells (PBMC). Whole heparinized blood at room temperature was exposed to shear stresses of 50, 200, or 500 dyne/cm^2 for 5 min or 30 sec and to 980 dyne/cm^2 for 5 sec. PBMC were then separated from sheared blood and cultured for 24 hr with or without lipopolysaccharide (LPS) or *S. epidermidis (S. epi.)*. Total (intra- plus extracellular) cytokine synthesis was measured by specific radioimmunoassay. Viability of cultured PBMC, determined by trypan blue exclusion and lactate dehydrogenase release, was not significantly affected by shear stress. Shear stress without LPS or *S. epi* stimulation did not affect synthesis of IL-1 or TNF-α but did enhance synthesis of IL-1Ra. LPS- or *S. epi*- induced synthesis of IL-1 was not significantly altered by shear stress. In contrast, LPS-induced TNFα synthesis increased with increasing shear stress and was significantly elevated over unsheared controls, whereas *S. epi*-induced TNFα and LPS- or *S. epi*-induced IL-1Ra synthesis were not significantly enhanced by shear. Thus, sublytic trauma, such as exposure to shear stress, affects *in vitro* responses of PBMC to secondary stimuli.

1.2 Introduction

Extracorporeal circulation through devices, as in cardiopulmonary bypass, leukapheresis, plasmapheresis, and hemodialysis, often causes short- and long-term deleterious post-perfusion syndromes (Kaplow and Goffinet, 1968; Craddock et al., 1977a; Hammerschmidt et al., 1978; Henderson et al., 1983; Kieklin et al., 1983; McLeod et al., 1983; Shaldon et al., 1985; Dinarello et al., 1988; Shaldon et al., 1988). Some symptoms, such as transient leukopenia associated with pulmonary sequestration of leukocytes, are caused by contact activation of the complement cascade via the alternative pathway (Craddock et al., 1977a; Craddock et al., 1977b; Hammerschmidt et al., 1978; Kieklin et al., 1983; McLeod et al., 1983; Cheung and Henderson, 1986). Clinically, joint pain, fever, hypotension, headache, and sleepiness occur and many chronic effects of long-term dialysis maintenance such as osteopenia, joint calcification, and degeneration and wasting, may be attributable to the induction of cytokine production, particularly interleukin-1 (IL-1) and tumor necrosis factor (TNF), as a consequence of extracorporeal circulation (Henderson et al., 1983; Shaldon et al., 1985; Dinarello et al., 1988; Shaldon et al., 1988; Dinarello, 1991a; Haeffner-Cavaillon et al., 1993).

Increased IL-1 bioactivity is found in the circulation after *in vivo* (Weingast et al., 1985; Lonnemann et al., 1987; Luger et al., 1987; Bingel et al., 1988) and *in vitro* dialysis (Bingel et al., 1986; Lonnemann et al., 1988a; Lonnemann et al., 1988b). Complement activation alone is not sufficient to induce IL-1 or TNFα synthesis during *in vivo* or *in vitro* dialysis in the absence of a bacterial stimulant such as lipopolysaccharide (LPS). Although the complement fragment C5a induces transcription of cytokine mRNA (Schindler et al., 1990; Schindler et al., 1993), increases in cytokine protein synthesis require subsequent exposure to LPS (Schindler et al., 1990). Pumping blood through a dialyzer associated with very low

levels of complement activation increases synthesis of IL-1β and TNFα in response to subsequent exposure to LPS (Schindler et al., 1990), suggesting that fluid shear stresses may mediate cytokine production. Unlike other mechanisms of bioincompatibility related to shear stress in extracorporeal circulation (Hellums and Hardwick, 1981; McIntire and Martin, 1981; Colton, 1987a; Colton, 1987b; Colton et al., 1994), the effects of shear stress on cytokine synthesis have not been studied. Therefore, we investigated the effect of exposure of human whole blood to controlled shear stress on production of IL-1β, IL-1α, and TNFα by cultured peripheral blood mononuclear cells (PBMC). In addition, the effect of shear stress on the synthesis of interleukin-1 receptor antagonist (IL-1Ra), a naturally occurring IL-1 inhibitor which blocks IL-1 activity by binding to IL-1 receptors (Dinarello, 1991b), was also investigated. Whole blood rather than isolated PBMC suspensions was sheared in order to better maintain physiological rheology and interactions between different cell types.

Blood was sheared in the gap of a coaxial cylinder device consisting of a rotating inner cylinder and a concentric stationary outer cylinder. Concentric cylinder devices have been commonly employed to study the effects of shear on blood cells (Hellums and Hardwick, 1981; McIntire and Martin, 1981; Dewitz et al., 1977; Dewitz et al., 1978; Dewitz et al., 1979; Chittur et al., 1988). This configuration was selected over flow in hollow fibers because of several important advantages: shear stress and residence time could be arbitrarily varied over a wide range without concern for pressure drop limitations in a practical device with a small priming volume, and with a ratio of surface area to contained blood volume that was invariant with shear stress level.

1.3 Materials and Methods

1.3.1 Blood Shearing Procedure

Whole blood was sheared in the gap of a Plasmacell-C® rotating membrane plasma separation device (Fenwal Laboratories, Deerfield, IL), the construction and operation of which has been previously described (Ohashi et al., 1988; Beaudoin and Jaffrin, 1989; Jaffrin et al., 1989; Kaplan et al., 1989). The device, which had a gap width of 0.67 mm and a priming volume of 5 ml was modified by replacing the cylindrical membrane-covered rotor with a non-permeable rotating polycarbonate inner cylinder (kindly provided by Dr. Donald Schoendorfer, Fenwal Laboratories). Blood was sheared at rotation rates of 570, 1250, 2300 and 3600 rev/min (RPM). At 570 RPM, there was Couette flow in the gap, and the shear stress, which was nearly uniform throughout the gap, was calculated from:

$$\tau_{wc}=\frac{\mu\Omega R_i}{d} \tag{1}$$

where μ is the blood viscosity, Ω is the angular velocity (rad/sec), R_i is the radius of the inner cylinder, and d is the gap width. At the higher rotation rates, Taylor vortices were present, and cells were instantaneously exposed to a wide range of shear stresses within the device. The average wall shear stress was estimated from (Beaudoin and Jaffrin, 1989)

$$\tau_w=0.23\tau_{wc}\sqrt{Ta} \tag{2}$$

where Ta is the Taylor number given by

$$Ta=\frac{R_i\Omega d}{\nu}\sqrt{\frac{d}{R_i}} \tag{3}$$

and where ν is the kinematic viscosity. Blood samples were assumed to have a hematocrit of 40%, and blood viscosity was estimated to be 4 cP (Wintrobe et al., 1981; Zydney et al., 1991). The calculated wall shear stresses at the four rotation rates were approximately 50, 200, 500 and 980 dyne/cm^2 , respectively.

Prior to use, the shearing device was disassembled, cleaned, and sterilized with a 3% formalin solution in water which had been subjected to ultrafiltration through a polysulfone membrane to remove pyrogen (Schindler and Dinarello, 1989). The device was then stored assembled and filled with the 3% formalin solution. Before addition of blood, the device was drained and rinsed with 1200 ml of sterile, pyrogen-free isotonic saline (Abbott Laboratories, N. Chicago, IL).

The study was approved by the Human Investigation Review Committee of the New England Medical Center. Heparinized blood samples (10 U/ml) were collected by venipuncture from healthy donors who had not taken any medication for at least seven days. Two 5-ml blood samples were diluted with 10 ml of normal saline in 50-ml sterile polypropylene centrifuge tubes (Beckon and Dickinson, Lincoln Park, NJ) and set aside until the completion of the experiment as controls unexposed to the device (unexposed controls [UE]). Whole blood samples, 5 ml each, were introduced into the shearing device, then inlet and outlet ports were closed, and the blood was sheared. Times for exposure to shear were 5 min or 30 sec at shear stresses of 50 to 500 dyne/cm^2 or 5 sec at 980 dyne/cm^2. A 30 sec exposure time was selected to equal or exceed a typical single-pass exposure time of blood in a hemodialyzer (Colton and Lowrie, 1981) and the 5 min exposure was selected to examine the effect of a residence time substantially longer than that which occurs during extracorporeal circulation. The 5 sec exposure condition was selected to simulate the clinical operation of the Plasmacell-C® device from which our shearing device was constructed. Shearing was

performed at room temperature (≈23 °C). Samples introduced into the device for 5 min or 30 sec without subsequent shearing served as controls exposed to the device (exposed controls [E]). The order of collection of control samples and of the shearing run conditions was varied for each experiment. For some experiments, blood temperature during shearing was monitored with a digital thermometer (Digital Thermometer 500, VWR Scientific, San Francisco, CA). After shear exposure, blood was drained from the device into a 50 ml polypropylene tube. The device was then flushed with 10 ml normal saline which was collected and added to the sheared blood sample, henceforth referred to as the saline-diluted blood sample. Between samples, the shearing device was rinsed with 300 ml normal saline, filled with normal saline, spun at 4000 RPM for 1 min, then rinsed with an additional 300 ml normal saline to remove residue from the previous sample.

1.3.2 Preparation and Culture of PBMC

PBMC were isolated from the saline-diluted blood samples by centrifugation (400×g, 20 °C for 45 min) over Ficoll/Hypaque (specific weight = 1.077 g/ml) (Ficoll Type 400, Sigma Chemical Co., St. Louis, MO; Hypaque-M, 90%, Winthrop Breon Laboratories, New York, NY) prepared with ultrafiltered water. PBMC were harvested from the interface between the Ficoll/Hypaque layer and the saline-diluted plasma layer, washed three times with 45 ml of normal saline, and re-suspended in ultrafiltered RPMI 1640 culture medium (BioWhittaker Walkersville, MD) supplemented with 2 mM L-glutamine, 100 U/ml penicillin and 100 μg/ml streptomycin (GIBCO Laboratories, Grand Island, NY), and 2% (v/v) heat-inactivated human AB serum at a concentration of 5×10^6 viable cells/ml. The harvested PBMC suspensions contain primarily PBMC (lymphocytes and monocytes) but also may include red cells, platelets, and polymorphonuclear leukocytes (PMN) as contaminants.

Cell concentration was determined with a hemocytometer (Reichert Scientific Instruments, Buffalo, NY) and was based on the total number of viable cells present in the PBMC preparations (lymphocytes, monocytes, PMN, and red cells). Viability was determined by Trypan Blue dye exclusion.

To each well of a 24-well tissue culture plate (Falcon 3047, Becton Dickinson Labware, Lincoln Park, NJ), was added a 0.25 ml aliquot of the PBMC preparation and an equal volume of culture medium alone or culture medium containing LPS (0.5 ng/ml final concentration in well, LPS from *E.coli* 055:B5, Sigma) or heat-killed *S.epidermidis* (20 organisms/cell). All LPS was taken from a single lot which was divided into single-use portions and stored at -70°C until used. Cultures were incubated at 37°C in a humidified atmosphere containing 5% CO_2 /95% air for 24 hr. In addition, samples of the saline-diluted plasma were frozen at -20°C until further assay.

After staining with Wright-Giemsa (Diff Quik, Baxter Healthcare Corporation, Miami, FL), differential cell counts were performed in a blinded fashion on slides prepared from whole blood samples and from isolated PBMC suspensions.

1.3.3 Assay for Plasma Hemoglobin

Hemoglobin concentration in saline-diluted plasma samples was measured with a colorimetric assay (Lijana and Williams, 1979) (Diagnostics Procedure 527, Sigma, St. Louis, MO). Hemoglobin concentration in the undiluted plasma and percent red cells lysed was estimated by assuming an average hematocrit of 40%, a hemoglobin concentration of 325 mg/ml RBC (Bacher and Williams, 1970), and negligible volume change in the saline-diluted plasma during PBMC separation.

1.3.4 Assays for Cultured Cell Viability

The viability of cultured cells after 24 hr incubation was determined by Trypan Blue exclusion. In addition, samples of the cultured cells were centrifuged at 1500×g at 4 °C for 40 min, and the cell-free supernatant was assayed for lactate dehydrogenase (LDH) activity by colorimetry (Amador et al., 1963) (Diagnostics Procedure No. 228-UV, Sigma, St. Louis, MO). LDH activity in the supernatant samples was compared to that measured with an equivalent number of cells incubated under the same culture conditions and lysed by the addition of an equal volume of 1% Triton-X100 (Sigma) in 0.2 M Tris-HCl buffer pH 8.2, and the results were expressed as percent lysis of cultured cells. Complete cell lysis in the control suspensions was verified by light microscopy.

1.3.5 Assays For IL-1β, IL-1α, TNFα, IL-1Ra, C5a (des Arg), and C3a (des Arg)

Total cytokine synthesis (cell-associated and secreted) was measured in cultured PBMC samples subjected to three freeze-thaw cycles to lyse the cells (Endres et al., 1988). Cytokine concentrations in the samples were measured by competitive radioimmunoassay (RIA) as previously described and validated for IL-1β (Endres et al., 1988), IL-1α (Lonnemann et al., 1988c), TNFα (van der Meer et al., 1988), and IL-1Ra (Poutsiaka et al., 1991). A binding level of competing, radiolabled cytokine equal to 95% that of a standard containing no cytokine was taken as a measure of the sensitivity of the assays. The 95% binding sensitivity levels were 40 ± 15 pg/ml (n=6) for IL-1β, 65 ± 44 pg/ml (n=2) for IL-1α, 156 ± 5 pg/ml (n=3) for TNFα, and 225 ± 102 pg/ml (n=3) for IL-1Ra.

For determination of C3a (des Arg) and C5a (des Arg), samples of the saline-diluted plasma fraction collected after the Ficoll/Hypaque separation of PBMC were added to Vacutainer tubes containing ethylenediaminetetraacetic acid tripotassium salt (EDTA) (Becton

Dickinson, Rutherford, NJ) at a final concentration of 4 mM and centrifuged at 1000×g for 30 min at 4 °C to remove platelets. The diluted plasma samples were then stored at -70°C until assay. In some experiments, saline-diluted whole blood from unexposed control and device-exposed control samples were collected in EDTA before separation of PBMC, and the saline-diluted plasma was obtained by centrifugation at 1000×g for 30 min at 4°C and stored at -70°C until assay. Positive control samples for complement activation consisted of saline-diluted plasma added to tubes containing zymosan (Sigma) activated by boiling in normal saline with 10 mM disodium EDTA for 15 min at a concentration of 0.5 mg/ml diluted plasma. C3a (des Arg) and C5a (des Arg) concentrations in the saline-diluted plasma samples were measured using commercially available RIA kits (Amersham, UK), and the equivalent concentrations in undiluted plasma were estimated assuming an average hematocrit of 40% and negligible volume change of the saline-diluted plasma during PBMC separation. The sensitivity of the assays was 20 ng/ml and 6 ng/ml of sample for C3a (des Arg) and C5a (des Arg), respectively.

1.3.6 Statistical Analysis

Data were expressed as mean ± SEM of the indicated number of experiments. Differences between results obtained at different shear stresses and a fixed exposure time were analyzed for significance by Repeated Measures Analysis of Variance and the Scheffe F-test (Stat-View software, Brain Power, Calabasas, CA). For experiments including more than one exposure time, differences between long and short exposure times at each shear stress were analyzed for significance using the paired Student's t-test.

1.4 Results

1.4.1 Effect of Shear Stress on Hemoglobin Release, Blood Temperature, and Cell Viability.

Plasma hemoglobin concentration was measured to assess the level of red blood cell lysis in sheared whole blood. Plasma hemoglobin concentration rose with increasing shear stress and with increasing exposure time (table 1.1).

TABLE 1.1 *Plasma Hemoglobin Concentration in Sheared Whole Blood for Exposure Times of 5 sec, 30 sec, and 5 min.*

	Hemoglobin released (mg/dl)(mean ± SEM)		
Exposure time	**5 sec (n=3)**	**30 sec (n=4)**	**5 min (n=8)**
Shear Stress (dyne/cm²)			
0 (Exposed)	a	14 ± 11	15 ± 4
50	a	18 ± 10	17 ± 4
200	a	18 ± 10	42 ± 12
500	a	34 ± 16	126 ± 21
980	35 ± 10	a	a

Unexposed, unsheared controls released 3.5 ± 1.6 mg/dl of hemoglobin (n=8).
a indicates condition not tested.

For 5 min exposure time, cells sheared at 500 dyne/cm^2 shear stress released more hemoglobin than did cells exposed to lower shear stress ($p<0.001$). For 30 sec exposure, there was no significant elevation in plasma hemoglobin concentration over device-exposed controls ($p>0.05$). Similarly, hemoglobin levels for cells exposed to 980 dyne/cm^2 for 5 sec were not significantly elevated over device-exposed controls. More hemoglobin was released with 5 min versus 30 sec shear stress exposure for blood exposed to 500 dyne/cm^2 ($p<0.01$) and 200 dyne/cm^2 ($p<0.04$). The highest concentration measured (126 ± 21 mg/dl) is near or below the level considered clinically toxic (100-160 mg/dl, (Guccione, 1967; Goodale and

maximum temperature rise during shearing was 5.1 ± 0.6 °C (mean ± SD, n=3) with blood sheared at 500 dyne/cm^2 for 5 min. Initially blood was at ambient room temperature.

The viability of cultured cells was determined with sheared samples both pre- and post-24 hr incubation and with device-exposed and unexposed unsheared control samples. Viability determined by Trypan Blue exclusion was consistently greater than 90 % and was not significantly affected by shear stress exposure. In addition, lactate dehydrogenase (LDH) activity measured in cell-free culture medium supernatant from cell cultures after 24 hr incubation was between 9-14 % of the total LDH activity present in equivalent samples in which the cells were lysed. There were no significant differences between unsheared controls and sheared cells.

1.4.2 Effect of Device Exposure and Shear on Complement Activation.

Plasma C3a (des Arg) concentrations were not significantly altered by device or shear exposure (table 1.2). C3a (des Arg) concentrations for device-exposed and unexposed control samples collected immediately after device exposure and before PBMC separation did not significantly differ but were less than the samples collected after PBMC separation ($p<0.01$ by Student's t-test). C5a (des Arg) levels were at or below the detection limit of the assay for each sample.

TABLE 1.2 *C3a Concentrations in Plasma From Sheared Whole Blood for Exposure Times of 5 sec, 30 sec, and 5 min.*

	Plasma C3a (ng/ml)(mean ± SEM)			
	Pre-PBMC isolation	Post-PBMC isolation		
Exposure Time	**5 min (n=4)**	**5 sec (n=3)**	**30 sec (n=4)**	**5 min (n=4)**
Shear Stress (dyne/cm²)				
0 (Exposed)	820 ± 190	a	1880 ± 530	1650 ± 180
50	a	a	1640 ± 250	1790 ± 250
200	a	a	1750 ± 280	1770 ± 120
500	a	a	1790 ± 200	1900 ± 140
980	a	1870 ± 250	a	a

Plasma C3a levels for unexposed, unsheared controls were 670 ± 130 ng/ml pre-PBMC isolation (n=4) and 1760 ± 280 ng/ml post-PBMC isolation (n=4).
a indicates condition not tested.

1.4.3 Characterization of Cell Populations.

No significant changes in differential counts between samples exposed to shear stress and control samples were observed for whole blood smears. In contrast, red cells in the PBMC preparations increased with shear stress for 5 min exposure times (table 1.3). Red cell concentrations were higher for 500 dyne/cm^2 than for other test conditions ($p<0.04$, 500 vs. 200 dyne/cm^2; $p<0.001$, 500 dyne/cm^2 vs. each other condition). This red cell contamination led to a decrease in cultured PBMC concentration for samples exposed to 500 dyne/cm^2 ($p<0.05$, 500 vs. 200 dyne/cm^2; $p<0.001$, 500 dyne/cm^2 vs. all other conditions). Cytokine synthesis results were reported on the basis of the number of PBMC present (not including contaminating cells). No significant differences between test conditions were observed for 30

sec exposures. Polymorphonuclear leukocyte (PMN) concentration and monocyte to lymphocyte ratio in PBMC preparations did not vary in any of the test conditions studied.

TABLE 1.3 *PBMC Fraction Differential Cell Counts After 5 min Exposure to Shear Stress*

Shear Stress (dyne/cm^2)	PBMC* %	PMN %	Red cells %
0 (Unexposed)	80 ± 5	3 ± 1	17 ± 5
0 (Exposed)	80 ± 4	6 ± 2	15 ± 5
50	77 ± 4	4 ± 1	18 ± 4
200	70 ± 4	4 ± 2	26 ± 4
500	60 ± 5	4 ± 2	36 ± 6

* Defined as lymphocytes plus monocytes
Results represent % of total cells counted in 10 samples for each test condition (mean ± SEM)

1.4.4 Effect of Shear Stress Exposure on Synthesis of IL-1β, TNFα, and IL-1Ra by Cells Cultured in Standard Cell Culture Media.

Concentrations of IL-1β and TNFα were at or below the sensitivity limit for each assay in the absence of bacterial stimulation, indicating that higher IL-1β and TNFα levels measured in other experiments are the result of de novo synthesis and that these cytokines are not stored in the unstimulated cells at levels detectable by the assay (figure 1.1 top and center). In contrast, the amount of IL-1Ra measured (figure 1.1 bottom), for which human serum in the media acts as a stimulus (Poutsiaka et al., 1991), was much greater than that of IL-1β and TNFα. Furthermore, after 5 min exposure time, there was a shear-dependent increase in IL-1Ra synthesis. IL-1Ra induced by 500 dyne/cm^2 was 3.4 times greater than that measured for exposed controls and was elevated over other test conditions ($p<0.001$). Compared with 30 sec, 5 min exposure time induced more IL-1Ra synthesis for shear stresses

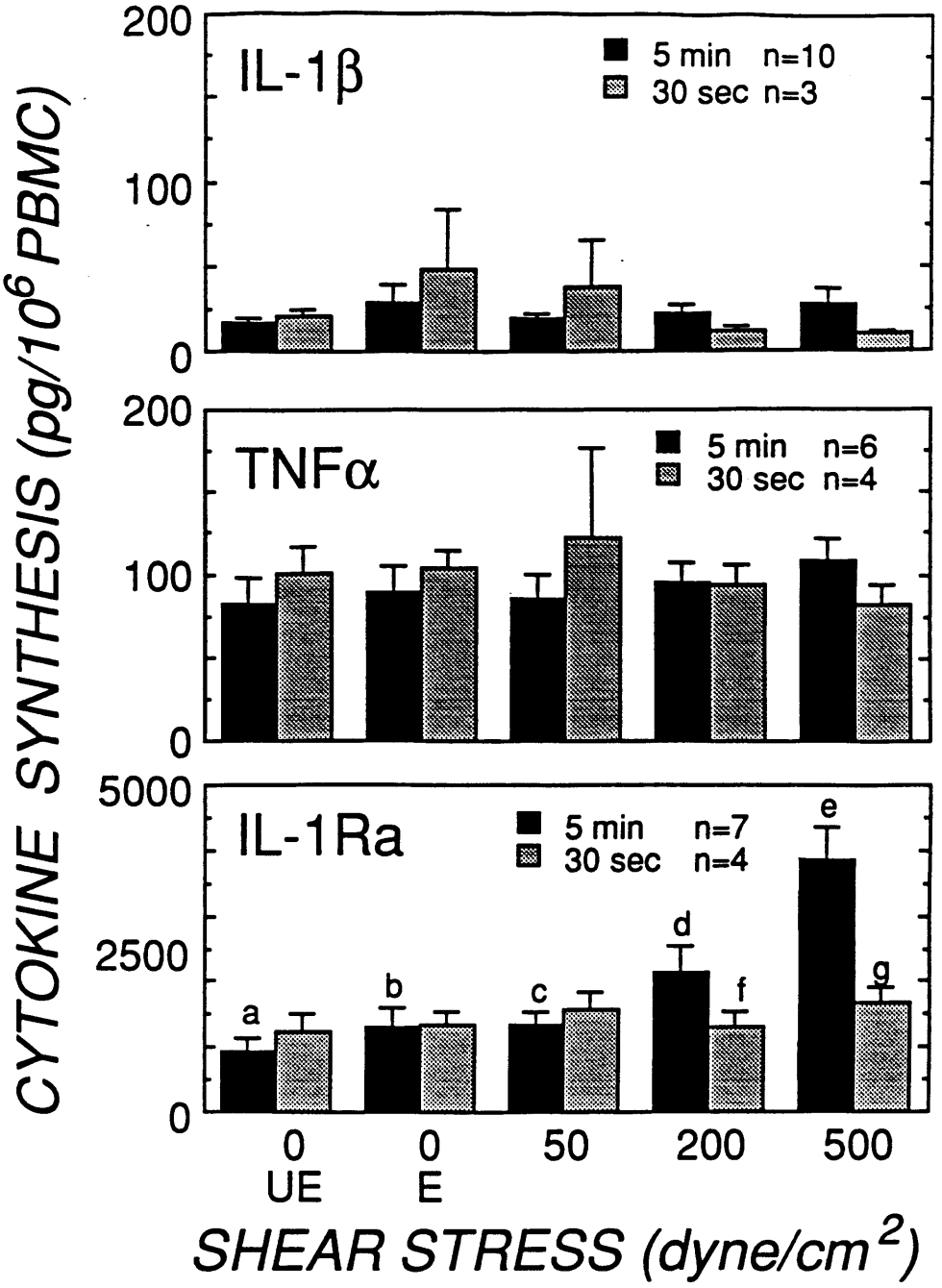

Figure 1.1 Effect of shear stress exposure on synthesis of IL-1β, TNFα, and IL-1Ra by PBMC cultured without bacterial stimulants. PBMC were separated from whole blood samples, cultured for 24 hr in RPMI 1640 supplemented with 1% human AB serum, and IL-1β, TNFα , and IL-1Ra concentrations were determined by RIA. Test conditions included UE (unexposed, unsheared control) and E (device-exposed, unsheared control). Exposure times are 5 min (solid bars) or 30 sec (shaded bars). Results shown are mean ± SEM for n experiments. For IL-1Ra and 5 min exposure time the following differences are significant: e vs. a, e vs. b, e vs. c ($p<0.001$) and e vs. d ($p<0.01$). In addition, for the experiments which included a 30 sec exposure time, IL-1Ra levels are greater for 5 min than for 30 sec exposure for d vs. f and e vs. g ($p<0.05$).

of 200 and 500 dyne/cm^2 ($p<0.01$). Exposure to 30 sec of shear did not affect IL-1Ra synthesis.

1.4.5 Effect of Shear Stress Exposure on Synthesis of IL-1β, IL-1α, TNFα, and IL-1Ra in Response to a Low Concentration of LPS.

Cells not exposed to shear or the shearing device (unexposed controls) and subsequently incubated with LPS synthesized 2550± 330 pg of IL-1β, 8300 ± 1600 pg of IL-1α, 1030 ± 170 pg of TNFα, and 5800 ± 1000 pg of IL-1Ra per 10^6 PBMC. Thus, LPS induced a 10- to 100-fold increase in synthesis of these cytokines. Shear exposure did not affect LPS-induced synthesis of IL-1β, IL-1α, and IL-1Ra (figure 1.2). In contrast, LPS-induced TNFα synthesis rose in response to increasing shear stress after 5 min exposure ($p<0.005$, 500 vs. 200 dyne/cm^2; $p<0.001$, 500 dyne/cm^2 vs. each other condition) (figure 1.2 bottom left). Synthesis of TNFα by cells exposed to 500 dyne/cm^2 for 5 min was 3-fold greater than that of device-exposed controls and over 4-fold greater than that of unexposed controls. Shear stress exposure for 30 sec also increased TNFα production but to a lesser extent ($p<0.05$, 500 dyne/cm^2 vs. device-exposed controls). In cells exposed to 50 or 500 dyne/cm^2, 5 min of shear induced more TNFα than did 30 sec ($p<0.04$).

1.4.6 Effect of Shear Stress Exposure on Synthesis of IL-1β, IL-1α, TNFα, and IL-1Ra in Response to *S. epidermidis* Stimulation.

Cells unexposed to shear or the shearing device and subsequently incubated with *S. epidermidis* synthesized 6000 ± 1700 pg of IL-1β, 6000 ± 1450 pg of IL-1α, 6700 ± 2100 pg of TNFα, and 6000 ± 940 pg of IL-1Ra per 10^6 PBMC. In contrast to LPS stimulation, *S. epidermidis* did not induce significant changes in cytokine synthesis after shear or device exposure (figure 1.3). Specifically, there was no effect on TNFα production.

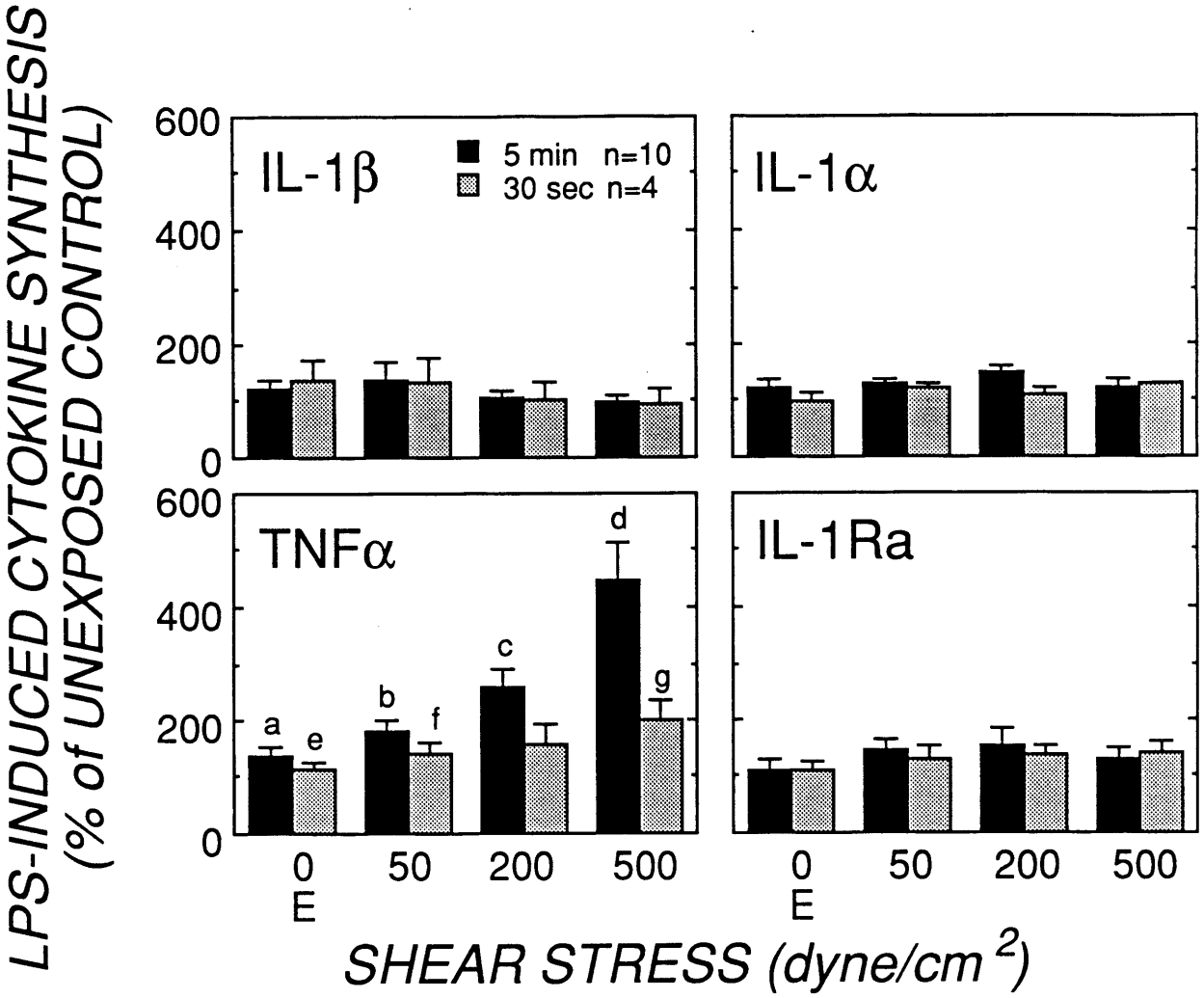

Figure 1.2 Effect of shear stress exposure on Il-1β, IL-1α, TNFα, and IL-1Ra synthesis by cultured PBMC in response to LPS stimulation. PBMC were separated from whole blood samples, cultured for 24 hours in RPMI 1640 containing 0.5 ng/ml LPS, and IL-1β, IL-1α, TNFα, and IL-1Ra concentrations were determined by RIA. Results shown are relative cytokine production as a percentage of unexposed control levels (mean ± SEM) for n experiments. Unsheared, unexposed control cytokine concentration = 100% for each experiment (see text for values). For TNFα and 5 min exposure time the following differences are significant: d vs. a, d vs. b ($p<0.001$); d vs. c ($p<0.005$). For TNFα and 30 sec exposure time, g vs. e is significant ($p<0.04$). In addition, for the experiments which included a 30 sec exposure time, TNFα levels are greater for 5 min exposure than for 30 sec exposure for b vs. f and d vs. g ($p<0.04$).

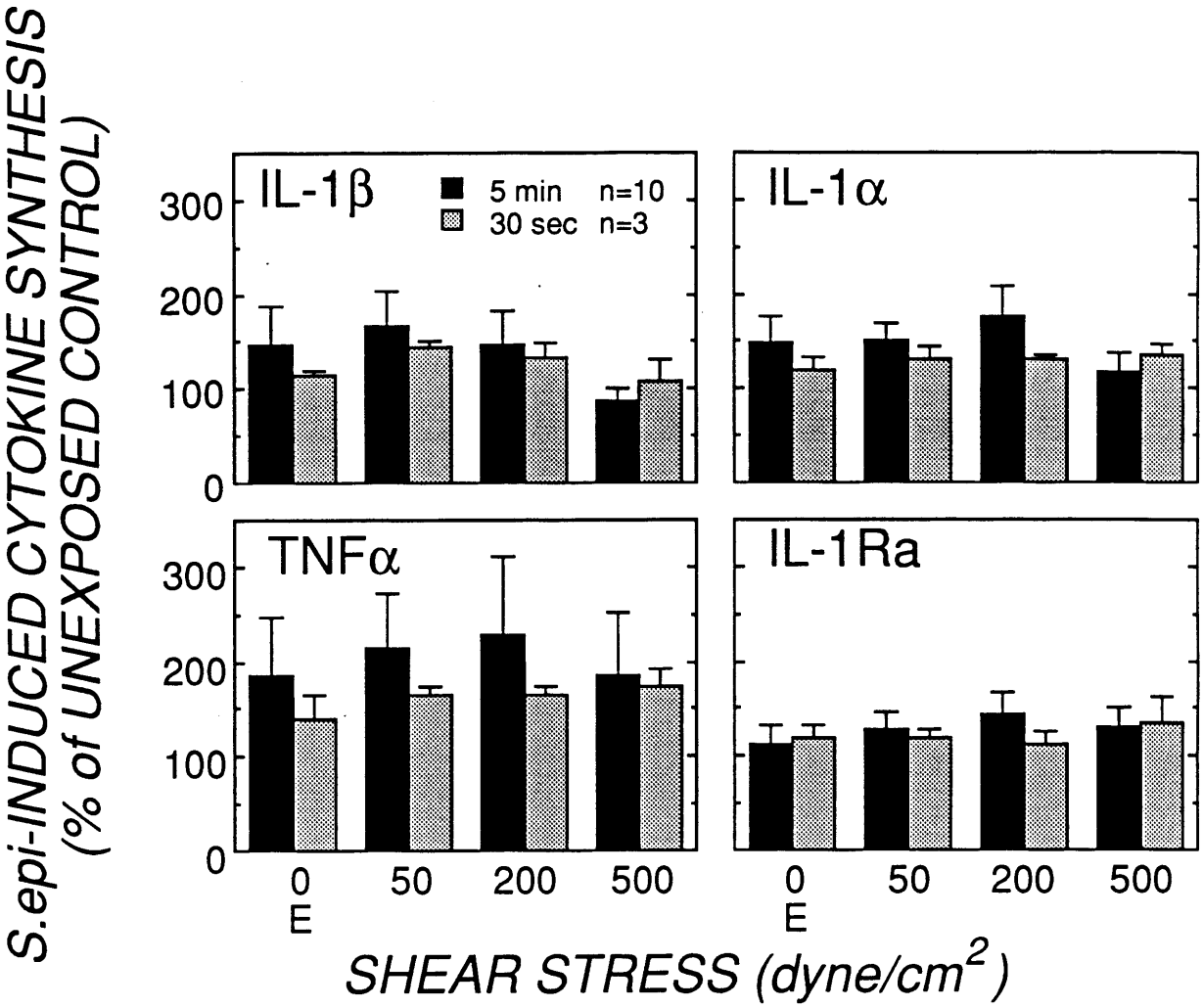

Figure 1.3 Effect of shear exposure on IL-1β, IL-1α, TNFα, and IL-1Ra synthesis by cultured PBMC in response to stimulation by *S. epidermidis*. PBMC were separated from whole blood samples, cultured for 24 hr. in RPMI containing heat-killed *S. epidermidis* (20 organisms/cultured cell), and IL-1β, IL-1α, TNFα, and IL-1Ra levels were determined by RIA. Results shown are relative cytokine production as a percentage of unexposed control levels ± SEM for n experiments. Unsheared, unexposed control cytokine concentration = 100% for each experiment (see text for values).

Exposure of cells to the highest shear stress tested, 980 dyne/cm^2, for 5 sec had no effect on the synthesis of the cytokines studied (figure 1.4).

1.5 Discussion

Our results show that after exposure of whole blood to relatively high shear stresses (500 dyne/cm^2 for 5 min or 980 dyne/cm^2 for 5 sec), isolated PBMC remain viable and functional. Exposure to shear stress did not induce spontaneous synthesis of IL-1β or TNFα by PBMC cultured for 24 hr. By contrast, the synthesis of serum-induced IL-1Ra and LPS-induced TNFα increased in a shear and exposure time dependent fashion. These effects were cytokine and stimulant specific: shear stress exposure did not alter IL-1β, IL-1α, nor LPS-induced IL-1Ra synthesis nor *S. epidermidis*-induced synthesis of the cytokines studied. Thus, nonspecific alteration of cytokine synthesis after shear stress exposure did not occur. This suggests that shear stress differentially regulates synthesis of different cytokines.

We chose to shear whole blood, rather than isolated PBMC, in order to maintain the intercellular interactions and physiological blood rheology. Because of the complex nature of blood, it is difficult to elucidate definitive causes of the observed effects. For example, effects on PBMC may be mediated by shear stress exposure alone or in addition by bioactive substances released from other cell types, such as platelets, which might be present in the sheared blood sample prior to PBMC isolation or might be released by contaminating cells present in the cultured PBMC preparations. The mechanism of the "priming" effect of shear stress exposure on IL-1Ra synthesis and LPS-induced TNFα synthesis is unknown. Shear exposure could alter gene transcription, post-transcriptional processing, or translational efficiency of these cytokines. For example, shear stress has been demonstrated to selectively regulate gene expression in vascular endothelial cells via a *cis*-acting shear stress response

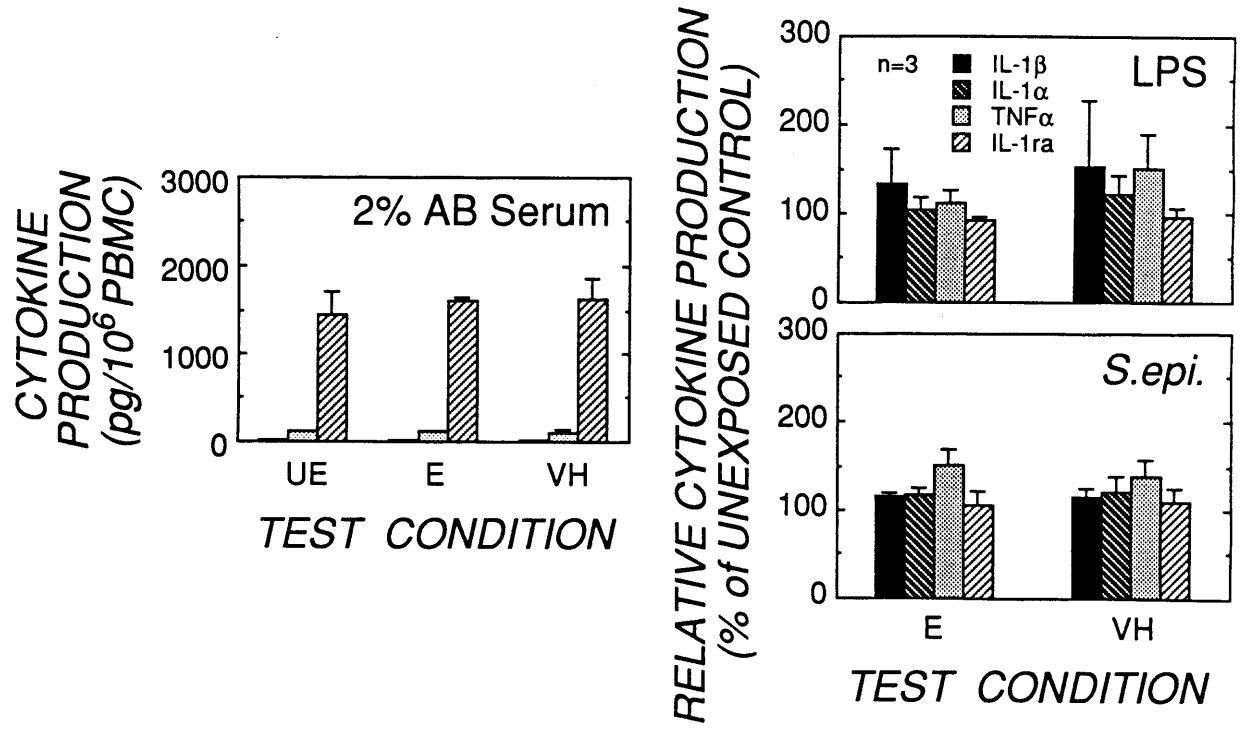

Figure 1.4 Effect of 5 sec exposure to very high shear (980 dyne/cm^2) on IL-1β, IL-1α, TNFα, and IL-1Ra synthesis by cultured PBMC without bacterial stimulation (left), or in response to stimulation by LPS (right top) or *S. epidermidis* (right bottom) PBMC were separated from whole blood samples and cultured as previously described for each stimulation condition, and IL-1β (solid bars), IL-1α (dark diagonal lined bars), TNFα (shaded bars), and IL-1Ra (light diagonal lined bars) levels were determined by RIA. IL-1α was not measured for samples cultured without bacterial stimulation (left). Results shown are actual cytokine production (synthesis) in pg/10^6 PBMC for samples cultured without bacterial stimulants (2 % AB Serum, left), or relative cytokine production as a percentage of unexposed control levels (unsheared, unexposed control cytokine concentration = 100%) for LPS- and *S. epi.*-stimulation (right). Results shown are mean ± SEM for n = 3 experiments.

element within the promoter of genes whose transcriptional activity is shear-stress sensitive (Resnick et al., 1993; Nagel et al., 1994). Evidence also indicates that extracellular signaling ligands which bind to certain receptors on mononuclear cells activate a common nuclear signal transduction pathway which, through differential use of latent cytoplasmic proteins, can evoke differential and synergistic responses in gene activation (Sadowski et al., 1993; Darnell et al., 1994). Thus, interactions with other shear-exposed cells or shear-induced release of other cell products may also be important. For example, shear stresses in the range of the 200 to 500 dyne/cm^2 for 5-10 min duration cause platelet aggregation, release of ATP, ADP, and serotonin, and substantial platelet lysis (Brown et al., 1975; Anderson et al., 1979; Hellums and Hardwick, 1981). Shear stress also affects PMN, inducing increased aggregation and adhesion (McIntire et al., 1976; Dewitz et al., 1978; Rhee and McIntire, 1986a) and sublytic release of both primary and specific granules (McIntire and Martin, 1981; Dewitz et al., 1977; Dewitz et al., 1979). Responses in PMN and platelets may be coupled via arachidonic acid metabolites (Rhee and McIntire, 1986a; Rhee and McIntire, 1986b; McIntire et al., 1987). In addition, exposing PBMC suspensions to shear stress interferes with T cell activation in response to the lectin phytohemagglutinin-P and inhibits IL-2 synthesis by T cells (Chittur et al., 1988).

Activated complement fragments (especially C5a) stimulate transcription of IL-1β and TNFα mRNA and cause priming of IL-1β and TNFα protein synthesis in response to a secondary challenge with LPS (Schindler et al., 1990). This effect may explain why extracorporeal devices which expose blood to complement-activating materials, such as cellulose, induce more cytokine synthesis than those constructed of low-complement-activating materials (Bingel et al., 1988). Synthesis of IL-1Ra and LPS-induced TNFα by PBMC exposed to 500 dyne/cm^2 for 5 min was over 300% greater than that of device-

exposed controls. By comparison, *in vitro* circulation of blood through a cuprammonium dialyzer, which generates C5a and induces TNFα mRNA, increased TNFα synthesis 219% over control levels after stimulation with LPS (Schindler et al., 1990). Thus, "priming" by shear exposure can exceed that of complement activating materials. In our experiments, saline-diluted plasma collected in EDTA after PBMC separation contained no detectable C5a activity. Plasma C3a activity was less than half that reported in plasma collected from efferent lines of extracorporeal devices with cellulosic membranes (Chenoweth, 1984). This activity may be due in part to classical pathway activation during the time the blood is stored anticoagulated with heparin before the addition of EDTA to the plasma after PBMC separation (Hugli and Chenoweth, 1980). In addition, C3a activity was not affected by shear stress or device exposure, thus differences in complement activation cannot account for differences in cytokine synthesis observed in our experiments.

Exposure of blood to shear stress is an unavoidable aspect of extracorporeal circulation. Most extracorporeal devices, such as hemodialyzers, subject blood to fluid shear stresses less than 50 dyne/cm^2 with exposure times of 1 min or less (Colton and Lowrie, 1981). Our results suggest that at these levels of shear stress, cytokine synthesis by cultured PBMC is indistinguishable from cultured PBMC isolated from unsheared whole blood. However, shear-dependent increases in IL-1Ra and LPS-induced TNFα synthesis suggest differences in the *in vivo* consequences of extracorporeal circulation at high shear stresses, especially with additional stimuli such as endotoxin contamination of dialysate fluid, infections, or absorption of microbial products via lung or intestinal capillaries. The present study is especially relevant to devices employing Taylor vortices for enhanced mass transfer, such as the rotating membrane filter for plasma separation from blood (Ohashi et al., 1988; Beaudoin and Jaffrin, 1989; Jaffrin et al., 1989; Kaplan et al., 1989). We have observed that

neither the onset of Taylor vortex flow, nor typical clinical operating conditions of the rotating plasma filter (980 dyne/cm^2 for 5 sec) significantly affects cytokine synthesis by PBMC.

In summary, mechanical trauma such as shear stress at sublytic levels can enhance the synthesis of some but not all cytokines after exposure to a secondary challenge. Shear stress levels required to alter cytokine synthesis exceeded those typically found in most extracorporeal devices. In addition, shear stress alone did not alter *in vitro* cytokine synthesis in any of our experiments. Investigation of cytokine-related consequences of shear stress exposure after clinical use of extracorporeal circuits would enhance understanding of the contribution of shear stress to extracorporeal circulation bioincompatibility.

1.6 Acknowledgements

This research was supported in part by a grant from the Whitaker Health Sciences Fund. The authors thank Drs E.Vannier, D. Poutsiaka, E.V. Granowitz, B.D. Clark, and L. Shapiro. Also Scott F. Orencol, Nathan H. Margolis and Michael Callahan for valuable assistance and helpful discussions.

1.7 References

Amador E., L.E. Dorfman, and W.E.C. Wacker. 1963. Serum lactate dehydrogenase activity: Analytical assessment of current assays. *Clinical Chemistry*. 9:391-399.

Anderson G.H., J.D. Hellums, J. Moake, and C.P. Alfrey. 1979. Platelet response to shear stress: Changes in serotonin uptake, serotonin release, and ADP induced aggregation. *Thrombosis Research*. 13:1039-1047.

Bacher R.P., and M.C. Williams. 1970. Hemolysis in capillary flow. *Journal of Laboratory and Clinical Medicine*. 76:485-496.

Beaudoin G., and M.Y. Jaffrin. 1989. Plasma filtration in couette flow membrane devices. *Artificial Organs*. 13:43-51.

Bingel M., G. Lonnemann, S. Shaldon, K.M. Koch, and C.A. Dinarello. 1986. Human interleukin-1 production during hemodialysis. *Nephron*. 43:161-163.

Bingel M., G. Lonnemann, K.M. Koch, C.A. Dinarello, and S. Shaldon. 1988. Plasma interleukin-1 activity: The influence of dialysis membranes. *Nephron*. 50:273-276.

Brown C.H., L.B. Leverett, C.W. Lewis, C.P Alfrey, and J.D. Hellums. 1975. Morphological, biochemical, and functional changes in human platelets subjected to shear stress. *Journal of Laboratory and Clinical Medicine.* 86:462-471.

Chenoweth D.E. 1984. Complement activation during hemodialysis: Clinical observations, proposed mechanisms and theoretical implications. *Artificial Organs.* 8:281-287.

Cheung A.K., and L.W. Henderson. 1986. Effects of complement activation by hemodialysis membranes. *American Journal of Nephrology.* 6:81-91.

Chittur K.K., L.V. McIntire, and R.R. Rich. 1988. Shear stress effects on human T cell function. *Biotechnology Progress.* 4:89-96.

Colton C.K., and E.G. Lowrie. 1981. Hemodialysis: physical principles and technical considerations. *In* The Kidney 2nd ed., vol. 2. B.M. Brenner, and F.C. Rector Jr., editors. Saunders, New York, NY. 2425-2489.

Colton C.K. 1987a. Analysis of membrane processes for blood purification. *Blood Purification.* 5:202-251.

Colton C.K. 1987b. Quantitation of membrane biocompatibility. *Contributions to Nephrology.* 59:110-125.

Colton C.K., R.A. Ward, and S. Shaldon. 1994. Scientific basis for assessment of biocompatibility in extracorporeal blood treatment. *Nephrology Dialysis Transplantation.* 9 [Suppl. 2]: 11-17.

Craddock P.R., J. Fehr, K.L. Brigham, R.S. Kronenberg, and H.S. Jacob. 1977a. Complement and leukocyte-mediated pulmonary dysfunction in hemodialysis. *New England Journal of Medicine.* 296:769-774.

Craddock P.R., J. Fehr, D. Hammerschmidt, J.G. White, A.P. Dalmasso, and H.S. Jacob. 1977b. Complement (C5a)-induced granulocyte aggregation *in vitro*: A possible mechanism of complement-mediated leukostasis and leukopenia. *Journal of Clinical Investigation.* 60:260-264.

Darnell Jr. J.E., I.M. Kerr, and G.R. Stark. 1994. Jak-STAT pathways and transcriptional activation in response to IFNs and other extracellular signaling proteins. *Science.* 264:1415-1421.

Dewitz T.S., R.R. Martin, T.C. Hung, and L.V. McIntire. 1977. Mechanical trauma in leukocytes. *Journal of Laboratory and Clinical Medicine.* 90:728-736.

Dewitz T.S., R.R. Martin, R.T. Solis, J.D. Hellums, and L.V. McIntire. 1978. Microaggregate formation in whole blood exposed to shear stress. *Microvascular Research.* 16:263-271.

Dewitz T.S., L.V. McIntire, R.R. Martin, and H.P. Sybers. 1979. Enzyme release and morphological changes in leukocytes induced by mechanical trauma. *Blood Cells.* 5:499-510.

Dinarello C.A., K.M. Koch, and S. Shaldon. 1988. Interleukin-1 and its relevance in patients treated with hemodialysis. *Kidney International.* (Supp 33):S21-S26.

Dinarello C.A. 1991a. Interleukin-1 and interleukin-1 antagonism. *Blood.* 77:1627-1652.

Dinarello C.A., and R.C. Thompson. 1991b. Blocking IL-1: Interleukin 1 receptor antagonist *in vivo* and *in vitro*. *Immunology Today.* 12:404-410.

Endres S., R. Ghorbani, G. Lonnemann, J.W.M. van der Meer, and C.A. Dinarello. 1988. Measurement of immunoreactive interleukin-1β from human mononuclear cells: Optimization of recovery, intrasubject consistency, and comparison with interleukin-1α and tumor necrosis factor. *Clinical Immunology and Immunopathology.* 49:424-438.

Goodale R.H., and F.K. Widmann. 1969. Clinical interpretation of laboratory tests 6th ed.. F.A. Davis Co., Philadelphia.

Guccione E. 1967. Biomedical engineering. *Chemical Engineering.* 74:107-124.

Haeffner-Cavaillon N., G. Jahns, J.L. Poignet, and M.D. Kazatchkine. 1993. Induction of interleukin-1 during hemodialysis. *Kidney International.* 43 (Suppl 39):S139-S143.

Hammerschmidt D.E., P.R. Craddock, J. McCullough, R.S. Kronenberg, A.P. Dalmasso, and H.S. Jacob. 1978. Complement activation and pulmonary leukostasis during nylon fiber filtration leukapheresis. *Blood.* 51:721-730.

Hellums J.D., and R.A. Hardwick. 1981. Response of platelets to shear stress - A review. *In* The Rheology of Blood, Blood Vessels and Associated Tissues. D.R. Gross, and N.H.C. Hwang, editors. Sijthoff and Noordhoff, Inc., Alphenaan den Rijn, The Netherlands. 160-183.

Henderson L.W., K.M. Koch, C.A. Dinarello, and S. Shaldon. 1983. Hemodialysis hypotension: The interleukin hypothesis. *Blood Purification.* 1:3-8.

Hugli T.E., and D.E. Chenoweth. 1980. Biologically active peptides of complement: Techniques and significance of C3a and C5a measurement. *In* Immunoassays: Clinical laboratory techniques for the 1980s. R.M. Nakamura, W.R. Dito, and E.S. Tucker III, editors. Alan R. Liss, Inc., New York. 443-460.

Jaffrin M., G. Beaudoin, L.H. Ding, and N. Djennaoui. 1989. Effect of membrane characteristics on the performance of couette rotating plasma separation devices. *ASAIO Transactions.* 35:690-693.

Kaplan A.A., S.E. Halley, J. Reardon, and J. Sevigny. 1989. One year's experience using a rotating filter for therapeutic plasma exchange. *ASAIO Transactions.* 35:262-264.

Kaplow L.S., and J.A. Goffinet. 1968. Profound neutropenia during the early phase of hemodialysis. *Journal of the American Medical Association.* 203:133-135.

Kirklin J.K., S. Westaby, E.H. Blackstone, J.W. Kirklin, D.E. Chenoweth, and A.D. Pacifico. 1983. Complement and the damaging effects of cardiopulmonary bypass. *Journal of Thoracic Cardiovascular Surgery.* 86:845-857.

Lijana R.C., and M.C. Williams. 1979. Tetramethylbenzidine: A substitute for benzidine in hemoglobin analysis. *Journal of Laboratory and Clinical Medicine.* 94:266-276.

Lonnemann G., M. Bingel, K.M. Koch, S. Shaldon, and C.A. Dinarello. 1987. Plasma interleukin-1 activity in humans undergoing hemodialysis with regenerated cellulosic membranes. *Lymphokine Research.* 6:63-70.

Lonnemann G., M. Bingel, J. Floege, K.M. Koch, S. Shaldon, and C.A. Dinarello CA. 1988a. Detection of endotoxin-like interleukin-1 activity during in vitro dialysis. *Kidney International.* 33:29-35.

Lonnemann G., K.M. Koch, S. Shaldon, and C.A. Dinarello. 1988b. Studies on the ability of hemodialysis membranes to induce, bind, and clear human interleukin-1. *Journal of Laboratory and Clinical Medicine.* 112:76-86.

Lonnemann G., S. Endres, J.W.M. van der Meer, T. Ikejima, J.G. Cannon, and C.A. Dinarello. 1988. A radioimmunoassay for human interleukin-1 alpha: Measurement of IL-1 alpha produced *in vitro* by mononuclear cells stimulated with endotoxin. *Lymphokine Research.* 7:75-84.

Luger A., J. Kovarick, H.K. Stummvoll, A. Urbanska, and T.A. Luger TA. 1987. Blood-membrane interaction in hemodialysis leads to increased cytokine production. *Kidney International.* 32:84-88.

McIntire L.V., T.S. Dewitz, and R.R. Martin. 1976. Mechanical trauma effects on leukocytes. *ASAIO Transactions.* 22:444-449.

McIntire L.V., and R.R. Martin RR. 1981. Mechanical trauma induced PMN leukocyte dysfunction. *In* The Rheology of Blood, Blood Vessels and Associated Tissues. D.R. Gross, and N.H.C. Hwang, editors. Sijthoff and Noordhoff, Inc., Alphenaan den Rijn, The Netherlands. 214-236.

McIntire L.V., J.A. Frangos, B.G. Rhee, S.G. Eskin, and E.R. Hall. 1987. The effect of fluid mechanical stress on cellular arachidonic acid metabolism. *Annals of the New York Academy of Science.* 516:513-524.

McLeod B.C., A. Viernes, and R.J. Sassetti. 1983. Complement activation by plasma separation membranes. *Transfusion.* 23:143-147.

Nagel T., N. Resnick, W.J. Atkinson, C.F. Dewey, and M.A. Gimbrone Jr. 1994. Shear stress selectively upregulates Intercellular Adhesion Molecule-1 expression in cultured human vascular endothelial cells. *Journal of Clinical Investigation.* 94:885-891.

Ohashi K.-I., K. Tashiro, F. Kushiya, T. Matsumoto, S. Yoshida, M. Endo, T. Horio, K. Ozawa, and K. Sakai. 1988. Rotation-induced Taylor vortex enhances filtrate flux in plasma separation. *ASAIO Transactions.* 34:300-307.

Poutsiaka D.D., B.D. Clark, E. Vannier, and C.A. Dinarello. 1991. Production of interleukin-1 receptor antagonist and interleukin-1β by peripheral blood mononuclear cells is differentially regulated. *Blood.* 78:1275-1281.

Resnick N., C.F. Dewey, W. Atkinson, T. Collins, and M.A. Gimbrone Jr. 1993. Platelet-derived growth factor B chain promoter contains a *cis*-acting fluid shear-stress-responsive element. *Proceedings of the National Academy of Sciences USA.* 90:4591-4595.

Rhee B., E.R. Hall, and L.V. McIntire. 1986a. Platelet modulation of polymorphonuclear leukocyte shear induced aggregation. *Blood.* 67:240-246.

Rhee B., and L.V. McIntire. 1986b. Effect of shear stress on platelet-PMN leukocyte interactions. *Chemical Engineering Communications.* 47:147-161.

Sadowski H.B., K. Shuai, J.E. Darnell Jr., and M.Z. Gilman. 1993. A common nuclear signal transduction pathway activated by growth factor and cytokine receptors. *Science.* 261:1739-1743.

Schindler R., and C.A. Dinarello. 1989. A method for removing interleukin-1- and tumor necrosis factor-inducing substances from bacterial cultures by ultrafiltration with polysulfone. *Journal of Immunological Methods.* 116:159-165.

Schindler R., G. Lonnemann, S. Shaldon, K.M. Koch, and C.A. Dinarello CA. 1990. Transcription not synthesis of interleukin-1 and tumor necrosis factor by complement. *Kidney International.* 37:85-93.

Schindler R., S. Linnenweber, M. Schulze, M. Oppermann, C.A. Dinarello, S. Shaldon, and K.M. Koch. 1993. Gene expression of interleukin-1 beta during hemodialysis. *Kidney International.* 43:712-721.

Shaldon S., G. Deschodt, B. Branger, C. Granolleras, C.A. Baldamus, K.M. Koch, M.J. Lysaght, and C. A.Dinarello. 1985. Hemodialysis hypotension: The interleukin-1 hypothesis restated. *Proceedings of the European Dialysis and Transplantation Association.* 22:229-243.

Shaldon S., C.A. Dinarello, K.M. Koch, G. Lonnemann, M. Bingel, C. Granolleras, G. Deschodt, B. Branger, R. Oules, and J. Fourcade. 1988. Interleukin-1 and dialysis. *Advances in Nephrology.* 17:423-424.

van der Meer J.W.M., S. Endres, G. Lonnemann, J.G. Cannon, T. Ikejima, S. Okusawa, J.A. Gelfand, and C.A. Dinarello. 1988. Concentrations of immunoreactive human tumor necrosis factor alpha produced by human mononuclear cells *in vitro*. *Journal of Leukocyte Biology*. 43:216-223.

Weingast J.A., K.M. VanDeKerkhore, S.M. Eiger, M.J. Kluger, and F.K. Port. 1985. Release of pyrogens during clinical hemodialysis. *Transactions of the American Society of Artificial Internal Organs*. 31:359-361.

Wintrobe M.M., G.R. Lee, D.R. Boggs, T.C. Bithell, J. Foerster, J.W. Athens, and J.N. Lukens. 1981. Clinical Hematology. Lea & Febiger, Philadelphia.

Zydney A.L., J.D. Oliver, and C.K. Colton. 1991. A constitutive equation for the viscosity of stored red cell suspensions: Effect of hematocrit, shear rate, and suspending phase. *Journal of Rheology*. 35:1639-1680.

Chapter 2. A Mathematical Analysis of Immunoaffinity Cell Adsorption on Porous Substrates with Cell Detachment by Physical Forces

2.1 Abstract

Selective cell separation has widespread utility in clinical medicine, research, and industrial applications. Immunoaffinity cell separation techniques take advantage of non-covalent molecular interactions between molecules on cell surfaces and solid substrates. Immunoaffinity cell separation techniques show great promise for attaining high selectivity, but currently employed substrates and configurations suffer shortcomings when applied to positive cell separation where it is desirable to recover target cells in a pure and viable state. In this study, we describe a novel concept for performing selective positive cell separations employing porous, functionalized, substrates such as polymer membranes. Porous substrates have several advantages for performing positive cell separations over existing methods. One key advantage is the ability to apply reproducible and well controlled physical forces to adsorbed cells to effect purification and removal. In our proposed configuration, we take advantage of the hydraulic permeability of the substrate both in cell deposition and in generating forces for cell removal.

We performed a mathematical analysis of cell adhesion and detachment to study the effects of design and operating parameters on the feasibility of using shear forces, and normal forces, generated by imposing a pressure drop across the porous support so that the pressure is higher on the side of the support opposite to that on which the cell is adsorbed (back-pressure), for cell removal. Our analysis indicated that the shape and morphology of the

adsorbed cells is critical to the effectiveness of removal by different forces. We showed that shear forces are most effective for removing fully rounded cells. However, for porous substrates having hydraulic permeabilities in the range typical of microporous or loose ultrafiltration membranes, forces generated by modest back-pressure (10 to 1000 mmHg) were predicted to be an effective means for removing adsorbed cells with flattened contact areas having radii > 1μm and separated from the solid substrate by distances on the order of expected bond lengths (10^2 Å). The efficiency of transmitting forces created by application of back-pressure to the cell contact area depends strongly on the internal structure of the porous substrate. Our analysis suggests that substrates which are anisotropic in morphology (i.e. exclude flow within the plane of the substrate or have a transmembrane pressure drop-determining region at the surface to which cells attach which is very thin (on the order of the contact area radius or less)), are the most efficient at force transmission. The overall cell attachment strength depends strongly on the number of ligands and cell surface markers, the mobility of cell surface markers within the plane of the cell membrane, and more weakly on bond affinity. Our analysis suggests that porous substrates, such as polymer membranes, may be an excellent solid phase for immunoaffinity cell separation and cell adhesion studies.

2.2 Introduction

This chapter is the first of five concerned with the design, development, and characterization of a novel immunoaffinity cell separation concept utilizing porous polymer membranes as the solid substrate. In this chapter, we develop a basic mathematical description of cell adhesion and detachment in order to assess feasibility, guide development and experimentation, and investigate the probable effects of important operating parameters. Immunoaffinity methods for cell separation utilize the specificity of non-covalent, reversible,

antibody-antigen/receptor-ligand type bonds between target molecules on a cell surface (markers) and molecules on a solid substrate (ligands) to which they have affinity. Various forms of these methods have been used recently in clinical medicine (Anderson et al., 1990; Foresta et al., 1990; Berenson et al., 1991; Yannelli, 1991; Kato and Radbruch, 1993; Sargent et al., 1994; Brugger et al., 1995), research (Spangrude et al., 1988; Golubev and Sidorva, 1989; Tanaka et al., 1989; Berson et al., 1996), and production of monoclonal antibodies (Horton et al., 1989; Hasthorpe et al., 1990). Currently, the most common techniques employed include column affinity chromatography (Hertz et al., 1985; Berenson et al., 1986a; Berenson et al, 1986b; Berenson et al., 1991), adsorption of cells to derivatized plates and flasks ("panning") (Mage et al., 1977; Wysocki and Sato, 1978; Larsson et al., 1989; Nordon et al., 1994; Berson et al., 1996), adsorption of cells to fibers and meshes (Rutishauser et al., 1974; Jasiewicz et al., 1976; Kokkinopoulos et al., 1992), and adsorption of cells to magnetic beads (Gaudernack et al., 1986; Horton et al., 1989; Tanaka et al., 1989; Foresta et al., 1990) or magnetic colloids (Miltenyi et al., 1990; Manyonda et al., 1992; Kato and Radbruch, 1993). Unfortunately, these solid-phase immunoadsorption techniques have shortcomings when used for positive selection. Serious problems include contamination of target cells with non-specifically adhered or retained cells (low selectivity), and difficulty in removing the positively selected cells from the substrate as well as low capacity and lack of reproducibility. Techniques which employ packed beds or beads such as column affinity chromatography and magnetic beads have a tendency to retain non-target cells through non-specific adherence and physical trapping of cells within the matrix of beads (Basch et al., 1983; Skuse et al., 1988; Janssen and Rios, 1989). In addition to non-specific retention of non-target cells, target cells can be difficult to elute. Common techniques employed to remove cells include treatment with exogenous agents (Basch et al., 1983; Thomas et al.,

1989; Civin et al., 1990; Rasmussen et al., 1992) and physical agitation (Berenson et al., 1986b; Berenson et al., 1991; Colter et al., 1992). These procedures can add undesirable agents to the recovered cell fraction or tend to use physical forces which are not well characterized or reproducible. "Panning" procedures using flat plate or tissue culture flask devices are limited by device size constraints to smaller cell loads ($< 10^8$) and cells are typically detached by long incubations, with physical agitation of the plate or flask, or by scraping the cells off the surface to which they are adsorbed (Mage et al., 1977; Wysocki and Sato, 1978; Berson et al., 1996).

Recently, permeable membranes have also been employed as a solid phase for immunoaffinity cell separation (Mandrusov et al., 1995; Nordon et al., 1996; Nordon et al., 1997). Membranes possess many intrinsic advantages as a cell separation substrate. Since cells adsorb to a flat surface, non-specific entrapment of non-target cells by the matrix can be reduced or eliminated. Also, since membranes can be made in a hollow-fiber geometry, it is possible to design a practical device which has sufficient surface area to process clinical cell loads by packing the fibers close together in a shell and tube-type device. It is also much easier to generate reproducible and uniform detachment forces with shear flow when cells are attached to the lumen of hollow fibers. The membranes utilized by these investigators, however, had very low hydraulic permeabilities (dialysis membranes), and it was necessary to remove cells with the aid of exogenous agents such as hydrochloric acid (Mandrusov et al., 1995) or protease (Nordon et al., 1996) in addition to shear flow.

The goal of this chapter, and the remainder of this thesis, is to investigate a new method of utilizing porous membranes for selective cell separation which more directly utilizes the hydraulic permeability of the membranes for cell adsorption and detachment. Figure 2.1 shows a schematic diagram of the proposed method. The technique comprises a

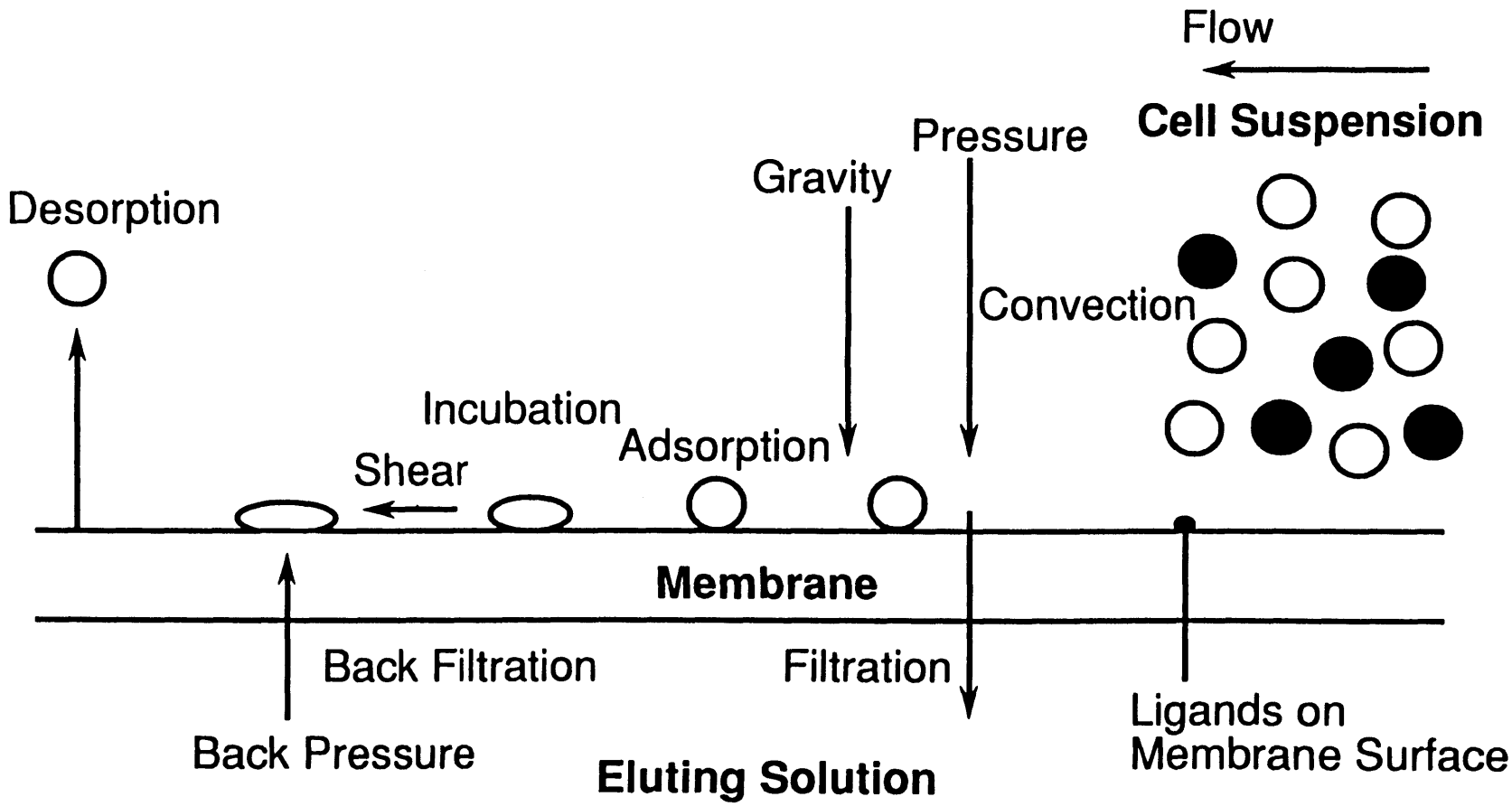

Figure 2.1 A new approach to selective cell separation using ligands immobilized to porous membranes

system in which cell surface marker specific ligands, such as monoclonal antibodies, are covalently immobilized onto porous membranes. The membranes could, in theory, be constructed in many different geometries such as hollow fibers with ligand immobilized to a retentive inside (lumenal) surface, hollow fibers with ligand immobilized to a retentive outside surface, or flat sheets.

The cell separation procedure proceeds via four steps: 1) loading cell mixture, 2) incubation to increase target cell attachment, 3) washing to remove non-specifically adsorbed cells, and 4) detachment of positively selected cells. In step 1, the membrane would initially be free of bound cells. A cell suspension would be introduced into the device so that it is in contact with the functionalized membrane. The cells could either be allowed to settle onto the surface by gravity, or could be brought to the surface by convection by applying an increased pressure to the side of the membrane to which the cells adhere. In step 2, to strengthen target cell adhesion relative to that of non-target cells, the cells would be incubated under static conditions for enough time to form a sufficient number of bonds to secure the cell during washing, and to potentially allow for the development of a flattened contact area. In step 3, the non-specifically-adsorbed cells would be removed from the membrane with laminar shear forces. Finally in step 4, specifically adsorbed cells would be removed by imposing a negative transmembrane pressure drop (back-pressure) where the pressure is greater on the side of the membrane opposite that of cell attachment. The force generated by back-pressure and induced back-filtration must be of sufficient magnitude to rupture the specific bonds formed during the incubation period. The negative transmembrane pressure drop may also be combined with a shearing cross-flow in order to increase detachment force.

The use of back-pressure for cell detachment as opposed to shear flow has several potential advantages. For example, it may provide a more uniform removal than shear for

membranes that are heavily coated with cells. On heavily coated membranes, cells can become shielded from flow forces and torques by the presence of surrounding cells. In addition, cells could potentially be eluted with much smaller volumes of fluid. Forces generated on the cell due to back-pressure may also dislodge the cell more gently than shear since the force acts on the cell in a normal direction and almost exclusively on the contact area reducing the tearing or peeling tendency of shear forces. In addition to supplying removal forces, use of back-filtration can be used to effectively deliver exogenous, bond disrupting agents directly under the contact area where bonds are present while the body of the cell is protected by a buffered cross-flow. Also, since the detachment force due to back-pressure is unique, in that it is a normal force which may act relatively evenly over the contact area, the technique may prove to be a useful new experimental platform to study cell adhesion and detachment behavior.

In practice, cell adhesion strength and cell detachability depend on many parameters. Forces acting on cells in close proximity to a surface may be both specific (such as those mediated by receptor-ligand type interactions) and non-specific (such as those acting between any two surfaces in close proximity including electrostatic attraction or repulsion, van der Waals attraction, and repulsion due to steric exclusion (eg. Dolowy, 1980; Chang and Hsu, 1990)). For many types of materials, such as the functionalized polymer membranes used in our laboratory for protein binding and cell separation (see chapter 3), these non-specific forces are small in comparison to forces of adhesion mediated by receptor-ligand type specific bonds (see also Bell, 1978). Therefore, in our analysis, we will consider only attachment forces caused by specific bond formation. Other critical parameters include the number of target cell surface markers present on the surface of the cell, their mobility within the plane of the cell membrane, and the extent to which they are anchored to the cytoskeletal support structure of

the cell. Also influencing the number of bonds which will be formed is the ligand concentration on the substrate and the affinity of the bonds formed between the ligand and the target cell surface markers.

Critical parameters governing cell detachment by applied back-pressure and shear forces will include cell shape, contact area size and morphology, and, especially for removal by back-pressure, the separation between the contact area and the membrane. Also important for cell removal with back-pressure will be the internal structure and hydraulic permeability of the porous membrane. In order for a pressure-induced force applied to the surface of a porous membrane opposite to that which a cell is attached to be efficiently transferred to the cell-surface contact area, the membrane internal structure needs to be anisotropic, in other words, excluding flow within the plane of the membrane or having a transmembrane pressure drop determining region adjacent to the surface to which cells bind which is thin compared to the radius of the contact area. Otherwise, the force on the contact area, due to an applied transmembrane pressure drop, will be greatly diminished due to flow within the plane of the membrane beneath the contact area.

Several models describing affinity cell adhesion phenomena have been developed of varying levels of complexity in recent years (for reviews see Lauffenburger, 1991; Hammer and Tirrell, 1996). The theoretical framework we will employ in this chapter is a relatively simple deterministic one based on the reaction kinetics of reversible receptor-ligand bond formation which was first proposed by G.I. Bell (Bell, 1978). In the model, Bell proposed a constitutive relationship between the stress on a specific bond and the dissociation rate of the receptor-ligand pair. In this formulation, the reverse reaction rate constant increases exponentially with the applied stress, thereby increasing the rate of bond disruption and ultimately causing cell detachment. This framework has the advantage of simplicity, while

still having the flexibility to investigate the effects of important operating parameters. In addition, since we will assume that all of the bonds in the contact are equally stressed and must be disrupted simultaneously (as opposed to sequential bond breakage for removal by peeling) for cell detachment to occur, it will also tend to yield a conservative (high) estimate of adhesion strength and detachment force which is desirable in determining feasibility and choosing suitable membrane characteristics. In fact, since back-pressure will tend to create a removal pressure which acts normal to, and relatively evenly over, the contact area, even bond stresses and simultaneous bond disruption may be a favored mechanism of cell removal. Also, since we are utilizing a kinetic framework, non-equilibrium effects such as the time required to approach equilibrium can be analyzed. Finally, the effects of cell surface marker redistribution and clustering in the contact area on equilibrium bond density and adhesion strength is easy to incorporate into this framework (Bell, 1979).

Detachment forces on a cell have been described for removal of cells from a surface with laminar shear flow (Hammer and Lauffenburger, 1987). The problem of detachment forces on cell contact areas for cells attached to porous membranes due to back-pressure has not been previously addressed. The problem is, however, analogous to other fluid mechanical situations involving lubrication and levitation. The solution we propose in this study is based on an analysis initially performed to describe drop levitation above a porous plate (Goldshtik, et al., 1986). In our analysis, we treat cell and contact area geometry and morphology as independent parameters to be specified by experimental observation of actual cells. In this chapter, we include a range of probable geometry and morphology in our analysis.

Our results indicate that the number of bonds formed at equilibrium and cell attachment strength depends strongly on ligand density, cell surface marker density (concentration), and cell surface marker mobility, but more weakly on the affinity of the bond.

Cell detachment depends strongly on the shape and size of the cell and contact area. Shear forces are most effective for fully rounded cells with small contact areas, while back-pressure is most effective for cells with larger, more flattened contact areas. Our analysis suggests that for sufficiently anisotropic membranes, back-pressure can be practical and effective at detaching specifically adsorbed cells with separation distances on the order of a typical antibody-receptor bond length and with contact area radii on the order of > 1 μm.

2.3 Mathematical Description of Affinity-Mediated Cell Attachment and Detachment

The goal of this analysis is to develop simple models of cell attachment to and detachment from affinity membranes in order to provide what we believe is a realistic but conservative (high) estimate of the cell detachment forces necessary for cell removal, and to yield a framework with which to investigate the effect of parameters such as cell surface marker/ligand density, bond affinity, and cell shape. We begin by proposing the kinetic framework for cell attachment mediated by specific, reversible , receptor-ligand-type bonds. We then use this framework to estimate the number of bonds at equilibrium and the bond formation rate. The effect of cell surface marker redistribution upon equilibrium bond density is then analyzed. A method for determining the appropriate values for rate and equilibrium constants for reactions between molecules attached to two surfaces (such as a cell contact area and a solid substrate) from the values measured for reactants in solution is then given. Finally, we determine the critical force required to disrupt the bonds attaching the cell to the substrate and the critical transmembrane pressure drops and shear stresses required to apply this force to attached cells.

2.3.1 Cell Adhesion Mediated by Specific Cell Surface Marker-Ligand Bonds

In order to estimate the number of bonds formed between a cell and the affinity membrane, we used a kinetic framework first proposed by G. I. Bell (Bell, 1978) for adhesion between cells or between cells and surfaces when the adhesion is mediated by reversible bonds. The bonds formed between the cell and the affinity membrane surface are non-covalent, antibody-antigen type bonds which form between molecules on the surface (ligands) and target molecules on the cell surface (cell surface markers). For the case where total ligand and cell surface marker concentration is constant over the course of the reaction time, bond formation rate is given by

$$\frac{dN_b}{dt} = k_+^m(N_1 - N_b)(N_2 - N_b) - k_-^m N_b \tag{1}$$

where N_b is the number of bound cell surface markers per unit area in the contact zone, N_1 is the total number of cell surface markers per unit area in the contact zone, and N_2 is the total number of active ligand molecules per unit area in the contact zone. k_+^m and k_-^m are the forward and reverse rate constants for reactants restricted to a two dimensional surface such as a membrane (denoted by superscript m). At equilibrium, ignoring migration of additional cell surface markers into the contact area, the number of bonds is found by equating equation 1 to zero and solving the resulting quadratic equation. Only the negative value of the root is used since the positive value yields a physically impossible bond density (higher than that of the limiting reagent density)

$$N_b = \frac{1}{2}\left[\left(N_1 + N_2 + \frac{1}{K^m}\right) - \sqrt{\left(N_1 + N_2 + \frac{1}{K^m}\right)^2 - 4N_1N_2}\right] \tag{2}$$

where K^m is the effective association constant $K^m = k_+^m/k_-^m$. The time required to approach

kinetic equilibrium can be determined by solving equation 1 for N_b as a function of time (Lauffenburger and Delisi, 1983)

$$N_b(t) = \frac{N_1 p_+ [1 - \exp((p_+ - p_-)k_+^m N_1 t)}{1 - \frac{p_+}{p_-}\exp((p_+ - p_-)k_+^m N_1 t)} \tag{3}$$

where

$$p_+ = \frac{1}{2}\left[\left(1 + \frac{k_+^m N_2 + k_-^m}{k_+^m N_1}\right) + \sqrt{\left(1 + \frac{k_+^m N_2 + k_-^m}{k_+^m N_1}\right)^2 - 4\frac{N_2}{N_1}}\right]$$

and

$$p_- = \frac{1}{2}\left[\left(1 + \frac{k_+^m N_2 + k_-^m}{k_+^m N_1}\right) - \sqrt{\left(1 + \frac{k_+^m N_2 + k_-^m}{k_+^m N_1}\right)^2 - 4\frac{N_2}{N_1}}\right]$$

When the contact time between a cell and surface is not small and cell surface markers are free to diffuse within the plane of the cell membrane, equation 2 will underestimate the number of bonds formed if $N_2 > N_1$ because additional cell surface markers will diffuse into the contact area and form additional bonds. Since we are interested in a system where incubation times of cells with surfaces will be on the order of minutes, cell surface marker redistribution, if it can occur, will probably be an important factor. The effect of free cell surface marker migration into the contact area on the equilibrium bond density N_b can be accounted for by including a balance on those cell surface marker/ligand molecules which can become reactants in the model (Bell, 1979). In the present case, assuming that cell surface markers are freely mobile and that ligands on the substrate are fixed, equation 1 can be rewritten in terms of the free cell surface marker density N_{1f} and free ligand density N_{2f} as follows,

$$\frac{dN_b}{dt} = k_+^m N_{1f} N_{2f} - k_-^m N_b \tag{4}$$

At long times, assuming that binding and diffusion have reached local and global equilibrium over the entire cell, the density of free cell surface markers will be constant over the entire cell membrane. Since the ligands on the substrate (surface 2) are fixed, total ligand density in the contact area will remain constant Then within the contact area at equilibrium

$$N_b = K^m N_{1f} N_{2f} \tag{5}$$

If the reactant densities were N_1 and N_2 prior to contact, and the cell has a surface area A_1, and the substrate has a surface area A_2, then a balance on markers and ligands yields

$$A_1 N_1 = A_1 N_{1f} + a N_b \tag{6}$$

and

$$A_2 N_2 = (A_2 - a) N_2 + a(N_{2f} + N_b) \tag{7}$$

where a is the area of the contact zone available for bond formation. If the substrate is a porous membrane with a surface porosity ε, and it is assumed that the cell is in intimate contact over the entire contact zone then

$$a = \pi R_o^2 (1 - \varepsilon) \tag{8}$$

where R_o is the radius of the contact area. Solving equations 6 and 7 for free marker and ligand densities yields, respectively,

$$N_{1f} = N_1 - \lambda N_b \tag{9}$$

$$N_{2f} = N_2 - N_b \tag{10}$$

where $\lambda = a/A_1$. The total cell marker density in the contact area at equilibrium N_T is equal to the sum of N_{1f} and N_b

$$N_T = N_1 + N_b(1 - \lambda) \tag{11}$$

The equilibrium bond density in terms of N_1 and N_2 is found by substituting equations 9 and 10 into equation 5 and solving for N_b

$$N_b = \frac{1}{2\lambda}\left[\left(N_1 + \lambda N_2 + \frac{1}{K^m}\right) - \sqrt{\left(N_1 + \lambda N_2 + \frac{1}{K^m}\right)^2 - 4\lambda N_1 N_2}\right] \tag{12}$$

An approximate estimate of the mean time for diffusion of a freely mobile cell surface marker into the contact area, assuming that all of the markers which enter the contact area remain there, has been given by G.I. Bell (Bell, 1979)

$$T_d = \frac{2R_c^2}{D^m} \ln\frac{R_c}{R_o} \tag{13}$$

where R_c is the cell radius and D^m is the diffusion constant for the cell surface marker in the plane of the membrane. The equation is only strictly valid when the contact area radius is small compared to the cell radius and for spherical cell geometry . The equation predicts that the mean diffusion time will increase as the radius of the contact area decreases. For example, for a 5 μm cell radius and a diffusion constant of 10^{-10} cm^2/s (typical values range from 10^{-9}-10^{-12} cm^2/s (Axelrod et al., 1978; Aizenbud and Gershon, 1984; Jacobson et al., 1984; Weigel, 1984; Edidin, 1987)), T_d would be about 2 hrs for a contact area radius of 1 μm. But, even though the mean diffusion time into small contact areas is fairly long, the time required for a significant increase in the cell surface marker density in the contact area due to receptor migration is much lower. The mean rate at which cell surface markers enter the

disk, J_d, will equal the total number of markers on the cell outside the contact area ($4\pi R_c^2 N_1$ - $\pi R_o^2 N_1$) divided by T_d

$$J_d = \frac{\pi D^m N_1 (4 - (R_o/R_c)^2)}{2\ln(R_c/R_o)} \tag{14}$$

Now consider a typical binding situation where the ligand density on the substrate is in excess of the initial cell surface marker density by a factor of 10. In this case, the time required to increase the cell surface marker density in the contact area by a factor of 10 ($10x$) to saturate the ligand molecules can be approximated as the number of markers which must enter the contact area divided by the mean rate at which cell surface markers enter the contact area. In general for an increase in cell marker density in the contact area of nx.

$$T_{nx} = \frac{(n-1)\pi R_o^2 N_1}{J_d} = \frac{2(n-1)R_o^2}{D^m(4 - (R_o/R_c)^2)} \ln\frac{R_c}{R_o} \tag{15}$$

For R_c and D^m as before, the time required for cell marker redistribution to come to equilibrium (when all available ligands on the substrate are occupied) for a ten-fold excess ligand density and a contact area of 1μm radius is only about 12 min. Our own experimental observations of specifically adsorbed cells on porous membranes (see chapters 3 to 5) indicate that cell contact area radii were larger than for the case outlined above, and typically were about 0.4 to 1.1 times as large as the average initial (unbound) cell radius; so that, our actual mean diffusion times for cell surface markers could be shorter than the previous estimate. Thus for cell-surface contact times on the order of minutes or more for freely mobile cell surface markers, it is likely that a significant amount of cell surface marker redistribution will occur. The result will be that equation 2 will tend to significantly underestimate N_b and equation 12 will yield a more realistic and conservative (high) estimate of bond density and

attachment strength.

Passive cell receptor redistribution upon binding to a surface with complementary ligands has also been observed directly for the binding of rat basophilic leukemia cells, with fluorescently labelled target receptors (Fcε receptors), to liposomes containing anti-receptor ligands (McCloskey and Poo, 1986). The authors observed qualitatively nearly complete redistribution of the target cell receptors to the contact area within about 15-45 min. In addition, for some experiments they also quantitatively measured the relative fluorescence intensity in the contact area and found that it went up by about a factor of 2 in about 15 min. The authors determined the average cell radius to be 6.45 μm and the average contact area radius to be about 1.8 μm. For means of comparison, for these parameters, equation 15 predicts the time for a 2 fold increase in receptor density in the contact area to be about 4 min and for a ten fold increase to be about 30 min.

2.3.2 Estimation of Rate and Equilibrium Constants for Reaction Between Cell Surface Markers and Ligands on a Solid Substrate

In this section we present a method for applying data obtained from affinity constant and rate constant measurements for reactants in solution to the restricted environment of reaction between a cell and a surface. In solution, reactant molecules are free to move and rotate in three dimensions. Surface-surface reactions restrict translational and rotational freedom to a two-dimensional plane, therefore, the diffusional contribution to the observed reaction rates will be different.

In solution, the reaction of an antigen or hapten with an antibody is theorized to occur via a two-step process, the first of which is diffusion of the reactants into proximity to form an encounter complex AB, and the second of which is the actual binding step to form the bond C

$$A + B \rightleftharpoons AB \rightleftharpoons C \tag{16}$$

where the diffusional rate constants for the first step are d_+ and d_- and the intrinsic reaction rate constants for the second step are r_+ and r_-. Experimentally, however, it is the overall parameters (k_+ and k_-) which are measured for the following reaction

$$A + B \rightleftharpoons C \tag{17}$$

If it is assumed that the concentration of the encounter complex (AB) is small, then the constants for the overall reaction can be expressed as

$$k_+ = \frac{d_+ r_+}{d_- + r_+} \quad , \quad k_- = \frac{d_- r_-}{d_- + r_+} \tag{18}$$

The overall equilibrium constant $K = k_+/k_-$ will be equal to d_+r_+/d_-r_- or simply the product of the intrinsic reaction rate equilibrium constant ($K_r = r_+/r_-$) and a diffusional equilibrium defined as $K_d = d_+/d_-$

$$K = K_r K_d \tag{19}$$

For reactants in solution the diffusional rate constants are (Eigen, 1974)

$$d_+^s = 4\pi (D_A^s + D_B^s) R_{AB} \tag{20}$$

$$d_-^s = 3(D_A^s + D_B^s) R_{AB}^{-2} \tag{21}$$

where the superscript s denotes "in solution" values. $D_A{}^s$ and $D_B{}^s$ are the diffusion constants of species A and B in solution. ($D_A{}^s$ for an antibody is typically about 5×10^{-7} cm^2/s, and $D_B{}^s$ for a ligand of molecular weight 400 would be about 5×10^{-6} cm^2/s (Bell, 1978; Lauffenburger and Delisi, 1983)). R_{AB} is the radius of the encounter complex (typically about 10-20 Å (Bell, 1978; Lauffenburger and Delisi, 1983)). The diffusional equilibrium constant

for reactants in solution will then be

$$K_d^s = \frac{4\pi}{3} R_{AB}^3 \tag{22}$$

For interactions between two cells or between a cell and a surface, the diffusional rate constants reflect the translational and rotational diffusivity of the reactants in the plane of the cell membrane or substrate surface, and can be estimated by (Bell, 1978; Lauffenburger and Delisi, 1983)

$$d_+^m \approx 2\pi \frac{(D_A^m + D_B^m)}{\ln \frac{b}{R_{AB}} - \frac{3}{4}} \tag{23}$$

$$d_-^m \approx 2 \frac{(D_A^m + D_B^m)}{R_{AB}^2 \left(\ln \frac{b}{R_{AB}} - \frac{3}{4} \right)} \tag{24}$$

where the superscript m denotes membrane bound reactants and b is the average separation distance between reactant molecules. The separation b can be estimated as half the mean distance between reactant centers. In the contact area, the total reactant density will be the sum of the cell surface marker and ligand densities, $(N_1 + N_2)$. If we assume that each molecule occupies a disk, then half the separation distance between reactant centers will simply be the radius of the disk,

$$b \approx \sqrt{\frac{1}{\pi (N_1 + N_2)}} \tag{25}$$

The diffusional equilibrium constant now becomes

$$K_d^m = \pi R_{AB}^2 \tag{26}$$

Since the intrinsic reaction rate constants (r_+ and r_-) and equilibrium constant (K_r) are invariant, only differences in the diffusional constants need to be considered when determining constants for reactants on membranes or surfaces from constants measured for reactions in solution. For example, in order to determine forward and reverse rate constants for reactants on membranes or surfaces from values measured with soluble reagents, the intrinsic rate constants r_+ and r_- are calculated from the measured overall rate constants in solution, k_+^s and k_-^s with the relationships given by equations 18, 20, and 21. The diffusive rate constants for two-dimensional reactions are then calculated with equations 23 and 24. Finally, the overall rate constants for a two-dimensional system are determined from equation 18 with r_+, r_-, d_+^m, and d_-^m. To convert from equilibrium constants measured for soluble reagents to an appropriate equilibrium constant for surface-constrained reagents equation 19 is employed noting that the intrinsic reaction rate equilibrium constant (K_r) is invariant. Thus, K^m for surface reactions is related to K^s measured in solution by

$$K^m = K^s\left(\frac{K_d^m}{K_d^s}\right) \tag{27}$$

using the expressions for the diffusional equilibrium constants given by equations 22 and 26

$$K^m = \frac{3}{4}\frac{K^s}{R_{AB}} \tag{28}$$

with R_{AB} = 20 Å, $K^m = K^s(6.225 \times 10^{-15}$ cm^2 moles/L). Table 2.1 shows a range of rate and equilibrium constants calculated for a cell binding to a surface via typical antibody-antigen type bonds. The values for reagents in solution represent a range of typical values measured for antibody-antigen and antibody-hapten reactions (values from Pecht and Lancet, 1977).

The computations were performed assuming a 5 μm radius cell with 10^4 cell surface markers (typical range 10^3-10^5 (Bell, 1978, Darnell et al., 1990)) . Ligand density on the surface was taken as 10 times the cell surface marker density. It was assumed that ligand activity was not affected by immobilization. D_A^s and D_B^s were assumed to be 5×10^{-7} and 5×10^{-6} cm^2/s respectively; R_{AB} was taken as 20 Å; D_A^m for cell surface markers was taken as 1×10^{-10} cm^2/s (Edidin et al., 1976; Bell, 1978; Edidin, 1987), and D_B^m was taken as 0 (antibody immobilized to substrate will not diffuse).

Table 2.1 *Typical Rate and Equilibrium Constant Data for Antibody-Antigen Bonds*

k_+^s ($M^{-1}s^{-1}$)	k_-^s (s^{-1})	K^s (M^{-1})	k_+^m (cm^2/s)	k_-^m (s^{-1})	K^m (cm^2)
6.0×10^8	6.0×10^4	1.0×10^4	3.2×10^{-10}	5.2	6.2×10^{-11}
1.3×10^8	53	2.4×10^6	3.2×10^{-10}	2.1×10^{-2}	1.5×10^{-8}
8.7×10^7	6.7	1.3×10^7	3.2×10^{-10}	4.0×10^{-3}	8.1×10^{-8}
1.9×10^8	1,300	1.5×10^5	3.2×10^{-10}	0.36	9.1×10^{-10}
1.4×10^7	2.4×10^{-4}	5.8×10^{10}	3.2×10^{-10}	8.6×10^{-7}	3.6×10^{-4}
1.1×10^7	1,400	7.9×10^3	3.2×10^{-10}	6.5	4.9×10^{-11}
1.1×10^7	1.2×10^{-3}	9.2×10^9	3.2×10^{-10}	5.6×10^{-6}	5.7×10^{-5}
4.1×10^5	4.9×10^{-4}	8.3×10^8	2.7×10^{-10}	5.1×10^{-5}	5.2×10^{-6}

The values for rate and equilibrium constants for membrane-substrate interactions may now be used with the equations developed earlier to determine reaction rate and bond density. Note in table 2.1 that for the entire range of forward rate constants for reaction in solution, the corresponding values for surface reactions k_+^m are nearly invariant at their diffusion limited value d_+^m which is 3.2×10^{-10} cm^2/s.

2.3.3 Critical Force Required for Breaking Specific Bonds

In this section we develop a method to estimate the force required to rapidly dissociate

an antibody-antigen type bond and to dissociate cells from surfaces which are attached by such bonds. Bell has proposed a method of adjusting the dissociation rate constant k_-^m to account for the reduced lifetime of stressed reversible bonds (Bell, 1978). His method is based on the kinetic theory of the strength of solids (Zhurkov, 1965). Based on this theory, it is postulated that the appropriate reverse rate constant for a bond under stress is

$$k_-^f = k_-^m \exp\left(\frac{\gamma F_b}{kT}\right) \tag{29}$$

where k_-^f is the adjusted reverse rate constant under stress, F_b is the force applied to a bond, k is Boltzman's constant, T is the absolute temperature,and γ is the range in distance of the free-energy minimum of the bond interaction (about 5 Å (Bell, 1978)). When considering the removal of a cell from a surface, the largest estimate of the total force required to break the bonds will be to assume that the bonds in the contact area are equally stressed and must break simultaneously. For such a case equation 29 becomes

$$k_-^f = k_-^m \exp\left(\frac{\gamma F_t}{kTN_b a}\right) \tag{30}$$

where F_t is the total force applied to the cell, N_b is the bond density, and a is the contact area. The bond formation rate with an applied force is obtained from equation 1 with k_-^f replacing k_-^m. The number of bonds at equilibrium for a cell bound to a surface under an applied removal force can be determined from equation 2 or 12 with K^f replacing K^m where

$$K^f = K^m \exp\left(\frac{-\gamma F_t}{kTN_b a}\right) \tag{31}$$

Since the lifetimes for bonds stressed beyond the critical point for breakage will be very short ($<<$ 1 s (Bell, 1978)) compared to the times required for cell surface marker redistribution,

equation 2 is more appropriate to use for determining critical detachment forces than equation 12, so that with an applied force, at equilibrium

$$N_b = \frac{1}{2}\left[\left(N_1 + N_2 + \frac{1}{K^f}\right) - \sqrt{\left(N_1 + N_2 + \frac{1}{K^f}\right)^2 - 4N_1N_2}\right] \tag{32}$$

where K^f is given by equation 31. Figure 2.2 shows a plot of N_b versus F_t for a cell-surface contact area of 5 μm radius and a substrate porosity of 0.1 for low (1), medium (2), and high critical detachment force (3) cases. For an applied force of zero, the equilibrium bond density is given by the non-zero intercept of the curves with the y axis. For low applied forces, the bond density will follow the upper part of the curve (lower part of the curve predicts that bond density increases with removal force and is thus not physically meaningful). Beyond a certain level of total applied force F_t^{crit} there is no longer a solution for N_b and the cell will detach. This critical force can be determined more conveniently by first solving equations 31 and 32 for F_t and noting that the function $F_t(N_b)$ will have a maximum value at F_t^{crit}. Solving equations 31 and 32 for F_t yields

$$F_t = \frac{kTaN_b}{\gamma}\ln(u) \tag{33}$$

where

$$u = K^m\left(N_b - N_1 - N_2 + \frac{N_1N_2}{N_b}\right)$$

Equation 33 will have a maximum value at F_t^{crit} where the first derivative with respect to N_b is equal to zero with

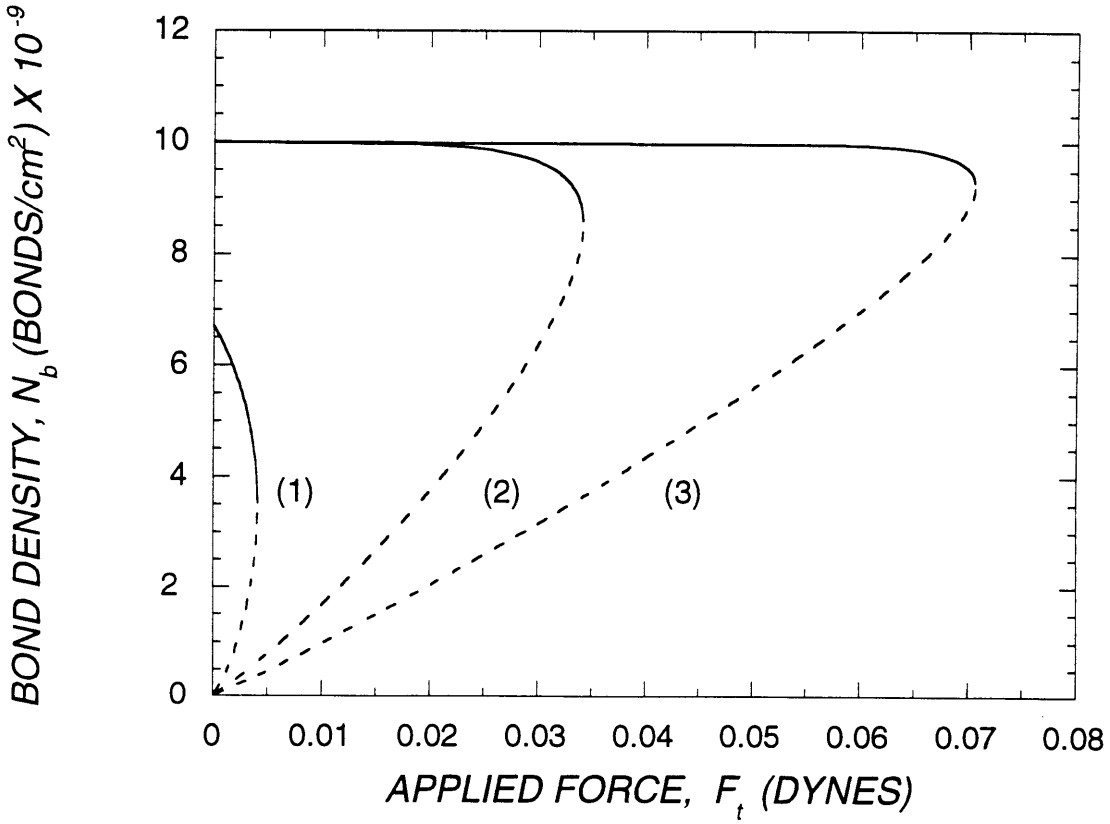

Figure 2.2 Bond density N_b versus total applied force on cell F_t from equation 32 for a contact area of radius $R_o = 5$ μm on a substrate with porosity $\varepsilon = 0.1$. (1) $N_2 = N_1 = 1 \times 10^{10}$ cm^{-2}, $K^s = 10^5$ M^{-1}. (2) $N_2 = 10N_1$, $N_1 = 1 \times 10^{10}$ cm^{-2}, $K^s = 10^7$ M^{-1}. (3) $N_2 = 100N_1$, $N_1 = 1 \times 10^{10}$ cm^{-2}, $K^s = 10^9$ M^{-1}.

$$\frac{dF_t}{dN_b} = \frac{kTa}{\gamma}\left(\ln(u) + \frac{N_b}{u}\frac{du}{dN_b}\right) \tag{34}$$

where

$$\frac{du}{dN_b} = K^m\left(1 - \frac{N_1 N_2}{N_b^2}\right)$$

The critical detachment force is then found by setting equation 34 equal to zero, solving for N_b, and then substituting this value into equation 33 to find F_t^{crit}. The critical force per bond, F_b^{crit} is found by dividing the critical total force by the number of bonds at equilibrium before the application of force calculated with equation 2 or 12, N_{bo}, so that $F_b^{crit} = F_t^{crit}/(N_{bo}\, a)$.

2.3.4 Detachment Force on Cells Due to Back-Filtration Through Porous Membranes and Shear Stress

The force applied to the contact area between a cell and a porous membrane due to back-filtration depends strongly on the size of the contact area, and the separation distance between the cell and the surface. When the separation distance, h, between the cell and the surface is large (order R_c or more) the cell will be acted upon by a force on the order of that predicted for Stoke's Law for drag on a sphere

$$F_t = 6\pi\mu R_c v_o \tag{35}$$

where R_c is the cell radius, μ is the fluid viscosity, and v_o is the fluid velocity given by Darcy's Law

$$v_o = \frac{k_p}{\mu}\Delta P \tag{36}$$

where k_p is the membrane permeability, and ΔP is the pressure drop across the membrane. As the separation decreases to values much smaller than R_c, for a cell with a circular flattened contact area of radius R_o, assuming a fixed v_o, and neglecting forces on the cell outside the contact area, the problem becomes analogous to the force acting on a disk moving towards a plane in a viscous fluid (Denn, 1980) where

$$F_t = \frac{3}{2}\pi\mu v_o \frac{R_o^4}{h^3} \tag{37}$$

Clearly, as h approaches zero, equation 37, which predicts an infinite force, is no longer valid. There exists a scale, h^*, at which the contact area begins to restrict, or "choke" the flow under it. In the limit of $h = 0$, the force cannot exceed $F_t = \pi R_o^2 \Delta P$. Where $\Delta P = P_1 - P_o$ with P_1 being the pressure applied to the porous membrane, and P_o the ambient pressure in the fluid surrounding the cell. This limiting pressure is only attainable when resistance to flow through the membrane is small compared to resistance to flow within the plane of the membrane; this would be the case for anisotropic membranes where the resistance to flow within the plane of the membrane is much higher than for flow through the membrane, or for any membrane where the majority of the pressure drop occurs across a thickness that is small compared to R_o. Comparing $F_t = \pi R_o^2 \Delta P$ to equation 37 with v_o defined by equation 36 suggests that $h^* \sim (k_p R_o^2)^{1/3}$. For a typical hydraulic permeability for a microporous membrane of about 1×10^{-12} m and R_o of 2.5 μm, h^* would be about 200 Å, or very close to the minimum expected gap width for a cell attached to a smooth surface by an antibody which is about 160 Å long (Feinstein and Beale, 1977).

A solution to an analogous flow problem (drop suspension above a porous plate) has been derived for separation distances on the order h^* (Goldshtik et al., 1986). The solution

for anisotropic membranes derived here follows that of Goldshtik et al. We treat the contact area as a flat disk with radius R_o, separated from an anisotropic porous membrane with permeability k_p by a constant gap width h (see figure 2.3 for geometry and notation). Additional forces on the cell due to viscous drag of fluid on the areas of the cell outside the contact area are neglected. The flow over the gap can be described by the Stokes equations in terms of a thin layer lubrication approximation (Batchelor, 1970; Denn, 1980). Assuming that the pressure is uniform in the z direction across the width of the gap, the equations of motion reduce to

$$\frac{\partial p}{\partial r} = \mu \frac{\partial^2 u}{\partial z^2}, \quad \frac{\partial p}{\partial z} = 0 \tag{38}$$

with equation of continuity

$$\frac{1}{r}\frac{\partial ru}{\partial r} + \frac{\partial v}{\partial z} = 0 \tag{39}$$

where u is the radial fluid velocity, and v is the fluid velocity under the gap in the z direction. Equation 38 can be solved with the boundary conditions $u = 0$ at $z = 0$, and $u = 0$ at $z = h$ to yield an expression for the radial velocity u

$$u = -\frac{1}{2\mu} z(h - z)\frac{dp}{dr} \tag{40}$$

The boundary conditions for flow in the z direction are

$$v = 0 \quad at \quad z = h \tag{BC 1}$$

and from Darcy's Law, at the porous membrane surface

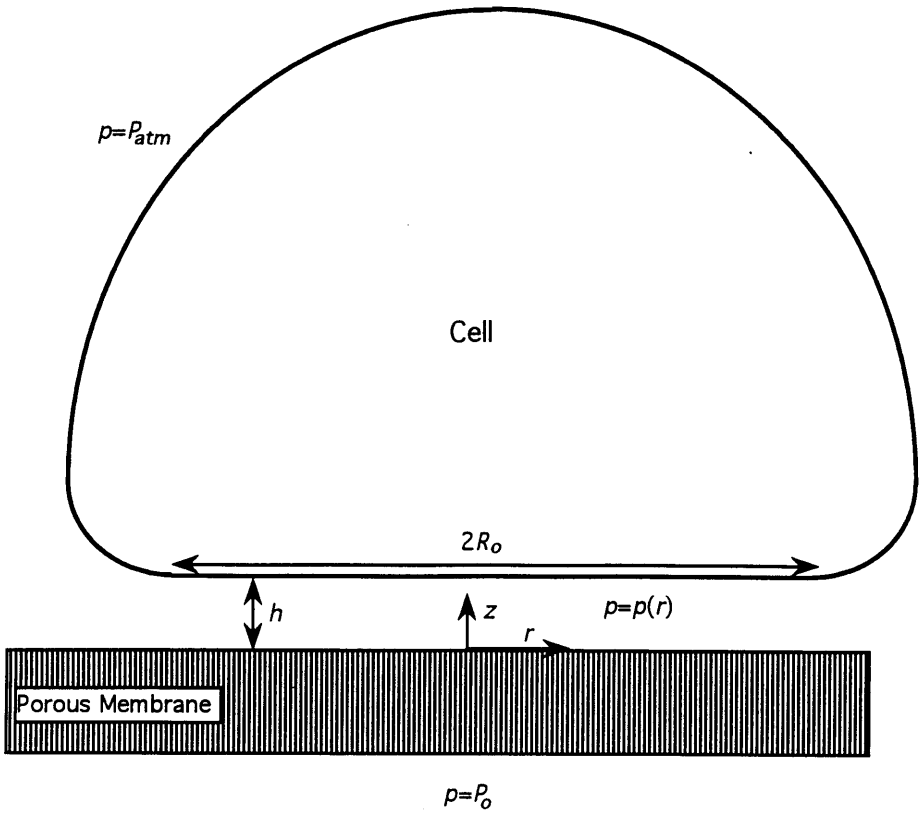

Figure 2.3 Assumed geometry and notation for force applied to a cell contact area due to back-filtration through anisotropic porous membranes. Physical forces outside the contact area are neglected. In reality, cell will appear as a sphere with a flattened base (contact area) whose radius depends upon the tendency of the cell to flatten on the substrate.

$$v = \frac{k_p}{\mu}(P_o - p) \quad at \quad z = 0 \tag{BC 2}$$

where P_o is the pressure applied to the porous membrane. An expression for the radial pressure distribution can be obtained by substituting equation 40 into the equation of continuity and integrating across the gap from $z = 0$ to h

$$v(h) - v(0) = \frac{1}{12\mu r}\frac{d}{dr}\left(h^3 r \frac{dp}{dr}\right) \tag{41}$$

Applying BC 1 and BC 2 yields

$$\frac{d}{dr}\left(rh^3\frac{dp}{dr}\right) + 12k_p r(P_o - p) = 0 \tag{42}$$

Assuming h is constant, equation 42 may be solved for p with the following boundary conditions

$$\frac{dp}{dr} = 0 \quad at \quad r = 0 \tag{BC 1}$$

and

$$p = P_{atm} \quad for \quad r \geq R_o \tag{BC 2}$$

Equation 42, and boundary conditions 1 and 2 above can be conveniently expressed in non-dimensional form with the following substitutions

$$y = \frac{r}{R_o}, \quad \phi = \frac{(P_o - p)}{\Delta P} \quad where\ \Delta P = P_o - P_{atm} \tag{43}$$

In non-dimensional form, equation 42 is

$$\frac{d}{dy}\left(y\frac{d\phi}{dy}\right) - \beta y\phi = 0 \tag{44}$$

with boundary conditions

$$\frac{d\phi}{dy} = 0 \quad at \quad y = 0 \tag{BC 1}$$

$$\phi = 1 \quad at \quad y \geq 1 \tag{BC 2}$$

where

$$\beta = \frac{12k_pR_o^2}{h^3} = \left(\frac{h*}{h}\right)^3 \quad where \quad h* = (12k_pR_o^2)^{\frac{1}{3}} \tag{45}$$

The gap width given by h^* is the "choking" scale for the problem and is of the same form shown previously. The solution to equation 44 which is a modified form of Bessel's equation, has the general solution (Hildebrand, 1976)

$$\phi = C_1I_o(\beta^{\frac{1}{2}}y) + C_2K_o(\beta^{\frac{1}{2}}y) \tag{46}$$

where I_o is a modified Bessel function of the first kind of order zero, K_o is a modified Bessel function of the second kind of order zero, and C_1 and C_2 are constants to be determined from the boundary conditions. Applying the boundary conditions to equation 46 yields

$$\phi = \frac{I_o(\beta^{\frac{1}{2}}y)}{I_o(\beta^{\frac{1}{2}})} \tag{47}$$

The functions are evaluated with the following general formula

$$I_m(x) = \sum_{n=0}^{\infty} \frac{(x/2)^{2n+m}}{n!(n+m)!} \tag{48}$$

with the following asymptotic behavior for small values of the argument x (≤ 1)

$$I_m(x) \sim \frac{1}{2^m m!} x^m \tag{49}$$

and for large values (≥ 100)

$$I_m(x) \sim \frac{\exp(x)}{\sqrt{2\pi x}} \tag{50}$$

Figure 2.4 shows a plot of $(1 - \phi(y))$, which, for P_{atm} taken as zero, is equal to the ratio of the pressure under the cell contact area to the pressure applied to the porous membrane (p/P_o), versus the radial position y as calculated from equation 47. The figure indicates that the pressure under the contact area is a strong function of the separation distance, and, for small values of h/h^* (< 0.25), the pressure under the contact area of the cell is fairly constant with radial position and is nearly equal to the pressure applied to the porous membrane.

The total force applied to the contact area can be determined by integrating the pressure difference between the gap and the fluid outside the contact area across the entire contact area

$$F_t = \int_0^{R_o} \int_0^{2\pi} r(p(r) - P_{atm}) d\theta\, dr = \int_0^{R_o} 2\pi r(p(r) - P_{atm}) dr \tag{51}$$

or in dimensionless form

$$F_t = \int_0^1 2\pi R_o^2 y \Delta P (1 - \phi) dy \tag{52}$$

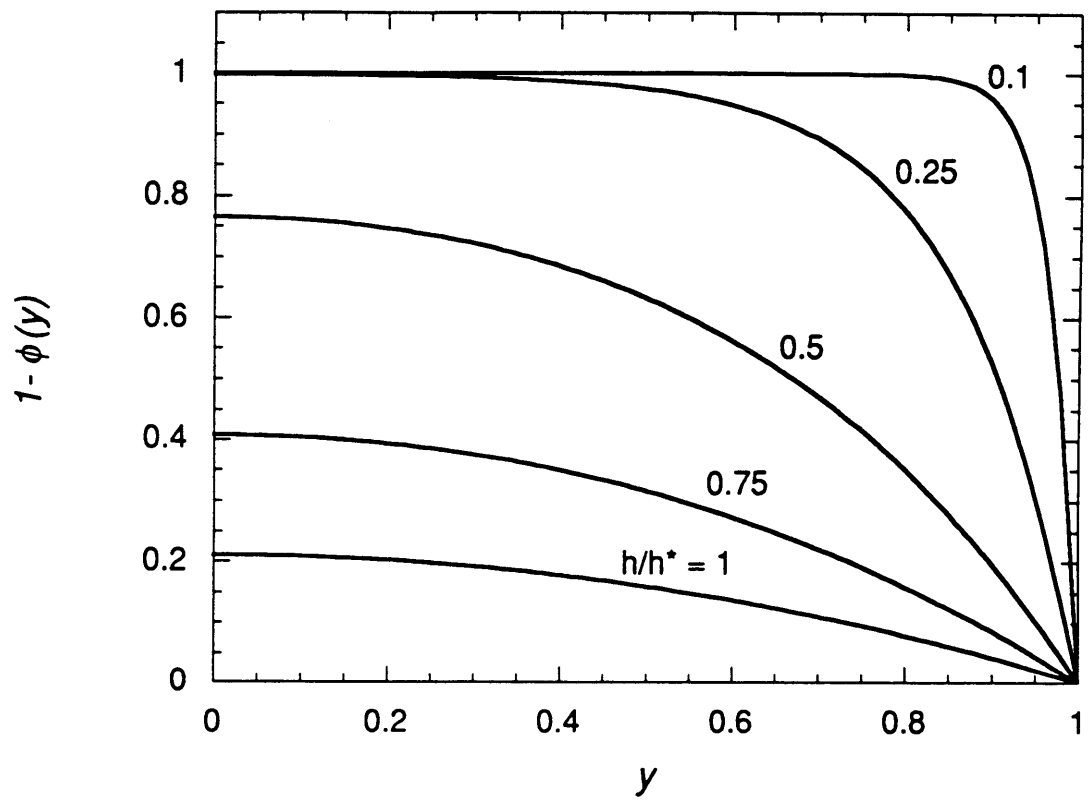

Figure 2.4 Dimensionless pressure under a cell-porous membrane contact area due to a pressure applied to the porous membrane as a function of dimensionless radial position as calculated from equation 47.

Substituting equation 47 for ϕ and performing the integration yields

$$F_t = \pi R_o^2 \Delta P f(\beta) \tag{53}$$

where $f(\beta)$ is equivalent to a dimensionless force equal to the ratio of the actual applied force to the maximum force ($\pi R_o^2 \Delta P$) as $h \rightarrow 0$ and is given by

$$f(\beta) = 1 - \frac{2I_1(\beta^{\frac{1}{2}})}{\beta^{\frac{1}{2}} I_o(\beta^{\frac{1}{2}})} \tag{54}$$

Figure 2.5 shows the function $f(\beta)$ plotted versus $h/h^* = \beta^{-1/3}$ using equation 48 for evaluation of the Bessel functions. Also plotted are the limiting asymptotes for small β (large h/h^*) and large β (small h/h^*). Since the value of $f(\beta)$ is a strong function of h/h^*, this indicates that the efficiency of force transmission to the contact area from an applied pressure on the porous membrane to which the cell is attached will increase with decreasing h, and increasing R_o and k_p.

For the case of a porous membrane which is not anisotropic, and where flow parallel to the membrane surface is significant in the region across which the majority of the pressure drop occurs, the efficiency of force transmission to the contact area will be much less due to diversion of flow around the contact area within the membrane. Describing the force in such a situation is complex and requires a detailed knowledge of the internal structure of the porous membrane, and a model which describes the flow within the membrane as well as under the cell contact area. In the limiting case of a purely isotropic membrane (one where there is a constant pressure drop per unit length everywhere within the membrane along all flow paths), it is possible to estimate the maximum possible force on a cell contact area brought about by a pressure applied to the porous membrane by considering the length of the

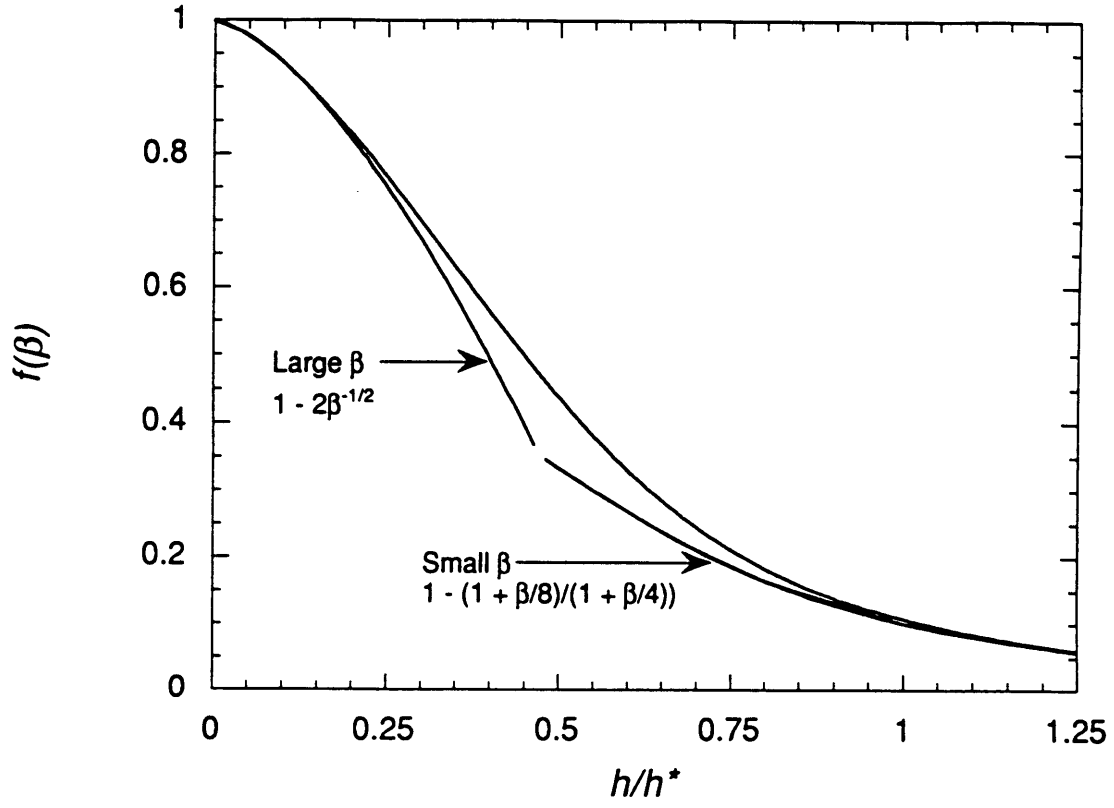

Figure 2.5 Dimensionless force $f(\beta)$ acting on cell contact area as a function of dimensionless separation distance. Also plotted are limiting asymptotic curves for small and large β given by the equations shown on the plot. h^* is the "choking" scale separation distance.

flow path for fluid diverting around the contact area directly under the cell. For a purely isotropic membrane, pressure will decrease linearly along the length of the flow path. For the case where the separation between the cell and the porous membrane surface approaches zero ($h \rightarrow 0$) and where L is the distance over which the fluid has traveled within the membrane, the equation for the pressure drop as a function of L is

$$\Delta P(L) = \Delta P_o\left(1 - \frac{L}{T + R_o - r}\right)$$

where $\Delta P(L) = p(L) - P_{atm}$, $\Delta P_o = P_o - P_{atm}$, T is the thickness of the pressure-drop determining region of the membrane, and r is the radial position under the cell contact area which varies from zero in the center of the contact area to R_o at the edge. For $P_{atm} = 0$, the maximum possible pressure at any position, r, under the contact area will be equal to the pressure directly beneath the cell contact area which is $\Delta P(T)$.

$$\Delta P(T) = \Delta P_o\left(\frac{R_o - r}{T + R_o - r}\right) \tag{55}$$

Equation 55 shows that for large T, $\Delta P(T)$ is a small fraction of ΔP_o but that for small T, $\Delta P(T)$ approaches ΔP_o. For example, when T is equal to R_o, the pressure at the center of the contact area will be $\Delta P_o/2$. Substituting equation 55 into equation 51 yields an expression for the maximum force

$$F_t = 2\pi \Delta P_o\left[\frac{1}{2}T^2 - R_o^2 + (T + R_o)\left[\frac{3}{2}(T + R_o) - 2T + T\ln\left(\frac{T}{T + R_o}\right)\right]\right] \tag{56}$$

Note that since h was taken as zero, flow under the cell contact area between the cell and the substrate will be zero, the force will be due purely to hydrostatic pressure, and the total force

will be invariant with respect to the hydraulic permeability. It may be observed from equation 56 that F_t becomes very small as R_o becomes much smaller than T.

Finally we consider the removal force generated on a cell attached to a surface by a uniform laminar shear flow. We assume that the shape of the cell outside of the contact area is approximately spherical, that the flow field is uniform thus undisturbed by neighboring cells, and that the bonds in the contact area are equally stressed. The shear flow will exert both a translational force, F, and a torque, t. The force and torque on a spherical object (cell) in close proximity to a surface due to a uniform shear flow has been shown to be (Goldman et al., 1967)

$$F = 6\pi\tau R_c(h + R_c)F* \tag{57}$$

$$t = 4\pi\tau R_c^3 t* \tag{58}$$

where h is the separation distance between the cell and the surface, R_c is the cell radius, τ is the shear stress and F^* and t^* are functions of $(h + R_c)/R_c$ which for $h << R_c$ are given by: $F^* \approx 1.7$ and $t^* \approx 0.94$. These results have been employed to determine the total force tending to detach a cell with a flattened contact area of finite size which is bound to a surface by uniformly stressed bonds (Hammer and Lauffenburger, 1987). The total force is given by

$$F_t = 6\pi R_c^2\tau\sqrt{\left(1 + \frac{h}{R_c}\right)^2 F*^2\left(\frac{9\pi^2R_c^2}{16R_o^2} + 1\right) + \frac{3\pi^2R_c^2}{4R_o^2}F*t*\left(1 + \frac{h}{R_c}\right) + \frac{\pi^2R_c^2}{32R_o^2}t*^2} \tag{59}$$

where R_o is the radius of the contact area. Substituting $F^* \approx 1.7$ and $t^* \approx 0.94$ and solving for τ will yield the critical shear stress to remove a cell with a uniform shear flow

$$\tau = \frac{F_t}{6\pi R_c^2 \sqrt{2.89\left(1 + \frac{h}{R_c}\right)^2\left(\frac{9\pi^2 R_c^2}{16R_o^2} + 1\right) + 1.598\left(\frac{3\pi^2 R_c^2}{4R_o^2}\right)\left(1 + \frac{h}{R_c}\right) + 0.8836\left(\frac{\pi^2 R_c^2}{32R_o^2}\right)}} \quad (60)$$

For significantly flattened cells, the assumption of spherical geometry for estimating F^* and t^* will tend to underestimate the critical shear required for cell detachment for a given R_c.

2.4 Results and Analysis

2.4.1 Kinetics of Bond Formation

Bond formation as a function of time, as calculated with equation 3, is presented in figure 2.6. The figure shows results for a cell which would display slow attachment kinetics (relatively low N_1), having 10^4 cell surface markers ($N_1 = 3 \times 10^9$ cm^{-2}) and with $R_c = 5$ μm. Figure 2.6 (A) presents the case where the active ligand density on the surface is a factor of 10 higher than the cell surface marker density, and (B) the case where marker and ligand densities are equal. Migration of additional cell surface markers into the contact area was neglected. For (1), the values for the rate constants are from row 1 of table 2.1, for (2), from row 5, and for (3), from row 8. The figure shows that even for the slowest solution kinetics shown in table 2.1 given by curve (3) (row 8 in table 2.1), bond density is at or near maximal values within 10 sec., much shorter than typical times required for significant cell marker redistribution by diffusion. Comparing (A) and (B) also shows that the time to reach equilibrium decreases as the ligand density increases and becomes saturating. Also, since the forward rate constants for reagents on membranes or surfaces (k_+^m) are almost invariant at their diffusion-limited value for a very wide range of intrinsic forward reaction rates (table 2.1), the time to reach equilibrium depends primarily on the reverse rate constant, so that kinetics are generally faster for reactions with lower affinity constants (compare (1) to (2)).

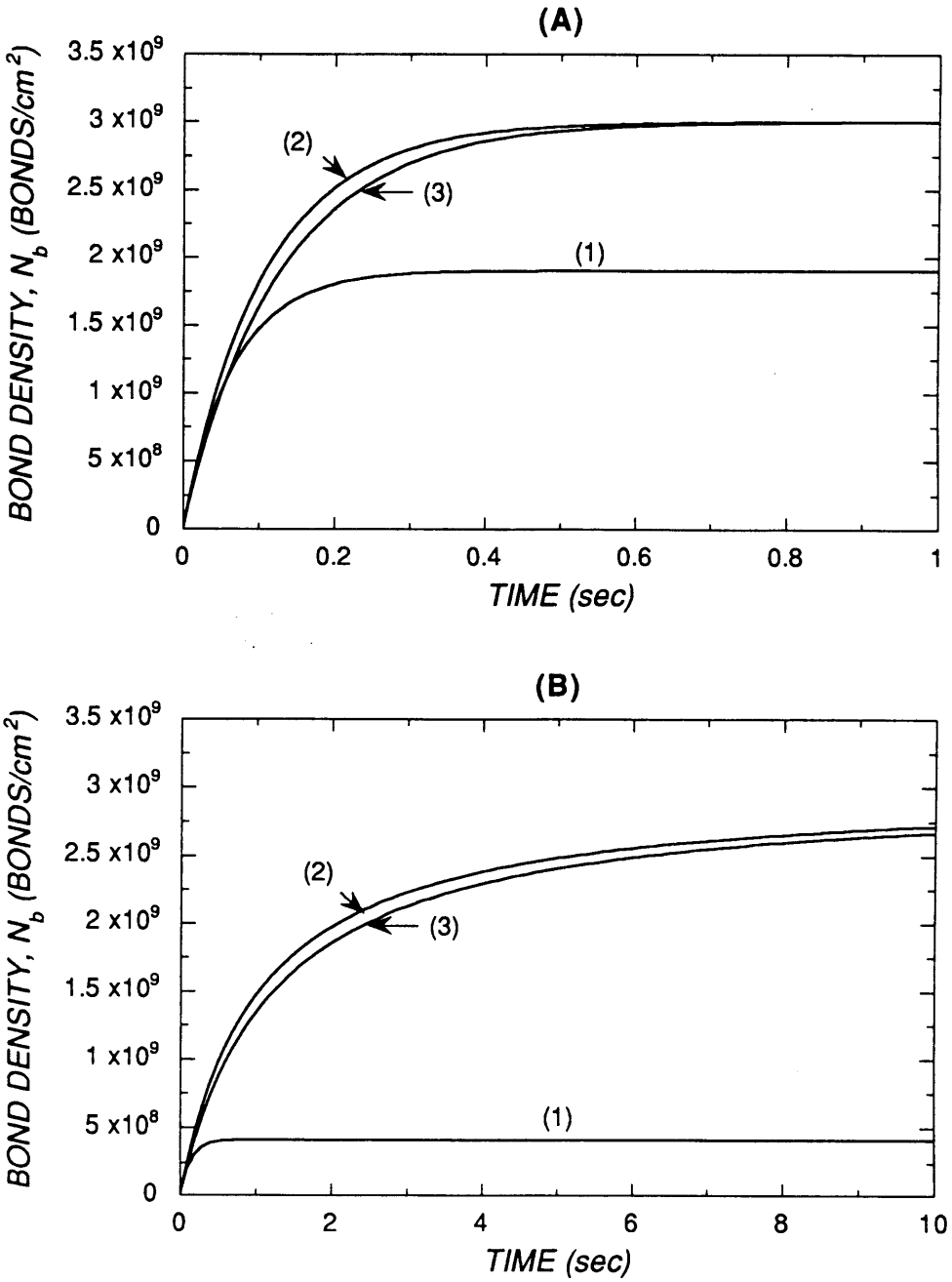

Figure 2.6 Bond density as a function of time for cells without cell surface marker redistribution. Bond density, as calculated from equation 3, for a cell with R_c = 5 μm, having 10^4 cell surface markers ($N_1 = 3 \times 10^9$ cm^{-2}) binding to a surface with ligand density: (A) 10 N_1 and (B) N_1. For curve (1), k_+^m and k_-^m from row 1 of table 2.1; (2) k_+^m and k_-^m from row 5 of table 2.1; and (3) k_+^m and k_-^m from row 8 of table 2.1.

2.4.2 Equilibrium Bond Density for Cell Attachment in the Absence of Detachment Forces

2.4.2.1 Effect of Ligand Density, Cell Surface Marker Mobility, and Contact Area

Figure 2.7 presents data showing equilibrium bond density (N_b) as a function of ligand density for a cell with R_c = 5 μm, having a cell surface marker density of 1 × 10^{10} cm^{-2} (about 31,000 cell surface markers) attaching to a porous surface with a porosity of 0.1 where the equilibrium association constant (K^a) is 10^7 M^{-1}, and contact area radius is 1 μm (curves (1) and (2)), or 5 μm (curves (3) and (4)). For curves (1) and (3), cell surface markers were immobile and N_b was determined with equation 2. For curves (2) and (4), cell surface markers were freely mobile and N_b was determined with equation 12. The figure shows that without cell surface marker migration, the bond density is directly proportional to the density of the limiting reagent. Both curves (1) and (3) reach a maximum at $N_b \sim N_1$ since no additional cell surface markers can enter the contact area to form additional bonds. In addition, N_b is independent of the contact area. In contrast, with cell surface marker redistribution, bond density is directly proportional to the ligand density until (for sufficiently large contact areas) nearly all of the receptors on the cell are involved with bonds in the contact area. Thus, much higher bond densities and total bond numbers can form when markers are free to migrate. The figure also indicates that reducing total attachment strength via reducing the number of bonds by decreasing the ligand density will only be effective when the ligand density becomes limiting ($N_2 < N_1$ for fixed markers or $N_2 < 4 \pi R_c^2 N_1/a$ for freely mobile markers).

The effect of the contact area available for bond formation is shown more directly in figure 2.8. In this figure, we plot the equilibrium bond density and the total number of bonds formed as a function of the substrate porosity ε (ε = (1- fractional contact area available for bond formation)). For curves (1) and (3), cell surface markers were fixed

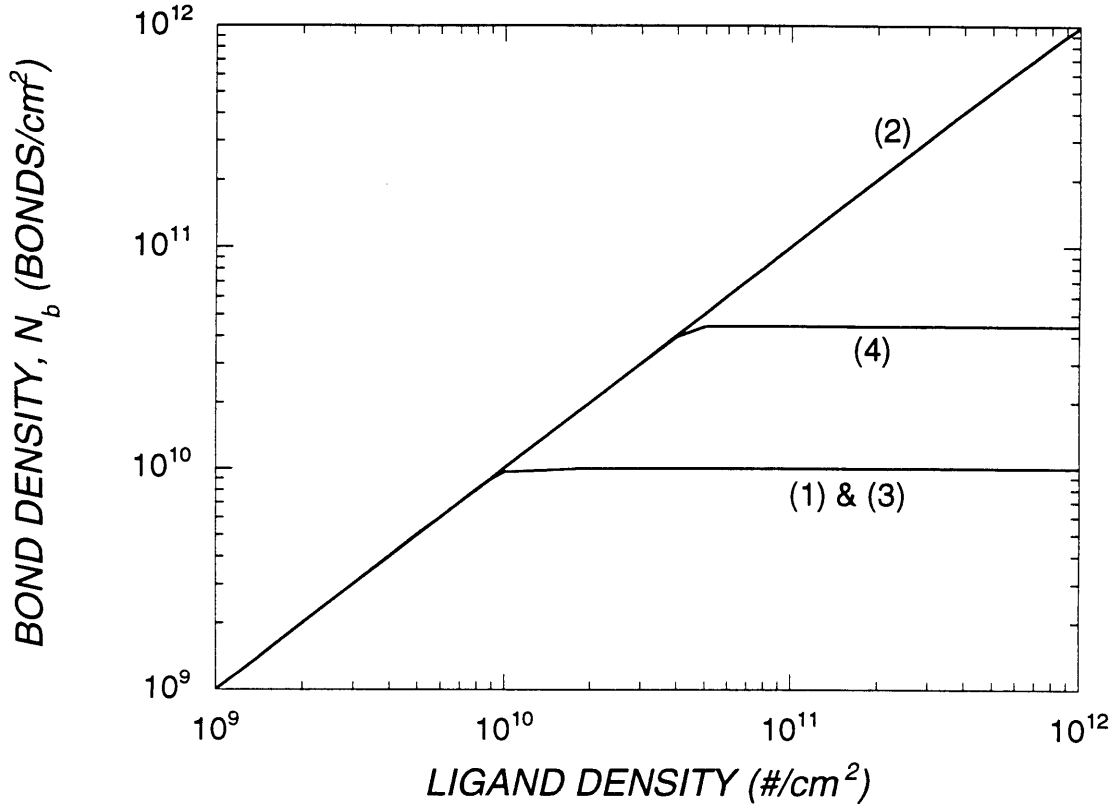

Figure 2.7 Effect of ligand density, cell surface marker mobility, and contact area on equilibrium bond density with no applied detachment force. Bond density as a function of ligand density for a cell with R_c = 5 μm, N_1 = 1 × 10^{10} cm^{-2} attached to a porous surface with a porosity of 0.1. The equilibrium association constant K^s is 10^7 M^{-1}, and the contact area radius is 1μm for curves (1) and (2), and 5 μm for curves (3) and (4). Cell surface markers for curves (1) and (3) are fixed, while for curves (2) and (4) they are freely mobile.

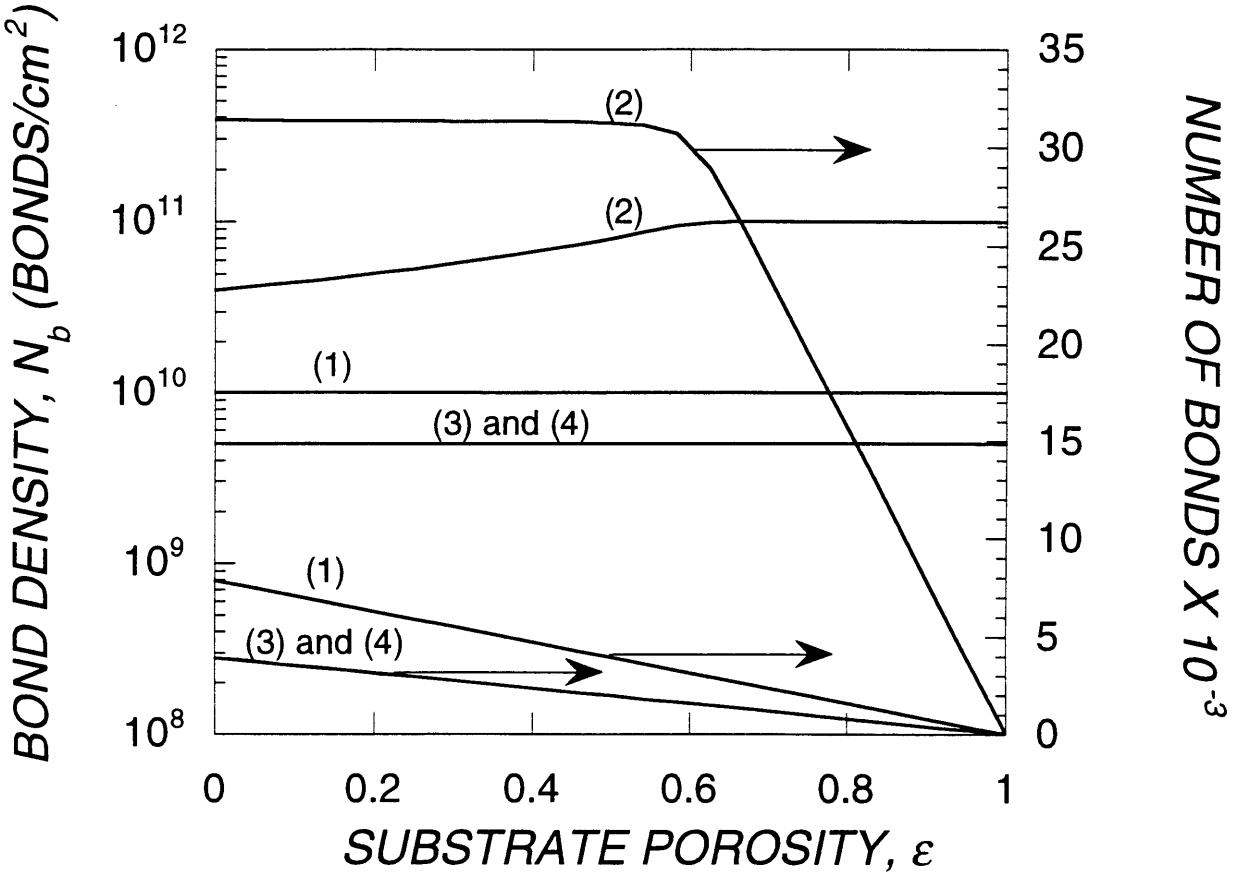

Figure 2.8 Effect of substrate porosity, ligand density, and cell surface marker mobility on equilibrium bond density and bond number with no applied detachment force. Bond density and bond number as a function of substrate porosity for a cell with R_c = 5 μm, $N_1 = 1 \times 10^{10}$ cm^{-2}. The equilibrium association constant K^s is 10^7 M^{-1}, and the contact area radius is 5 μm. Ligand density, N_2, is $10N_1$ for curves (1) and (2), and $0.5N_1$ for curves (3) and (4). Cell surface markers for curves (1) and (3) are fixed, while for curves (2) and (4) they are freely mobile.

and N_b was determined from equation 2. For curves (2) and (4), cell surface markers were free to migrate and N_b was determined from equation 12. In all cases, N_1 was 1×10^{10} cm^{-2}, and $R_c = R_o = 5$ μm. For curves (1) and (2), $N_2 = 10N_1$, and for (3) and (4), $N_2 = 0.5N_1$. The figure shows that for fixed cell surface markers, N_b is invariant with porosity and is approximately equal to the density of the limiting reagent. Also, the number of bonds is directly proportional to the fraction of the substrate available for bond formation. For the case where the cell surface markers redistribute, the dependence of N_b and bond number on porosity depends on whether the ligand or the initial cell marker density is limiting. When ligand density is limiting, curve (4), the dependence of bond density and bond number on porosity is nearly identical to that for fixed markers (values for bond density and bond numbers are the same to within less than 1%). In contrast, when the ligand density is in excess, curve (2), the bond density will be nearly equal to the ligand density for large values of porosity, and the bond density will rise in proportion to the fractional surface area available for bond formation over this range. However, as the surface area available for bond formation increases (porosity decreases) eventually the cell becomes depleted of free cell surface markers. At this point, the bond density begins to decrease, and the total number of bonds levels off at a value close to the total number of cell surface markers on the cell. The implication of this behavior is that while reducing the area available for bond formation is an effective means of decreasing bond number and attachment strength for cell with fixed markers, for cells with mobile markers, reducing the area available for bond formation is ineffective in reducing the number of bonds at equilibrium until the ligand density on the substrate becomes limiting.

2.4.2.2 Effect of Equilibrium Association Constant

Figure 2.9 shows equilibrium bond density (N_b) as a function of equilibrium

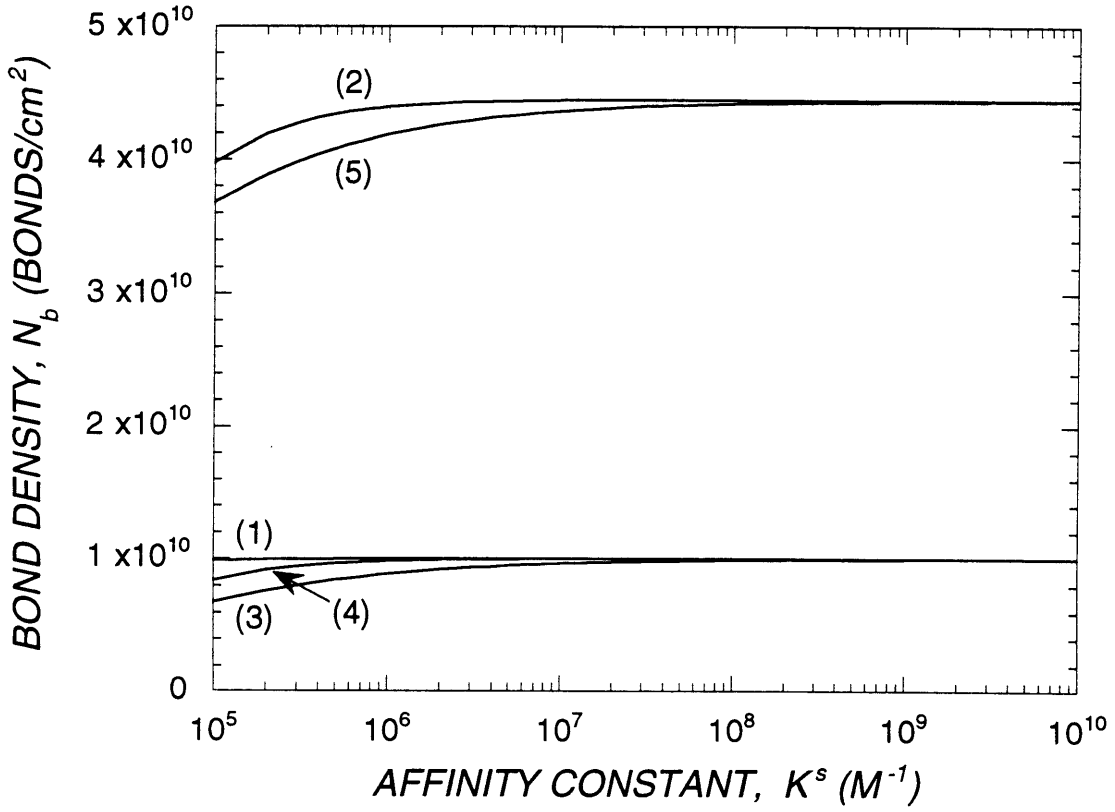

Figure 2.9 Effect of affinity constant on equilibrium bond density for cell attachment in the absence of detachment forces. Bond density as a function of affinity constant, as measured for soluble reagents, for a cell with $R_c = R_o = 5$ μm, and having $N_1 = 1 \times 10^{10}$ cm^{-2} for curves (1)-(4) or 4.4×10^{10} cm^{-2} for curve (5) bound to a porous surface with porosity of 0.1, and ligand density of 1×10^{11} cm^{-2} for curves (1) and (2), 1×10^{10} cm^{-2} for curves (3) and (4), and 4.4×10^{10} cm^{-2} for curve (5). Cell surface markers for curves (1), (3), and (5) are fixed, while for curves (2) and (4) they are freely mobile.

association constant as measured for soluble reagents (K^s) for a cell with $R_c = R_o = 5$ μm having a cell surface marker density (N_1) of 1×10^{10} cm^{-2} (about 31,000 total markers) for curves (1)-(4) or 4.4×10^{10} cm^{-2} (about 1.4×10^5 total markers) for curve (5), bound to a porous surface with a porosity of 0.1 and ligand density (N_2) of 1×10^{11} cm^{-2} for curves (1) and (2), 1×10^{10} cm^{-2} for curves (3) and (4), and 4.4×10^{10} cm^{-2} for curve (5). N_b was calculated with equation 2 for fixed cell surface markers for curves (1), (3) and (5), or with equation 12 for freely mobile cell surface markers for curves (2) and (4). The most important result to be drawn from the figure is that the equilibrium bond density is a very weak function of the association constant over the entire range of typical values of K^s for the range of expected cell marker and ligand densities chosen for this plot. In general, the bond density will be a weak function of the affinity constant as long as $1/K^m$ is small compared to N_1 and N_2. The bond density is virtually invariant with the affinity constant when one of the reagents is in excess at equilibrium as with curve (1). When neither reagent is in large excess at equilibrium, the bond density is a stronger function of the affinity constant for cells with fixed cell surface markers (compare curves (3) with (4), and (2) with (5).

2.4.3 Critical Force per Bond for Cell Detachment

The critical force per bond, F_b^{crit}, required to detach a cell from a surface was determined for cells with $R_c = R_o = 5$ μm, having freely mobile cell surface markers present at an initial density (N_{1o} before contact with the ligand-coated surface) of 1×10^{10} cm^{-2} (about 31,000 markers), and bound to a surface with a porosity of 0.1 as follows. First the equilibrium bond density (N_{bo}) and bond number were calculated with equation 12 for cell attachment without a detachment force. Second, equations 33 and 34 were used to determine the total force for cell removal (F_t^{crit}) with $N_1 = N_T$, where N_T is the total cell surface marker density at equilibrium before application of force calculated from equation 11. The critical

force per bond, F_b^{crit}, is defined as $F_t^{crit}/N_{bo}a$, the total force for cell removal divided by the number of bonds attaching the cell to the surface before the application of force. The results are plotted in figure 2.10 as a function of the log of the affinity constant for N_2 = 0.1, 1, 10, and 100 times N_{1o}. The figure shows that the critical force per bond ranges from about 1 to 12 μdynes over the full range of typical values chosen. In addition, the critical force per bond is very nearly a linear function of the log of the affinity constant. Also, the critical force is relatively invariant with the concentration of the ligand density when it is the limiting reagent (compare N_2 = 0.1 and 1 times N_{1o} where N_2 is limiting), but increases with ligand density when it is in excess (compare curves for N_2 = 10 and 100 times N_{1o} where N_2 is in excess).

2.4.4 Pressures and Shear Stresses Required for Cell Detachment with Back-Filtration Through Anisotropic Membranes and Shear Flow

2.4.4.1 Critical Separation Distances Between Cell Contact Areas and Anisotropic Membranes for "Choking" Scale Flow.

The critical "choking" scale separation distance (h^*) below which the dimensionless pressure $f(\beta)$, and consequently the efficiency of transmission of force to the contact area, increases sharply (figure 2.5) is shown in table 2.2 for a range of typical microporous/loose ultrafiltration membrane hydraulic permeabilities. The hydraulic permeability (L_p) is given in units of L(hr m^2 mmHg)$^{-1}$ and is equal to the measured solvent flux or velocity divided by the applied transmembrane pressure drop ($v_o/\Delta P$). The permeability constant is determined from equation 36 for μ = 0.9 cp (the viscosity of water at 25 °C).

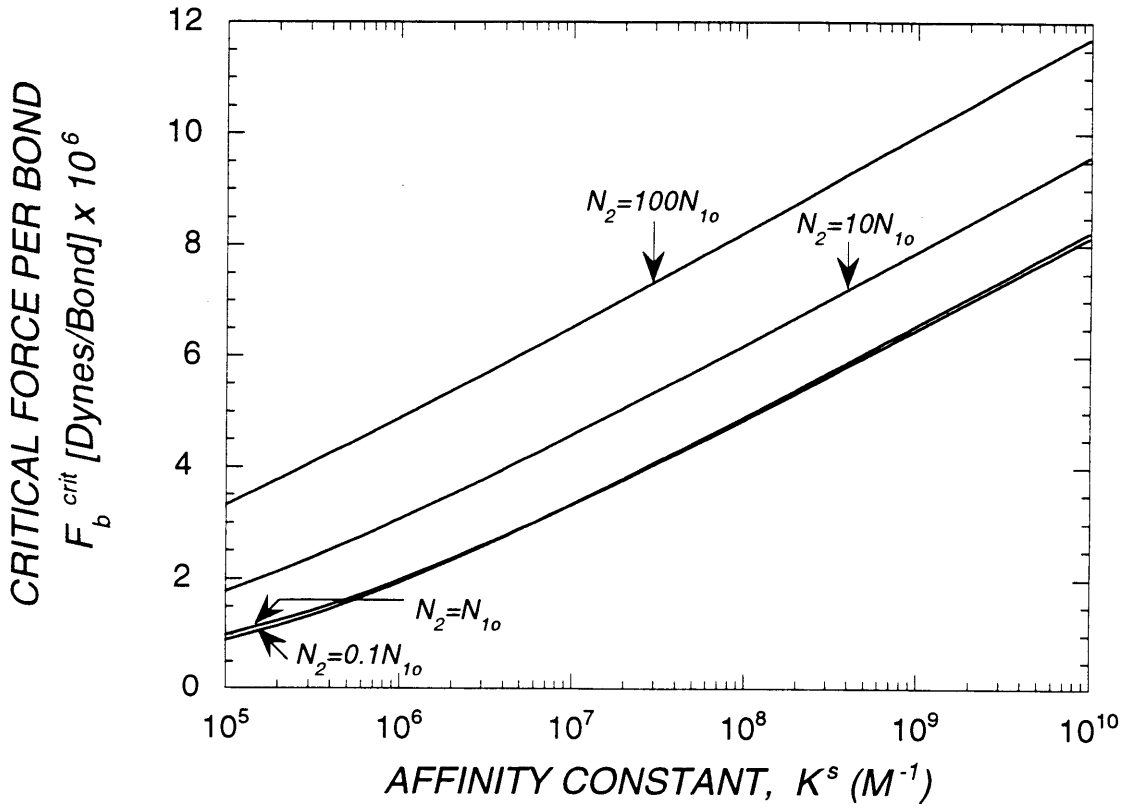

Figure 2.10 Critical force per bond required for cell detachment. Critical force per initial bond as a function of affinity constant for a cell with $R_o = R_c = 5$ μm and freely mobile surface markers present at an initial density on the cell membrane (before attachment) of $N_{1o} = 1 \times 10^{10}$ cm^{-2}. Cell is bound to a surface with porosity of 0.1 and with ligand density (N_2) indicated on the figure. See text for calculation procedure.

Table 2.2 *Separation Distances (h*) for Flow Choking*

L_p ($Lhr^{-1}m^{-2}mmHg^{-1}$)	k_p ($m \times 10^{12}$)	Critical Separation h^* (Å)				
		R_o = 1 μm	2 μm	3 μm	4 μm	5 μm
0.27	0.5	182	288	378	458	531
0.54	1	229	363	476	577	669
1.1	2	288	458	600	727	843
1.6	3	330	524	687	832	965
2.2	4	363	577	756	916	1,060
2.7	5	391	621	814	986	1,140
5.4	10	493	783	1,030	1,240	1,440
10.8	20	621	986	1,290	1,570	1,820

The data indicate that this range of hydraulic permeabilities yields a range of critical separation distances which are close to those expected for two surfaces separated by immunoglobins (about 160 Å each in length).

2.4.4.2 Effect of Morphology of Attached Cell on Pressure and Shear Stress Required for Detachment

The critical back-pressure which must be applied to an anisotropic membrane and the critical shear stress for cell detachment was determined with equations 53 and 60 respectively where F_t was taken as the critical detachment force per bond necessary for cell removal, F_b^{crit}, multiplied by the total number of bonds. Figure 2.11 presents the results for such a calculation for a cell with radius of 5 μm attached to a porous membrane having a permeability constant of 1×10^{-12} m for a bond density, N_b, of 1×10^{10} equally stressed bonds/cm^2 and a separation distance, h, of 500 Å. The critical force per bond for cell detachment F_b^{crit} = 4 μdynes/bond, and the critical transmembrane pressure drop and shear stress for cell removal is plotted as a

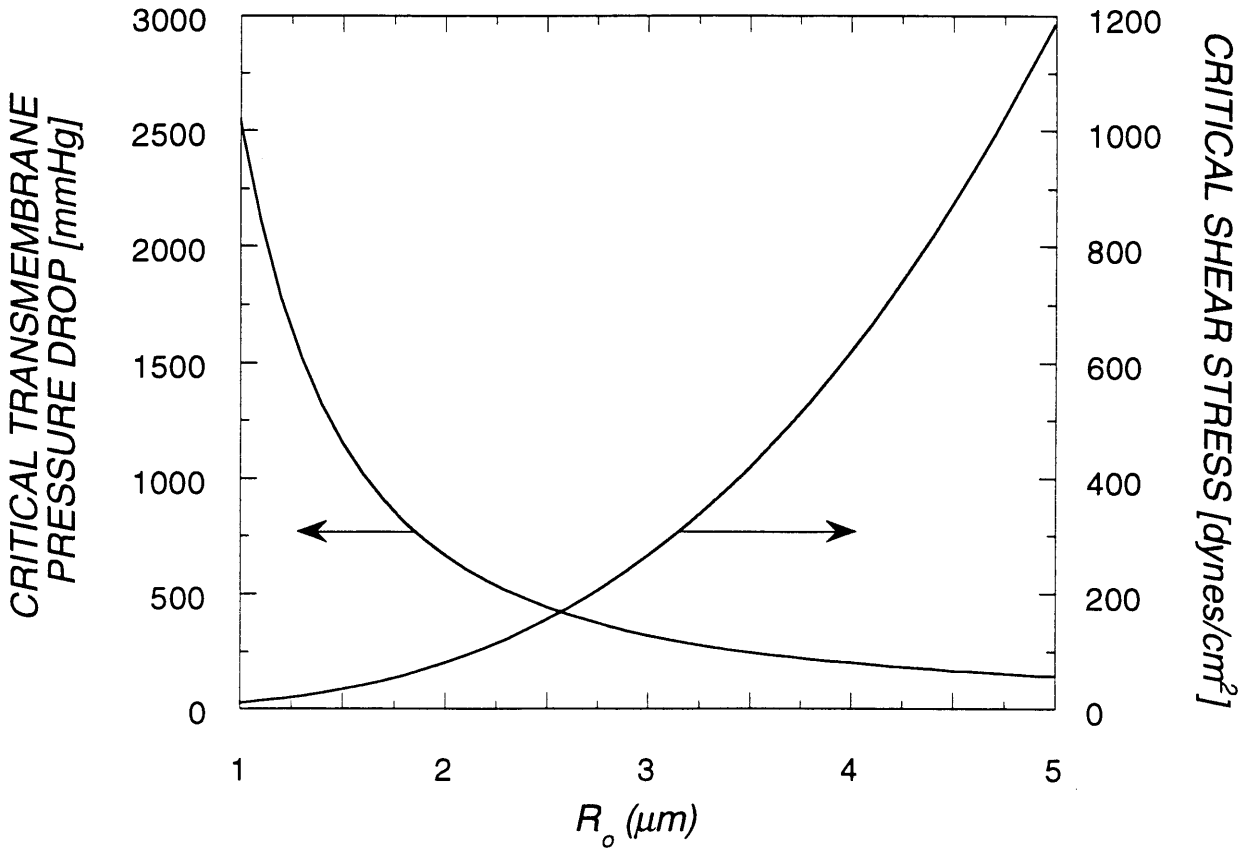

Figure 2.11 Critical transmembrane pressure drop and shear stress for cell removal from a porous anisotropic membrane. Critical transmembrane pressure drop (left axis) and critical shear stress (right axis) are plotted as a function of the radius of the contact area (R_o) for a cell bound to an anisotropic membrane with a porosity of 0.1, and a hydraulic permeability k_p = 1 × 10^{-12} m by a bond density of 1 × 10^{10} cm^{-2}. The critical force for breaking each bond is 4 μdynes, and the bonds in the contact area are evenly stressed. The cell radius, R_c, is 5 μm, and the separation distance between the cell contact area and the anisotropic membrane is 500 Å.

function of the contact area radius (R_o). The dependence of the critical transmembrane pressure drop and shear stress on the contact area size is very different. Cells become much harder to remove with shear stress but easier to remove with back-pressure as the contact area size increases and the total number of bonds, $(N_b\ a)$, increases. In the case of the transmembrane pressure drop, if the efficiency of transmitting the force due to back-pressure to the contact area (as given by $f(\beta)$) were not a function of the contact area diameter, then the critical transmembrane pressure drop for cell removal would be invariant with contact area, and thus R_o, since both the force applied to the contact area for a given transmembrane pressure drop and the total number of bonds in the contact area are directly proportional to contact area size (πR_o^2). However, $f(\beta)$ for R_o = 5 μm is about 17 times $f(\beta)$ for R_o = 1 μm yielding the observed dependence of transmembrane pressure drop on R_o. The figure makes clear the importance of adsorbed cell morphology on the efficiency of the mode of detachment. In contrast to removal with back-pressure, for removal by shear stress , not only does the total force necessary increase due to the increase in the number of bonds with R_o, but the efficiency of shear at transmitting force to the contact area decreases (in a nearly linear fashion for typical parameter values, see equation 60 and figure 2.12) as the contact area increases in size. Another important conclusion is that the for these reasonable values of binding and detachment parameters, the critical back-pressures fall into a range which would be easy to apply in a typical device (about 150 - 2500 mmHg or 3 - 48 psig).

Figure 2.12 displays similar data for a range of hydraulic permeabilities, critical bond strengths, and separation distances. The figure shows the critical transmembrane pressure and shear stress required to break 1,000 bonds with a strength of 2, 4, and 8 μdynes/bond for figure 2.11 (A), (B), and (C) respectively. The figure shows a similar dependence of pressure and shear on contact area as figure 2.11, and also shows that increasing the separation

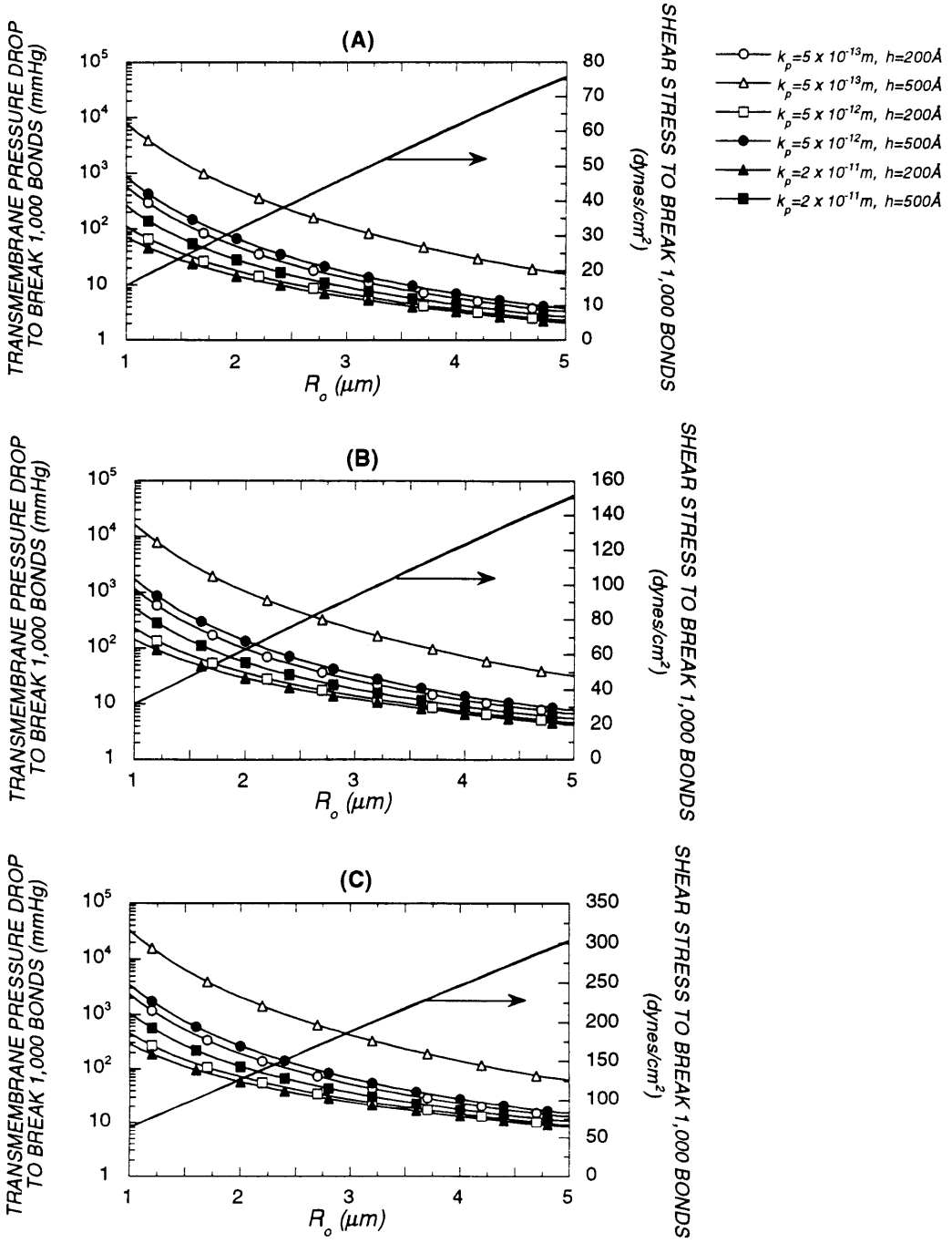

Figure 2.12 Critical transmembrane pressure drop and shear stress necessary to rupture 1,000 bonds for cell removal from an anisotropic membrane with a porosity of 0.1. Critical transmembrane pressure and shear stress are plotted as a function of the contact area radius (R_o). Hydraulic permeabilities are k_p = 5 × 10^{-13} m, 5 × 10^{-12} m or 2 × 10^{-11} m, and the critical force for breaking each bond is 2, 4 and 8 μdynes for (A), (B), and (C) respectively. Bonds in the contact area are evenly stressed. The cell radius, R_c, is 5 μm, and the separation distance between the cell contact area and the membrane is 200 Å (hollow symbols) or 500 Å (solid symbols) (curves for the two separation distances for shear stress overlap).

distance can drastically increase the critical pressure, especially for small permeabilities and contact areas but has virtually no effect on the critical shear stress (lines for h = 200 and 500 Å are within 1% of each other and overlap on figure). Both the critical pressure and shear stress are directly proportional to the strength per bond. The curve representing the critical pressure with h = 500 Å and k_p = 5×10^{-13} m is significantly separated from the rest of the group in the direction of higher pressure. This is the only condition where $h > h^*$ over nearly the entire range of R_o, illustrating the importance of flow "choking". Again, the required pressures fall into a very practical range, even for as many as 1 to 5×10^4 bonds, for large contact areas ($R_o > 3$ μm).

2.4.5 Cell Attachment and Detachment: Case Study

To illustrate a particular scenario, we will consider a cell 10 μm in diameter, having 20,000 fixed or freely mobile target cell surface markers ($N_1 = 6.4 \times 10^9$ cm^{-2}) binding to a porous surface ($\varepsilon = 0.1$) having an active ligand density $N_2 = 2 \times 10^{11}$ cm^{-2} via bonds characterized by an affinity constant of $K^s = 10^8$ M^{-1}. Initially, the cell attaches until an equilibrium number of bonds are formed, at which point the cell is subject to removal forces. The number of bonds formed before removal force is applied was determined using equations 2 or 12. The critical force for cell removal was then determined as described in section 2.4.3. And finally the critical shear stress and transmembrane pressure drop for detachment from an anisotropic membrane were calculated with equations 60 and 53. In addition, an estimate was made from equation 56 of the minimum transmembrane pressure drop (for $h \rightarrow 0$) required for detachment of cells attached to an isotropic membrane 200 μm thick. For detachment from anisotropic membranes, the separation distance between the cell and membrane in the contact area was assumed to be 300 Å, or approximately the length of two IgG antibody molecules.

Table 2.3 *Cell Attachment and Removal From a Porous Membrane: Case Study Results*

	Attachment (Fixed/Mobile)	Detachment (Fixed/Mobile)			
R_o (μm)	# Bonds	F_b^{crit} (μdynes/bond)	τ (dynes/cm²)	ΔP Anisotropic (mmHg)	ΔP_{min} Isotropic (mmHg)
1	180/5,700	7.0/5.8	10/260	150/3,900	$(0.18/4.7) \times 10^5$
2	720/19,960	7.0/6.0	80/1,900	66/1,600	$(0.09/2.2) \times 10^5$
3	1,600/19,997	7.0/6.8	270/3,200	50/590	$(0.61/7.2) \times 10^4$
4	2,900/19,999	7.0/6.9	630/4,300	44/300	$(0.46/3.1) \times 10^4$
5	4,500/19,999	7.0/7.0	1,200/5,300	40/180	$(0.37/1.6) \times 10^4$

The results are shown in table 2.3 and the values are presented in the table as those obtained for fixed/freely mobile cell surface markers. The analysis indicates that for contact area radii greater than or equal to 2 μm, nearly all of the freely mobile cell surface markers are involved with bonds in the contact area before the application of removal force. By contrast, the number of bonds formed for fixed markers cannot exceed the number of markers initially in the contact area, and is subsequently much less than the for mobile markers in all cases making the cells much easier to detach. The critical force per bond is nearly constant, ranging from about 6 to 7 μdynes. The critical shear stress for cell removal ranges from about only 10 dynes/cm^2 for the smallest contact area to 1,200 dynes/cm^2 for the largest for a cell with fixed markers, or from about 260 dynes/cm^2 for the smallest contact area to over 5,000 dynes/cm^2 for the largest for a cell with freely mobile markers. For an anisotropic membrane, critical removal back-pressure decreases from about 150 mmHg (2.9 psi) for the smallest contact area to about 40 mmHg (0.8 psi) for the largest for a cell with fixed markers, or from about 4000 mmHg (77 psi) for the smallest contact area to only about 180 mmHg

(3.5 psi) for the largest. By contrast, the minimum critical pressure for an isotropic membrane which is 200 μm thick is at least a factor of 100 greater than for the anisotropic membrane, and is about 3,700 mmHg (70 psi) for fixed markers and 1.6×10^4 mmHg (290 psi) for mobile markers even for the largest contact area. It is likely that these pressures would be greater than the burst pressure of most membrane materials. For these particular cells, it may be concluded that the most practical means of removing the cell from an anisotropic membrane depends on the morphology of the adsorbed cell, with cells having very small contact areas more easily removed by shear, and cells with more flattened contact areas by back-pressure. For cells with fixed cell surface markers, back-pressure would be a practical means to remove the cells over the entire range of contact area sizes analyzed. The analysis also suggests that back-pressure would probably not be practical or effective for cells adsorbed to completely isotropic membranes unless they were very thin or the bond density was very low.

2.5 Discussion

Using a simple mathematical description of immunoaffinity cell adhesion and detachment, we have determined the expected effects of important design and operating parameters and have demonstrated the theoretical feasibility of using porous substrates, such as membranes, for selective cell separation. We found that for a range of typical values of antibody-antigen reaction rate constants, reaction equilibrium is attained quickly, and that receptor redistribution occurs on a time scale which may be less than our experimental incubation times. We also found that attachment strength is directly proportional to the concentration of the ligand density or the number of target cell surface markers depending on which is the limiting reagent. We observed that the ability of cell surface markers to

redistribute and collect within the contact area drastically increases the bond density and attachment strength. The affinity constant of the ligand-marker reaction had a much smaller effect on final bond density, and thus attachment strength, than did ligand or cell surface marker density.

The critical force necessary to rupture a specific bond ranged from about 1 to 12 μdynes for a wide range of typical parameter values. The critical force was approximately proportional to the logarithm of the affinity constant and increased with increasing ligand density when it was in excess. Both of these results were previously predicted by Bell (Bell, 1978) from his analysis of the limiting case where ligand density is much greater than bond density. The dependence of total adhesion strength on the logarithm of the bond affinity constant has also been demonstrated experimentally with antibody-coated polystyrene spheres attached to functionalized surfaces and detached with shear flow (Kuo and Lauffenburger, 1993). The magnitude of the critical bond rupture force which we predicted is similar to that predicted by Bell (about 4 μdynes, Bell, 1978) and is in the same range as values subsequently measured with shear detachment studies for hard spheres (Kuo and Lauffenburger, 1993) and endothelial cells (Xiao and Trusky, 1996), or directly for individual bonds by atomic force microscopy (Dammer, et al., 1996).

We demonstrated that the most efficient method of cell detachment depends strongly on the morphology of the adsorbed cell, with fully rounded cells easier to remove with shear, and cells with flattened contact areas, whose size is on the order of the cell radius, more easily detached by pressurizing the gap under the contact area with a back-pressure applied to the porous substrate. The efficiency of transmitting a force due to back-pressure on a porous membrane to the contact area of a cell depended strongly on the morphology of the contact area and the structure of the porous membrane. The minimum separation distances in the

contact area are expected to be on the order of the size of the molecules involved in the bond. For antibody-antigen/receptor-ligand type bonds, this would be on the order of about 100 to 1000 Å. The hydraulic permeabilities necessary in order to efficiently transmit force due to back-pressure to a cell-sized contact area for such separation distances is in the range typical for microporous or high permeability ultrafiltration membranes (about 10^{-13} to 10^{-11} m). The membranes must also be anisotropic so that flow within the plane of the membrane is subject to much greater resistance than flow through the membrane; otherwise, the membrane must be very thin (on the order of the cellular radius) in order to transmit sufficient force to detach typical cells at reasonable transmembrane pressures. With suitable membranes, for a wide range of expected parameter values, we showed that large numbers of bonds ($> 10^4$) can be ruptured with very reasonable back-pressures (10 to 1,000 mmHg).

Our objective in this chapter was to derive a conservative (err on the high side) but reasonable estimate of the forces necessary to detach specifically adsorbed cells from porous membranes. During the analysis, several assumptions were made which may limit the utility of the analysis for real systems. The most critical assumptions are those related to the geometry and morphology of the cell-surface contact area, the stress distribution on bonds within the contact area, and the mechanism of detachment of the cell. We assumed that target cells will have some tendency to spread and form a flattened contact region in close proximity to the substrate surface as opposed to remaining essentially spherical. This relatively large flattened area enables the formation of a very large number of bonds at global equilibrium (involving nearly all of the target cell surface markers when they are freely mobile and the ligand density is high) yielding a very high attachment strength. Our own experimental observations of normally non-spreading leukemia and lymphoma cells have confirmed this tendency for formation of flattened contact areas when cells bind to porous membranes after

loading by gravity or filtration with a subsequent static incubation time of about 1 hr (see chapters 3 and 4). This tendency for passive flattening of contact areas during bond formation has also been observed for leukemia cell binding by other investigators (McCloskey and Poo, 1986). Our experimental observations yielded average contact area diameters (areas which were substantially flattened and had points of close contact, $\leq$ 500 Å, with the porous membrane) which were approximately 60 - 80 % of the overall cell diameters and minimum separation distances of about 200 Å. The contact areas were not, however, perfectly smooth, and some portion of most contact areas was separated from the porous membrane by distances ranging from 500 to a few thousand angstroms. These distances are probably too large to be bridged by bonds to the substrate.

Our experimental observations of adsorbed cellular morphology have two implications. First, it the fractional area of the cell over which bonds can actually form is somewhat smaller than we assumed in our analysis where we allowed bonds to form over the entire contact area. Thus, it is possible that the actual number of bonds formed, and total attachment strength, would be smaller than we predict, especially when ligand densities are low (see figure 2.8). Secondly, we may have significant error in our prediction of the actual removal force on the contact area due to back-pressure with our assumption that the separation distance is constant over the contact area, and is equal to the length of the molecular cross-bridge. The extent, and even the direction, of this error is difficult to determine. While the regions of larger separation distance could lead to a channeling of the flow under the cell and a reduction of the pressure under the contact area if they are interconnected, it is also likely that the roughness and irregularity of both the cell and porous membrane surface would lead to a greater resistance to flow under the cell than we predicted by considering the two surfaces to be smooth and flat. In addition, the gap between the cell

and the substrate will not be empty space as we approximate, but is, in fact, at least partially filled with other cell-surface receptors and glycoprotein molecules which comprise the dense membrane glycocalyx (Bell et al., 1984). The presence of this material within the gap under the contact area would add to the resistance to fluid flow and tend to increase the force on the contact area compared to flow through an empty gap.

Another important assumption concerned the distribution of applied stress on the bonds in the contact area and the mechanism of cell detachment. In our analysis, we assumed that bonds are equally stressed and rupture simultaneously causing the cell to "pop" off the substrate. For a given number of bonds of a certain strength, this assumption will yield a higher estimate of removal force necessary for cell detachment than for a mechanism of detachment where bonds are unevenly stressed and rupture sequentially ("peeling"). In actuality, the mechanism of detachment will depend on the type of applied force, the mechanical properties of the cell, and the linkage between the target surface markers and the cell cytoskeleton. Theoretical analysis suggests that tangential or shearing forces will tend to create a more uneven distribution of stress within a contact area (with the greatest stresses at the leading edge of the contact area) (Chang and Hammer, 1996) and tend to favor sequential bond rupture compared to forces acting in a direction normal to the contact area. However, some experimental studies using hard spheres or cells with a shear generated detachment force have found that a model assuming equally stressed bonds yielded estimates for bond strengths which were similar to those measured directly for individual bonds using an atomic force microscope (Dammer, et al., 1996), and were similar to (Xiao and Trusky, 1996), or closer to (Kuo and Lauffenburger, 1993), the measurements for individual bonds than estimates derived from a peeling model of detachment.

The physics of cell removal with back-pressure is such that the force is directed

normal to the contact area, and is nearly constant over the contact area for small separation distances. The pressure under the cell is highest in the center of the contact area and lowest at the periphery. This type of applied force may favor a relatively even distribution of stress over the contact area and a mechanism of cell detachment by "popping". In fact, because of this unique force distribution, this technique could prove to be a valuable experimental tool for studying cell adhesion and detachment. While "peeling" may be desirable when removing cells with shear since the critical total force necessary for detachment will be less, it may not be favorable for cell removal with reverse pressurization. If cell peeling from the edge of the contact area were the predominate detachment mechanism, the contact area size would decrease as the cell detached, thereby decreasing contact area over which the back-pressure acts and the critical separation distance for flow choking and thus the efficiency of the transmission of force to the contact area. For all but low bond densities, it is possible that such a cell would simply round up until the force on the contact area became insufficient to rupture the remaining bonds. Of course at this point the cell should be much easier to remove with shear than in its initial configuration.

Finally, considering the magnitude of the critical level of force per bond necessary for rupture, it is possible that in certain situations certain forms of cell mechanical failure may occur instead of, or in addition to, bond dissociation. One possibility is that bound cell surface markers could be pulled out of the cell membrane. The force necessary for pulling a typical receptor which is not anchored to the cytoskeleton through the membrane has been estimated to be on the order of 10 μdynes, similar to the critical forces for bond cleavage (Bell, 1978). Removal of a cell via receptor extraction could adversely affect cell viability, phenotype, or function. Another possibility which should be considered is that the force transmitted to the cell membrane via the bond during detachment could exceed the yield stress

of the membrane and cause plastic deformation of the membrane in the form of long tethers. The minimum force required to pull a single tether from a neutrophil membrane has recently been measured to be about 4.5 μdynes (Shao and Hochmuth, 1996). This value falls right in the middle of the range we predict for bond dissociation. Formation of tethers would tend to move the cell away from the porous substrate, without completely detaching it, to a separation distance where the force on the contact area due to back-pressure would be small. In such a configuration, one would have to rely on shear forces to complete detachment. One mitigating consideration, however, is that the force required per bond to pull out many tethers from a cell attached to a surface by a large number of attachment points distributed over a large area may be considerably larger than the minimum force required to pull a single tether.

In summary, we have demonstrated with a simple mathematical analysis that immunoaffinity cell adsorption to porous membranes with cell detachment by reverse pressurization and/or shear stress may be a practical and efficient means to perform selective cell separations and cell adhesion studies.

2.6 Acknowledgements

I would like to thank Professor Robert Davies at the University of Colorado at Boulder, for helpful suggesting the fluid mechanical reference (Goldshtik, et al., 1986) which proved very helpful in modeling the detachment force on a cell due to reverse-filtration.

2.7 References

Aizenbud, B.M., and N.D. Gershon. 1984. Diffusion of molecules on microvillous biological membranes. In. Perelson, A.S., C. DeLisi, and F.W. Wiegel eds. Cell Surface dynamics: concepts and models. Marcel Dekker Inc., New York, NY. pp.151-166.

Anderson, K.C., R. Soiffer, and R. Delage. 1990 T-cell depleted autologous bone marrow transplantation therapy: analysis of immune deficiency and late complications. *Blood.* 76:235-244.

Axelrod, D., P.M. Ravedin, and T.R. Podleski. 1978. Control of acetylcholine receptor mobility and distribution in cultured muscle membranes: a fluorescence study.

Biochimica et Biophysica Acta. 511:23-38.
Basch, R.S., J.W. Berman, and E. Lakow. 1983. Cell separation using positive immunoselective techniques. *Journal of Immunological Methods.* 56:269-280.
Batchelor, G.K. 1970. An introduction to fluid dynamics. Cambridge University Press, Cambridge, UK.
Bell, G.I. 1978. Models for the specific adhesion of cells to cells. *Science.* 200:618-627.
Bell, G.I. 1979. Theoretical models for cell-cell interactions in immune responses. In. DeLisi, C., and R. Blumenthal eds. Physical chemical aspects of cell surface events in cellular recognition. Elsevier, New York, NY. pp.371-392.
Bell, G.I., M. Dembo, and P. Bongrand. 1984. Cell adhesion: competition between nonspecific repulsion and specific bonding. *Biophysical Journal.* 45:1051-1064.
Berenson, R.J., W.I. Bensinger, D. Kalamasz, and P. Martin. 1986a. Elimination of Daudi lymphoblasts from human bone marrow using avidin-biotin immunoadsorption. *Blood.* 67:509-515.
Berenson, R.J., W.I. Bensinger, and D. Kalamasz. 1986b. Positive selection of viable cell populations using avidin-biotin immunoadsorption. *Journal of Immunological Methods.* 91:11-19.
Berenson, R.J., W.I. Bensinger, R.S. Hill, R.G. Andrews, J. Garcia-Lopez, D.F. Kalamasz, B.J. Still, G. Spitzer, C.D. Buckner, I.D. Bernstein, and E.D. Thomas. 1991. Engraftment after infusion of CD34+ marrow cells in patients with breast cancer or neuroblastoma. *Blood.* 77:1717-1722.
Berson, A.E., K.M. Knobel, D. Rood, K. Chen, D. Lamons, M.A. McNally, T.B. Okarma, and J.S. Lebkowski. 1996. Selection of murine lymphoid and hematopoietic cells using polystyrene tissue culture devices containing covalently immobilized antibody. *BioTechniques.* 20:1098-1103.
Brugger, W., S. Heimfeld, R.J. Berenson, R. Mertelsmann, and L. Kanz. 1995. Reconstitution of hematopoiesis after high dose chemotherapy by autologous progenitor cells generated ex vivo. *New England Journal of Medicine.* 333:283-287.
Chang, K.-C., and D.A. Hammer. 1996. Influence of direction and type of applied force on the detachment of macromolecularly-bound particles from surfaces. *Langmuir.* 12:2271-2282.
Chang, Y., and J. Hsu. 1990. The effect of multivalent cations on adhesion time for cellular adhesion to solid surfaces. *Journal of Theoretical Biology.* 147:509-516.
Civin, C.I., L.C. Strauss, M.J. Fackler, T.M. Trischmann, J.M. Wiley, and M.R. Loken. 1990. Positive stem cell selection - basic science. In: Gross, S., Gee, A.P., Worthington-White, D.A., eds. Bone Marrow Purging and Processing: Proceedings of the Second International Symposium on Bone Marrow Purging and Processing. Wiley-Liss, New York, NY. pp.387-402.
Colter, M., B. Fogarty, K. McGuire, R. Berenson, and S. Heimfeld. 1992. Rapid isolation of CD4 or CD8 T-cell subsets using the CEPRATE LC laboratory cell separation system. *Transplantation Proceedings.* 24:2801-2802.
Dammer, U., M. Hegner, D. Anselmetti, P. Wagner, M. Dreier, W. Huber, and H.-J. Güntherodt. 1996. Specific antigen/antibody interactions measured by force microscopy. *Biophysical Journal.* 70:2437-2441.
Darnell, J., H. Lodish, and D. Baltimore. 1990. Molecular cell biology. 2nd ed. Scientific American Books, New York, NY.
Denn, M.M. 1980. Process fluid mechanics. Prentice-Hall, Inc., Engle Cliffs, New Jersey.

Dolowy, K. 1980. A physical theory of cell-cell and cell-substratum interactions. In: Curtis, A.S.G., and J.D. Pitts, eds. The third symposium of the British Society for Cell Biology: cell adhesion and motility. Cambridge University Press, Cambridge, UK. pp.39-63.

Edidin, M., Y., Zagyansky, and T.J. Lardner. 1976. Measurement of membrane protein lateral diffusion in single cells. *Science.* 191:466-468.

Edidin, M. 1987. Rotational and lateral diffusion of membrane proteins and lipids: phenomena and function. *Current Topics in Membranes and Transport.* 29:91-127.

Eigen, M. 1974. Diffusion control in biochemical reactions. In. Mintz, S.L., and S.M. Widmayer, eds. Quantum statistical mechanics in the natural sciences. Plenum Press, New York, NY. pp.37-61.

Feinstein, A., and D. Beale. 1977. Models of immunoglobulins and antigen-antibody complexes. In. Glynn, L.E., and M.W. Steward, eds. Immunochemistry, an advanced textbook. Wiley, New York, NY. pp.263-306.

Foresta, C., A. Varotto, and A. Caretto. 1990. Immunomagnetic method to select human sperm without sperm surface-bound autoantibodies in male autoimmune infertility. *Archives of Andrology.* 24:221-225.

Gaudernack, G., T. Leivestad, J. Ugelstad, and E. Thorsby. 1986. Isolation of pure functionally active CD8+ T cells: Positive selection with monoclonal antibodies directly conjugated to monosized magnetic microspheres. *Journal of Immunological Methods.* 90:179-187.

Goldman, A.J., R.G. Cox, and H. Brenner. 1967. Slow viscous motion of a sphere parallel to a plane wall-II Couette flow. *Chemical Engineering Science.* 22:653-660.

Goldshtik, M.A., V.M. Khanin, and V.G. Ligai. 1986. A liquid drop on an air cushion as an analogue of Leidenfrost boiling. *Journal of Fluid Mechanics.* 166:1-20.

Golubev, A., and E. Sidorva. 1989. The use of targeted liposomes to isolate cells bearing immunoglobin receptors. *Journal of Immunological Methods.* 125:29-34.

Hammer, D.A., and D.A. Lauffenburger. 1987. A dynamical model for receptor-mediated cell adhesion to surfaces. *Biophysical Journal.* 52:475-487.

Hammer, D.A., and M. Tirrell. 1996. Biological adhesion at interfaces. *Annual Reviews in Materials Science.* 26:651-691.

Hasthorpe, S., J. Rogerson, S.L. Green, and J.M. Radley. 1990. Use of bone marrow somatic cell hybrid lines to generate monoclonal antibodies specifically reactive with rare marrow cells. *Experimental Hematology.* 18:223-227.

Hertz, C.M., D.J. Graves, D.A. Lauffenburger, and F.T. Serota. 1985. Use of cell affinity chromatography for separation of lymphocyte subpopulations. *Biotechnology and Bioengineering.* 27:603-612.

Hildebrand, F.B. 1976. Advanced calculus for applications. 2nd ed. Prentice-Hall, Inc., Englewood Cliffs, New Jersey.

Horton, J.K., O.M. Evans, K. Swann, and S. Swinburne. 1989. A new rapid method for the selection and cloning of antigen-specific hybridomas with magnetic microspheres. *Journal of Immunological Methods.* 124:225-230.

Jacobson, K., D. O'Dell, and J.T. August. 1984. Lateral diffusion of a 80,000 dalton glycoprotein in the plasma membrane of murine fibroblasts: relationships to structure and function. *Journal of Cell Biology.* 99:1624-1633.

Janssen, W.E., and A.M. Rios. 1989. Non-specific cell binding characteristics of para-magnetic polystyrene microspheres used for antibody-mediated selection. *Journal of*

Immunological Methods. 121:289-294.

Jasiewicz, M.L., D.R. Schoenberg, and G.C. Mueller. 1976. Selective retrieval of biotin-labeled cells using immobilized avidin. *Experimental Cell Research.* 100:213-217.

Kato, K., and A. Radbruch. 1993. Isolation and chacterization of $CD34^+$ hematopoietic stem cells from human peripheral blood by high gradient magnetic cell sorting. *Cytometry.* 14:384-392.

Kokkinopoulos, D., S. Perez, R. Sotiradou, J. Stinios, and M. Papamichail. 1992. The use of nylon wool for the isolation of T lymphocyte subpopulations. *Journal of Immunological Methods.* 154:1-6.

Kuo, S.C., and D.A. Lauffenburger. 1993. Relationship between receptor/ligand binding affinity and adhesion strength. *Biophysical Journal.* 65:2191-2200.

Larsson, P.H., J. Hed, S.G.O. Johansson, U. Persson, and M. Wahlström. 1989. Improved cell depletion in a panning technique using covalent binding of immunoglobins to surface modified polystyrene dishes. *Journal of Immunological Methods.* 116: 293-298.

Lauffenburger, D.A., and C. DeLisi. 1983. Cell receptors: physical chemistry and cellular regulation. *International Review of Cytology.* 84:269-302.

Lauffenburger, D.A. 1991. Models for receptor-mediated cell phenomena: adhesion and migration. *Annual Reviews in Biophysics and Biophysical Chemistry.* 20:387-414.

Mage, M.G., L.L. McHugh, and T.L. Rothstein. 1977. Mouse lymphocytes with and without surface immunoglobin: preparative scale separation in polystyrene tissue culture dishes coated with specifically purified anti-immunoglobin. *Journal of Immunological Methods.* 15:47-56.

Mandrusov, E., A. Houng, E. Klein, and E.F. Leonard. 1995. Membrane-based cell affinity chromatography to retrieve viable cells. *Biotechnology Progress.* 11:208-213.

Manyonda, I.T., A.J. Soltys, and F.C. Hay. 1992. A critical evaluation of the magnetic cell sorter and its use in the positive and negative selection of CD45RO+ cells. *Journal of Immunological Methods.* 149:1-10.

McCloskey, M.A., and M. Poo. 1986. Contact-induced redistribution of specific membrane components: local accumulation and development of adhesion. *The Journal of Cell Biology.* 102:2185-2196.

Miltenyi, S., W. Muller, W. Weichel, and A. Radbruch. 1990. High gradient magnetic cell separation with MACS. *Cytometry.* 11:231-238.

Nordon, R.E., B.K. Milthorpe, K. Schindhelm, and P.R. Slowiaczek. 1994. An experimental model of affinity cell separation. *Cytometry.* 16:25-33.

Nordon, R.E., D.N. Haylock, L. Gaudry, and K. Schindhelm. 1996. Hollow-fiber affinity cell separation system for $CD34^+$ cell enrichment. *Cytometry.* 24:340-347.

Nordon, R.E., and K. Schindhelm. 1997. Design of hollow fiber modules for uniform shear elution affinity cell separation. *Artificial Organs.* 21:107-115.

Pecht, I., and D. Lancet. 1977. Kinetics of antibody-hapten interactions. In. Pecht, I., and R. Rigler, eds. Chemical relaxation in molecular biology. Springer-Verlag, Berlin, Germany. pp.306-338.

Rasmussen, A.-M., E.B. Smeland, B.K. Erikstein, L. Caignault, and S. Funderud. 1992. A new method for detachment of Dynabeads from positively selected lymphocytes. *Journal of Immunological Methods.* 146:195-202.

Rutishauser, U., I. Yahara, and G.M. Edelman. 1974. Morphology, motility, and surface behavior of lymphocytes bound to nylon fibers. *Proceedings of the National*

Academy of Science USA. 71:1149-1153.

Sargent, I.L., Y.S. Choo, and C.W.G. Redman. 1994. Isolating and analyzing fetal leukocytes in maternal blood. *Annals of the New York Academy of Science*. 731:147-153.

Shao, J.-Y., and R. M. Hochmuth. 1996. Micropipette suction for measuring piconewton forces of adhesion and tether formation from neutrophil membranes. *Biophysical Journal*. 71:2892-2901.

Skuse, D.R., W. Müller, and D.E. Brooks. 1988. Column chromatographic separation of cells using aqueous polymeric two-phase systems. *Analytical Biochemistry*. 174:628-635.

Spangrude, G.J., S. Heimfeld, and I.L. Weissman. 1988. Purification and chacterization of mouse hematopoietic stem cells. *Science*. 241:58-62.

Tanaka, H.,Y. Ishida, T. Kaneko, and N. Matsumoto. 1989. Isolation of human megakaryocytes by immunomagnetic beads. *British Journal of Hematology*. 73:18-22.

Thomas, T.E., H.J. Sutherland, and P.M. Lansdorp. 1989. Specific binding and release of cells from beads using cleavable tetrameric antibody complexes. *Journal of Immunological Methods*. 120:221-231.

Wiegel, F.W. 1984. Diffusion of proteins in membranes. In. Perelson, A.S., C. DeLisi, and F.W. Wiegel eds. Cell Surface dynamics: concepts and models. Marcel Dekker Inc., New York, NY. pp.135-150.

Wysocki, L.J., and V.L. Sato. 1978. "Panning" for lymphocytes: a method for cell selection. *Proceedings of the National Academy of Science USA*. 75:2844-2848.

Xiao, Y., and G.A. Truskey. 1996. Effect of receptor-ligand affinity on the strength of endothelial cell adhesion. *Biophysical Journal*. 71:2869-2884.

Yannelli, J.R. 1991. The preparation of effector cells for use in the adoptive cellular immunotherapy of human cancer. *Journal of Immunological Methods*. 139:1-16.

Zhurkov, S.N. 1965. Kinetic concept of strength of solids. *International Journal of Fracture Mechanics*. 1:311-323.

Chapter 3. A Novel Immunoaffinity Method for Selective Cell Separation Using Hollow-Fiber Membranes

3.1 Abstract

Adsorption of cells to a surface for cell separation has widespread applications, such as bone marrow processing, laboratory research, and monoclonal antibody production. We have developed a novel method of positive, reversible cell separation using hollow-fiber membranes which were chemically modified so that proteins, such as monoclonal antibodies (mAbs) or recombinant Protein A (rpA), can be covalently attached to the surface. The cell separation procedure described in this study proceeds via four steps: (1) surface loading of cells onto membranes by gravity sedimentation, (2) incubation to strengthen cell attachment, (3) washing, and (4) detachment. Reverse filtration, produced with a negative transmembrane pressure (back-pressure) with neutral pH (7.4) or low pH (2.5) buffers, was used to remove cells in step (4).

We have performed experiments utilizing a direct binding approach, where mAbs directed against a target cell receptor were attached, and using an indirect binding approach where rpA was attached to fibers. We employed human leukemia (HL-60) and lymphoma (Namalwa) cell lines as model cells for separation. For direct binding experiments, $CD19^+$ cells were incubated with fibers coated with anti-CD19 mAb (test condition). Control experiments included incubating anti-CD19-coated fibers with a $CD19^-$ cell line and incubating $CD19^+$ cells with fibers coated with an antibody without immunospecificity for $CD19^+$ cells. The number of bound cells per cm of fiber edge was determined by brightfield microscopy. Fibers were then pressurized at 0 and 20 psig with a neutral pH buffer to remove cells, after which cells bound to the same fiber edge were counted. Binding under

test conditions yielded up to 500 ± 120 (mean ± SEM) cells bound per cm of fiber edge vs. only 33 ± 18 for control conditions. In addition, 32 ± 12 % of these initially bound cells were removed when fibers were attached to the pressure supply mechanism but not pressurized (0 psig), whereas, an additional 86 ± 5 % of remaining cells were removed when the fiber was pressurized at 20 psig. For indirect binding experiments, $CD33^+$ cells were first pre-incubated with anti-CD33 mAbs and then incubated with rpA-coated fibers (test condition). Control experiments included pre-incubating $CD33^-$ cells with anti-CD33 mAbs and incubating $CD33^+$ cells with mAbs without immunospecificity for $CD33^+$ cells both with subsequent incubation of cells with rpA-derivitized fibers. For some indirect binding experiments, the fibers were pressurized with a low pH buffer. Binding under test conditions yielded 352 ± 37 cells bound per cm fiber edge vs. 0.4 ± 0.3 for control conditions. In addition, 56 ± 11 % of these initially bound cells were removed when fibers were attached to the pressure supply mechanism but not pressurized (0 psig), whereas, an additional 73 ± 10 % of remaining cells were removed when the fiber was pressurized at 20 psig with a neutral pH buffer and 96 ± 2 % with a pH 2.5 buffer. Experiments were also performed in which $CD33^+$ cells and $CD33^-$ cells were separately pre-incubated with different fluorescent vital stains, incubated with anti-CD33, mixed together (1:1) and incubated with rpA-derivitized fibers. The fibers were then observed with epi-fluorescence microscopy and the purity of target cells (HL-60) bound to the fiber was determined. The final purity of target cells was 97.6 ± 1.5 %.

3.2 Introduction

The use of immunoaffinity methods for selective cell separation has widespread applications in clinical medicine such as bone marrow processing (Anderson et al., 1990; Foresta et al., 1990; Berenson et al., 1991; Yannelli, 1991; Kato and Radbruch, 1993;

Sargent et al., 1994; Brugger et al., 1995), research (Spangrude et al., 1988; Golubev and Sidorva, 1989; Tanaka et al., 1989; Berson et al., 1996), and monoclonal antibody production (Horton et al., 1989; Hasthorpe et al., 1990). Many different techniques and geometric configurations have been used for affinity-based cell separations. The techniques fall into two broad categories: separations using solid phase substrates (immunoaffinity adsorption) and separations which are liquid-phase procedures. Common solid phase techniques include column affinity chromatography (Hertz et al., 1985; Berenson et al., 1986a; Berenson et al, 1986b; Berenson et al., 1991), adsorption of cells to derivatized plates and flasks ("panning") (Mage et al., 1977; Wysocki and Sato, 1978; Larsson et al., 1989; Nordon et al., 1994; Berson et al., 1996), adsorption of cells to fibers and meshes (Rutishauser et al., 1974; Jasiewicz et al., 1976; Kokkinopoulos et al., 1992), and adsorption of cells to magnetic beads (Gaudernack et al., 1986; Horton et al., 1989; Tanaka et al., 1989; Foresta et al., 1990) or magnetic colloids (Miltenyi et al., 1990; Manyonda et al., 1992; Kato and Radbruch, 1993). Liquid-phase techniques include fluorescence activated cell sorting (FACS) (Spangrude et al., 1988; Hoven, et al., 1989; Szilvassy et al., 1989; Sargent et al., 1994; Tse, et al., 1994), immuno-targeted toxins (Montgomery et al, 1990; Uckun et al, 1990), and complement-mediated depletion (Slaper-Cortenbach et al., 1990).

Each of these methods has strengths and weaknesses. Destructive methods such as immunotoxins and complement lysis can only be used for negative selection (purging) of unwanted cells and cannot be used to positively select and recover a single cell type except in extremely simple cell mixtures. FACS and solid-phase immunoaffinity techniques can be used for positive selection. FACS yields positively selected populations of high purity, but is relatively slow and cannot process large clinical-scale ($>10^9$) cell loads. In addition, yield and viability of FACS-separated cells is typically low. The solid-phase immunoadsorption

techniques mentioned also have shortcomings when used for positive selection. Serious problems are contamination of target cells with non-specifically adhered or retained cells (low selectivity), and difficulty in removing the positively selected cells from the substrate as well as low capacity and lack of reproducibility. Techniques which employ packed beds or beads such as column affinity chromatography and magnetic beads have a tendency to retain non-target cells through non-specific adherence and physical trapping of cells within the matrix of beads (Basch et al., 1983; Skuse et al., 1988; Janssen and Rios, 1989). In addition to non-specific retention of non-target cells, target cells can be difficult to elute. Common techniques employed to remove cells include treatment with exogenous agents (Basch et al., 1983; Thomas et al., 1989; Civin et al., 1990; Rasmussen et al., 1992) and physical agitation (Berenson et al., 1986b; Berenson et al., 1991; Colter et al., 1992). These procedures can add undesirable agents to the recovered cell fraction or tend to use physical forces which are not well characterized or reproducible. "Panning" procedures using flat plate or tissue culture flask devices are limited by device size constraints to smaller cell loads ($< 10^8$) and cells are typically detached by long incubations, with physical agitation of the plate or flask, or by scraping the cells off the surface to which they are adsorbed (Mage et al., 1977; Wysocki and Sato, 1978; Berson et al., 1996).

In this report we describe a novel method for selective cell separation utilizing immunoadsorption to porous polymer membranes. Membranes have the ability to be used for negative or positive cell selection. The method we employ takes advantage of the permeability of microporous membranes. Membranes can be functionalized with ligands, such as monoclonal antibodies, which have specificity to adsorb directly to cell surface markers, or a linker molecule, such as Protein A which has specificity for the Fc portion of immunoglobin G (IgG). In the latter instance, cells are pre-incubated with an anti-cell surface

marker antibody and are attached indirectly to the polymer membrane via the linker molecule. Cells may be deposited onto one side of the membrane by gravity sedimentation or cells may be filtered onto the surface. Non-specifically adhered cells can be removed from the surface by applying a shearing force. Selectively adsorbed cells can be removed from the surface by applying a back-pressure which induces back-filtration and creates a removal force on the cell proportional to the applied pressure drop and the cell-surface contact area. The force applied to a cell attached to a porous surface imposed by an applied back-pressure and back-filtration is sensitive to cell shape, contact area, separation distance and fiber membrane morphology and permeability (see section 3.12 and chapter 2). Back-pressure is most effective for removing cells which are very closely adsorbed to a membrane (separation distances on the order of 10^{-8} to 1×10^{-7}m), and which have substantially sized, flattened contact areas. Back-pressure is also most effective for removing cells from membranes which are anisotropic in morphology. In addition, the force applied to a cell due to back-pressure increases as the hydraulic permeability of the membrane increases This removal force may be combined with the imposition of shear forces and exogenous agents in the eluting solution if necessary.

A membrane-based device has the ability to apply controllable and reproducible forces on adhered cells, large surface areas for adsorption can be constructed in reasonably sized devices especially when utilizing hollow-fiber membranes in shell and tube configurations, and cells adsorb in a monolayer on a flat surface minimizing non-specific entrapment. Thus, membrane-based devices have the potential to overcome many of the shortcomings of currently available cell-separation methods. In addition, hollow-fiber membrane devices for cell separation have the potential to be completely automated and computer controlled much like modern plasmapheresis and hemodialysis equipment, potentially reducing operator-induced reproducibility problems. In the current study, we demonstrate the feasibility of

using microporous hollow-fiber membranes for the positive selection of cells loaded onto single fibers under the influence of gravity. We show that target cells can be adsorbed to single hollow fibers with high selectivity, and that they can be removed in a viable state using reverse pressurization with and without an exogenous agent (low pH buffer).

3.3 Materials and Methods

3.3.1 Hollow-Fiber Membranes

Two lots of polyethersulfone/polyethylene oxide hollow-fiber microporous membranes (kindly provided by Sepracor Inc., Marlborough, MA) were employed, designated by the manufacturer as lots XC3089B1 (Lot 1) and X3257B2 (Lot 2). The hollow-fibers were treated with ethylene glycol diglycidyl ether (EGDGE), coated with polymers containing hydroxyl groups or imine groups, and further functionalized with chemically reactive groups in order to reduce non-specific adsorption and facilitate the immobilization of protein by one of the procedures outlined below (Azad and Goffe, 1990).

3.3.1.1 Hydrazide Functionalization

For some experiments, polyethylene imine was coated onto hollow-fiber membranes following treatment with EGDGE. The fibers were sequentially treated with glutaraldehyde and then adipic acid dihydrazide, resulting in a surface containing hydrazide groups which are reactive with aldehyde groups on oxidized glycosylated proteins (Azad and Goffe, 1990).

The density of surface bound hydrazide groups was assayed by placing small segments of the fibers in boiling water for 30 min with ninhydrin reagent solution (Sigma, St. Louis, MO) which reacts with the hydrazide groups, forming a soluble product which absorbs at 570 nm (Hermanson et al., 1992). A standard curve was generated by treating samples containing known quantities of adipic acid dihydrazide (AAD). The absorbance of the

samples containing fiber segments was compared to that of the samples containing AAD to determine the total number of hydrazide groups present.

3.3.1.2 2-Fluro-1-Methylpyridinium Toluene-4-Sulfonate (FMP) Functionalization

For some experiments, hydroxyethylcellulose (Aqualon, Wilmington, DE) was coated onto the hollow-fiber membranes following treatment with EGDGE (Azad and Goffe, 1990; Klein et al., 1994). The hydroxyl groups were then activated by reaction with FMP in the presence of a slight excess of a tertiary amine (triethylamine) in anhydrous acetonitrile, which resulted in a surface containing 2-alkylopyridinium salts which are reactive with nucleophiles such as amino groups (Ngo, 1986).

The density of surface-bound FMP groups was assayed by reacting small segments of the fibers with excess ethanolamine in water 6% (v/v). The soluble product formed from the reaction between the active surface groups and the ethanolamine, 1-methyl-2-pyridone, was detected by its absorbance at 297nm using an extinction coefficient of 5.9 (Ngo, 1986).

3.3.2 Chacterization of Membranes

3.3.2.1 Hollow-Fiber Dimensions and Structure

Hollow-fibers were sectioned with a sharp razor and examined by light microscopy. Inside and outside diameters were determined for each fiber lot by measuring two perpendicular diameters of fiber cross-sections with an eye piece reticle inscribed with a linear scale. Total membrane volume including void volume was defined as:

$$V_m = \pi \frac{L}{4}(d_o^2 - d_i^2) \qquad (1)$$

where d_0 is the outer diameter of the fiber, d_i is the inner diameter of the fiber, and L is the length of the fiber sample. Membrane structure of base fibers (fibers which have not been

chemically modified) for samples coated with 30-40 Å of gold/palladium using a high resolution ion beam coater (Model 681, Gatan Inc., Warrendale, PA) was observed by scanning electron microscopy (SEM) on a JEOL-6320F (JEOL, Peabody, MA) or a Cambridge 250 microscope (Leica Cambridge Ltd., Cambridge, England). Cross-sectional views were prepared by scoring the fiber lightly with a sharp razor blade, submersing it in liquid nitrogen, and then quickly fracturing it at the score. The range of pore sizes on the retentive surface of the base fibers was determined by measuring the effective diameters of the largest and smallest pores visible on SEM photomicrographs of a minimum of two separate areas of the retentive surface at magnifications ranging from 20,000 × to 60,000 × representing a minimum analyzed area of 40 μm^2 for Lot 1 fibers and 125 μm^2 for the Lot 2 fibers. The total number of pores analyzed was about 6,000 for both fiber types. Measurements of the largest and smallest pores visible on each photomicrograph were made with precision calipers (Mitutoyo Corporation, Tokyo, Japan), and an effective diameter was defined as the geometric mean of the largest and smallest diameters for each pore. Pore size distribution of the base fibers was also measured using a Coulter® porometer (Coulter Electronics Limited, Luton, England) with Coulter Porofil® as the wetting fluid.

Surface area of the base fibers was measured by nitrogen gas porosimetry at 77 K using a Micrometrics Flowsorb II® Model 2300 (Micrometrics Instrument Corp., Norcross, GA) employing the Brunauer, Emmett, Teller equation (BET) to analyze the adsorption/desorption isotherms. The surface area determined in this fashion was used to calculate the surface density of chemical groups and immobilized ligand on the fibers.

3.3.2.2 Hydraulic Permeability

Hydraulic permeability was measured with individual fibers placed in small modules. The outlet of the fiber lumen was clamped, water was pumped through the fiber wall, and the

inlet pressure was measured. The hydraulic permeability was calculated from

$$J_v = \frac{Q}{\pi d L} \tag{2}$$

where Q is the measured filtrate flowrate (L/hr), d is the diameter of the retentive fiber surface (m), and L is the fiber length (m). The hydraulic permeability was evaluated from

$$L_p = \frac{J_v}{\Delta P_{TM}} \tag{3}$$

where ΔP_{TM} is the transmembrane pressure difference (mmHg).

3.3.3 Attachment of Ligands to Functionalized Fibers

3.3.3.1 Attachment of Antibodies to Hydrazide-Functionalized Fibers

Hydrazide-functionalized fibers were used for site-directed immobilization of antibodies which contain carbohydrate moieties located predominantly on the Fc portion of the molecule (O'Shannessy, 1990). The antibodies immobilized were as follows: affinity- and HPLC-purified mouse monoclonal IgG1 antibody to human CD19 cell surface antigens (kindly provided by Immunogen, Inc., Cambridge, MA); and non-immunospecific affinity-purified mouse polyclonal IgG1 (Lampire Biological Laboratories, Pipersville, PA). The hydroxyl groups on the carbohydrate moieties of antibodies were oxidized under acidic pH conditions (pH 5) with 0.01 M sodium metaperiodate in 50 mM sodium acetate 150 mM NaCl buffer. The oxidized antibody in 50 mM sodium acetate, 150 mM NaCl buffer (pH 5) was incubated with the fibers with agitation provided by an orbital shaker for 16-20 hr at room temperature (23 ± 2°C). The covalent bond formed between the aldehyde and hydrazide groups was reduced and stabilized by a 1 hr incubation with 0.05 M sodium cyanoborohydride (Holton and Vicalvi, Jr., 1991). Fibers with immobilized ligand were

stored at 4° C in phosphate buffered saline (PBS : 0.01 M phosphate, 0.138 M NaCl, 0.0027 M KCl, pH 7.4) with 0.02% w/v sodium azide (PBSA) and 1% w/v bovine serum albumin (BSA).

3.3.3.2 Attachment of Recombinant Protein A (rpA) to FMP-Functionalized Fibers

Covalent coupling of rpA (Repligen, Cambridge, MA) to FMP-functionalized fibers via primary amine groups on the rpA was carried out by incubating slightly alkaline (pH 8-9) aqueous rpA solution (25 mM sodium tetraborate buffer) with agitation provided by an orbital shaker (Ngo, 1986). Residual active groups remaining on the fiber were deactivated by hydrolysis with sodium hydroxide. Fibers with immobilized ligand were stored at 4° C in PBSA.

3.3.3.3 Quantification of Immobilized Protein

The amount of protein immobilized on the functionalized fibers was measured by incubating small segments of protein-coated fibers with BCA® protein assay reagent (Pierce, Rockford, IL), measuring absorbance of the soluble reaction product at 562 nm, and comparing measured values to a standard curve prepared with solutions containing known amounts of a protein similar to the immobilized protein (Stich, 1990; Holton and Vicalvi, Jr., 1991). To measure antibody immobilized to hydrazide-functionalized fibers, controls (functionalized fiber with no immobilized protein) were included because components of the functionalized fiber catalyzed the reaction of the BCA® protein assay reagent. The controls produced a baseline absorbance which was subtracted from the absorbance measured for fibers with immobilized protein.

3.3.3.4 Adsorption Capacity of Immobilized rpA

Because the intended function of the rpA-coated fibers was to adsorb cells that have been coated with antibodies, the capacity of the fibers for specific adsorption of antibody and

non-specific adsorption of an inert protein was tested. One centimeter segments of fibers were incubated with 0.5 ml of a 1 mg/ml solution of the test protein in PBSA for 4-24 hr at room temperature. The fibers were then extensively washed with protein-free buffer until the wash buffer was free of protein as determined by UV absorption at 280 nm. The adsorbed protein was then eluted with a solution containing 50 mM glycine and 150 mM NaCl (pH 2.5). Eluted protein concentration was determined by UV absorption at 280 nm. Test proteins included human polyclonal IgG (Gammagard, Hyland Div., Baxter Healthcare, Glendale, CA), a mouse myeloma monoclonal IgG2b (Sigma, St. Louis, MO) protein of the same isotype as the anti-CD33 monoclonal antibody subsequently used in cell adsorption experiments, and IgG-free BSA (Miles Inc., Kankakee, IL) as a non-specific adsorption control.

3.3.4 Cell Lines

Two human cell lines, Namalwa and HL-60 were used for experiments. Namalwa is a Burkitt's lymphoma cell line (Nadkarni et al., 1969) which expresses CD19 on its membrane but not CD33 as determined by immunostaining and flow cytometry (see section 3.7). HL-60 is a pro-myelocyte leukemia cell line (Collins et al., 1977) which expresses CD33 but not CD19 (see section 3.7). Cell lines were grown in continuous suspension culture in tissue culture flasks at 37° C in a humidified air atmosphere containing 5% CO_2 in RPMI media supplemented with 25 mM HEPES buffer, 10% fetal bovine serum (FBS), 4 mM L-glutamine, 50 IU/ml penicillin and 50 μg/ml streptomycin (BioWhittaker, Walkersville, MD). Cells were used for experiments while in their log growth phase (see section 3.8).

3.3.5 Cell Adsorption Experiments

3.3.5.1 Direct Adsorption of Cells to Hydrazide-Functionalized Hollow Fibers Coated with Anti-CD19 mAb

Single hollow-fibers 5 cm in total length were coated with immobilized anti-CD19 mAb in order to selectively adsorb Namalwa target cells to the outer fiber surface. Two types of control experiments were carried out to assess non-specific adsorption: (1) incubation of Namalwa target cells ($CD19^+$) with fibers to which a non-immunospecific mouse IgG1 protein was immobilized, and (2) incubation of HL-60 cells ($CD19^-$) with fibers to which anti-CD19 mAb was immobilized.

Figure 3.1 shows a schematic diagram of the functionalized hollow-fibers employed. Small (1 cm) lengths of plastic (Tygon) tubing were glued to each end to facilitate handling and pressurization, and orientation marks were placed on the ends of the plastic tubing. After the plastic tubing was attached, the active length of the fiber available for cell adsorption was about 4 cm. The fibers were then coated with antibody or rpA as previously described before being employed for cell adsorption. Prior to use, the fibers were extensively washed by soaking each fiber for 4 × 15 min intervals in a 50 ml test tube filled with modified Dulbecco's phosphate buffered saline without calcium and magnesium at pH 7.4 (DPBS, Sigma, St. Louis, MO) to remove any trace of sodium azide in the storage buffer. An aliquot of cells from culture were added to a test tube containing Trypan Blue dye, and live and dead cells were counted with a hemacytometer (Reichert Scientific Instruments, Buffalo, NY). A sufficient number of cells to perform the experiment were centrifuged (400 × g, 10 min, room temperature) and resuspended in DPBS to wash the cells free of serum and culture media. This was repeated for a total of two washes. The cells were resuspended in 5 ml DPBS with 1% w/v BSA at a concentration of 5×10^6 viable cells/ml and incubated at room temperature

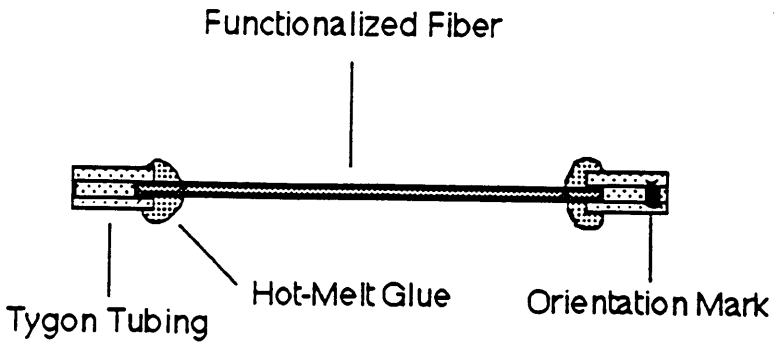

Figure 3.1 Schematic Diagram of Functionalized Hollow Fiber Membranes. Single hollow fibers, 5 cm in length, were activated with hydrazide or FMP chemistry. Small pieces of Tygon® tubing were attached with a hot-melt glue gun, and an orientation mark was placed on the Tygon® tubing. These fibers were then coated with antibodies (hydrazide) or rpA (FMP) in preparation for cell binding experiments.

with a fiber placed along the bottom edge of a T25 tissue culture flask (Falcon, Beckton Dickinson, Franklin Lakes, NJ) tilted at a 45° angle to maximize the number of cells which settle onto the fiber surface by gravity during a 1 hr incubation. The fluid was very gently agitated manually at 15 min intervals to resuspend unadsorbed cells. The supernatant was then slowly aspirated, leaving behind enough liquid to cover the fiber. The fiber was gently washed three times with 25 ml DPBS dispensed at about 25 ml/min from a pipette into the flask, but away from the fiber, and the wash fluid was aspirated each time.

The fiber was removed from the flask by gripping the plastic tubing with tweezers, and placed into a 60 mm diameter petri dish filled with DPBS. Care was taken to perform the transfer quickly but gently to minimize disruption of cells on the fiber by contact with air. The fiber was observed with an inverted microscope in brightfield at low magnification (100x) and an orientation was chosen which had the highest visible cell density along the edges of the fiber. All of the cells adsorbed to both visible edges of the fiber were counted using a linear scale reticle. In regions where cells overlapped, the average distance between cell centers was assumed to be 10 μm. Cell diameters ranged from about 6 to 20 μm with a mean cell diameter of about 12 - 14 μm (see sections 3.9 and 3.10). In cases where the adsorbed cell density for non-specific cell adsorption control experiments was 5% or more of the value with target cells, both fibers were flushed identically with a 3.5 ml transfer pipet by aspirating some of the DPBS in the dish and gently dispensing it (about 1 ml/s flowrate) along the length of the fiber and directly incident on the fiber edges being observed with the microscope. The cells along the same edges were then recounted.

The cells were removed from the outer fiber surface by reverse filtration of DPBS (pH 7.4) through the fiber wall for 5 min with a back-pressure of 20 psig applied to the fiber lumen. The fiber was transferred to a larger diameter (150 mm) petri dish filled with DPBS.

Figure 3.2 shows the apparatus for reverse pressurization. The plastic tubing at one end of the fiber was sealed with a polyethylene plug; to the other end was attached a polyethylene connector which was in turn attached to Tygon tubing connected to a 60 ml syringe in a syringe pump. Pressure in the tubing was measured with a stainless steel pressure gauge (0 - 60 psig, Ashcroft, Stratford, CT) connected via a T branch. With the tubing clamped, the syringe pump (Model 975, Harvard Apparatus, South Natick, MA) was turned on, thereby increasing the pressure in the line. When the pressure reached 20 psig, the clamp was released, the fiber experienced the full pressure immediately, and the fiber was observed to assure that no gross leaks were present. In some experiments, the fiber was first transferred to a 15 ml centrifuge tube containing 7-10 ml RPMI 1640 with 10 % v/v FBS and 25 mM HEPES. Eluted cells were centrifuged (400 × g, 15 min), the supernatant was aspirated, and the cells were resuspended in 1 ml RPMI 1640 with 10 % v/v FBS and 25 mM HEPES, and assessed for viability by Trypan Blue exclusion as previously described. After reverse pressurization, the fiber was transferred back to the petri dish used for microscopic observation, and cells along the visible edges were recounted with the fiber in the same orientation as when previously counted. Controls for cell detachment experiments with Lot 1 fibers consisted of exposing an identically prepared fiber with adsorbed cells to identical handling conditions but without reverse pressurization. With Lot 2 fibers, a single fiber acted as its own control. Initially, the procedure was the same as for Lot 1 detachment controls. The same fiber was then subjected to back-pressure, after which, the cells remaining on the fiber were counted with the light microscope. For both the handling control step and the back-pressure step, the fraction of the cells removed was defined as the number of cells removed during each step as a fraction of the cells present on the fiber immediately prior to performing the step.

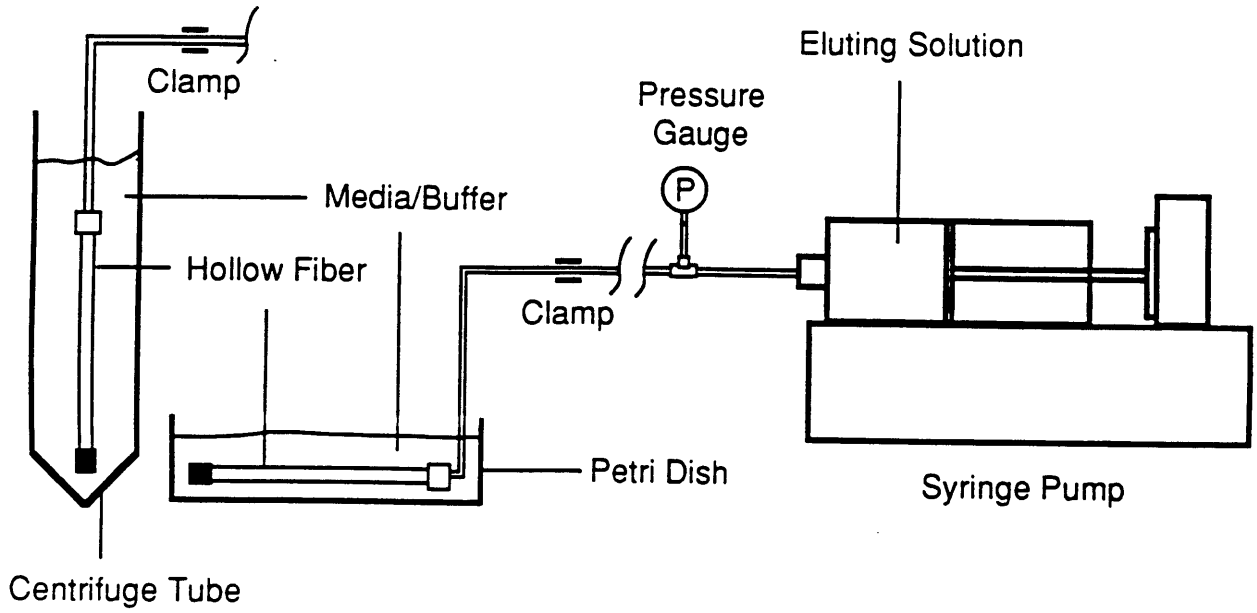

Figure 3.2 Pressurization apparatus used for cell desorption with back-pressure. During pressurization, one end of the Tygon® tubing on the cell-covered hollow fiber was sealed, and to the other end was connected a polypropylene connector which was in turn attached to plastic tubing connected to a 60 ml syringe in a syringe pump. Pressure in the tubing was measured with a stainless steel pressure gauge connected via a T branch. Fibers were either pressurized in a petri dish, or for some experiments where desorbed cells were collected, in a 15 ml centrifuge tube.

3.3.5.2 Indirect Adsorption of mAb-coated Cells to FMP-Functionalized Hollow-Fibers Coated with rpA

The protocol was similar to that used for direct adsorption except that anti-MY-9 anti-CD33 IgG2b mAb (Griffin et al., 1984) was first bound to the HL-60 target cells and rpA was covalently immobilized to the surface of the hollow-fiber. Cells in culture were counted, and viability was determined by Trypan Blue exclusion as previously described. The cells were centrifuged (400 × g, 4 °C) and the pellet was resuspended and incubated for 30 min in cold (4 °C) RPMI media containing 10 % FBS and a 1:500 dilution of ascites containing approximately 5 mg/ml of the anti-CD33 mAb at a concentration of 10^7 cells/ml. The cells were washed twice with cold DPBS, resuspended at 5×10^6 cells/ml in cold DPBS with 1% w/v BSA, and incubated with the fiber at 4 °C for 30 min and then at room temperature for an additional 45 min. Non-specific adsorption control experiments included: (1) incubation of the fibers with Namalwa cells ($CD33^-$) which had first been pre-incubated with anti-CD33 mAb, and (2) incubation of the fibers with HL-60 cells which had first been pre-incubated with a non-immunospecific mouse IgG2b mAb. The remainder of the protocol was the same as that described for direct adsorption experiments using Lot 2 fibers. In some experiments, fibers were pressurized with 50 mM glycine buffer (pH 2.5) containing 150 mM NaCl instead of DPBS (pH 7.4). Detached cells were collected in 15 ml centrifuge tubes as previously described which contained a large enough volume of media supplemented with 25 mM HEPES to maintain the final pH above 6.6.

3.3.5.3 Purification of HL-60 Target Cells from a 50:50 Mixture of HL-60 and Namalwa Cells Using Indirect Adsorption.

HL-60 and Namalwa cells were counted and aliquots of each type containing equal numbers of cells were centrifuged to pellet cells, resuspended in RPMI 1640 media containing

one of two fluorescent vital stains (10 μM Cell Tracker Orange® or 6μM Cell Tracker Green®, Molecular Probes, Eugene, OR) and incubated in the dye-containing media for 30 min at 37 °C, 5% CO_2/ 95% air. Each cell sample was incubated with a different stain so that it would fluoresce in different colors. Cell Tracker Orange® is a rhodamine derivative with an excitation maximum at 541 nm and an emission maximum at 565 nm, and Cell Tracker Green® is a fluorescein derivative with an excitation maximum at 490 nm and an emission maximum at 520 nm. Stained cells were centrifuged and resuspended in dye-free RPMI and incubated for 45 min to remove excess stain. The cells were washed in cold RPMI 1640 with 10% v/v FBS and incubated with anti-CD33 mAb. The two cell samples were mixed together to yield a 50:50 mixture and incubated with a single FMP-functionalized hollow-fiber (Lot 2) containing immobilized rpA. After incubation and gentle washing, the fiber was observed under epi-fluorescence and several areas (minimum of 4) with adsorbed cells were photographed, with a filter set appropriate for one stain and then with another appropriate for the other stain. The filter set used for observing orange stained cells ("orange filter") had a 546 ± 10 nm excitation filter with a ≥ 590 nm emission filter for some experiments or a 580 ± 30 nm emission filter in series with the ≥ 590 nm emission filter for others. The filter set used for observing green stained cells ("green filter") had a 485 ± 22 nm excitation filter with a 530 ± 30 nm emission filter. Cells were then counted from the processed color slides with a slide viewer (Simon Slide Viewing System model SVS 5822, Tim Simon Inc, Tiburon, CA). Cells removed from the fiber by pressurization were recovered in a centrifuge tube, centrifuged, and resuspended in a small volume. A small aliquot of this suspension was placed on a glass microscope slide, covered with a cover slip, observed with the appropriate filter set, and counted directly.

3.3.5.4 Electron Microscopic Observation of Attached Cells

Environmental scanning electron microscopy (ESEM) and transmission electron microscopy were used to observe the morphology of cells adsorbed to fibers. For ESEM observation, cells were adhered to fibers, and then were fixed with a mixture of 1 % w/v formaldehyde and 1.25 % w/v glutaraldehyde in PBS (pH 7.4) at room temperature for 20 min. Fibers were then washed with PBS and samples were observed at 10 kV with the ESEM (Model E-3, Electroscan Corp., Danvers, MA) in a saturated water vapor environment. For TEM, cells adhered to fibers were fixed with 1 % w/v glutaraldehyde in PBS (pH 7.4) at room temperature for 1 hr, washed three times with cold 0.1 M cacodylate buffer (pH 7.4) and post fixed with 2 % w/v osmium tetroxide in 0.1 M cacodylate buffer for 1 hr at 4°C. Fibers were then washed with the cacodylate buffer and dehydrated through a graded series of ethanol/water mixtures (20%, 50%, 70%, 90%, and 100% ethanol). During the dehydration step with 70 % v/v ethanol, 0.5 % w/v uranyl acetate was added for en bloc staining. The dehydrated samples were then infiltrated with Spurr's low viscosity resin (Polysciences, Inc., Warrington, PA) in three steps through a series of propylene oxide/Spurr's resin mixtures. After infiltration and curing of the resin, thin sections were prepared (70 nm) and stained with 1% w/v potassium permanganate for 5 min, 2 % w/v uranyl acetate for 20 min, and Reynolds (Reynolds, 1963) lead citrate for 5 min before observation at 80 kV with the TEM (JEOL 1200 EX II, JEOL, Peabody, MA).

3.4 Results

3.4.1 Characterization of the Non-Functionalized and Functionalized Membranes

3.4.1.1 Hollow-fiber dimensions and structure

Inside diameter of fiber cross-sections was 598 ± 37 μm (n = 10) for Lot 1 fibers and

590 ± 21 μm (n = 10) for Lot 2 fibers. Outside diameter was 1055 ± 58 μm (n = 10) for Lot 1 and 1016 ± 30 μm (n = 10) for Lot 2 fibers. Total membrane volume was calculated to be 0.0059 ± 0.0013 and 0.0054 ± 0.0005 mlmv per cm of fiber length for Lot 1 and Lot 2 fibers respectively. SEM photomicrographs of the hollow fibers employed are shown in figure 3.3. SEM and TEM photomicrographs of the hollow-fibers indicated that the fibers were anisotropic with a surface region near the outside surface which had a substantially lower porosity and pore size than did the bulk of the membrane. The thickness of this low porosity region was estimated from SEM and TEM cross-sections (for TEM examples see figures 3.7-3.9 to follow) and varied from about 1 - 6 μm for Lot 1, and 0.5 - 4 μm for Lot 2 fibers. Pore size estimation from surface micrographs gave effective pore diameters ranging from 0.01 to 0.05 μm for Lot 1 and 0.01 to 0.26 μm for Lot 2 fibers.

The minimum pore diameter measurable with the porometer was 0.07 μm. For Lot 1 fibers, porometer results indicated that all pore diameters were smaller than 0.174 μm, and the mean flow pore size (defined as the pore size giving the same pressure-flow behavior for a fiber with all pores of the same size) was 0.088 μm. Lot 2 fibers had a pore size range of 0.08 μm to 3 μm with a mean flow pore size of 1.25 μm. However, only about 0.5% of the pores were larger than 1 μm, and about 50% of the pores were between 0.08 and 0.12 μm.

The surface area of the hollow-fibers was 6.7 m^2/mlmv for Lot 1 and 3.8 m^2/mlmv for Lot 2. Hydraulic permeability was measured in both the base non-functionalized fibers and the functionalized fibers. With base fibers, hydraulic permeability was 1.0 $Lm^{-2}hr^{-1}mmHg^{-1}$ for Lot 1 and 3.3 $Lm^{-2}hr^{-1}mmHg^{-1}$ for Lot 2. Lot 1 fibers functionalized with hydrazide groups had a hydraulic permeability of 0.35 $Lm^{-2}hr^{-1}mmHg^{-1}$. Lot 2 fibers with hydrazide groups had a permeability of 5.6 $Lm^{-2}hr^{-1}mmHg^{-1}$. For fibers functionalized with FMP, surface functional groups were hydrolyzed with 0.1 N NaOH before flux measurement.

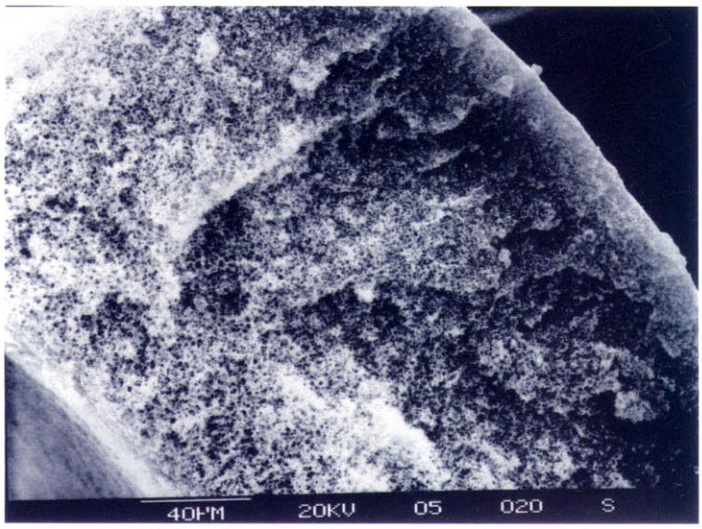

(a)

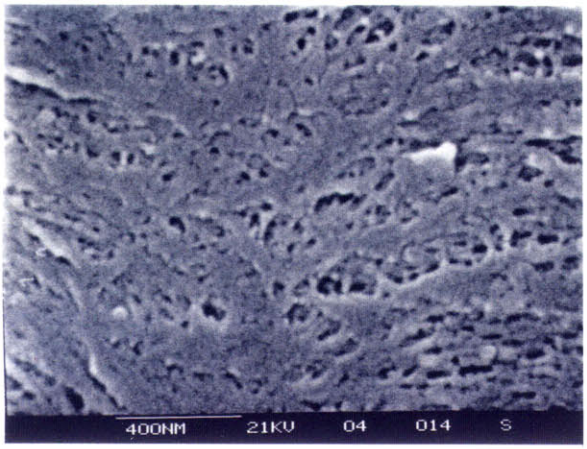

(b)

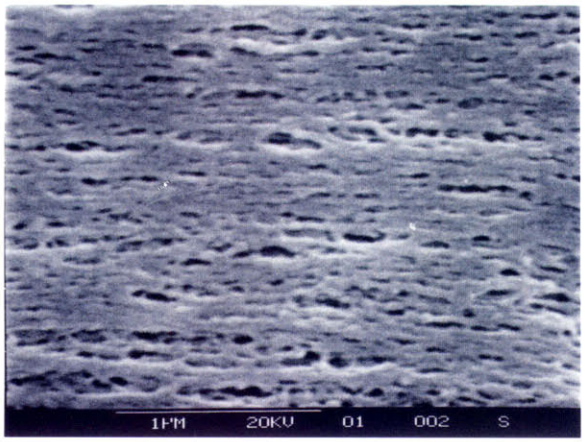

(c)

Figure 3.3 SEM micrographs of hollow fiber membranes. Fibers were coated with about 30Å of gold/palladium. Figure 3.3 (a) shows a cross-section of a Lot 1 fiber. Cross-section was prepared by fracturing a fiber after freezing in liquid nitrogen. Figures 3.3 (b) and (c) show the low porosity outside retentive surface to which cells were bound for Lot 1 and Lot 2 fibers respectively. Bars in captions of photomicrographs represent 40 μm, 400 nm, and 1 μm for (a), (b), and (c) respectively.

Hydraulic permeability of Lot 2 fibers thus treated was 1.1 $Lm^{-2}hr^{-1}mmHg^{-1}$.

3.4.1.2 Amount of ligand immobilized on functionalized fibers

The concentration of functional hydrazide groups on hydrazide-functionalized fibers was 43 μmol/mlmv for Lot 1 and 23 μmol/mlmv for Lot 2. The concentration of functional FMP groups on FMP-functionalized fibers was 33 μmol/mlmv for Lot 2.

Monoclonal anti-CD19 antibody was immobilized to hydrazide-functionalized fibers from both lots. As shown in table 3.1, ligand densities ranged from 1×10^{10} to 3.2×10^{11} mAb/cm^2, where about 1×10^{12} mAb/cm^2 is a monolayer, assuming that each antibody occupies a square 100 Å on each side.

Table 3.1 *Ligand Immobilization Results*

Protein	Immobilized (mg/mlmv)	% Immobilized	Ligand Density x 10^{-11} (molec/cm^2)	Mean Distance Between Molecules (Å)
mAb	0.2 - 3.4	5 - 30	0.1 - 3.2	180 - 1000
rpA	7.2 - 8.4	43 - 56	27 - 35	53 - 61

Table 3.1 also shows the fraction of the antibody initially present in the load solution which was immobilized. This immobilization efficiency ranged from 5 - 30%. The mean distance between mAb molecules on the fiber surface, assuming that the molecules were arranged in a square lattice was 180 to 1000 Å. Non-immunospecific mouse IgG1 was also immobilized to both lots of hydrazide-functionalized fiber; the immobilization results were very similar to those for mAb and fell within the range shown for the mAb in table 3.1. For some fibers where a lower surface concentration of mAb was desired, mixtures of one part anti-CD19 mAb to 4 or 9 parts non-immunospecific IgG1 were immobilized to fibers. rpA ligand densities on FMP-functionalized Lot 2 fibers ranged from 27 to 35×10^{11} rpA/cm^2 (see table 3.1), representing approximately a full monolayer of protein, assuming that each rpA molecule

occupies a square 50 Å on each side.

3.4.1.3 Adsorption capacity of Lot 2 FMP-functionalized, rpA-coated fibers for various proteins

Table 3.2 shows the results of the static capacity measurements expressed as mean plus or minus one standard deviation for n measurements. Over one and a half times more human IgG was adsorbed by the fibers compared to mouse IgG2b (21 ± 7 vs. 12 ± 2 mg/mlmv) while non-specific adsorption (IgG-free BSA) was only 0.2 ± 0.2 mg/mlmv.

Table 3.2 *IgG - Capacity Measurements For rpA-coated Lot 2 Fibers*

Protein	Capacity (mg/mlmv)
Human IgG	21.4 ± 6.6 (n = 6)
Mouse IgG2b	12.0 ± 1.9 (n = 4)
BSA	0.25 ± 0.21 (n = 3)

3.4.2 Cell Adsorption Experiments

3.4.2.1 Direct Adsorption of Cells to Single Hydrazide-Functionalized Hollow-Fibers Coated with Anti-CD19 Monoclonal Antibody (mAb)

Results from cell adsorption and detachment experiments utilizing direct adsorption to mAb-coated fibers is summarized in table 3.3. Results from the two different adsorption control experiments were similar and were pooled. Figure 3.4 shows a brightfield photograph of target cells adsorbed to edge of a mAb-coated hollow fiber for a typical region where there is a large degree of cell overlap. For Lot 1 fibers we found that for the highest ligand densities (1×10^{11} to 3.2×10^{11} mAb/cm^2), on average 216 ± 30 cells adsorbed per cm of fiber edge compared to 7 ± 3 ($p=0.0001$, unpaired Student's t test). This represents a selectivity for target cells of about 97%. With these fibers 47 ±10% of the adsorbed cells

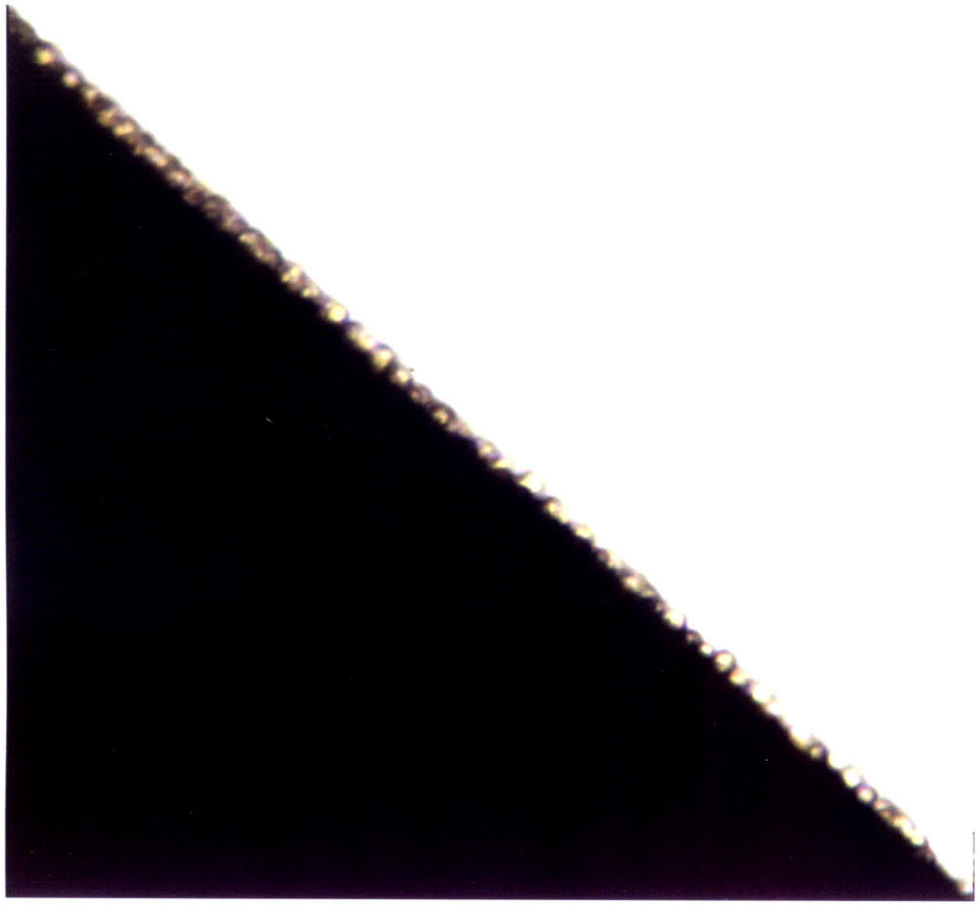

Figure 3.4 Brightfield image of $CD19^+$ Namalwa cells adsorbed to the edge of an anti-CD19-coated fiber (Lot 1). Fiber is black region in lower left.

were removed by pressurization at 20 psi while 11 ± 3% of cells were removed in desorption controls (p=0.03, unpaired Student's t test). For a ten fold reduction in ligand density (1.2 × 10^{10}mAb/cm^2) 360 ± 70 cells adsorbed per cm of fiber edge (p=0.0001 vs. control, unpaired Student's t test) representing a target cell selectivity of about 98 %. With these fibers , 62 ± 17 % of the cells were desorbed by back-pressure and 10.7 ± 0.3 % by mechanical forces or brief air exposure during handling and manipulation for desorption controls. A further ten-fold reduction in ligand density resulted in specific adsorption of 170 ± 40 cells adsorbed per cm of fiber edge (p=0.0001 vs. control, unpaired Student's t test) representing a target cell selectivity of about 96 %. However, with these fibers, cells removed by unpressurized desorption controls, 80 ± 15 %, was comparable to that removed with pressurization, 80 %, indicating cells were weakly adsorbed.

Table 3.3 *Adsorption and Desorption of Cells: Direct Binding with anti-CD19*

Ligand Density (mAbs/cm^2)x10^{-11}	Adsorption Cells bound/cm of fiber edge		Desorption Fraction of cells removed (%)	
	Test	Control	ΔP = 20 psi	ΔP = 0 psi
Lot 1				
1 - 3.2	216 ± 30 (n = 25)	7 ± 3 (n = 28)	47 ± 10 (n = 4)	11 ± 3 (n = 3)
0.12	360 ± 70 (n = 6)		60 ± 15 (n = 4)	10.7 ± 0.3 (n = 2)
0.01	170 ± 40 (n = 13)		80 (n = 1)	80 ± 15 (n = 2)
Lot 2				
0.8 - 3.0	500 ± 120 (n = 5)	33 ± 18 (n = 5)	86 ± 5* (n = 5)	32 ± 12 (n = 5)

Results expressed as mean ± SEM for n measurements

* Viability of Cells (Trypan Blue Exclusion): Prior to Adsorption ≥ 95%
Recovered After Desorption 90 ± 10% (n = 2)

Lot 2 fibers, which had a 15-fold higher hydraulic permeability, had ligand densities comparable to the highest ligand density Lot 1 fibers (0.8×10^{11} to 3.0×10^{11} mAb/cm^2). For these fibers, 500 ± 120 target cells adsorbed per cm fiber edge compared to 33 ± 18 for control experiments (p=0.005, unpaired Student's t test), representing a target cell selectivity of about 93 %. Desorption of cells by back-pressure removed 86 ± 5 % of the cells vs. 32 ± 12 % removed for desorption controls (p=0.006, paired Student's t test). The fraction of cells removed by pressurization for Lot 2 fibers was also significantly higher than for Lot 1 (p=0.008, unpaired Student's t test). In addition, desorbed cells from experiments with Lot 2 fibers were collected and assessed for viability. Prior to adsorption, cells were ≥ 95 % viable. Cells recovered after desorption were 90 ± 10 % viable.

3.4.2.2 *Indirect Adsorption of Cells to Single FMP-Functionalized Lot 2 Hollow-Fibers Coated with Recombinant Protein A (rpA)*

Results from cell adsorption and detachment experiments utilizing indirect adsorption to rpA-coated fibers is summarized in table 3.4.

Table 3.4 *Adsorption and Desorption of Cells: Indirect Binding with anti-CD33 and rpA*

Adsorption Cells/cm edge		Desorption Fraction of cells removed (%)			Viability Fraction of recovered cells (%)		
Test	Control	ΔP=20 psi (pH 7.4)	ΔP=20 psi (pH 2.5)	ΔP=0 psi	ΔP=20 psi (pH 7.4)	ΔP=20 psi (pH 2.5)	ΔP=0 psig
Lot 2							
352 ± 37 (n = 7)	0.4 ± 0.3 (n = 5)	73 ± 10 (n = 3)	96 ± 2 (n = 3)	56 ± 11 (n = 6)	80 ± 10 (n = 3)	82 ± 5 (n = 3)	97 ± 2 (n = 4)

Results expressed as mean ± SEM for n measurements

Results from the two different adsorption control experiments were similar and were pooled. For these fibers, 352 ± 37 target cells adsorbed per cm fiber edge compared to 0.4 ± 0.3 for control experiments (p=0.0001, unpaired Student's t test), representing a target cell selectivity

of about 99.9%. Cell removal due to handling and manipulation or brief air exposure during the desorption control step was much higher in these experiments (more than half removed on average) than for direct binding indicating that cells may be less tightly bound. Desorption of cells by back-pressure with pH 7.4 eluent removed 73 ± 10 % of the remaining cells vs. 56 ± 11 % removed for desorption controls (difference significant with p=0.02, paired Student's t test for the three experiments where pH 7.4 eluent was used). A reduction of the eluent pH to 2.5 resulted in desorption of 96 ± 2 % (p=0.009 vs. desorption controls, paired Student's t test for the three experiments where pH 2.5 eluent was used). Viability of recovered desorbed cells was 80 ± 10 % for cells removed with pH 7.4 eluent, 82 ± 5 % for pH 2.5 eluent and 97 ± 2 % for desorption controls.

3.4.2.3 Purification of HL-60 Target Cells from a 50:50 Mixture of HL-60 and Namalwa Cells Using Indirect Adsorption to Single FMP-Functionalized Lot 2 Hollow Fibers with Immobilized rpA.

Epi-fluorescent photographs of the dye stained cells are shown in figure 3.5. Figure 3.5(a) shows a double exposure of the differentially stained load cell suspension. Figure 3.5 (b) and (c) show typical results for an experiment where the target cells were stained with green dye and the non-target cells with orange dye. Figure 3.5(b) shows many green-stained target cells adsorbed to a fiber as viewed en face using the "green filter" while (c) shows the exact same area using the "orange filter" to observe non-target cells. Figure 3.5 (d) and (e) show typical results for a similar experiment except that the target cells were stained with orange dye and the non-target cells with green dye. Figure 3.5(d) shows the absence of green-stained non-target cells on the fiber as viewed en face using the "green filter" while (e) shows many orange-stained target cells adsorbed to the fiber in the exact same area as viewed using the "orange filter". For four such experiments, the average purity of the target cells

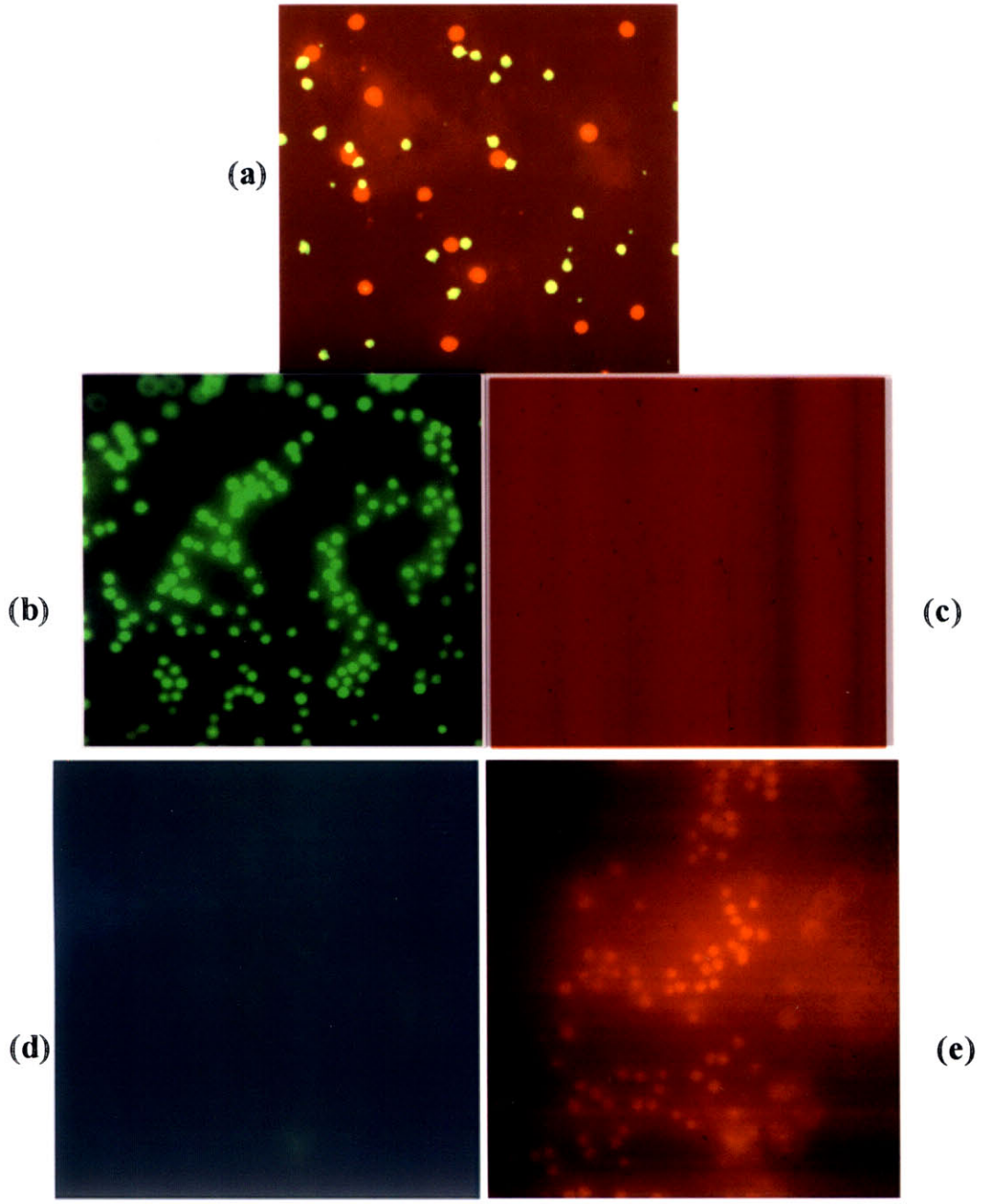

Figure 3.5 Epi-fluorescent en face images of fluorescently stained cells. (a) Double exposure of a 50/50 mixture of target cells (green) and non-target cells (orange) on a glass slide. (b)-(e) show en face views of the hollow fiber surface. (b) and (c) are images of the same area of the fiber for an experiment where target cells were green and non-target cells were orange. (b) View of hollow-fiber surface using "green filter" set (target cells). (c) View of same area of hollow fiber surface as in (b) but using the "orange filter" set (non-target cells). (d) and (e) are an equivalent pair to (b) and (c) except that for this experiment target cells were orange and non-target cells were green. (d) View of hollow-fiber surface using "green filter" set (non-target cells). (e) View of hollow-fiber surface using "orange filter" set (target cells).

observed while adsorbed to the fibers was 97.6 ± 1.5 % (p=0.0001 vs. population mean of 50 %, one sample Student's t test), while the average purity of target cells recovered after desorption by back-pressure was 90.3 ± 1.6 % (p=0.0001 vs. population mean of 50 %, one sample Student's t test). The purity of cells observed while adsorbed to the fibers was significantly higher than the purity of the recovered cells (p=0.05, paired Student's t test).

3.4.2.4 Electron Microscopic Observation of Attached Cells

Figure 3.6 shows ESEM photomicrographs of target cells adsorbed to fibers. Figure 3.6 (a) shows $CD19^+$ Namalwa cells directly adsorbed to anti-CD19 coated Lot 2 hydrazide fibers after a 1 hr incubation at room temperature. Figure 3.6 (b) shows anti-CD33 coated HL-60 cells adsorbed to rpA-coated Lot 2 FMP fibers after a 30 min incubation at 4 °C. These images show that adsorbed cells have a semi-hemispherical shape and a substantial contact area. Smooth surface morphology is probably an artifact caused by the retention of cell membrane-associated water which is opaque to the electron beam.

TEM images of anti-CD33 coated HL-60 cells adsorbed to rpA-coated Lot 2 FMP fibers after a 30 min incubation at 4 °C and subsequent 45 min incubation at room temperature (figures 3.7 to 3.9) corroborate the presence of a semi-hemispherical shape and substantial flattened region in proximity to the fiber surface, but these images also indicate that the area occupied by the points of actual contact is somewhat smaller than the whole contact area because the morphology of the contact area is not perfectly flat (figure 3.7, see also TEM micrographs in chapters 4 and 5). Morphometric analysis of TEM photomicrographs of about 25 HL-60 cells attached to Lot 2 rpA-coated fibers (see section 3.10) indicated that the cells were only slightly flattened (average diameter measured parallel to the fiber surface was 11.7 ± 2.4 μm vs. 10.7 ± 2.0 μm measured normal to the fiber surface). The diameter of the flattened contact area in close proximity to the fiber surface

(a)

(b)

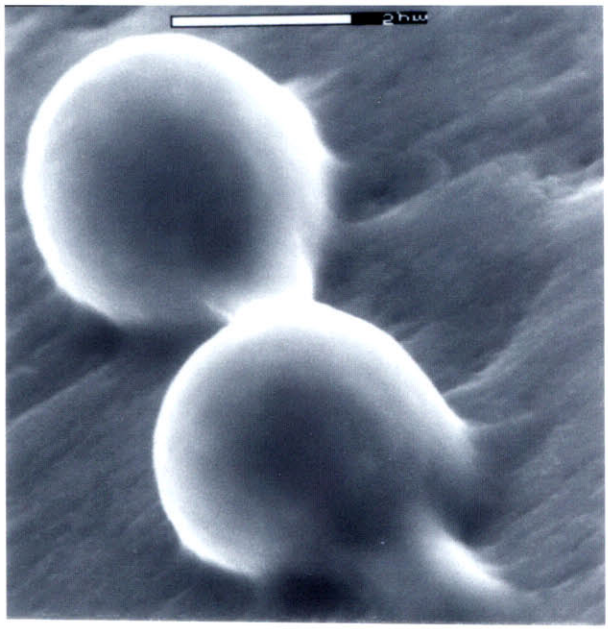

Figure 3.6 ESEM photomicrographs of target cells adsorbed to fibers (a) Namalwa cells on Lot 2 anti-CD19-coated fiber. Small bar in legend is 2 μm (b) Anti-CD33-coated HL-60 cells on Lot 2 rpA-coated fiber. Small bar in legend is 5 μm. Smooth surface morphology of cells may be artifactual (see text).

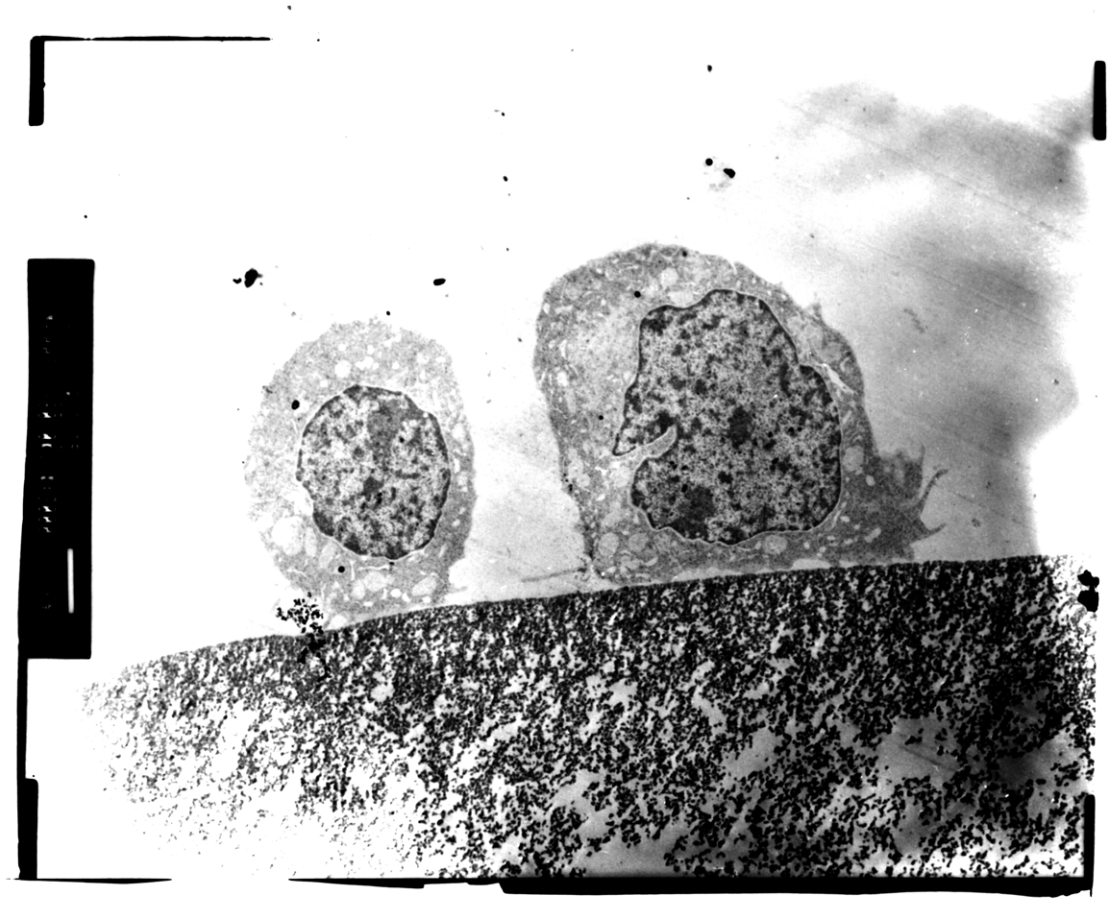

Figure 3.7

Figure 3.8

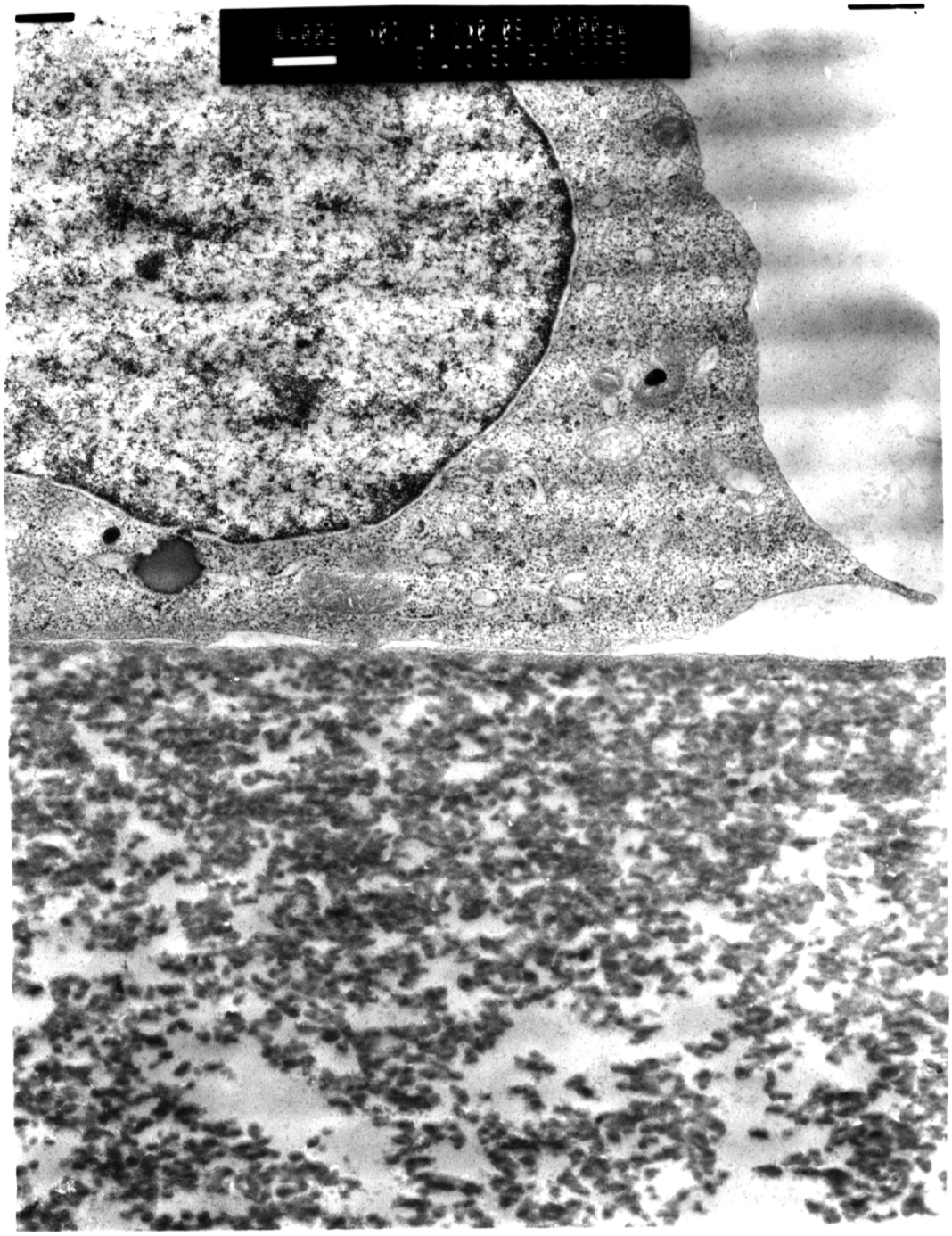

Figure 3.9

Captions for Figures 3.7 to 3.9

Figure 3.7 TEM photomicrograph of two anti-CD33-coated HL-60 cells loaded by gravity onto a rpA-coated Lot 2 fiber showing typical semi-hemispherical shapes and flattened contact area morphology. Bar in caption represents 2 μm.

Figure 3.8 TEM photomicrograph of an anti-CD33-coated HL-60 cell loaded by gravity onto a rpA-coated Lot 2 fiber showing typical semi-hemispherical shape and flattened contact area morphology. Bar in caption represents 2 μm.

Figure 3.9 TEM photomicrograph of the contact area of the anti-CD33-coated HL-60 cell loaded by gravity onto a rpA-coated Lot 2 fiber shown in figure 3.8. Bar in caption represents 500 nm.

was 9.9 ± 4.1 μm representing 81 ± 26 % of the cell diameter parallel to the fiber surface. The average minimum separation distance between the cell and the fiber in the contact area as measured for 8 cells ranged from 113 to 221 Å with a mean of 180 ± 41 Å.

3.5 Discussion

We have demonstrated that microporous polymer membranes functionalized with antibodies or Protein A (rpA) can adsorb target cells selectively, and that the cells can be removed with physical forces and, for rpA-coated membranes, with a low pH eluent. We have also shown that the eluted cell viability is over 80 %. We have shown the feasibility of using functionalized membranes for adsorbing cells using a direct adsorption strategy where immobilized monoclonal antibodies adsorb directly to cell surface markers on target cells, and an indirect adsorption strategy where immobilized Protein A adsorbs to target cells which have been pre-incubated with an anti-marker antibody. We have shown that target cells adsorb to membranes with a selectivity of over 90 % in all cases and as high as 99+ % for cells indirectly adsorbed to rpA-coated fibers. As many as 86 % of target cells adsorbed to membranes could be removed with physical forces applied to the cells during back- pressure and back-filtration elution steps. For cells indirectly adsorbed to rpA-coated membranes, lowering the pH of the eluent used for back-filtration raised the cell removal efficiency to 96 % without adversely affecting viability. These results indicate that porous polymer membranes could prove to be an excellent chromatographic substrate for the separation and recovery of cells.

To our knowledge, this is the first time that polymer membranes have been used for immunoaffinity adsorption and detachment of cells in a way which exploits the hydraulic permeability to generate physical forces for cell removal. Previously, anti-IgG-coated

cellulosic dialysis membranes had been used to adsorb and detach murine B-cells (Mandrusov et al., 1995; Nordon et al., 1996), but cell removal was accomplished only by using exogenous agents such as dilute hydrochloric acid with a pH range from 1 to 5 (Mandrusov et al., 1995), or a protease (Nordon et al., 1996). While these methods proved effective for cell removal, the use of disruptive agents such as these can have undesirable side effects such as the necessity to remove or neutralize the agent, and/or adverse effects on the viability of the recovered cells. For example in the study performed by Mandrusov et al., viability of recovered cells was not more than 60 % and as low as 10 %. Utilization of physical forces for cell removal can be faster and more gentle. In addition, the use of filtration membranes for cell separation provides an extra degree of flexibility in both rapid cell adsorption (by filtration of cells onto the surface) and desorption (by back-pressure/filtration and delivery of exogeneous eluent agents, such as low pH buffers, enzymes, or free ligand, by convection through the membrane).

In no instance did we observe complete desorption of target cells from membranes. This indicates that there may be significant heterogeneity in either cell attachment strength and/or the force applied for cell desorption. This was not surprising since there was likely a large degree of heterogeneity in both. The hollow-fiber membranes we used may not be homogeneous along their length with respect to porosity, permeability and surface morphology. In addition, the size and cell-surface marker expression levels are also heterogeneous for any given suspension of continuously growing cells. Finally, since the cells were loaded onto the surface by gravity, the time of cell-surface contact was heterogeneous which can lead to heterogeneity in both cell shape and contact area size as well as total number of bonds and adhesion strength. Also as expected, decreasing ligand density and increasing hydraulic permeability has a positive effect on the fraction of cells removed with

back-pressure.

We also observed that exposure of adsorbed cells to handling, including brief exposure to an air-liquid interface and air was able to remove up to about 1/3 of adsorbed cells for direct binding experiments, and over half for indirect binding experiments with rpA-coated fibers in a largely viable state. We believe that this effect deserves additional study as a potentially useful means of primary or supplemental cell detachment. Future work will be directed to experiments with hollow fibers potted in modules to enable loading of cells by filtration, application of more precisely controlled shear forces for non-specific cell removal, and scale up which will enable more quantitative recovery of desorbed cells.

3.6 Acknowledgements

Scanning electron microscopy was performed in the EM facility of the Center for Materials Science and Engineering at MIT, a Materials Science and Engineering Center supported by the National Science Foundation under grant number DMR 9400334. Special thanks to Dr. David C. Bell, and Mr. Michael Frongillo for assistance with sample coating and microscopy. Transmission electron microscopy was performed in the Biomedical Electron Microscopy Laboratory at MIT. The JEOL 1200 EX II was purchased through an NIH multi-user instrumentation program, BRS Shared Instrumentation Grant number S10 RR05734-01. Special thanks to Ms. Patricia Reilly for assistance with sample preparation and microscopy.

3.7 Appendix A: Determination of Surface Antigenicity of HL-60 and Namalwa Cells by Flow Cytometry

3.7.1 Purpose

The purpose of performing flow cytometry analysis on HL-60 and Namalwa cells was

to determine the surface antigenicity on a periodic basis (about every 6 mos.) to assure that the cell lines were not accidentally cross-contaminated during culture and that their phenotype remained positive with respect to the markers targeted in cell separation experiments (CD19 for Namalwa; CD33 for HL-60). In addition, we determined the concentration of anti-CD33 ascites required to saturate the CD33 receptors of HL-60 cells so that we could ensure, by incubating the cells with a saturating concentration of anti-CD33, that target HL-60 cells had maximal affinity for rpA-coated fibers. Also analyzed was surface expression of immunoglobin for Namalwa cells and Fc receptors for HL-60 cells, and the ability of surface immunoglobin or Fc-bound immunoglobin to bind to flourescently-labeled Protein A. We performed this analysis because surface immunoglobin has the potential of interacting with immobilized rpA, and could potentially lead to high levels of non-target Namalwa cells on rpA-coated fibers. Similarly, Fc receptors present on HL-60 cells may bind immunoglobins from the culture medium in which they are grown. These Fc receptor-bound immunoglobins may then interfere with specific binding of labeled target receptors to rpA-coated fibers by creating an additional, unwanted interaction.

3.7.2 Materials and Methods

Cells isolated during their growth phase were counted as described previously, and 5×10^6 cells per test condition were added to separate, labeled sterile polypropylene 12 mm × 75 mm test tubes. The cells were pelleted by centrifugation (400 × g, 4 °C, 10 min), and the supernatant was decanted. For HL-60 samples, unless otherwise specified, the cells were resuspended in 1 ml RPMI 1640 with 10 %v/v FBS and 0.5 % w/v human IgG (Gammagard, Baxter, Glendale, CA), incubated on ice for 30 min in order to saturate any Fc receptors, and re-pelleted by centrifugation (this step was unnecessary and was omitted for Namalwa samples). Cells were resuspended in 1 ml RPMI 1640 with 10 %v/v FBS containing a

dilution of the primary antibody solution or ascites (and 0.5 % w/v human IgG for HL-60 samples to maintain Fc receptor saturation). Samples were incubated on ice for 30 min and pelleted by centrifugation. Cells were then washed twice with cold DPBS and then resuspended with diluted fluorescein-labeled secondary antibody (Rockland, Gilbertsville, PA) in 1 ml RPMI 1640 with 10 %v/v FBS, or fluorescein-labeled Protein A (Pharmacia Biotech, Uppsala, Sweden) in 1 ml DPBS with 1 %w/v IgG-free BSA. Samples were incubated on ice for 30 min and pelleted by centrifugation. The cells were washed three times with cold DPBS and finally resuspended in 5 ml of PBS containing 1 % w/v formaldehyde (pH 7.4) to fix and preserve the cells until analysis. Samples were then analyzed on the flow cytometer (Epics XL, Coulter Corp., Hialeah, FL).

3.7.3 Results

3.7.3.1 Expression of CD19 and CD33 on Namalwa and HL-60 Cells

Figure 3.A.1 shows a typical result for a phenotyping test with Namalwa cells. The results are shown plotted as a histogram with the number of cells counted on the y axis (scale from 0 to 512 cells) versus the log of the fluorescence intensity (in arbitrary units from a lower limit of 15 ,vertical line at left, to an upper limit of 255) on the x axis (intensity levels depend on the tuning and settings of the machine and are comparable only for the samples shown in a given figure, which were analyzed on the same day, but not between samples in different figures). The total cell count for each sample was 10, 000. Only 3.58 % of the observed cells had a fluorescence intensity above the auto-fluorescence level (vertical line at left) for the non-specific binding control sample in panel (A). For this sample, the peak value above the auto-fluorescence level was 9 cells at an intensity of 58. Panel (B) shows the results for Namalwa cells incubated with the same concentration of anti-CD33 ascites (1:500 dilution) as that used in cell binding and separation experiments. The results show that anti-

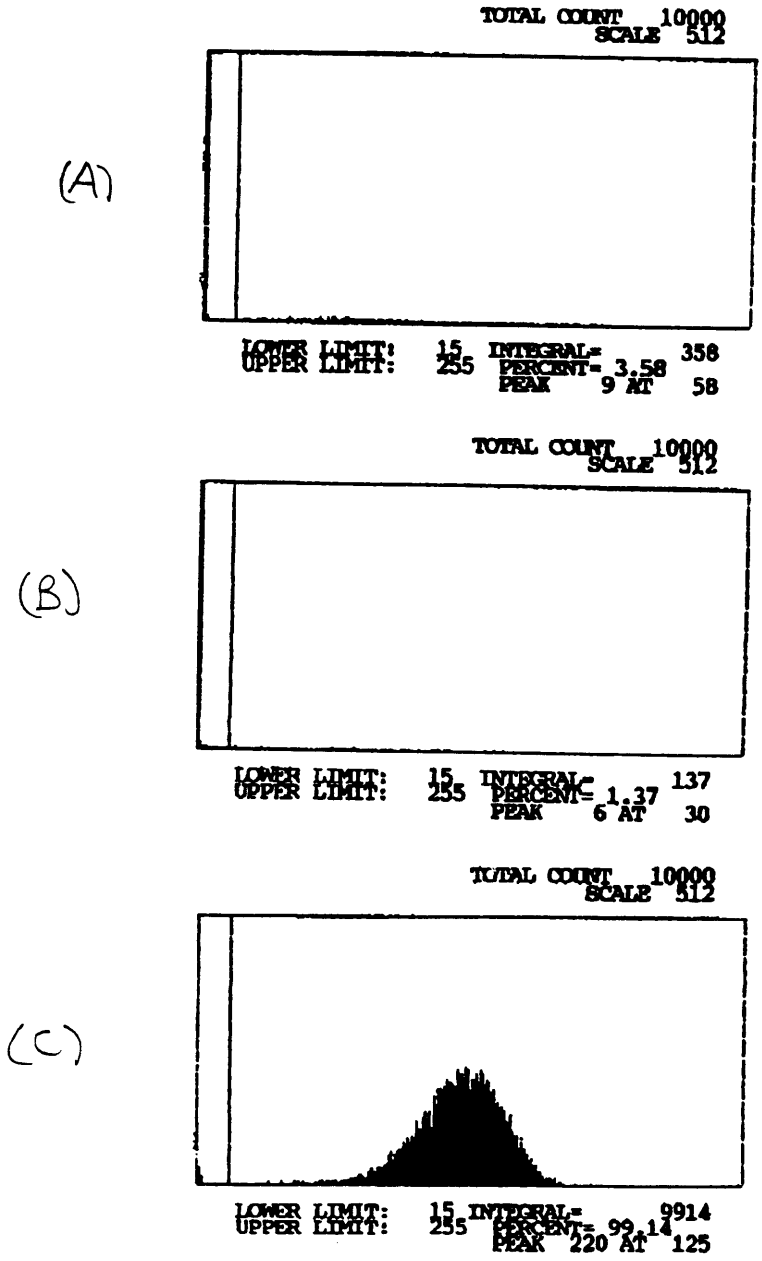

Figure 3.A.1. Flow cytometry results for characterization of Namalwa phenotype. Results are displayed as the number of cells counted on the y axis versus fluorescence intensity (in arbitrary units on a 3-log scale) on the x axis. The total cell count was 10, 000, and the lower limit (vertical line at left of plot frame) was set as the maximum intensity of a sample containing cells not incubated with fluorescein-labeled antibody. (A) Namalwa incubated with 1:500 dilution of mouse IgG2b myeloma protein (non-immunospecific), followed by a 1:200 dilution of fluorescein-labeled anti mouse IgG (rabbit). (B) Namalwa incubated with 1:500 dilution of anti-CD33 ascites, followed by a 1:200 dilution of fluorescein-labeled anti mouse IgG (rabbit). (C) Namalwa incubated with 10 μg/ml purified anti-CD19, followed by a 1:200 dilution of fluorescein-labeled anti mouse IgG (rabbit).

CD33 did not bind to Namalwa above the level observed for the non-specific binding control. For this case, 1.37 % of the observed cells had a fluorescence intensity above the auto-fluorescence level, and the peak value above the auto-fluorescence level was 6 cells at an intensity of 30. In contrast, when Namalwa were incubated with anti-CD19 (panel (C)), 99.14 % of cells had an intensity above the auto-fluorescence level, with a peak of 220 cells at an intensity of 125. These results indicate that Namalwa cells were $CD33^-$, $CD19^+$, and do not display significant Fc receptor activity (low non-specific binding intensity without Fc receptor saturation).

Figure 3.A.2 shows a typical result for a phenotyping test with HL-60 cells with pre-saturation of Fc receptor activity. The results are shown plotted as a histogram with the number of cells counted on the y axis versus the log of the fluorescence intensity (in arbitrary units) on the x axis (the axis label "Log FITC" refers to the intensity of the emission measured near the emission peak of fluorescein (about 520 nm)) analogous to Figure 3.A.1. The appearance of the histograms is different because the analysis was performed on a different machine. The total cell count for each sample was 5,000. Only 6.0 % of the observed cells had a fluorescence intensity above the auto-fluorescence level (cells in histogram whose intensity falls within the horizontal region spanned by bar F) for the non-specific binding control sample in panel (A). For this sample, the peak value above the auto-fluorescence level was 10 cells at an intensity of 1.06. Panel (B) shows the results for HL-60 cells incubated with anti-CD19. The results show that anti-CD19 did not bind to HL-60 above the level observed for the non-specific binding control. For this case, 1.9 % of the observed cells had a fluorescence intensity above the auto-fluorescence level (within bar U region), and the peak value above the auto-fluorescence level was 3 cells at an intensity of 1.25. In contrast, when HL-60 were incubated with anti-CD33 followed by fluorescein-

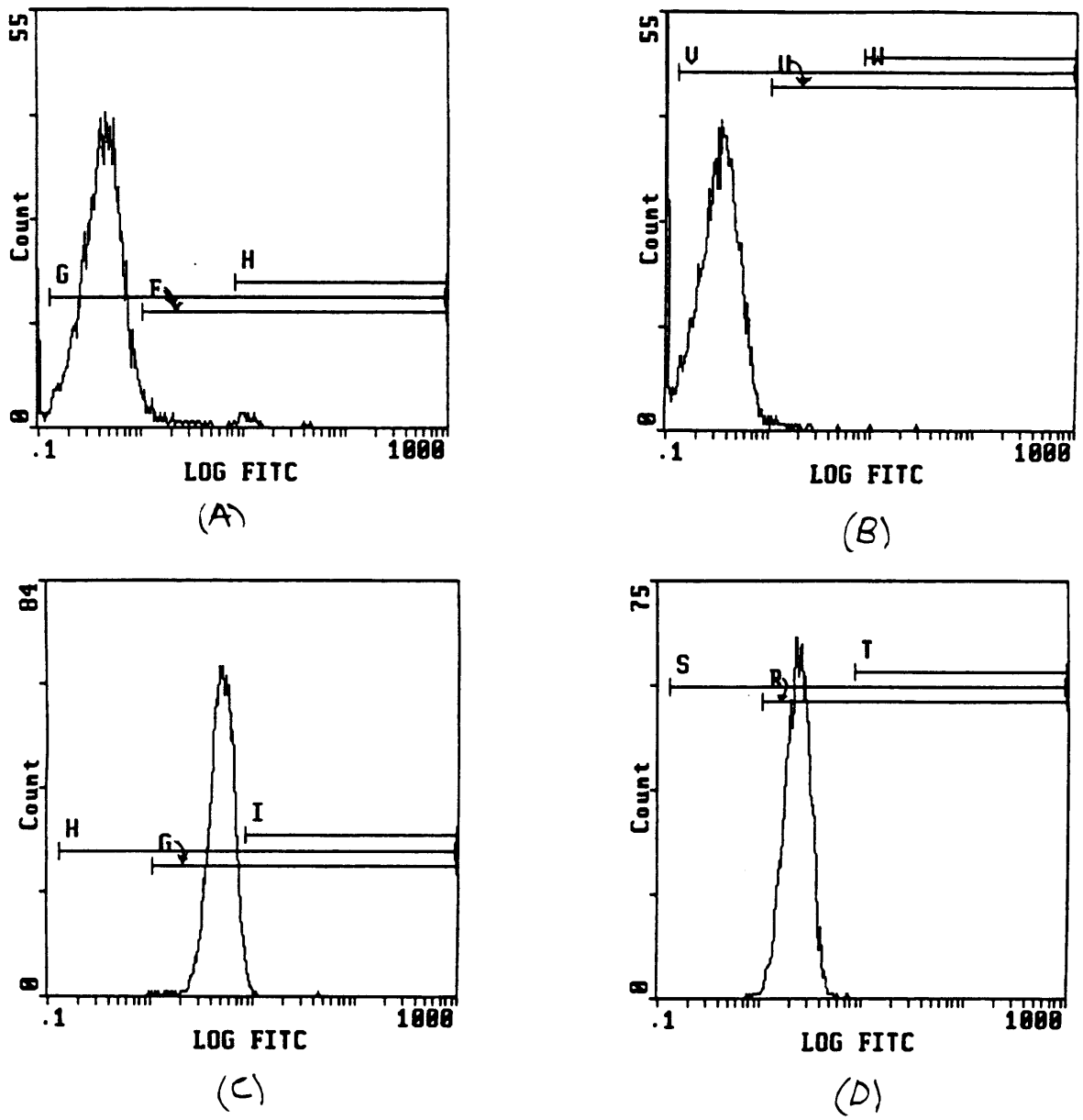

Figure 3.A.2. Flow cytometry results for characterization of HL-60 phenotype. Results are displayed as the number of cells counted on the y axis versus fluorescence intensity (in arbitrary unity on a 3-log scale) on the x axis. The total cell count was 5, 000, and the lower limit (x-axis value of the left end of the second bar from left of plot frame, bars F, U, G, and R for (A), (B), (C), and (D) respectively) was set as the maximum intensity of a sample containing cells not incubated with fluorescein-labeled antibody. (A) HL-60 incubated with 1:50 dilution of mouse IgG2b myeloma protein (non-immunospecific), followed by a 1:200 dilution of fluorescein-labeled anti mouse IgG (rabbit). (B) HL-60 incubated with 10 μg/ml purified anti-CD19, followed by a 1:200 dilution of fluorescein-labeled anti mouse IgG (rabbit). (C) HL-60 incubated with a 1:500 dilution of anti-CD33 ascites, followed by a 1:200 dilution of fluorescein-labeled anti mouse IgG (rabbit). (D) HL-60 incubated with a 1:500 dilution of anti-CD33 ascites, followed by 30 μg/ml fluorescein-labeled protein A.

labeled anti-mouse antibody (panel (C)), 99.8 % of cells had an intensity above the auto-fluorescence level (within bar G region), with a peak of 84 cells at an intensity of 5.17. When HL-60 were incubated with anti-CD33 followed by fluorescein-labeled Protein A without pre-incubation with human IgG (panel (D)), 99.4 % of cells had an intensity above the auto-fluorescence level (within bar R region), with a peak of 75 cells at an intensity of 2.86 which was not a result of Fc receptor binding (see figure 3.A.5 and associated discussion) indicating that the labeled target receptor was immunoreactive with Protein A as well as anti-immunoglobin. These results indicate that HL-60 were $CD33^+$, $CD19^-$, and that Protein A has affinity for the anti-CD33 mouse IgG2b ascites.

3.7.3.2 Saturation of CD33 Receptors on HL-60 Cells

Figure 3.A.3 shows the results for estimating the dilution of anti-CD33 ascites required to saturate CD33 receptors on HL-60 cells with pre-saturation of Fc receptor activity. The total cell count for each sample was 5,000. In each case after incubation of the cells with the indicated dilution of anti-CD33 ascites, the cells were incubated with a 1:200 dilution of fluorescein-labeled anti-mouse IgG (rabbit) Only 6.0 % of the observed cells had a fluorescence intensity above the auto-fluorescence level (within bar F region) for the non-specific binding control sample in panel (A). For this sample, the peak value above the auto-fluorescence level was 10 cells at an intensity of 1.06. For a 1:50,000 dilution of anti-CD33 ascites panel (B) shows that 30.7 % of cells had an intensity above the auto-fluorescence level (within bar A region), with a peak of 61 cells at an intensity of 1.10. For a 1:5,000 dilution, panel (C), 99.8 % of cells had an intensity above the auto-fluorescence level (within bar D), with a peak of 83 cells at an intensity of 3.36. For a 1:500 dilution, panel (D), 99.8 % of cells had an intensity above the auto- fluorescence level (within bar G), with a peak of 84 cells at an intensity of 5.17. And for a 1:50 dilution, panel (E), 99.8 % of cells had an

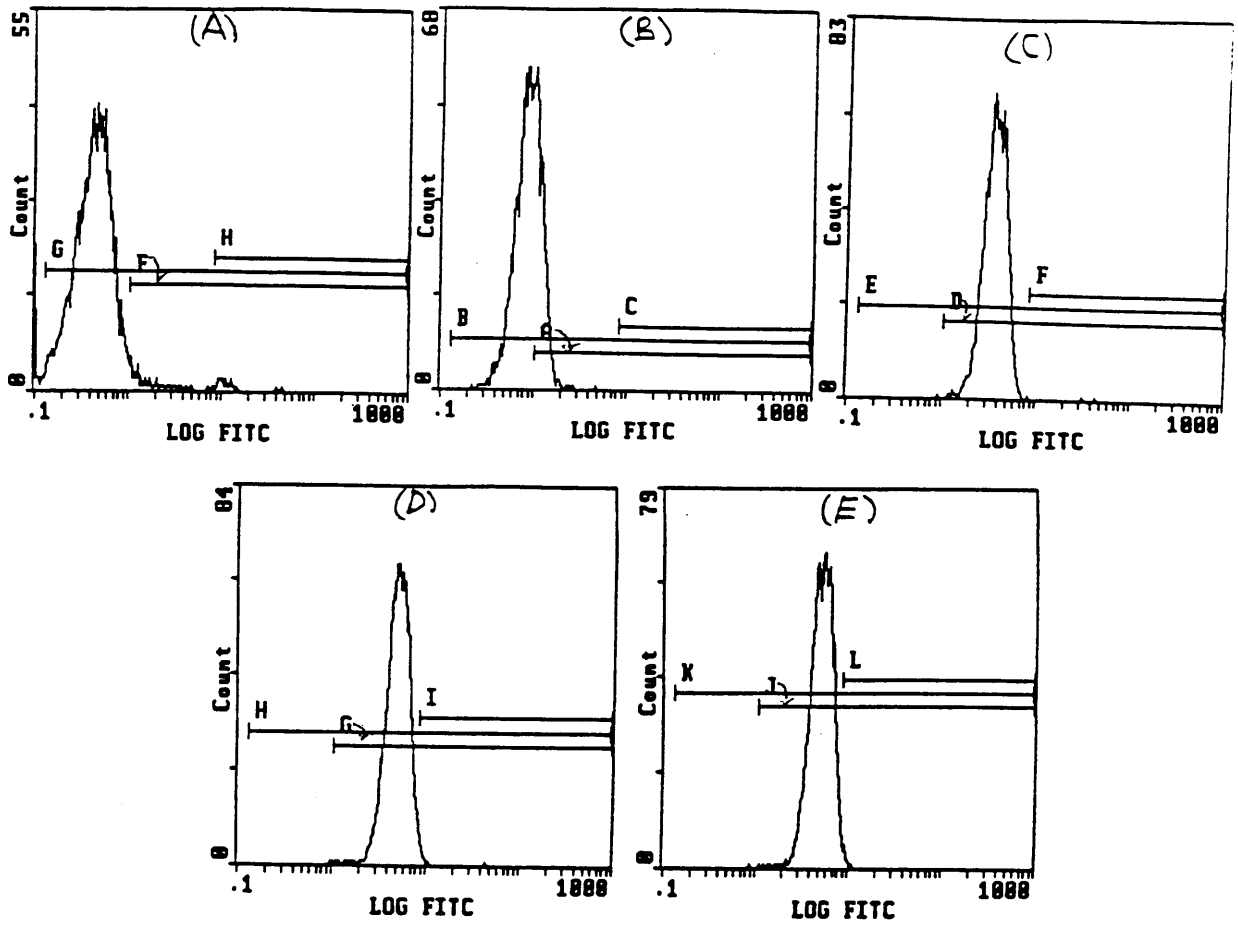

Figure 3.A.3. Flow cytometry results for saturation of CD33 on HL-60. Results are displayed in the same fashion as in figure 3.A.2 for the same total cell count. Cells were incubated with a 1:200 dilution of fluorescein-labeled anti-mouse IgG (rabbit) for secondary labeling in each case. (A) HL-60 incubated with 1:50 dilution of mouse IgG2b myeloma protein (non-immunospecific). (B) HL-60 incubated with a 1:50,000 dilution of anti-CD33 ascites. (C) HL-60 incubated with a 1:5,000 dilution of anti-CD33 ascites. (D) HL-60 incubated with a 1:500 dilution of anti-CD33 ascites. (E) HL-60 incubated with a 1:50 dilution of anti-CD33 ascites.

intensity above the auto-fluorescence level (within bar J), with a peak of 79 cells at an intensity of 4.94. These results indicate that CD33 receptor binding fell off dramatically between an anti-CD33 ascites dilution of 1:5,000 to 1:50,000, and that CD33 receptor saturation was evident, as judged by the peak fluorescence intensity level, at an anti-CD33 dilution of about 1:500.

3.7.3.3 Chacterization of Surface Immunoglobin Expression on Namalwa Cells

Figure 3.A.4 shows the results for the characterization of surface immunoglobin expression on Namalwa cells. The results are given in the same format as in 3.7.3.1. for 10,000 total cells. Only 1.26 % of the observed cells had a fluorescence intensity above the auto-fluorescence level (vertical line at left) for the non-specific binding control sample in panel (A) (using anti-CD33 as a non-specific primary antibody see figure 3.A.1). For this sample, the peak value above the auto-fluorescence level was 5 cells at an intensity of 69. panel (B) shows the results for Namalwa cells incubated with anti-human IgG (goat) followed by fluorescein-labeled anti-goat IgG (rabbit). The results show that anti-human IgG did not bind to Namalwa at levels significantly above the level observed for the non-specific binding control. For this case, 4.38 % of the observed cells had a fluorescence intensity above the auto-fluorescence level, and the peak value above the auto-fluorescence level was 33 cells at an intensity of 61. In contrast, when Namalwa were incubated with anti-human IgM (goat) followed by fluorescein-labeled anti-goat IgG (rabbit) (panel (C)), 92.14 % of cells had an intensity above the auto-fluorescence level, with a peak of 173 cells at an intensity of 98. Panel (D) indicates, however, that this surface IgM is not reactive with Protein A. Only 1.35 % of Namalwa cells incubated with anti-CD33 followed by fluorescein-labeled Protein A had a fluorescence intensity above the auto-fluorescence level, and the peak value above the auto-fluorescence level was 4 cells at an intensity of 177. These results indicate that most

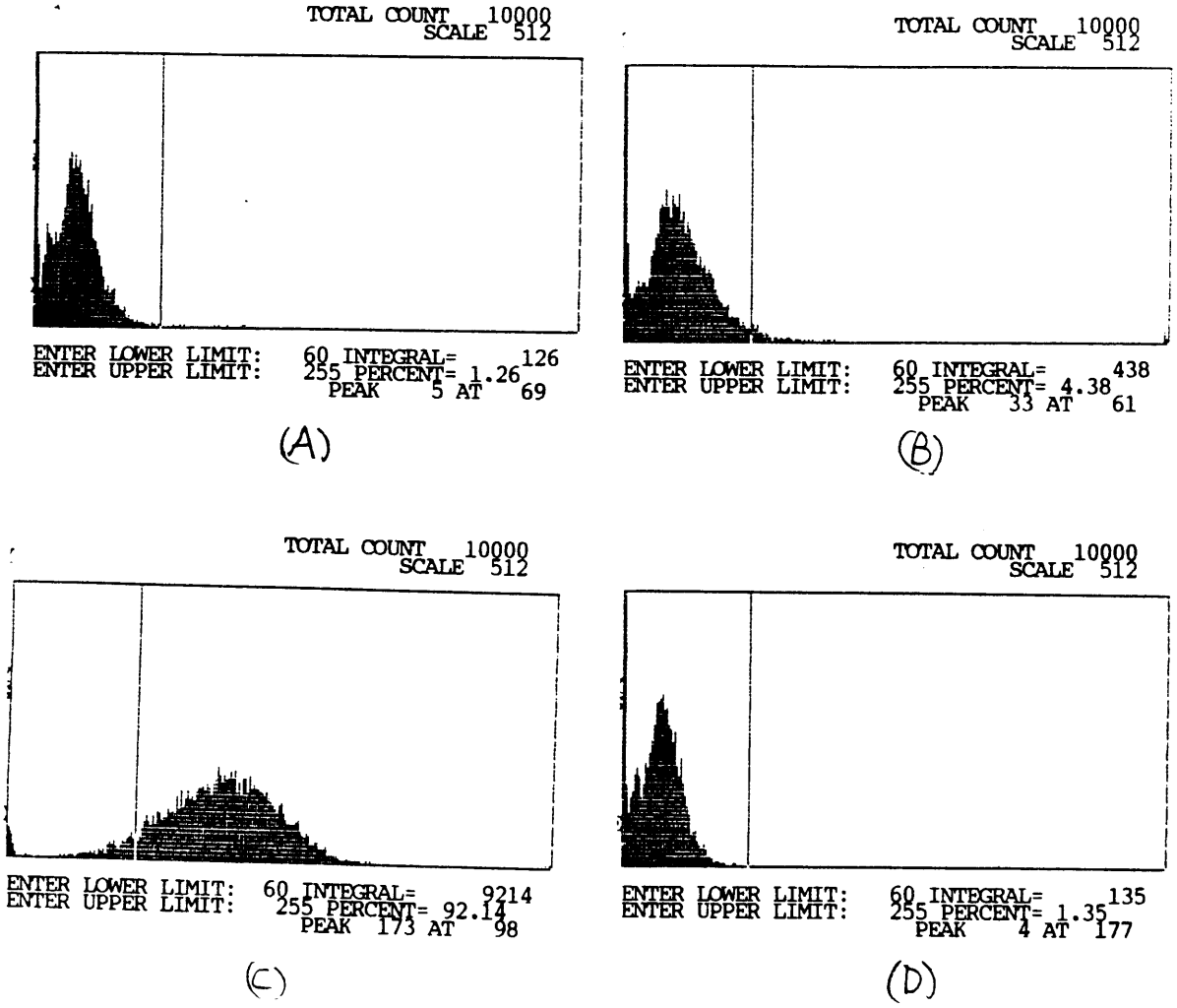

Figure 3.A.4. Flow cytometry results for characterization of surface immunoglobin expression on Namalwa cells. Results are displayed as in figure 3.A.1 for 10,000 total cells. (A) Namalwa incubated with 1:500 dilution of anti-CD33 ascites, followed by a 1:200 dilution of fluorescein-labeled anti mouse IgG (rabbit). (B) Namalwa incubated with 1:100 dilution of anti-human IgG (goat), followed by a 1:200 dilution of fluorescein-labeled anti goat IgG (rabbit). (C) Namalwa incubated with 1:200 dilution of anti-human IgM (goat), followed by a 1:200 dilution of fluorescein-labeled anti goat IgG (rabbit). (D) Namalwa incubated with 1:500 dilution of anti-CD33 ascites, followed by 30 μg/ml of fluorescein-labeled protein A.

Namalwa cells express surface IgM but not IgG, and that the surface IgM is not significantly immunoreactive with Protein A.

3.7.3.4 Characterization of Fc Receptor Binding on HL-60 Cells

Figure 3.A.5 shows the results for characterization of Fc receptor binding on HL-60 cells. The results are shown in the same format as in section 3.7.3.2. for 5,000 total cells. Only 6.0 % of the observed cells had a fluorescence intensity above the auto-fluorescence level (within bar F region) for the non-specific binding control sample with Fc receptor pre-saturation with human IgG shown in panel (A). For this sample, the peak value above the auto-fluorescence level was 10 cells at an intensity of 1.06. Panel (B) shows the equivalent results for HL-60 cells whose Fc receptors were not pre-saturated with human IgG. In this case, 98.8 % of cells had an intensity above the auto-fluorescence level (within bar C), with a peak of 55 cells at an intensity of 3.74. Panel (C) shows the results for HL-60 cells incubated with a 1: 200 dilution of anti-human IgG/IgM (goat) without pre-saturation of Fc receptors with human IgG, followed by fluorescein-labeled anti-goat antibody where only 4.3 % of cells had an intensity above the auto-fluorescence level (within bar I), with a peak of 5 cells at an intensity of 1.28. In contrast panel (D) shows the equivalent results as panel (C) for HL-60 cells whose Fc receptors were pre-saturated with human IgG. In this case, 90.8 % of cells had an intensity above the auto-fluorescence level (within bar L), with a peak of 58 cells at an intensity of 1.89. Panel (E) shows the results for HL-60 cells incubated with a 1: 500 dilution of non-immunospecific mouse IgG2b ascites followed by fluorescein-labeled Protein A where only 9.9 % of cells had an intensity above the auto-fluorescence level (within bar O), with a peak of 26 cells at an intensity of 1.08. These results indicate that most HL-60 cells express Fc receptors which are capable of binding mouse IgG of the same isotype as the anti-CD33 antibody used for cell binding and separation experiments (IgG2b),

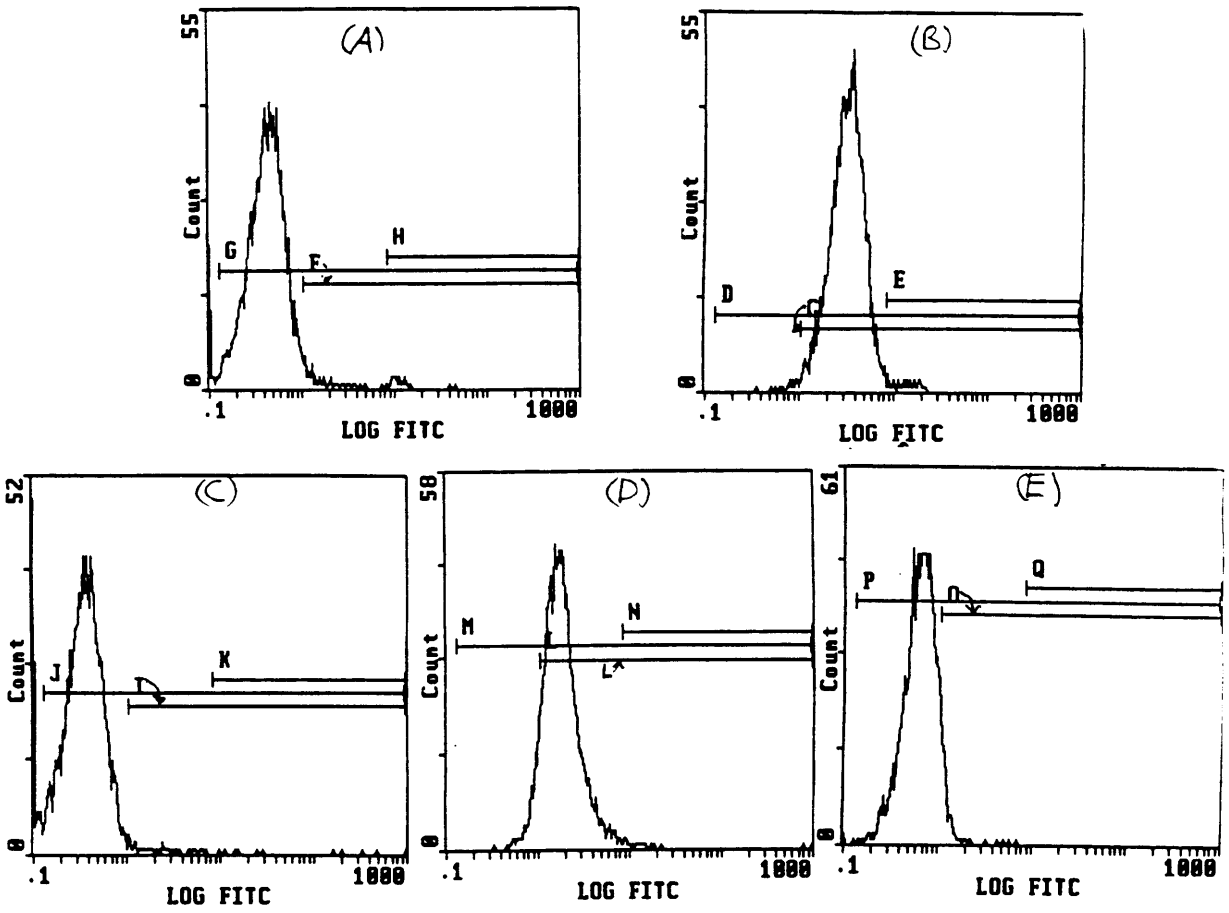

Figure 3.A.5. Flow cytometry results for characterization of Fc receptor binding for HL-60 cells. Results are displayed as before for 5,000 total cells. (A) HL-60 incubated with 1:50 dilution of mouse IgG2b myeloma protein (non-immunospecific) with pre-saturation of Fc receptors with human IgG, followed by a 1:200 dilution of fluorescein-labeled anti mouse IgG (rabbit). (B) HL-60 incubated with 1:50 dilution of mouse IgG2b myeloma protein (non-immunospecific) without pre-saturation of Fc receptors with human IgG, followed by a 1:200 dilution of fluorescein-labeled anti mouse IgG (rabbit). (C) HL-60 incubated with 1:200 dilution of anti-human IgG/IgM (goat) without pre-saturation of Fc receptors with human IgG, followed by a 1:200 dilution of fluorescein-labeled anti-goat IgG (rabbit). (D) HL-60 incubated with 1:200 dilution of anti-human IgG/IgM (goat) with pre-saturation of Fc receptors with human IgG, followed by a 1:200 dilution of fluorescein-labeled anti-goat IgG (rabbit). (E) HL-60 incubated with 1:500 dilution of mouse IgG2b myeloma protein (non-immunospecific) without pre-saturation of Fc receptors with human IgG, followed by 30 μg/ml fluorescein-labeled protein A.

and that this antibody is immunoreactive with anti-mouse antibody but not significantly immunoreactive with Protein A (compare figure 3.A.5 (A), (B), and (E)) so that any specific affinity for the rpA-coated fibers should be due only to labeled target receptors (CD33) and not to Fc-bound immunoglobin.

3.8 Appendix B. Growth Curves for HL-60 and Namalwa Cell Cultures

Figure 3.B.1 presents growth curves for HL-60 cell cultures (panel (A)) and Namalwa cell cultures (panel (B)). Cells were grown from an initial seed concentration of 5×10^5 cells/ml. Neither cell line showed evidence of a lag phase when seeded at this initial concentration. The log-growth phase (time period for exponential growth before stationary phase) was about 55 hr for HL-60 and about 60 hr for Namalwa. Doubling time was about 30 hr for HL-60 and 40 hr for Namalwa. Based on these results, cell cultures were seeded at 5×10^5 cells/ml and split every 48 to 60 hrs. Cells used for experiments were harvested after 24 to 48 hr in culture.

3.9 Appendix C. Cell Size Distributions for Namalwa and HL-60 Cell Cultures

Cell size distributions and average cell size was measured for Namalwa and HL-60 cultures after 48 hr growth time by light scattering using a CASY®1 cell analyzer (Schärfe System, Reutlinger, Germany). Results are shown in figure 3.C.1 and 3.C.2 for Namalwa and HL-60 cultures respectively. Results indicate that most Namalwa cells were between about 8 to 18 μm in diameter with an average diameter of about 13 μm. Most HL-60 cells were between about 7 to 20 μm in diameter with an average diameter of about 14 μm.

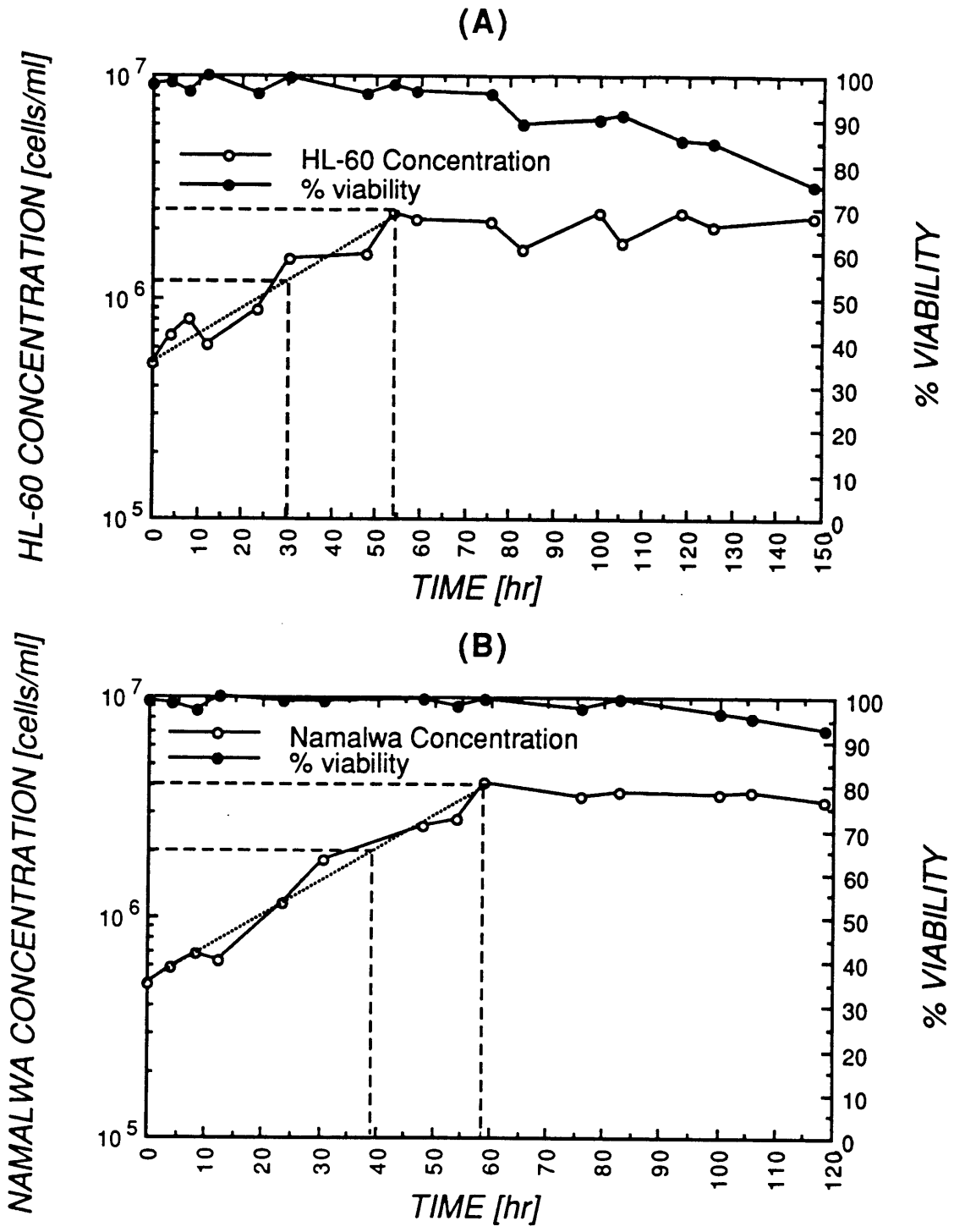

Figure 3.B.1. Growth curves for HL-60 cells (A) and Namalwa cells (B) in culture. Log of cell concentration is plotted on the left y axis, and corresponding cell viability as determined by Trypan blue dye exclusion is plotted on the right y axis. Dotted lines represent ideal log-growth, and dashed lines show the doubling time and concentration, and the time and concentration at the beginning of the stationary phase.

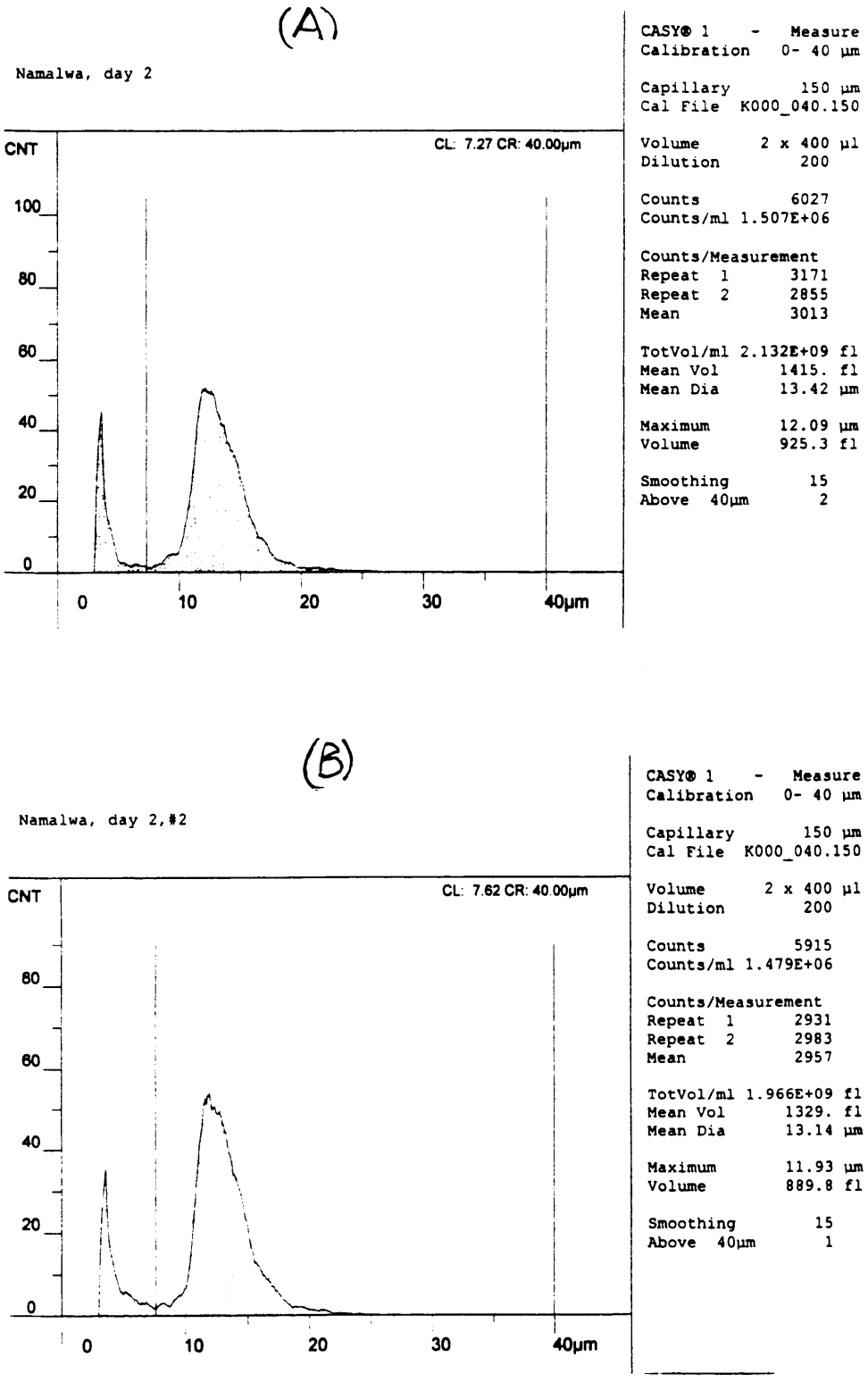

Figure 3.C.1. Light scattering results for cell size distribution for Namalwa cells after 48 hr in culture. (A) and (B) are identical measurements of samples from two different culture flasks.

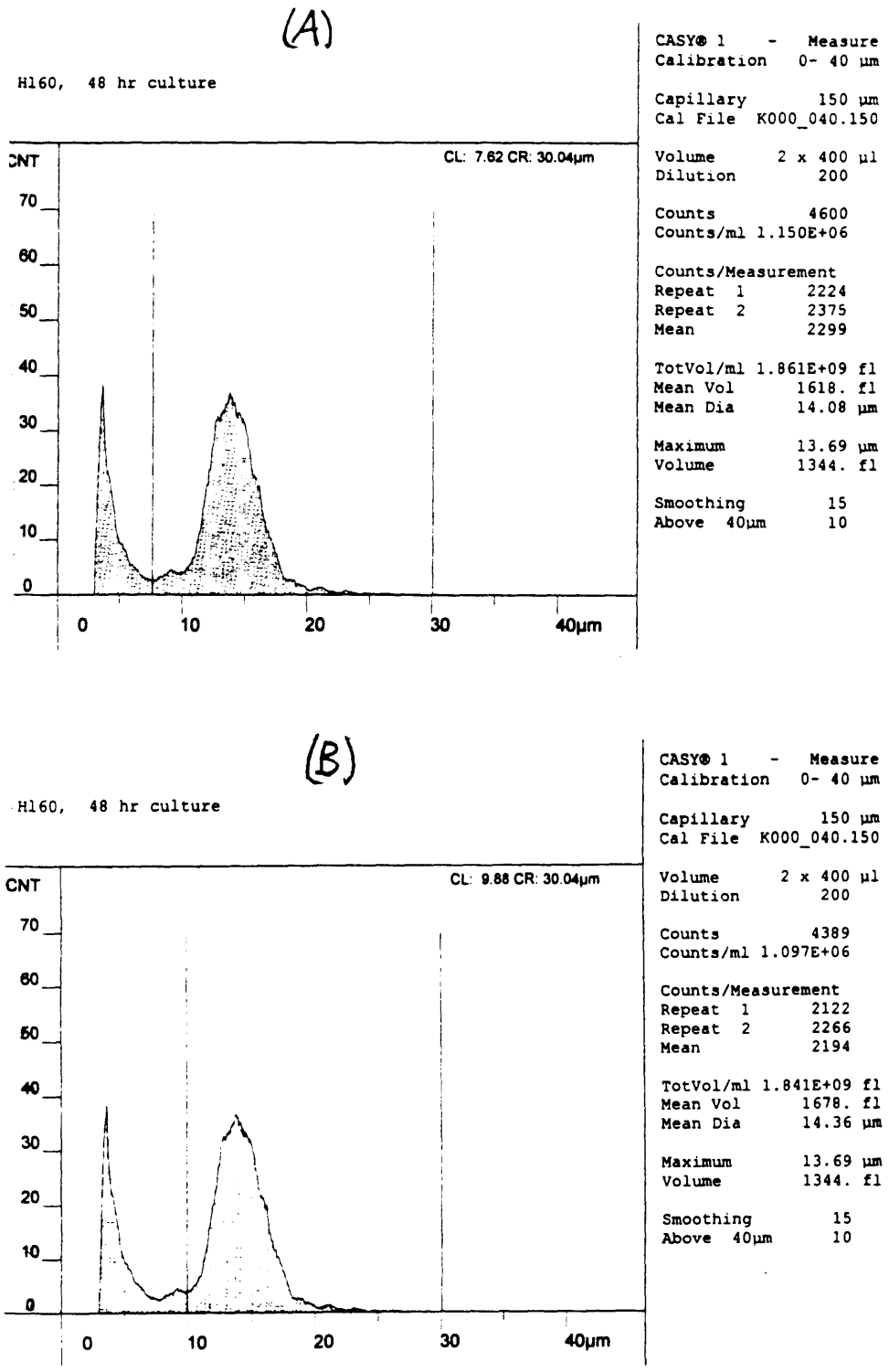

Figure 3.C.2. Light scattering results for cell size distribution for HL-60 cells after 48 hr in culture. (A) and (B) are identical measurements of samples from two different culture flasks.

3.10 Appendix D. Analysis of Electron Photomicrographs of Hollow-Fiber Membranes and Cells

3.10.1 Estimation of Surface Area Available for Specific Bond Formation for Lot 1 and Lot 2 Hollow Fiber Membranes.

In this appendix, we present an estimate of the fraction of the retentive surface available for specific bond formation between the cell and the fiber surface. The available fractional surface area for bond formation was defined as 100 % minus the percentage of the surface area occupied by pores. The fractional surface area occupied by pores was determined as follows. High-resolution photocopies (400 dots per inch) were made of SEM photomicrographs of two independent samples of the retentive surface of each fiber. The pores from each image were carefully dissected using a surgeon's scalpel. The dissected pores and the remaining pore-free image were independently weighed with an analytical balance (Model BA210S, Sartorius Corporation, Edgewood, NY). The mass of each fraction was converted to an equivalent area by multiplying the mass by the average mass of three samples of known size of the paper upon which the photocopies were made. The average mass for a sheet of white paper 603 cm^2 in area was 4.642 ± 0.026 g (n=3), and for an equivalent sheet of the same paper which was completely covered on one side with toner (black) was 5.146 ± 0.028 g (n=3). The average of these two values, 4.894 g was used as an estimate for gray colored paper. The corresponding area/mass ratios were 130, 117, and 123 cm^2 /g for white, black, and gray paper respectively. The mass of the dissected pores was converted to area units using the value of area/mass for black paper, and the mass of the pore-free surface image was converted to area units using the value of area/mass for gray paper. The results of the analysis are shown in table 3.D.1. Photomicrograph image

magnifications for the samples used were both 60,000× yielding a total surface area analyzed of ≈5 μm^2 for Lot 1, and 50,000 × and 40,000× yielding a total surface area analyzed of about 10 μm^2 for Lot 2.

Table 3.D.1. *Percentage of Hollow-Fiber Surface Area Available For Specific Bond Formation*

Hollow-Fiber	Percent of Retentive Surface Available For Bond Formation
Lot 1	94.1 ± 2.4
Lot 2	87.6 ± 1.2

Results are expressed as mean ± SD.

3.10.2 Morphometric Analysis of Gravity-Loaded HL-60 Target Cells Adsorbed to Hollow-Fiber Membranes.

HL-60 target cells (pre-incubated with a 1:500 dilution of anti-CD33 ascites) loaded by gravity onto rpA-coated Lot 2 fibers under identical conditions as described previously for cell binding experiments, were observed with transmission electron microscopy (TEM) using methods previously described. Typical results for Lot 2 rpA-coated fibers were shown in figures 3.7-3.9.

Quantitative measurements were taken from photographic enlargements of TEM photomicrographs with high-precision calipers (Mitutoyo Corporation, Tokyo, Japan) of cell diameters both parallel and perpendicular to the plane of the fiber membrane surface, cell contact area diameters, and minimum separation distances (taken from photomicrographs with magnification of 100 kx). The results for HL-60 target cells loaded by gravity onto rpA-coated fibers is shown in table 3.D.2. Measured values for maximum cell and contact area diameters were corrected to reflect the true three dimensional maximum diameters using morphometric analysis. For a distribution of spherical objects such as cells, or circular

objects oriented perpendicular to the section plane such as cell-fiber contact areas, which have a small size dispersion, it may be assumed that all of the particles have an equal probability of being cut by a random section. For such a case the appropriate correction factor which average measured diameters were multiplied by to obtain the true average maximum diameters is $4/\pi$ (Weibel, 1969).

Table 3.D.2. *Morphometric Analysis of Gravity-Loaded HL-60 Cells Specifically Adsorbed To Hollow-Fiber Membranes*

	Corrected Diameters (μm)			
	Cell			
Hollow-Fiber	**// to Surface**	**⊥ to Surface**	**Contact Area**	**Min. Separation (Å)**
Lot 2 rpA-Gravity	11.7 ± 2.4 (n=25)	10.7 ± 2.0 (n=25)	9.9 ± 4.1 (n=24)	180 ± 41 (n=8)

Results expressed mean ± SD for n cells.

The maximum corrected diameter of 11.7 μm is about 16 % less than that measured by light scattering for unfixed HL-60 in suspension (see section 3.9).

3.11 Appendix E. Quantification of Cell Removal From Hollow-Fibers: Comparison of Edge vs. En Face Observation

3.11.1 Purpose

To access the accuracy of edge counting by comparing quantification of the percent removal of adsorbed cells on fibers, as determined by counting cells along the edge of fibers as previously described. to counting fluorescently dyed cells observed en face on the fiber surface.

3.11.2 Materials and Methods

Namalwa target cells expressing CD19 cell surface markers were stained with Cell

Tracker Orange® vital stain, as previously described, and incubated, as previously described for direct binding experiments, with an anti-CD19-coated Lot 2 fiber. Cell adsorption and removal was quantified by two methods for the same fiber. After incubation with cells, the adsorbed cells were counted along the edges of the fiber; in addition, five precise locations on the fiber surface were observed en face using epi-fluorescence. Images were captured with a color video camera (Model DXC-960MD, Sony Corporation, Tokyo, Japan) using an Apple MacIntosh Quadra 950 computer and NIH Image software, and cell density was determined by counting cells on captured images. Cells were then removed with a combination of shear stress exposure, provided by the vigorously squirting of buffer along the length of the fiber with a transfer pipet, and handling of the fiber in a similar manner as fibers used for pressurization controls (gentle manipulation and brief air exposure). After cell removal, cells remaining on the fiber were counted again by the two methods outlined above for the same orientation and locations on the fiber. The results of the analysis are shown in table 3.E.1. Fraction surface coverage represents the percentage of a theoretical monolayer of 12 μm diameter cells, assuming a maximum fractional surface coverage of $\pi/4$ (see chapter 4). The results show that the values for percent removal were comparable for both methods (55 % for edge counting vs. 47 ± 18 % [mean ± SD] for en face measurements).

Table 3.E.1 *Comparison of Quantification of Cell Removal by Edge Counting and En Face Cell Density Measurements.*

Adsorption			Desorption				
Edge	En Face		Edge		En Face		
cells/cm	cells/mm^2	Fraction surface coverage (%)	cells/cm	Fraction desorbed (%)	cells/mm^2	Fraction surface coverage (%)	Fraction desorbed (%)
817	800 ± 110	11.5 ± 1.6	368	55	420 ± 70	6.1 ± 1.0	47 ± 8

Results expressed as mean ± SEM.

3.12 Appendix F: Comparison of Experimental Results With Theoretical Estimates of Attachment Strength and Removal Pressure

3.12.1 Purpose

The purpose of this appendix is to compare the magnitude of the experimentally applied pressure to the critical pressures predicted for cell removal by the methods discussed in the previous chapter, and also to qualitatively compare the effects of experimentally varied parameters, such as ligand density and hydraulic permeability, to those predicted by theory.

3.12.2 Methods

The theoretical models presented in chapter 2 were used to determine the equilibrium number of bonds/cell, the critical detachment force/bond, the critical transmembrane pressure for anisotropic fibers, the minimum transmembrane pressure for isotropic membranes, and the critical shear stress necessary for cell removal. In addition, a calculation to determine a minimum critical transmembrane pressure drop was performed assuming that the fibers had an asymmetric fiber morphology where the pressure drop determining region is a thin isotropic layer ("skin") adjacent to the surface to which cells are attached. The thickness of this "skin" was taken as the thickness of the region of low porosity measured from SEM and TEM cross-sections as discussed in section 3.4.1.1. Some parameters were assumed, while the majority were derived from measurements. The total number of target cell surface markers was assumed to be 50,000 per cell. Calculations were made both for fixed and freely mobile cell surface markers. For direct binding, the affinity constant, K^s, was taken as 10^{10} M^{-1} (as measured for reagents in solution), a conservative estimate representing a high affinity antibody-antigen type bond. For the indirect binding condition for rpA-coated fibers, the affinity constant, K^s, was taken as 6.25×10^6 M^{-1} which has been previously measured for a

protein A-mouse IgG bond at pH 7.4 (Kuo and Lauffenburger, 1993). This was also most likely a conservative estimate since it has been determined that for bonds in series, such as with our indirect binding case, the specific adhesion strength of the linkage is considerably less than for single bonds (Saterbak and Lauffenburger, 1996). For simulation of pressurization of rpA-coated fibers at pH 2.5, the affinity constant used for pH 7.4 was reduced by a factor of 40 (Kuo and Lauffenburger, 1993). For monoclonal antibody-coated fibers, the ligand density was taken from table 3.3 assuming that all of the immobilized antibody was active. For rpA-coated fibers, the active ligand density was determined from the capacity of the fiber to bind mouse IgG2b (from table 3.2) and the specific surface area of the fiber. The hydraulic permeability of the membranes was determined as discussed in the materials and methods section and the permeability constant was determined from the average value by multiplying by the viscosity of water at 25 °C (0.9 cp). The average cell diameter was determined by light scattering (section 3.9), and the average contact area diameter, minimum separation distance, fiber porosity, and fiber thickness from electron microscopic measurements discussed in the text and section 3.10. For direct binding simulations, it was assumed that the contact area diameter and separation distance were the same as for the indirect case where measurements were made.

3.12.3 Results

3.12.3.1 Direct Binding of Namalwa to anti-CD19 coated Lot 1 and Lot 2 Fibers.

Measured Parameter	Lot 1	Lot 2
Ligand density	(3.2, 0.12, and 0.01) × 10^{11} cm^{-2}	3 × 10^{11} cm^{-2}
Permeability constant	6.5 × 10^{-13} m	1.0 × 10^{-11} m
Cell diameter	13 μm	13 μm
Contact area diameter	9.9 μm	9.9 μm
Separation distance	180 Å	180 Å
Porosity	0.059	0.124
Fiber thickness	200 μm	200 μm
Thickness of low porosity region	3.5 μm	2.5 μm

The results of the simulation are shown in table 3.F.1. The simulation predicts the critical levels for which an average cell would be detached. In actuality, for each condition, it was observed experimentally that only a fraction of the cells were removed. Partial removal indicates the presence of heterogeneity in the experimental system. This heterogeneity was most likely present in both the cells and the fibers. Examples of parameters which are likely to be sources of significant heterogeneity are cell surface marker expression, contact area size and morphology (especially with respect to separation distance), as well as fiber porosity, morphology and surface characteristics. Since it would be very difficult to accurately determine the distribution of these and other properties for a given experiment, simulation results should be considered as only a semi-quantitative prediction of average behavior and the effect of experimental parameters.

Experimentally, we observed that for Lot 1 fibers (see table 3.3) 47 - 60 % of

adsorbed cells could be detached with a transmembrane pressure of 20 psi (1034 mmHg). The simulation results from table 3.F.1 indicate that for a cell with 50,000 markers, critical transmembrane pressures predicted for an anisotropic membrane are less than this value so that the cells should be removed. The predicted critical pressure is below the experimentally applied pressure even for freely mobile markers with the highest ligand density where nearly every marker is involved in a bond. Since the critical pressure for cell removal is roughly proportional to the total number of bonds, we would predict that as many as 67,000 bonds could be broken by the experimentally applied pressure. By contrast, if the membrane were completely isotropic in morphology, it would be unlikely that cells bound by more than about 1,000 bonds (as was the case for the lowest ligand density) could be removed. If the membrane were isotropic, but the vast majority of the pressure drop occurred across the thin region of low porosity observed in electron photomicrographs, then the experimentally applied pressure may be sufficient to remove cells except probably for cells with freely mobile markers on the highest ligand density membrane.

Experimentally, it was observed that a decrease in ligand density from 3.2×10^{11} to 1.2×10^{10} cm^{-2} was correlated with a modest 13 % increase in the fraction of cells removed. The simulation results indicate that the critical pressure and shear decreases over this range for both fixed and freely mobile markers, but that the decrease is far greater for cells with freely mobile markers and is only modest (about 30 %) for cells with fixed markers, perhaps suggesting that the CD19 antigen is not freely mobile in the experimental system. Our experimental results also showed that cells attached to the fibers with the lowest ligand density (1×10^{9} cm^{-2}) were weakly bound and easily removed (80 % removed in control). The simulation results confirm that cells bound to fibers with the lowest ligand density are attached by only a small fraction of the number of bonds as for the two higher ligand

densities. In addition, the critical shear required to dislodge cells for this condition is about 1 to 2 orders of magnitude less than for the other conditions.

Experimentally, nearly twice the fraction of cells removed from Lot 1 fibers were removed from Lot 2 fibers with a similar ligand density (86 % vs. 47 % see table 3.3). Lot 2 fibers had a hydraulic permeability about a 15-fold higher hydraulic permeability than Lot 1 fibers. The simulation results predict only a modest decrease (20 to 30 %) in the critical pressures required for cell removal, similar to, or less than that predicted for the reduction in ligand density from 3.2×10^{11} to 1.2×10^{10} cm^{-2} with Lot 1 fibers where the increase in experimentally observed cell removal was much less. This may indicate that there are other morphological differences between the fiber types which were not considered in this analysis.

Table 3.F.1 *Critical Detachment Pressures and Shear Stress from Theoretical Predictions for Direct Binding of Namalwa to anti-CD19 Coated Lot 1 and Lot 2 Hollow Fibers*

	Attachment (Fixed/Mobile)	Detachment (Fixed/Mobile)				
Ligand Density ($cm^{-2} \times 10^{-11}$)	**# Bonds**	**F_b^{crit} (μdynes)**	**τ_{crit} (dynes/cm²)**	**ΔP Anisotropic Membrane (mmHg)**	**ΔP_{min} Isotropic Membrane (mmHg)**	**ΔP_{min} Isotropic Skin Region (mmHg)**
Lot 1						
3.2	6,800/49,999	10.9/10.7	1,300/9,400	110/760	8,900/64,030	250/1,800
0.12	6,800/8,700	7.5/8.2	900/1,200	73/100	6,100/8,500	170/240
0.01	720/720	8.1/8.2	100/100	8.4/8.5	700/710	20/20
Lot 2						
3.0	6,400/49,999	10.8/10.6	1,200/9,300	73/570	8,200/64,000	190/1,500

3.12.3.2 Indirect Binding of anti-CD33 Coated HL-60 to rpA-Coated Lot 2 Fibers

Measured Parameter	Lot 2
Ligand density	1.27×10^{12} cm^{-2}
Permeability constant	2.0×10^{-12} m
Cell diameter	14 μm
Contact area diameter	9.9 μm
Separation distance	180 Å
Porosity	0.124
Fiber thickness	200 μm
Thickness of low porosity region	2.5 μm

The results of the simulation are shown in table 3.F.2 and can be compared with the experimental cell detachment results shown in table 3.4. The simulation results suggest that a typical HL-60 cell with as many as 50,000 bonds should be readily removed by the experimentally applied back-pressure for anisotropic membranes, but would not be for a completely isotropic membrane. The minimum critical pressure required for cell removal predicted for a membrane with a thin isotropic pressure drop-determining region is also less than the experimentally applied back-pressure. The simulation predicts a reduction by about a factor of two in critical pressures compared to the same fiber utilizing direct binding. This reduction was not reflected in the experimental percentage of cells removed. In fact, about 13 % fewer cells were removed by pressure for indirect binding. The simulation also predicts that the critical bond strength and removal pressures are reduced by almost half when pressurization is performed at low pH. Experimentally, it was observed that the percentage of cells removed increased from 73 % to 96 %. The high percentage of cells removed by

control conditions (handling) with indirect binding conditions compared to direct binding (56 % vs. 11 to 32 %) is not easily explained by the simulation results since the shear stress required for cell removal is very high in all cases (> 290 dynes/cm^2). Perhaps the rpA-IgG bond or multiple bonds in series are particularly sensitive to air exposure.

Table 3.F.2 *Critical Detachment Pressures and Shear Stress from Theoretical Predictions for Indirect Binding of HL-60 to rpA--Coated Lot 2 Hollow Fibers*

	Attachment (Fixed/Mobile)	Detachment (Fixed/Mobile)				
Ligand Density ($cm^{-2} \times 10^{-11}$)	**# Bonds**	**F_b^{crit} (μdynes)**	**τ_{crit} (dynes/cm^2)**	**ΔP Anisotropic Membrane (mmHg)**	**ΔP_{min} Isotropic Membrane (mmHg)**	**ΔP_{min} Isotropic Thin Region (mmHg)**
pH 7.4						
12.7	5,500/49,990	7.2/7.2	490/4,500	42/380	4,200/38,000	97/880
pH 2.5						
12.7	5,500/49,610	3.8/3.8	290/2,600	25/220	2,500/22,000	57/520

3.13 References

Anderson, K.C., R. Soiffer, and R. Delage. 1990 T-cell depleted autologous bone marrow transplantation therapy: analysis of immune deficiency and late complications. *Blood.* 76:235-244.

Azad, A.R.M., and R.A. Goffe. 1990. Process for the covalent surface modification of hydrophobic polymers and articles made therefrom. Patent Cooperation Treaty Publication No. WO 90/04609.

Basch, R.S., J.W. Berman, and E. Lakow. 1983. Cell separation using positive immunoselective techniques. *Journal of. Immunological Methods.* 56:269-280.

Berenson, R.J., W.I. Bensinger, R.S. Hill, R.G. Andrews, J. Garcia-Lopez, D.F. Kalamasz, B.J. Still, G. Spitzer, C.D. Buckner, I.D. Bernstein, and E.D. Thomas. 1991. Engraftment after infusion of CD34+ marrow cells in patients with breast cancer or neuroblastoma. *Blood.* 77:1717-1722.

Berenson, R.J., W.I. Bensinger, D. Kalamasz, and P. Martin. 1986a. Elimination of Daudi lymphoblasts from human bone marrow using avidin-biotin immunoadsorption. *Blood.* 67:509-515.

Berenson, R.J., W.I. Bensinger, and D. Kalamasz. 1986b. Positive selection of viable cell populations using avidin-biotin immunoadsorption. *Journal of Immunological Methods.* 91:11-19.

Berson, A.E., K.M. Knobel, D. Rood, K. Chen, D. Lamons, M.A. McNally, T.B. Okarma, and J.S. Lebkowski. 1996. Selection of murine lymphoid and hematopoietic cells using polystyrene tissue culture devices containing covalently immobilized antibody. *BioTechniques.* 20:1098-1103.

Brugger, W., S. Heimfeld, R.J. Berenson, R. Mertelsmann, and L. Kanz. 1995. Reconstitution of hematopoiesis after high dose chemotherapy by autologous progenitor cells generated ex vivo. *New England Journal of Medicine.* 333:283-287.

Civin, C.I., L.C. Strauss, M.J. Fackler, T.M. Trischmann, J.M. Wiley, and M.R. Loken. 1990. Positive stem cell selection - basic science. In: Gross, S., Gee, A.P., Worthington-White, D.A., eds. Bone Marrow Purging and Processing: Proceedings of the Second International Symposium on Bone Marrow Purging and Processing. Wiley-Liss, New York, NY. pp.387-402.

Collins, S.J., R.C. Gallo, and R.E. Gallagher. 1977. Continuous growth and differentiation of human myeloid leukemia cells in suspension culture. *Nature.* 270:347-349.

Colter, M., B. Fogarty, K. McGuire, R. Berenson, and S. Heimfeld. 1992. Rapid isolation of CD4 or CD8 T-cell subsets using the CEPRATE LC laboratory cell separation system. *Transplantation Proceedings.* 24:2801-2802.

Foresta, C., A. Varotto, and A. Caretto. 1990. Immunomagnetic method to select human sperm without sperm surface-bound autoantibodies in male autoimmune infertility. *Archives of Andrology.* 24:221-225.

Gaudernack, G., T. Leivestad, J. Ugelstad, and E. Thorsby. 1986. Isolation of pure functionally active CD8+ T cells: Positive selection with monoclonal antibodies directly conjugated to monosized magnetic microspheres. *Journal of Immunological Methods.* 90:179-187.

Golubev, A., and E. Sidorva. 1989. The use of targeted liposomes to isolate cells bearing immunoglobin receptors. *Journal of Immunological Methods.* 125:29-34.

Griffin, J.D., D. Linch, K. Sabbath, P. Larcom, and S.F. Schlossman. 1984. A monoclonal antibody reactive with normal and leukemic human myeloid progenitor cells. *Leukemia Research.* 8:521.

Hasthorpe, S., J. Rogerson, S.L. Green, and J.M. Radley. 1990. Use of bone marrow somatic cell hybrid lines to generate monoclonal antibodies specifically reactive with rare marrow cells. *Experimental Hematology.* 18:223-227.

Hermanson, G.T., A.K. Mallia, and P.K. Smith. 1992. Immobilized Affinity Ligand Techniques. Academic Press, Inc., San Diego, CA. pp. 282-284.

Hertz, C.M., D.J. Graves, D.A. Lauffenburger, and F.T. Serota. 1985. Use of cell affinity chromatography for separation of lymphocyte subpopulations. *Biotechnology and Bioengineering.* 27:603-612.

Holton, O.D., and J.J. Vicalvi, Jr. 1991. Optimization of monoclonal antibody immobilization on hydrazide-preactivated hollow fiber membrane. *BioTechniques.* 11:662-665.

Horton, J.K., O.M. Evans, K. Swann, and S. Swinburne. 1989. A new rapid method for the selection and cloning of antigen-specific hybridomas with magnetic microspheres. *Journal of Immunological Methods.* 124:225-230.

Hoven, M.Y., L. De Leij, J.F.K. Keij, and T.H. The. 1989. Detection and isolation of antigen-specific B cells by the fluorescence activated cell sorter (FACS). *Journal of Immunological Methods.* 117:275-284.

Janssen, W.E., and A.M. Rios. 1989. Non-specific cell binding characteristics of para-magnetic polystyrene microspheres used for antibody-mediated selection. *Journal of Immunological Methods.* 121:289-294.

Jasiewicz, M.L., D.R. Schoenberg, and G.C. Mueller. 1976. Selective retrieval of biotin-labeled cells using immobilized avidin. *Experimental Cell Research.* 100:213-217.

Kato, K., and A. Radbruch. 1993. Isolation and chacterization of $CD34^+$ hematopoietic stem cells from human peripheral blood by high gradient magnetic cell sorting. *Cytometry.* 14:384-392.

Klein, E., E. Eichholz, and D.H. Yeager. 1994. Affinity membranes prepared from hydrophilic coatings on microporous polysulfone hollow fibers. *Journal of Membrane Science.* 90:69-80.

Kokkinopoulos, D., S. Perez, R. Sotiradou, J. Stinios, and M. Papamichail. 1992. The use of nylon wool for the isolation of T lymphocyte subpopulations. *Journal of Immunological Methods.* 154:1-6.

Kuo, S.C., and D.A. Lauffenburger. 1993. Relationship between receptor/ligand binding affinity and adhesion strength. *Biophysical Journal.* 65:2191-2200.

Larsson, P.H., J. Hed, S.G.O. Johansson, U. Persson, and M. Wahlström. 1989. Improved cell depletion in a panning technique using covalent binding of immunoglobins to surface modified polystyrene dishes. *Journal of Immunological Methods.* 116: 293-298.

Mage, M.G., L.L. McHugh, and T.L. Rothstein. 1977. Mouse lymphocytes with and without surface immunoglobin: preparative scale separation in polystyrene tissue culture dishes coated with specifically purified anti-immunoglobin. *Journal of Immunological Methods.* 15:47-56.

Mandrusov, E., A. Houng, E. Klein, and E.F. Leonard. 1995. Membrane-based cell affinity chromatography to retrieve viable cells. *Biotechnology Progress.* 11:208-213.

Manyonda, I.T., A.J. Soltys, and F.C. Hay. 1992. A critical evaluation of the magnetic cell sorter and its use in the positive and negative selection of CD45RO+ cells. *Journal of Immunological Methods.* 149:1-10.

Miltenyi, S., W. Muller, W. Weichel, and A. Radbruch. 1990. High gradient magnetic cell separation with MACS. *Cytometry.* 11:231-238.

Montgomery, R.B., J. Kurtzberg, A. Rhinehardt-Clark, A. Haleen, S. Ramakrishnan, G.A. Olsen, W.P. Peters, C.A. Smith, B.F. Haynes, L.L. Houston, R.C. Bast Jr. 1990. Elimination of malignant clonogenic T cells from human bone marrow using chemoimmunoseparation with 2'-deoxycoformycin, deoxyadenosine and an immunotoxin. *Bone Marrow Transplantation.* 5:395-402.

Nadkarni, J.S., J.J. Nadkarni, P. Clifford, G. Manolov, E.M. Fenyö, and E. Klein. 1969. Chacterization of new cell lines derived from Burkitt lymphomas. *Cancer.* 23:64-79.

Ngo, T.T. 1986. Facile activation of sepharose hydroxyl groups by 2-fluoro-1 methylpyridinium toluene-4-sulfonate: Preparation of affinity and covalent chromatographic matrices. *Bio/Technology.* 4:134-137.

Nordon, R.E., B.K. Milthorpe, K. Schindhelm, and P.R. Slowiaczek. 1994. An experimental model of affinity cell separation. *Cytometry.* 16:25-33.

Nordon, R.E., D.N. Haylock, L. Gaudry, and K. Schindhelm. 1996. Hollow-fiber affinity cell separation system for $CD34^+$ cell enrichment. *Cytometry.* 24:340-347.

O'Shannessy, D.J. 1990. Hydrazido-derivatized supports in affinity chromatography. *Journal of Chromatography.* 510:13-21.

Rasmussen, A.-M., E.B. Smeland, B.K. Erikstein, L. Caignault, and S. Funderud. 1992. A new method for detachment of Dynabeads from positively selected lymphocytes. *Journal of Immunological Methods.* 146:195-202.

Reynolds, E.S. 1963. The use of lead nitrate at high pH as an electron opaque stain in electron microscopy. *Journal of Cell Biology.* 17:208.

Rutishauser, U., I. Yahara, and G.M. Edelman. 1974. Morphology, motility, and surface behavior of lymphocytes bound to nylon fibers. *Proceedings of the National Academy of Science USA.* 71:1149-1153.

Sargent, I.L., Y.S. Choo, and C.W.G. Redman. 1994. Isolating and analyzing fetal leukocytes in maternal blood. *Annals of the New York Academy of Science.* 731:147-153.

Saterbak, A., and D.A. Lauffenburger. 1996. Adhesion mediated by bonds in series. *Biotechnology Progress.* 12:682-699.

Skuse, D.R., W. Müller, and D.E. Brooks. 1988. Column chromatographic separation of cells using aqueous polymeric two-phase systems. *Analytical Biochemistry.* 174:628-635.

Slaper-Cortenbach, I.C.M., L.G. Admiraal, E.F. van Leeuwen, J.M. Kerr, A.E.G.K. von dem Borne, and P.A.T. Tetteroo. 1990. Effective purging of bone marrow by a combination of immunorosette depletion and complement lysis. *Experimental Hematology.* 18:49-54.

Spangrude, G.J., S. Heimfeld, and I.L. Weissman. 1988. Purification and chacterization of mouse hematopoietic stem cells. *Science.* 241:58-62.

Stich, T. 1990. Determination of protein covalently bound to agarose supports using bicinchoninic acid. *Annals of Biochemistry.* 159:138-142.

Szilvassy, S.J., P.M. Lansdorp, R.K. Humphries, A.C. Eaves, and C.J. Eaves. 1989. Isolation in a single step of a highly enriched murine hematopoietic stem cell population with competitive long-term repopulating ability. *Blood.* 74:930-939.

Tanaka, H.,Y. Ishida, T. Kaneko, and N. Matsumoto. 1989. Isolation of human megakaryocytes by immunomagnetic beads. *British Journal of Hematology.* 73:18-22.

Thomas, T.E., H.J. Sutherland, and P.M. Lansdorp. 1989. Specific binding and release of cells from beads using cleavable tetrameric antibody complexes. *Journal of Immunological Methods.* 120:221-231.

Tse, D.B., P. Anderson, S. Goldbard, A.M. Gown, C.S. Hawes, and A. Donnenfeld. 1994. Chacterization of trophoblast-reactive monoclonal antibodies by flow cytometry and their application for fetal cell isolation. *Annals of the New York Academy of Science.* 731:163-169.

Uckun, F.M., J.H. Kersey, D.A. Vallera, J.A Ledbetter, D. Weisdorf, D.E. Myers, R. Haake, and N.K.C. Ramsay. 1990. Autologous bone marrow transplantation in high-risk remission T-lineage acute lymphoblastic leukemia using immunotoxins plus 4-hydroperoxycyclophosphamide for marrow purging. *Blood.* 76:1723-1733.

Weibel, E.R. 1969. Stereological principles for morphometry in electron microscopic cytology. *International Review of Cytology.* 26:235-302.

Wysocki, L.J., and V.L. Sato. 1978. "Panning" for lymphocytes: a method for cell selection. *Proceedings of the National Academy of Science USA.* 75:2844-2848.

Yannelli, J.R. 1991. The preparation of effector cells for use in the adoptive cellular immunotherapy of human cancer. *Journal of Immunological Methods.* 139:1-16.

Chapter 4. Immunoaffinity Cell Adsorption and Recovery Utilizing Recombinant Protein-A-Coated Hollow-Fiber Membranes in Small Modules

4.1 Abstract

Previously we have shown that functionalized microporous, hollow-fiber membranes can be successfully used for immuno-selective adsorption of target cells, and that a large fraction of the cells can be removed using back-pressure and back-filtration (see chapter 3). In those experiments, unpotted hollow fibers were employed, and cells were loaded onto .the fiber under the influence of gravity. Recombinant protein A (rpA)-functionalized fibers were capable of adsorbing monoclonal antibody-coated target cells with over 99 % selectivity, and as much as 96 % could be removed using back-pressure and low pH (pH 2.5). In the present study, we performed similar experiments for rpA-coated hollow-fibers contained in specially designed small glass modules to enable more efficient cell recovery and cell loading by filtration at constant flowrate. With cells loaded onto the fiber by filtration, we were unable to replicate the positive results obtained in the previous study. Non-specific cell attachment to fibers and a lack of removal of cells by back-pressure using neutral pH (pH 7.4) or low pH (pH 2.5) buffers were problems encountered which were not previously observed in experiments with unpotted fibers where cells were loaded by gravity. Using membranes with higher hydraulic permeability did not improve performance. We also observed that for cells loaded by filtration, exposure of adsorbed cells to an air-liquid interface and brief air exposure may be a more effective cell removal method than back-pressure. Based on transmission electron microscopic observations of adsorbed cells, we propose that the high level of non-

specific cell attachment and difficulty in removing adsorbed target cells, especially with back-pressure, could be due to the infiltration of portions of the cell membrane and cytoplasm into the pore structure of the hollow fiber membranes during cell loading by filtration at applied pressure levels employed in the study.

4.2 Introduction

In this study, previous work in our laboratory performing positive cell separation with single, unpotted ligand-functionalized microporous hollow-fiber membranes (chapter 3) is expanded upon by designing a more practical system and apparatus for larger scale cell separations with quantitative recovery of adsorbed cells. In our previous work, we found that monoclonal antibody-coated target cells could be adsorbed to recombinant protein A (rpA) coated fibers with selectivities of over 99 %, and that 73 % and 96 % could be removed by elution procedures including back-filtration using pH 7.4 and pH 2.5 buffers, respectively, when cells were loaded onto the membranes by gravity. Because of these promising results and the flexibility and economical advantages of the rpA-coated fiber system, in this study we chose to work exclusively with this system.

We designed a small module system for performing cell binding and detachment studies with cells adhered to either the outside or lumen surface of a single fiber, each surface capable of binding about a million cells. With the apparatus, cells can be filtered onto the surface in shorter periods of time with less contact time variation before elution and with greater spatial uniformity than with loading by gravity. In addition, removal forces by both shear and back-pressure can be more easily controlled, and eluted cells can be recovered in a more quantitative fashion. Also, potential complicating factors in the experiments of the previous chapter such as mechanical stresses on the cells during handling of the fibers and

exposure of cells to an air liquid interface during the experiment can be eliminated or more rigorously studied. In this chapter, in addition to performing cell binding and detachment studies with target and non-target cells using X3257B2 fibers (Lot 2 previously, designated Type B in this chapter), we investigate several other fiber types with higher hydraulic permeabilities, two of which have lumenal retentive surfaces. We also investigate more systematically the effect of the passage of an air-liquid interface and air exposure on cell removal from fibers.

Our results suggest: that cells are more irreversibly attached when loaded by filtration imposed by hydrostatic pressure, that fibers with increased hydraulic permeability did not yield improved cell removal performance, and that exposure to air and/or an air liquid interface may play a substantial role in removal of viable cells. Our results also suggest that a possible mechanism for the apparent irreversibility of cell adsorption when loaded by filtration was infiltration of cell processes into the pore structure of the hollow-fiber membranes.

4.3 Materials and Methods

4.3.1 Functionalized Fibers

Four lots of polyethersulfone/polyethylene oxide hollow-fiber microporous membranes (kindly provided by Sepracor Inc., Marlborough, MA) were used in this study, designated by the manufacturer as lots A3194A4 (Type A), X3257B2 (Type B), X3257C2 (Type C), and XE3182A (Type E). The hollow fibers were coated with hydroxyethylcellulose and functionalized with 2-fluro-1-methylpyridinium toluene-4-sulfonate (FMP) as previously described in chapter 3 (Ngo, 1986; Azad and Goffe, 1990; Klein et al., 1994).

4.3.2 Characterization of Hollow-Fiber Membranes

Hollow fibers were sectioned with a sharp razor and examined by light microscopy. Inside and outside diameters were determined for each fiber lot by measuring two perpendicular diameters of fiber cross-sections with an eye piece reticle inscribed with a linear scale. Total membrane volume including void volume was defined as:

$$V_m = \pi \frac{L}{4}(d_o^2 - d_i^2) \quad (1)$$

where d_0 is the outer diameter of the fiber, d_i is the inner diameter of the fiber, and L is the length of the fiber sample. Membrane structure of base fibers (fibers which have not been chemically modified) was observed with gold/palladium-coated (30 Å) sections by field-emission scanning electron microscopy (FESEM) on a JEOL-6320F microscope (JEOL, Peabody, MA). Cross-sectional views were prepared by scoring the fiber lightly with a sharp razor blade, submersing it in liquid nitrogen, and then quickly fracturing it at the score. The range of pore sizes on the retentive surface of the base fibers was determined by measuring the effective diameters of the largest and smallest pores visible on SEM photomicrographs of a minimum of two separate areas of the retentive surface at magnifications ranging from 2000 × to 50,000 × representing a minimum analyzed area of 125 μm^2 for the smallest pore size membranes to 10,000 μm^2 for the largest. The total number of pores analyzed was about 6,000 for Type B fibers, 18,000 for Type A fibers, 22,000 for Type E fibers, and 45,000 for Type C fibers. Measurements of the largest and smallest pores visible on each photomicrograph were made with precision calipers (Mitutoyo Corporation, Tokyo, Japan), and an effective diameter was defined as the geometric mean of the largest and smallest diameters for each pore.

Surface area of the base fibers was measured by gas adsorption/desorption (BET analysis) using a Micrometrics Flowsorb II® Model 2300 (Micrometrics Instrument Corp., Norcross, GA). The surface area determined in this fashion was used to calculate the surface density of immobilized ligand on the fibers.

4.3.3 Attachment of Recombinant Protein A (rpA) to FMP-Functionalized Fibers

The density of surface-bound FMP groups was assayed by reacting small segments of the fibers with excess ethanolamine in water 6% (v/v). The soluble product formed from the reaction between the active surface groups and the ethanolamine, 1-methyl-2-pyridone, was detected by its absorbance at 297 nm using an extinction coefficient of 5.9 (Ngo, 1986).

Covalent coupling of rpA (Repligen, Cambridge, MA) to FMP-functionalized fibers as via primary amine groups on the rpA was carried out, as previously described in chapter 3, by incubating slightly alkaline (pH 8-9) aqueous rpA solution with agitation provided by an orbital shaker (Ngo, 1986). Residual active groups remaining on the fiber were deactivated by hydrolysis with sodium hydroxide. Fibers with immobilized ligand were stored at 4° C in PBSA.

4.3.3.1 Quantification of Immobilized Protein

The amount of protein immobilized on the functionalized fibers was measured by incubating small segments of protein-coated fibers with BCA® protein assay reagent (Pierce, Rockford, IL), measuring absorbance of the soluble reaction product at 562 nm, and comparing measured values to a standard curve prepared with solutions containing known amounts of a protein the same as, or similar to, the immobilized protein (Stich, 1990; Holton et al., 1991). Control samples including an equal amount of the same type of fiber, but without immobilized protein, were run in parallel to provide a baseline value of protein immobilized, which was subtracted from each test sample.

4.3.3.2 Adsorption Capacity of Immobilized rpA

The capacity of the fibers for specific adsorption of target antibody and non-specific adsorption of an inert protein was tested. One-centimeter segments of fibers were incubated with the test protein (1 mg/ml in PBSA) for 4 to 24 hr at room temperature. The fibers were then extensively washed with protein-free buffer until the wash buffer was free of protein as determined by UV absorption at 280 nm. The adsorbed protein was then eluted with a solution containing 50 mM Glycine and 150 mM NaCl (pH 2.5) or 0.1 M Citrate (pH 3.0). Eluted protein concentration was determined by UV absorption at 280 nm. Test proteins included human polyclonal IgG (Gammagard, Hyland Div., Baxter Healthcare, Glendale, CA), a mouse myeloma monoclonal IgG2b (Sigma, St. Louis, MO) protein of the same isotype as the anti-CD33 monoclonal antibody subsequently used in some cell loading experiments, and BSA as a non-specific adsorption control. Because the fibers are exposed to elevated buffer temperatures during the module assembly process (up to 60 °C as measured with a temperature probe inserted into the module during assembly), for some determinations, the segments of fiber were exposed to elevated temperatures (room temperature to 90 °C) for 10 min, after which the fibers were cooled to room temperature, and the capacity was measured as before.

4.3.4 Cell Lines

Two human cell lines, Namalwa and HL-60 were used for experiments. Namalwa is a Burkitt's lymphoma cell line (Nadkarni et al., 1969), and HL-60 is a pro-myelocyte leukemia cell line (Collins et al., 1977) which expresses CD33 markers on its surface. Cell lines were grown in continuous suspension culture in tissue culture flasks at 37° C in a humidified air atmosphere containing 5% CO_2 in RPMI media supplemented with 25 mM HEPES buffer, 10% fetal bovine serum (FBS), 4 mM L-glutamine, 50 IU/ml penicillin and 50 μg/ml

streptomycin (BioWhittaker, Walkersville, MD). Cell cultures were passaged approximately every 48 hr. Cells were used for experiments while in their log growth phase.

4.3.5 Experimental Apparatus For Loading Cells Onto Fibers by Filtration

Figure 4.1 (A) shows a schematic diagram of the FMP-functionalized hollow fibers used in this study drawn approximately 1.5× scale. Small (0.5 - 1.5 cm) lengths of 1/16 " inner diameter Tygon tubing (Tygon S-50-HL, Norton Performance Plastics Corporation, Akron, OH) were glued using a glue gun (Surebonder®, FPC Corporation, Wauconda, IL) with hot-melt glue (Surebonder®, FPC Corporation, Wauconda, IL) to each end to facilitate handling and pressurization. After the plastic tubing was attached, the active length of the fiber available for cell loading by filtration was 3 - 5 cm. The fibers were then coated with rpA. The shell of the small modules was constructed from Pyrex glass tubing (Corning Inc., Corning, NY) by the MIT glass blower (see figure 4.1 (B)). The main tube was 5 cm in length with an inner diameter of 5 mm and an outer diameter of 7 mm. The side tubes for cross-flow through the shell were 1 cm in length with an inner diameter of 2 mm and an outer diameter of 4 mm, and were located 0.5 cm from each end in the configuration shown in cross-section in figure 4.1 (B). For some experiments, the glass module was coated with a chlorinated organopolysiloxane (Sigmacote, Sigma Chemical Company, St. Louis, MO, used according to manufacturer's directions), or with poly(2-hydroxyethyl methacrylate) (poly(HEMA), Sigma Chemical Company, St. Louis, MO, used according to protocol outlined in Folkman and Moscona, 1978) to minimize non-specific adsorption of cells . For some experiments, modules were used in which a hole about 5 mm in diameter had been created in the center of the module to facilitate direct observation of cells adhered to the outer surface of hollow fibers (see figure 4.1(C)). The hole was covered with a section cut from a hemacytometer cover glass and sealed with epoxy. The rpA-coated fiber was placed into the

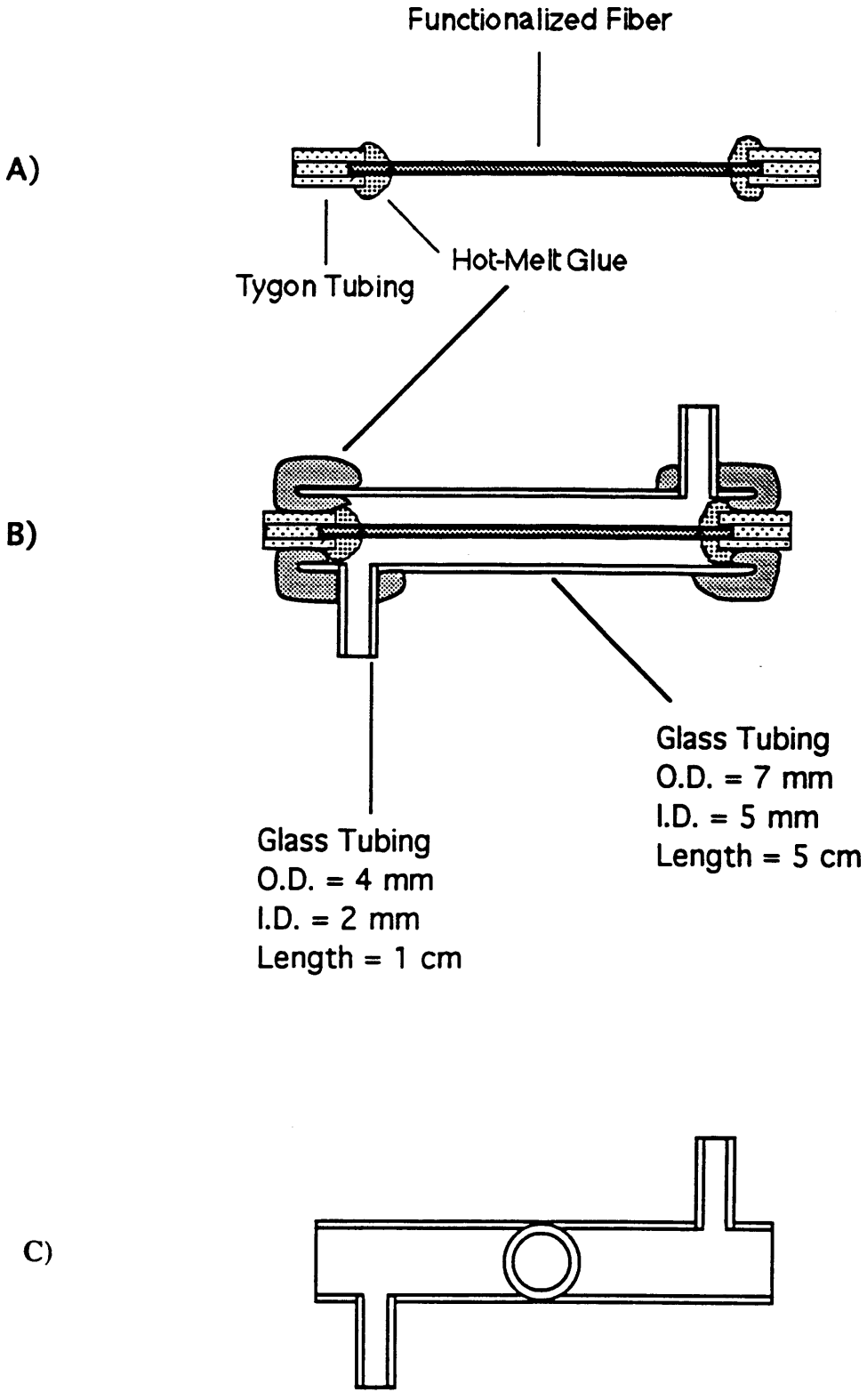

Figure 4.1 Schematic diagram of cross-section of functionalized fiber as prepared for cell loading/detachment experiments. A) Fiber alone. B) Fiber in module. C) Modified module with viewing window for direct observation of fiber.

shell and each end was sealed with hot-melt glue in such a way that the active length of the fiber was kept submerged at all times in PBSA. For experiments designed to perform a number balance on cells injected into the module shell, a 1 mm O.D. segment of copper wire was used in place of the rpA-coated fiber. Figure 4.2 (A) and (B) shows a schematic diagram of the set up used for measurement of hydraulic permeability and cell loading/detachment experiments for flow into the shell (A) and lumen (B). The apparatus was constructed 5/32 "I.D. Tygon tubing for the shell-side configuration shown in figure 4.2 (A), and 1/16 " I.D. Tygon tubing for the lumen-side configuration shown in figure 4.2 (B). Positive pressure and flow was generated using a two-channel syringe pump with a synchronous, surge-less motor (Model 975, Harvard Apparatus, South Natick, MA), and pressure was measured with a stainless steel test gauge (0-760 mmHg, Ashcroft, Stratford, CT) or a digital pressure monitor (Model SP1405, Gould Statham, Oxnard, CA). In addition, short lengths (2 - 10 cm) of 1/16 " I.D. Tygon tubing or silicone tubing (S/P Medical Grade, Baxter Healthcare Corporation, Deerfield, IL) with 3-way Luer stopcocks ((3) and (4) in figure 4.2) were attached to the fiber with small polypropylene fittings, and short lengths (2 - 3 cm) of 5/32 " I.D. Tygon tubing or silicone tubing were attached to the shell with a 3-way Luer stopcock (1) at the inlet, and a 1-way Luer stopcock at the outlet (2). For some experiments, the tubing attached to the module was passivated with poly(HEMA). The module and tubing was pressure tested for leaks at 20 psig in the lumen side and 10 psig in the shell side. The module was stored filled with PBSA until use.

4.3.5.1 Hydraulic Permeability

Hydraulic permeability was measured with rpA-coated fibers in small modules with the apparatus shown in figure 4.2. Measurements for flow from the lumen to shell and for flow from the shell to the lumen were taken. For flow from the lumen to the shell, the outlet

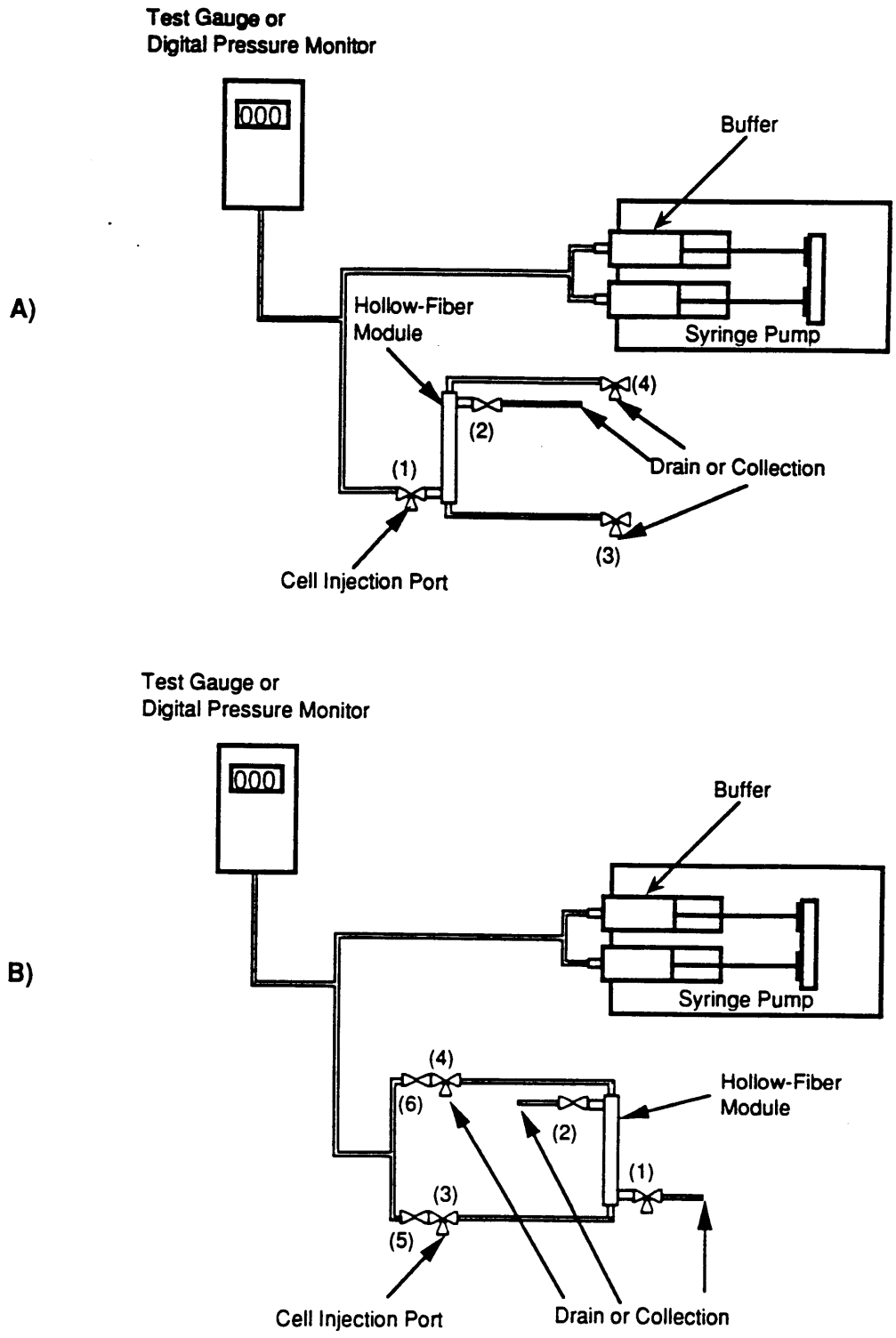

Figure 4.2 Schematic diagram of experimental apparatus as set up for loading cells from the shell side of the module onto the outside surface of fibers as in A), or loading cells onto the lumen of fibers as in B). Numbers in parentheses refer to stopcocks (see text).

stopcock (4) of the fiber lumen was closed, PBS was pumped into the lumen through valve (3), the inlet pressure was measured, and the permeate was collected through stopcock (2). For flow from the shell to the lumen, the outlet stopcock (2) of the shell was closed, PBS was pumped into the shell through stopcock (1), the inlet pressure was measured, and the permeate was collected through stopcock (4). The hydraulic permeability was calculated from

$$J_v = \frac{Q}{\pi d L} \tag{2}$$

where Q is the measured permeate flowrate (L/hr), d is the diameter of the retentive fiber surface (m), and L is the active fiber length (m). The hydraulic permeability was evaluated from

$$L_p = \frac{J_v}{\Delta P_{TM}} \tag{3}$$

where ΔP_{TM} is the transmembrane pressure difference (mmHg).

4.3.6 Procedure for Cell Loading and Detachment Experiments

Prior to use, the fibers in modules were washed extensively with Dulbecco's phosphate buffered saline without calcium and magnesium (DPBS, Sigma, St. Louis, MO) to remove the sodium azide in the storage buffer. An aliquot of cells from culture was added to a test tube containing Trypan Blue dye, and live and dead cells were counted with a hemacytometer (Reichert Scientific Instruments, Buffalo, NY). A sufficient number of cells to perform the experiment were centrifuged (400 × g, 4°C, 10 min) and the pellet was resuspended in cold DPBS (pH 7.4) for washing. The cells were centrifuged and washed once more with cold DPBS. For some experiments, HL-60 cells were made to have affinity for the rpA fiber by

resuspending the pellet from the first centrifugation, at a concentration of 5 to 10 × 10^6 cells/ml, in cold RPMI media containing 10 % FBS and diluted ascites containing approximately 5 mg/ml anti-CD33 mAb and incubating on ice for 30 min. These cells were subsequently washed twice with cold DPBS as above. Finally, the cells were centrifuged and resuspended at 2 to 10 × 10^6 cells/ml in cold DPBS supplemented with 1 % w/v BSA which had been pre-filtered through a 0.1 μm membrane. Cell suspensions were kept on ice until immediately prior to use.

For experiments with Type B or Type C fibers, whose retentive surface is the outside surface of the fiber, and number balances on cells, cells were injected into the shell side of the glass module. In addition, for experiments with Type B or Type C fibers, the cells in the shell were loaded onto the retentive outer surface of the fiber via filtration from the shell to the lumen. This was accomplished as follows. The shell was initially drained of buffer by opening stopcocks (1) and (2) in figure 4.2 (A). The cell suspension was then injected into stopcock (1) to fill the shell. For experiments where cells were loaded onto the fiber by filtration, stopcock (2) was closed, and stopcock (1) was set to receive flow from the pump. Stopcock (4) was opened and the pump was turned on and set for a constant flowrate (about 0.2 ml/min) of DPBS which was maintained until a sufficient volume of permeate was collected to ensure that 1 to 2 × 10^6 cells were filtered onto the fiber. The maximum pressure attained during filtration was recorded. The pump was then stopped, stopcock (4) was closed, stopcock (2) was opened, and excess cells were washed out of stopcock (1) and the shell by gently pumping DPBS first through stopcock (1) and then through the shell (about 12 ml/min). Five to ten fractions (about 2 to 5 ml each) of the wash suspension were collected in small polypropylene test tubes. For experiments where cells were loaded onto Type B or Type C fibers by filtration, after washing, the cells were eluted by pressurizing the lumen of

the fiber either with DPBS (pH 7.4), or 10 mM glycine buffered saline (pH 2.5) by closing stopcock (4), pre-pressurizing the line up to a one-way stopcock upstream of stopcock (3) (analogous to stopcock (5) in figure 4.2 (B)) to the desired back-pressure, opening the stopcock upstream of stopcock (3) and injecting buffer into stopcock (3) at a rate necessary to maintain the desired back-pressure (760 mmHg). In this way, the cells on the fiber experienced the full back-pressure instantaneously. During the pressurization period, a flow of DPBS supplemented with 25 mM HEPES and 1 % w/v BSA was established through the shell (about 4 - 5 ml/min) to flush out the eluted cells and neutralize the low pH buffer. For some experiments, the lumen was pressurized without additional shell-side flow of buffer for 1 - 4.5 min before the onset of supplemental shell-side buffer flow. Eluted cell suspensions were collected into a series of fractions in small test tubes. The volume of cell suspension in each collected fraction was measured with a serological pipet, cells were counted with a hemacytometer, and some fractions were checked for viability with Trypan Blue dye. All procedures were carried out at room temperature, however, collected cells were kept on ice until they were counted at the end of the experiment.

For experiments with Type E or Type A fibers, cells were loaded onto the retentive lumen surface of the fiber via filtration from the lumen to the shell. The lumen was initially drained of buffer by opening stopcocks (3) and (4) in figure 4.2 (B). The cell suspension was then injected into stopcock (3) to fill the lumen of the fiber and attached tubing. For some experiments the cells were loaded into both sides of the lumen simultaneously with the module in a horizontal position. In such cases, stopcocks (3) and (4) were set to receive flow of DPBS from the pump. Stopcock (2) was opened and the pump is turned on and set for a constant flowrate (about 0.2 ml/min) which was maintained until a sufficient volume of permeate is collected to ensure that 1 to 2 $\times$ 10^6 cells were filtered onto the fiber. For other

experiments, cells were loaded into one end of the lumen for half the time, and into the alternate end for the other half. In such cases, stopcock (3) or (4) was set to receive flow from the pump and flow to the other end of the fiber was prevented by closing stopcock (5) or (6). After one half the desired volume of permeate was collected through stopcock (2), stopcocks were adjusted to allow flow to the alternate end of the lumen. These measures were taken to ensure even distribution of the cells on the fiber surface. The maximum pressure attained during filtration was recorded. The pump was then stopped, stopcock (2) was closed, stopcock (4) was opened to collect cells, and excess cells were washed out of the fiber by gently pumping DPBS through the lumen (about 0.8 ml/min Type E, about 0.2 ml/min Type A). After washing, the cells were eluted either by pumping DPBS supplemented with 1 % w/v BSA through the lumen at increased flowrates for Type A fiber experiments (shear stress elution), or for experiments with Type E fibers, by pressurizing the shell of the module either with DPBS supplemented with 1 % w/v BSA (pH 7.4), or 10 mM glycine buffered saline (pH 2.5) by closing stopcocks (1) and (2) and pre-pressurizing the line up to stopcock (2), then suddenly opening stopcock (2) and injecting buffer into stopcock (2) at a rate necessary to maintain the desired back-pressure (500 mmHg). Eluted cell suspensions were collected into a series of fractions in small test tubes. Cells eluted with the low pH buffer were collected into an equal volume of DPBS supplemented with 25 mM HEPES and 1 % w/v BSA to neutralize the low pH buffer. The volume of cell suspension in each collected fraction was measured with a serological pipet, cells were counted with a hemacytometer, and some fractions were checked for viability with Trypan Blue dye. For some experiments with Type A fibers, the lumen-side inlet and outlet tubing and stopcocks were replaced between the cell loading and fiber washing steps in order to access possible contamination by cells adsorbed to tubing. In such cases, the load tubing was flushed with

wash buffer separately and cells were collected and counted along with the cells collected from washing and eluting the fiber. All procedures were carried out at room temperature, however, collected cells were kept on ice until they were counted at the end of the experiment.

For one experiment with Type A fibers, cells were loaded by gravity onto the fibers instead of by filtration. For this experiment, the length of the Tygon tubing attached to the end of the fiber (see figure 4.1(A)) was reduced as much as possible (0.5 cm in length) to eliminate hold up volume in the tubing between the outlet of the small polypropylene connector and the fiber. Otherwise, the fiber was contained in a module and a cell suspension containing 7×10^7 cells/ml, was loaded into the fiber lumen as described previously. The module was placed in a horizontal position, and the cells were allowed to settle for 10 min. The module was then flipped over, and the cells were allowed to settle onto the opposite side for an additional 10 min. The fiber was washed and cells were eluted as previously described for experiments with Type A fibers including replacement of lumen-side tubing and stopcocks after loading. All procedures were carried out at room temperature; however, collected cells were kept on ice until they were counted at the end of the experiment.

4.3.6.1 Direct Visualization of Cells on Type B fibers in Modules With Viewing Windows

In some experiments with Type B fibers, cell binding and detachment was quantified by observing the cells adsorbed to fibers directly through the viewing window of the modified modules shown in figure 4.1 (C). The cells were loaded, excess cells were washed out, and adsorbed cells were eluted as previously described, except that after each step, the cells bound to the edges of the fiber under the viewing window were observed and photographed in brightfield at 100× total magnification using an inverted microscope. For some experiments, the effect of exposure to air, and the passage of an air interface was investigated by draining

the shell, exposing the cells to air for 5 to 10 sec, and then refilling and washing the shell with about 2 to 3 ml of DPBS supplemented with 1 % w/v BSA at a flowrate of about 12 ml/min. The draining and filling steps each took about 5 sec to complete. Cells adsorbed to the fiber were observed and photographed after each drain/fill sequence. The number of cells/cm of fiber edge was determined by counting the number of cells visible on the photographs over a measured distance on the photo, and determining the actual distance on the fiber by comparison with a photograph of a calibrated scale taken at the same magnification. As discussed in chapter 3, in regions where cells overlapped, the average distance between cell centers was assumed to be 10 μm.

All fibers used for adsorption of target cells were newly prepared. Some fibers used for non-specific cell adsorption had been used previously. Before re-use for such experiments, the fibers were regenerated by cleaning with 0.1 M citrate (pH 3.0), and 0.1 N NaOH followed by neutralization with a large quantity of PBSA.

4.4 Description of Flows and Pressures in Hollow Fiber Membrane Modules

In this analysis we develop a general description of flows and pressures for laminar flow in a hollow fiber membrane module for the case where the shell side is much larger in volume than the fiber and provides a negligible resistance to permeate flow. Thus, we assume that shell-side pressure is constant along the length of the fiber. This assumption is reasonable for our single-fiber module design. We perform case studies to simulate conditions of loading cells onto fiber surfaces by filtration and removing cells from fiber surfaces with back-pressure or shear flow. In the first two cases, we want to determine the uniformity of the transmembrane pressure drop along the axial length of the fiber, and in the

latter case, we want to determine the uniformity of the axial velocity and shear stress. A schematic diagram of the hollow fiber module is shown in figure 4.3. The hollow fiber in the diagram has a radius (measured from the center point to the retentive surface) R and length L. Radial fluid velocity across the semipermeable wall of the hollow fiber is given by Darcy's Law.

$$V = \frac{k}{\mu}(p - Po) \tag{4}$$

where V is the transmembrane fluid velocity, p is the lumen pressure at the surface of the fiber, and k is the permeability of the fiber wall which is equal to $L_p \cdot \mu$, where μ is the fluid viscosity. Po is the shell pressure which is assumed to be constant. The pressure at the surface of the fiber is approximated by a radially averaged lumen-side pressure $\langle p \rangle$. The mean axial velocity $\langle u \rangle$ and lumen pressure $\langle p \rangle$ are defined as follows

$$\langle u \rangle = \frac{2}{R^2}\int_0^R r u(x,r)\,dr \tag{5}$$

$$\langle p \rangle = \frac{2}{R^2}\int_0^R r p(x,r)\,dr \tag{6}$$

where $\langle u \rangle$ and $\langle p \rangle$ are both functions of axial position x.

Variations in the mean axial velocity and lumen pressure are determined by solving a set of two equations established from a mass balance equation and Poiseuille's Law for flow in a tube (Granger et al., 1989). Performing a mass balance over a differential slice of fiber of thickness dx yields

$$\pi R^2 \langle u \rangle = \pi R^2 \left(\langle u \rangle + \frac{\partial \langle u \rangle}{\partial x} dx \right) + \frac{k}{\mu}(\langle p \rangle - Po) 2\pi R dx \tag{7}$$

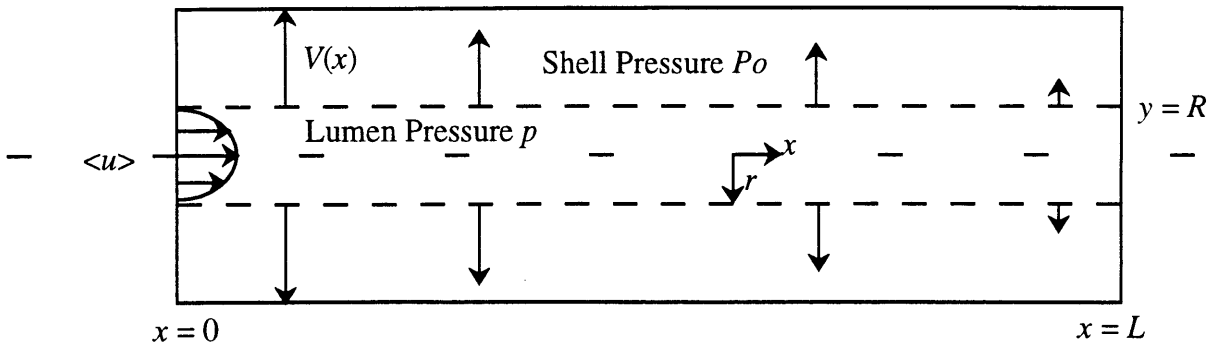

Configurations of Interest

1) Loading cells onto lumen surface by filtration or detaching cells from outside surface of fiber with pressure in lumen.

   Known: $\langle u \rangle(x=0)$ or $\langle p \rangle(x=0)$, Po, and $\langle u \rangle(x=L) = 0$
   Desired: $\langle p \rangle(x=L)/\langle p \rangle(x=0)$

2) Detaching cells from lumen surface of fiber with pressure in shell

   Known: $\langle u \rangle(x=0) = 0$, Po, and $\langle p \rangle(x=L) = Patm$
   Desired: $\langle p \rangle(x=0)/\langle p \rangle(x=L)$

3) Washing cells in lumen with shell closed

   Known: $\langle u \rangle(x=0)$ and $\langle u \rangle(x=L)$
   Desired: $\langle u \rangle(x=L/2)/\langle u \rangle(x=0)$

Figure 4.3 Schematic diagram of a hollow-fiber module with descriptions of operating conditions of interest.

which reduces to

$$\frac{d\langle u\rangle}{dx} = -\frac{2k}{\mu R}(\langle p\rangle - Po) \tag{8}$$

Poiseuille's law is used to relate the variation of the pressure $d\langle p\rangle$ to $\langle u\rangle$

$$\frac{d\langle p\rangle}{dx} = -\frac{8\mu\langle u\rangle}{R^2} \tag{9}$$

Equations 8 and 9 are nondimensionalized with the following dimensionless variables

$$X = \frac{x}{R}, \quad P = \frac{\langle p\rangle - Po}{Po}, \quad U = \frac{\langle u\rangle}{\langle u\rangle(x=0)} \tag{10}$$

where $\langle u\rangle(x=0)$ is the inlet velocity at $x = 0$.

Equations 8 and 9 then become

$$\frac{dU}{dX} = -\frac{2kPo}{\mu\langle u\rangle(x=0)}P \tag{11}$$

$$\frac{dP}{dX} = -\frac{8\mu\langle u\rangle(x=0)}{PoR}U \tag{12}$$

Taking the derivative of equation 11 yields

$$\frac{d^2U}{dX^2} = -\frac{2kPo}{\mu\langle u\rangle(x=0)}\frac{dP}{dX} \tag{13}$$

Substituting equation 12 into equation 13 gives a second order differential equation in U

$$\frac{d^2U}{dX^2} = \frac{16k}{R}U \tag{14}$$

Defining $M^2 = 16k/R$, equation 14 has the general solution

$$U = a \cosh MX + b \sinh MX \tag{15}$$

Equation 9 may be used to derive an expression for P from equation 15.

4.4.1 Variations in Mean Lumen Pressure During Cell Loading and Detachment

4.4.1.1 Case 1: Loading Cells Onto the Lumen Surface of the Hollow Fiber by Filtration, or Detaching Cells From the Outside Surface of the Fiber with Pressure in the Lumen

During the loading of cells onto the lumen surface of Type E or Type A hollow fibers with filtration, and during the removal of adsorbed cells on the outside surface of Type B and Type C fibers, fluid is pumped into the fiber at $x = 0$ at a constant flowrate or inlet pressure with the end of the fiber at $x = L$ closed. Permeate passes through the fiber into the shell which is open to the atmosphere ($Po = Patm$). In both cases, it is desired to know the uniformity of the pressure drop along the length of the fiber which determines the uniformity of the force tending to attach or detach cells along the length of the fiber. As shown in figure 4.3, in this case the inlet flowrate and pressure are known and the flow at $x = L$ will be zero. We want to determine the maximum deviation in pressure along the fiber length $\langle p \rangle(x=L)/\langle p \rangle(x=0)$. The final result obtained for a constant inlet flowrate is identical as that for a constant inlet pressure, so we will use the former in the following derivation.

Boundary Conditions:

$$\langle u \rangle = \langle u \rangle(x=0) \text{ at } x = 0 \quad \text{thus} \quad U = 1 \text{ at } X = 0 \tag{BC1}$$

$$\langle u \rangle = 0 \text{ at } x = L \quad \text{thus} \quad U = 0 \text{ at } X = \frac{L}{R} \tag{BC2}$$

Substitution of boundary condition 1 into equation 15 yields $a = 1$. Substitution of boundary condition 2 yields

$$b = -\frac{\cosh M\left(\frac{L}{R}\right)}{\sinh M\left(\frac{L}{R}\right)}$$

The solution for the velocity distribution from equation 15 is then

$$U = \cosh MX - \frac{\cosh M\left(\frac{L}{R}\right)}{\sinh M\left(\frac{L}{R}\right)} \sinh MX \tag{16}$$

The expression for pressure distribution is derived by substitution of equation 16 into equation 11 and solving for P

$$P = -\frac{\mu <u>(x=0) M}{2kPo}\left[\sinh MX - \frac{\cosh M\left(\frac{L}{R}\right)}{\sinh M\left(\frac{L}{R}\right)} \cosh MX\right] \tag{17}$$

The uniformity of the pressure drop along the length of the fiber can now be expressed by taking the ratio of $P(X=L/R)$ to $P(X=0)$

$$\frac{P\left(X=\frac{L}{R}\right)}{P(X=0)} = \cosh M\left(\frac{L}{R}\right) - \frac{\sinh^2 M\left(\frac{L}{R}\right)}{\cosh M\left(\frac{L}{R}\right)} \tag{18}$$

or, using the identity $\cosh^2 x - \sinh^2 x = 1$

$$\frac{P\left(X=\frac{L}{R}\right)}{P(X=0)} = \frac{1}{\cosh M\left(\frac{L}{R}\right)} \tag{19}$$

4.4.1.2 Case 2: Detaching Cells From the Lumen Surface of the Hollow Fiber with Pressure in the Shell

In this case, the inlet is closed ($<u> = 0$, at $x = 0$), there is a pressure in the shell *Po* which is constant and greater than $<p>$, and the outlet of the fiber is open to the atmosphere ($<p> = Patm$, at $x = L$). For this case, since ,$<u>(x=0) = 0$ we must redefine the dimensionless mean velocity as

$$U = \frac{<u>}{<u>(x=L)} \tag{20}$$

with this definition equation 11 becomes

$$\frac{dU}{dX} = -\frac{2kPo}{\mu <u>(x=L)} P \tag{21}$$

and equation 12 becomes

$$\frac{dP}{dX} = -\frac{8\mu <u>(x=L)}{PoR} U \tag{22}$$

and equation 13 becomes

$$\frac{d^2U}{dX^2} = -\frac{2kPo}{\mu <u>(x=L)} \frac{dP}{dX} \tag{23}$$

Equations 22 and 23 are combined and solved as before yielding an expression for *U* identical to equation 15. For this case the boundary conditions are as follows.

$$\langle u \rangle = 0 \text{ at } x = 0 \quad \text{thus} \quad U = 0 \text{ at } X = 0 \tag{BC 1}$$

$$\langle p \rangle = Patm \text{ at } x = L \quad \text{thus} \quad P = \frac{Patm - Po}{Po} \text{ at } X = \frac{L}{R} \tag{BC 2}$$

Applying boundary condition 1 to equation 15 yields $a = 0$, so that

$$U = b \sinh MX \tag{24}$$

Using equation 21 to derive an expression for P yields

$$P = -\frac{\mu \langle u \rangle (x=L) M}{2kPo} b \cosh MX \tag{25}$$

Applying boundary condition 2 to equation 25 yields

$$b = -\frac{(Patm - Po)2k}{\mu \langle u \rangle (x=L) M \cosh M\left(\frac{L}{R}\right)}$$

substituting into equation 25 gives

$$P = \frac{(Patm - Po)}{Po \cosh M\left(\frac{L}{R}\right)} \cosh MX \tag{26}$$

Taking the ratio of $P(X=0)/P(X=L/R)$ yields

$$\frac{P(X=0)}{P\left(X=\frac{L}{R}\right)} = \frac{1}{\cosh M\left(\frac{L}{R}\right)} \tag{27}$$

which is identical in value to the variation in pressure for case 1 given by equation 19.

4.4.1.3 Case 3: Washing or Detaching Cells on the Lumen Surface of Fiber Using Laminar Shear Flow in the Fiber with the Shell Closed

The uniformity of the shear stress applied to cells adsorbed to the lumen surface of

Type A and Type E during washing and shear elution is directly proportional to the uniformity of the mean axial velocity along the length of the fiber. During the washing and shear elution steps, the shell side is closed, and no permeate is removed from the module. Thus, the inlet and outlet mean axial velocities in the fiber must be equal. However, for sufficiently permeable fibers there may be a significant bypass flow of fluid through the shell. Near the inlet where the pressure in the fiber is highest, fluid will tend to flow from the fiber to the shell whose pressure will be lower. However, near the outlet where the pressure in the fiber is lowest, the flow of fluid will be in the opposite direction, from the shell to the fiber. We assume that the location of maximum deviation from the inlet and outlet mean velocities will be approximately in the center of the module at $x = L/2$. Since shell-side resistance to flow is assumed to be negligible compared to fiber resistance, the case of shell-side washing of cells bound to the outside of fibers is not considered.

Dimensionless variables for this case are defined as for case 1. The appropriate boundary conditions for the present case are the equality of mean velocity at the inlet and outlet of the fiber

$$\langle u \rangle = \langle u \rangle(x=0) \text{ at } x = 0 \quad \text{thus} \quad U = 1 \text{ at } X = 0 \qquad \text{(BC 1)}$$

$$\langle u \rangle = \langle u \rangle(x=0) \text{ at } x = L \quad \text{thus} \quad U = 1 \text{ at } X = \frac{L}{R} \qquad \text{(BC 2)}$$

Applying boundary conditions 1 and 2 to equation 15 yields $a = 1$ and

$$b = \frac{1 - \cosh M\left(\frac{L}{R}\right)}{\sinh M\left(\frac{L}{R}\right)}$$

yielding the following expression for U

$$U = \cosh MX + \left[\frac{1 - \cosh M\left(\frac{L}{R}\right)}{\sinh M\left(\frac{L}{R}\right)}\right] \sinh MX \tag{28}$$

The maximum change in mean axial velocity and shear stress is estimated as

$U(X=L/2R)/U(X=0)$

$$\frac{U\left(X=\frac{L}{2R}\right)}{U(X=0)} = \cosh M\left(\frac{L}{2R}\right) + \left[\frac{1 - \cosh M\left(\frac{L}{R}\right)}{\sinh M\left(\frac{L}{R}\right)}\right] \sinh M\left(\frac{L}{2R}\right) \tag{29}$$

4.4.2 Determination of Wall Shear Stress for Uniform Flow in Fibers and Shell

In this section we derive expressions for wall shear stress for flow through fibers or modules for the case where the fibers are essentially impermeable, in other words, for when the ratio for the maximum deviation in axial velocity given by equation 29 is close to one.

4.4.2.1 Uniform Flow in Fiber Lumen

Poiseuille's Law (equation 9) may be integrated from $x = 0$ to $x = L$ to yield

$$\langle u \rangle = \frac{\Delta p R^2}{8 \mu L} \tag{30}$$

where Δp is defined as $\langle p \rangle(x=0) - \langle p \rangle(x=L)$. Equation 30 can also be expressed in terms of the volumetric flowrate $Q = \pi R^2 \langle u \rangle$. The pressure drop along the fiber then becomes

$$\Delta p = \frac{8 \mu L Q}{\pi R^4} \tag{31}$$

The wall shear stress for laminar flow through a circular tube is (Bird et al, 1960)

$$\tau = \frac{\Delta p R}{2L} \tag{32}$$

which upon substitution of equation 31 becomes

$$\tau = \frac{4\mu Q}{\pi R^3} \tag{33}$$

The Reynolds number is given by

$$Re = \frac{2Q\rho}{\pi R\mu} \tag{34}$$

where ρ is the fluid density. The entrance length can be estimated by (Bird et al., 1960)

$$L_e = 0.07R \cdot Re \tag{35}$$

4.4.2.2 Uniform Flow in Module Shell

The detailed shear stress profile in the shell side will be complex due to the effects of the inlet and outlet geometry (see figure 4.1). In order to obtain a relative estimate with which to compare different conditions, we will simplify the flow field and consider uniform, laminar flow in an annular channel of length L, with inner radius (outside of fiber) $\dot{R}_1$ and outer surface R_2. The appropriate Navier-Stokes equation is

$$\frac{1}{r}\frac{d}{dr}\left(r\frac{du_x}{dr}\right) = \frac{1}{\mu}\frac{dp}{dx} \tag{36}$$

Integrating twice with respect to r yields

$$u_x = \frac{1}{2\mu}\frac{dp}{dx}\frac{r^2}{2} + a\ln(r) + b \tag{37}$$

The constants a and b can be determined by the following two boundary conditions:

BC 1: $u_x = 0$ at $r = R_1$, and BC 2: $u_x = 0$ at $r = R_2$ yielding

$$a = -\frac{1}{2\mu}\frac{dp}{dx}\frac{R_1^2 - R_2^2}{2\ln\left(\frac{R_1}{R_2}\right)}$$

$$b = \frac{1}{2\mu}\frac{dp}{dx}\frac{R_1^2 - R_2^2}{2\ln\left(\frac{R_1}{R_2}\right)}\ln(R_1) - \frac{1}{2\mu}\frac{dp}{dx}\frac{R_1^2}{2}$$

Substituting into equation 37 yields

$$u_x = -\frac{1}{2\mu}\frac{dp}{dx}\left[\frac{r^2 - R_1^2}{2} - \frac{R_1^2 - R_2^2}{2\ln\left(\frac{R_1}{R_2}\right)}\ln\left(\frac{r}{R_1}\right)\right] \tag{38}$$

An expression for shear stress in terms of the axial pressure drop can be determined with the following

$$\tau_{r,x} = -\mu\frac{du}{dr} \tag{39}$$

$$\frac{dp}{dx} = \frac{\Delta p}{L} \tag{40}$$

Applying equation 39 to equation 38 and substituting equation 40 yields

$$\tau_{r,x} = -\frac{R_2\Delta p}{2L}\left[\frac{\left(\frac{R_1^2}{R_2^2}\right) - 1}{2\ln\left(\frac{R_1}{R_2}\right)}\left(\frac{R_2}{r}\right) - \left(\frac{r}{R_2}\right)\right] \tag{41}$$

The radially averaged velocity $\langle u \rangle$ is defined as

$$\langle u \rangle = \frac{\int_0^{2\pi}\int_{R_1}^{R_2} u r dr d\theta}{\int_0^{2\pi}\int_{R_1}^{R_2} r dr d\theta} \tag{42}$$

Applying equation 42 to equation 38 yields

$$\langle u \rangle = -\frac{\Delta p R_2^2}{8\mu L}\lambda \tag{43}$$

where λ is defined as

$$\lambda = \left[\frac{\left(\frac{R_1}{R_2}\right)^2 - 1}{\ln\left(\frac{R_1}{R_2}\right)} - \left(\frac{R_1}{R_2}\right)^2 - 1\right] \tag{44}$$

The volumetric flowrate Q is given by

$$Q = \langle u \rangle \pi (R_2^2 - R_1^2) \tag{45}$$

Equations 43 - 45 can be used to solve for Δp in terms of the volumetric flowrate Q.

$$\Delta p = -\frac{8\mu L Q}{\pi R_2^2 (R_2^2 - R_1^2)\lambda} \tag{46}$$

Equation 46 can then be substituted into equation 41 to give an expression for the shear stress in terms of the volumetric flowrate. We are interested in the wall shear stress at the fiber surface where $r = R_1$ given by the following in terms of the volumetric flowrate

$$\tau_{R_1 x} = \frac{4Q\mu}{\pi R_2 (R_2^2 - R_1^2)\lambda}\left[\frac{\left(\frac{R_1}{R_2}\right)^2 - 1}{2\ln\left(\frac{R_1}{R_2}\right)}\left(\frac{R_2}{R_1}\right) - \left(\frac{R_1}{R_2}\right)\right] \tag{47}$$

where λ is defined by equation 44. The appropriate Reynolds number in this case is

$$Re = \frac{2\rho Q(R_2 - R_1)}{\pi \mu (R_2^2 - R_1^2)} \quad (48)$$

and an entrance length can be roughly estimated by equation 35 with $R = 1/2(R_2 - R_1)$.

4.5 Results

4.5.1 Characterization of the Non-Functionalized and Functionalized Membranes

4.5.1.1 Hollow fiber dimensions and structure

The inside diameter and outside diameters and total membrane volume of the fibers is given in table 4.1. Figure 4.4 shows SEM photomicrographs of the outside retentive surfaces of Type B fibers (A) , and Type C fibers (B). Figure 4.5 shows the inside retentive surfaces of Type E (A), and Type A (B). Figure 4.6 shows cross-sectional views of the fibers

Table 4.1 *Inner and Outer Diameters and Total Volume of Hollow-Fiber Membranes*

Fiber Type	Outer Diameter (μm)	Inner Diameter (μm)	Total Volume (mlmv/cm)
B	1016 ± 30	590 ± 21	0.0054 ± 0.0005
C	1020 ± 45	584 ± 38	0.0055 ± 0.0008
E	1545 ± 43	1006 ± 39	0.011 ± 0.001
A	1028 ± 26	592 ± 24	0.0055 ± 0.0005

from which cells were eluted by back-pressure. Figure 4.6 (A) shows a cross-sectional view of a Type B fiber photographed near the outer surface. SEM and TEM (see section 4.9 and chapter 3) cross-sections indicate that the fiber morphology is anisotropic, with a region of relatively low porosity penetrating approximately 0.5 - 4.0 μm below the outside surface. Figure 4.6 (B) shows a full cross-sectional view of a Type C fiber. Type C fibers have a similar morphology, except that the cross-sectional views show less anisotropy and the region

(A)

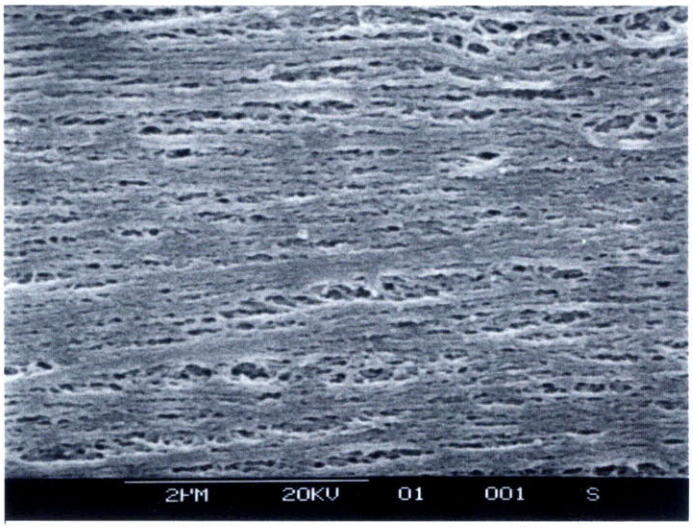

(B)

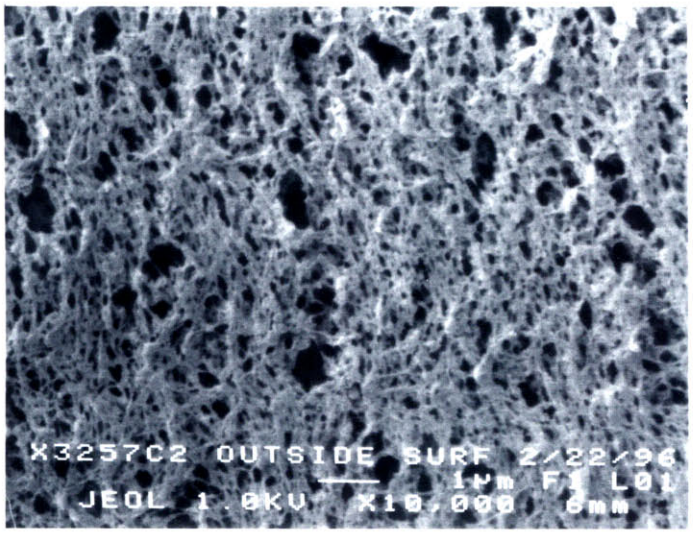

Figure 4.4 SEM photomicrographs of "outside skin" hollow-fiber membranes. (A) Type B, bar = 2 μm; (B) Type C, bar = 1 μm.

(A)

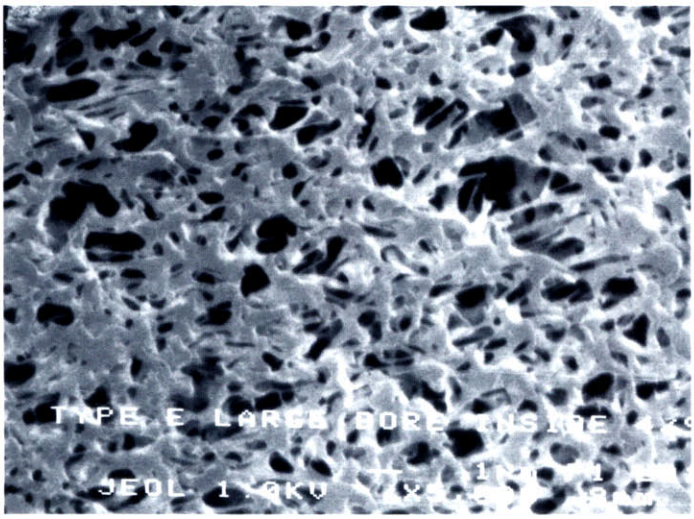

(B)

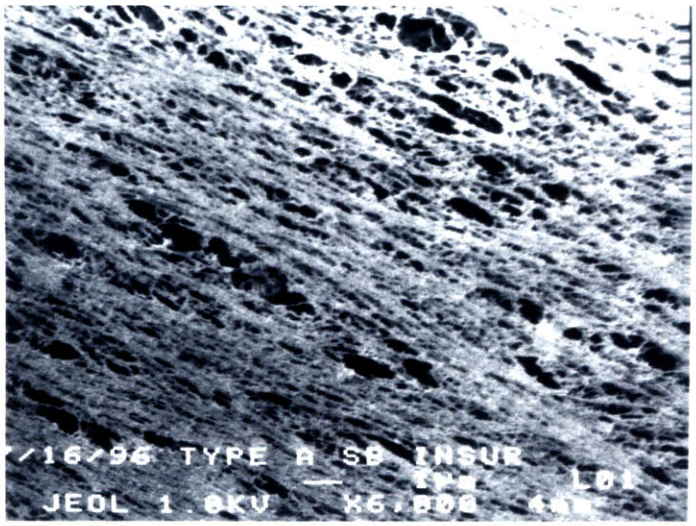

Figure 4.5 SEM photomicrographs of "inside skin" hollow-fiber membranes. (A) Type E, (B) Type A, bars = 1 μm.

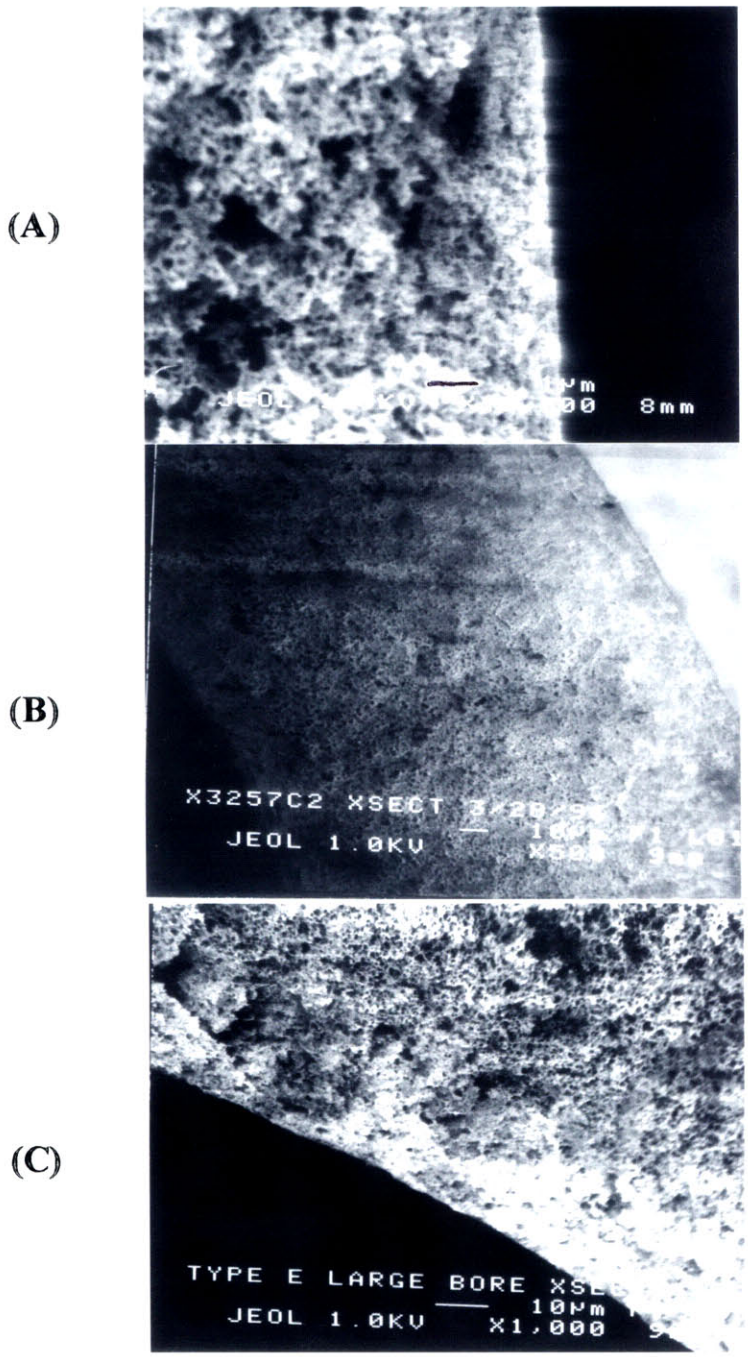

Figure 4.6 SEM photomicrographs of cross-sections of hollow-fiber membranes used in pressure elution studies. (A) Type B outer edge, bar = 1 μm; (B) Type C, bar = 10 μm; (C) Type E inner edge, bar = 10 μm.

of relatively lower porosity penetrates deeper below the outer retentive surface (about 5 to 15 μm). Figure 4.6 (C) shows a cross-sectional view of a Type E fiber photographed near the inner retentive surface. Type E fibers have a similar morphology as Type C membranes, with the region of relatively lower porosity penetrating below the inner retentive surface to a depth of about 3 to 12 μm). The physical properties of the membranes are summarized in table 4.2. Figures 4.4 and 4.5 show that the surface morphology and pore size and shape for the membranes was very heterogeneous. Type B (figure 4.4 (A)) and Type A (figure 4.5 (B)) membranes had long, narrow pores aligned axially along the fiber length. Type C (figure 4.4 (B)) and Type E (figure 4.5 (A)) had more randomly oriented and shaped pores. For all membranes, the pore structure and flow path of permeate appeared irregular and tortuous in dimension and direction. Total available surface area available for rpA immobilization was

Table 4.2 *Physical Properties of Hollow-Fiber Membranes*

Fiber Type	**Surface Area** (m^2/mlmv)	**Surface Pore Diameter Range** (μm)	**Hydraulic Permeability** (L/m^2hrmmHg)
B	3.8	0.01 - 0.26	0.27 ± 0.18 (n=9)
C	3.7	0.02 - 1.3	3.4 ± 0.1 (n=2)
E	3.8	0.14 - 2.1	3.7 ± 1.5 (n=3)
A	4.3	0.04 - 1.5	1.8 ± 0.4 (n=6)

similar for all membranes and ranged from 3.7 to 4.3 m^2/mlmv. Type B fibers had the smallest range of pore diameters of the membranes used (0.01 to 0.26 μm). Table 4.2 indicates that Type A and Type C fibers were similar in pore diameter range (although not in shape as previously discussed) with the largest pores observed having an effective diameter of 1.3 to 1.5 μm for Type C and Type A respectively. Type E fibers had the largest pores with

a pore diameter range of 0.14 to 2.1 μm. Hydraulic permeabilities of rpA-coated fibers shown in table 4.1 roughly correlate with surface pore sizes with Type B having the lowest permeability, Type E the highest, and Types C and A intermediate.

Flow porometry was also performed on Type B and Type C fibers as described in chapter 3 to characterize pore size distribution. The minimum pore diameter measurable with the porometer was 0.07 μm. For Type B fibers, porometer results indicated that fibers had a pore size range of 0.08 μm to 3 μm with a mean flow pore size (defined as the pore size giving the same pressure-flow behavior for a fiber with all pores of the same size) of 1.25 μm. However, only about 0.5% of the pores were larger than 1 μm, and about 50% of the pores were between 0.08 and 0.12 μm. This behavior is indicative of a fiber containing primarily very small pores with scattered defects of larger pore size. Type C fibers had a pore size range of 0.09 μm to 1 μm with a mean flow pore size of 0.2 μm.

4.5.1.2 Active FMP groups, rpA Ligand Immobilized, and Functional IgG Capacity

The surface chemical properties of the FMP-activated, rpA-coated hollow-fiber membranes are summarized in table 4.3.

Table 4.3 *FMP Surface Groups and rpA Ligand Density*

Fiber Type	FMP Surface Concentration (μmole/mlmv)	rpA Immobilized (mg/mlmv)	rpA Ligand Density (molec./cm^2 × 10^{-12})
B	20 ± 1 (n=3)	7.7 ± 0.6 (n=2)	2.7 ± 0.2 (n=2)
C	33	9.1 ± 0.9 (n=2)	3.3 ± 0.3 (n=2)
E	30	7.2 ± 0.7 (n=2)	2.5 ± 0.2 (n=2)
A	42	8.8	2.8

Table 4.3 shows that the surface chemical properties were similar for the ligand-coated functionalized membranes. The amount of rpA immobilized ranged from about 7 to 9 mg/mlmv representing a surface ligand density of approximately 3×10^{12} molecules/cm^2 and a mean distance between molecules of about 60 Å. The functional IgG capacities of the ligand-coated hollow-fibers are summarized in table 4.4.

Table 4.4 *IgG Adsorption Capacity of Functionalized Membranes.*

	IgG Capacity (mg/mlmv)		
Fiber Type	Human	Mouse IgG2b	BSA
B	21 ± 2 (n=4)	8.0	1.1 ± 0.5 (n=4)
C	25.9 ± 0.5 (n=3)	8.5	0.7 ± 0.8 (n=3)
E	25.5 ± 0.5 (n=2)	8.9	0.6 ± 0.2 (n=2)
A	36	n.d.	0.9

Specific adsorption of human IgG ranged from a low of 21 to a high of 36 mg/mlmv (for Type B and Type A fibers, respectively). Binding capacities of mouse monoclonal IgG2b was about one third that for human IgG for all membranes tested, and non-specific binding, as assessed with IgG-free BSA, was below 1.1 mg/mlmv. The effect of brief exposure of rpA-coated hollow-fibers to elevated temperatures on adsorption capacity of human IgG is shown in table 4.5.

Table 4.5 *Effect of Temperature Exposure on IgG Adsorption Capacity of Functionalized Membranes.*

Temperature (°C)	Human IgG Capacity (mg/mlmv)
23	36
57	32
92	35

Table 4.5 shows that the activity of the immobilized rpA groups was stable over the temperature range tested.

4.5.2 Flows and Pressures in Hollow-Fiber Modules

Table 4.6 presents the results of the analysis for the determination of the uniformity of the pressure during cell loading and detachment, and for the uniformity in the fluid mean velocity, and thus shear stress, during washing and shear elution. The permeability k was calculated using a fluid viscosity equal to that of water at 25 °C (0.9 cp), and was based on the surface area of the lumen. The maximum pressure drop deviation along the fiber was calculated using equation 19 or 27, and the maximum mean velocity deviation was determined with equation 29. Fiber length was taken as 5 cm.

Table 4.6 *Uniformity of Pressure Drop and Mean Axial Flow in Hollow-Fibers*

Fiber Type	$k \times 10^{12}$ (m)	$M \times 10^{4}$	L/R	$\Delta p_{min}/\Delta p_{max}$	$\langle u \rangle_{min}/\langle u \rangle_{max}$
B	0.83	2.10	167	0.9994	0.9998
C	10.8	7.59	167	0.9920	0.9980
E	6.9	4.70	100	0.9989	0.9997
A	3.3	4.22	167	0.9975	0.9994

The results of the analysis presented in table 4.6 indicate the maximum deviation in pressure

drop between the lumen of the fiber and the shell during cell loading and detachment, and the maximum deviation in mean axial velocity and shear stress is less than 1 % in all cases. Therefore, for the purposes of calculating the force on cells due to the transmembrane pressure drop, the transmembrane pressure drop may be assumed to be constant along the length of the fiber. Also, for calculating wall shear stresses and axial pressure drops due to axial flow in the fibers during washing and shear elution, the effect of the fiber permeability may be safely ignored.

In contrast, when cells are loaded onto the lumen surface of Type E or Type A fibers by dead-ended filtration, or are removed from the lumen surface by an applied transmembrane pressure drop, an axial flow, due to permeation of fluid through the fiber wall, will be induced in the fiber which will vary from zero at closed end of the fiber lumen to a maximum value at the open end of the fiber. In these cases, the wall shear stress, which is proportional to the axial flowrate, will vary in an approximately linear fashion along the length of the fiber from zero to a maximum value given by equation 33 for a given pump flowrate Q. In our experiments, for the loading of cells onto lumen retentive fibers, the maximum induced shear stress was a small fraction of the shear stresses induced during washing or shear stress elution. The particular values of the maximum flows and shear stresses induced by permeation are given in the description of each experiment.

4.5.3 Cell Binding and Detachment Experiments

Cell binding and detachment experiments were designed to determine the recoverability of target and non-target cells attached to hollow-fiber membranes after loading by filtration. Specifically, we attempted to define removal conditions where target cells could be separated from non-target cells based on their respective attachment strengths to the fibers. First, we designed experiments to determine a reasonable flowrate and shear stress for

recovering non-target cells from modules. In subsequent experiments, this level of shear stress was the minimum level used for washing the fiber surface to remove non-specifically, or loosely, attached cells before elution of cells more firmly attached to the fiber was performed using increased levels of shear stress or back-filtration. For each experiment, total cell recovery, as a percentage of the total number of cells initially injected into the module or fiber, was determined for each step, and, in addition, total cell recovery during elution steps, after washing to remove loosely attached cells, was determined as a percentage of the number of cells which the fiber was theoretically capable of binding as determined by available surface area. Our strategy was to load enough cells to ensure that at least a monolayer had been filtered onto the surface. In order to accomplish this objective, enough time was allowed during loading to bring about 2-3 monolayers of cells to the fiber surface.

4.5.3.1 Shell-Side Cell Number Balance Experiments

The results from shell-side cell balance experiments are shown in figure 4.7. In these experiments, cells were injected into the shell side of a module with a solid wire in place of a hollow-fiber, allowed to stand for 5 min, and then flushed out with DPBS. The purpose of the experiments was to determine reasonable washing conditions for recovery of non-specifically adsorbed cells. The results in figure 4.7 are expressed as the percentage of cells initially injected into the module which were recovered in each collected fraction. Also shown is the cumulative percent recovered versus fraction collected. The fraction denoted as inlet flush, contains the cells in the excess cell suspension not completely injected into the module which were recovered by flushing the cell injection port on stopcock 1 with wash buffer (see figure 4.2 (A)). The number of cells initially injected into the modules ranged from 4.9 to 6.6 $\times$ 10^6. Figure 4.7 (A) shows cell balance results for experiments with HL-60 and Namalwa cells for a wash flowrate of 8.6 ml/min. This flowrate yields a calculated wall

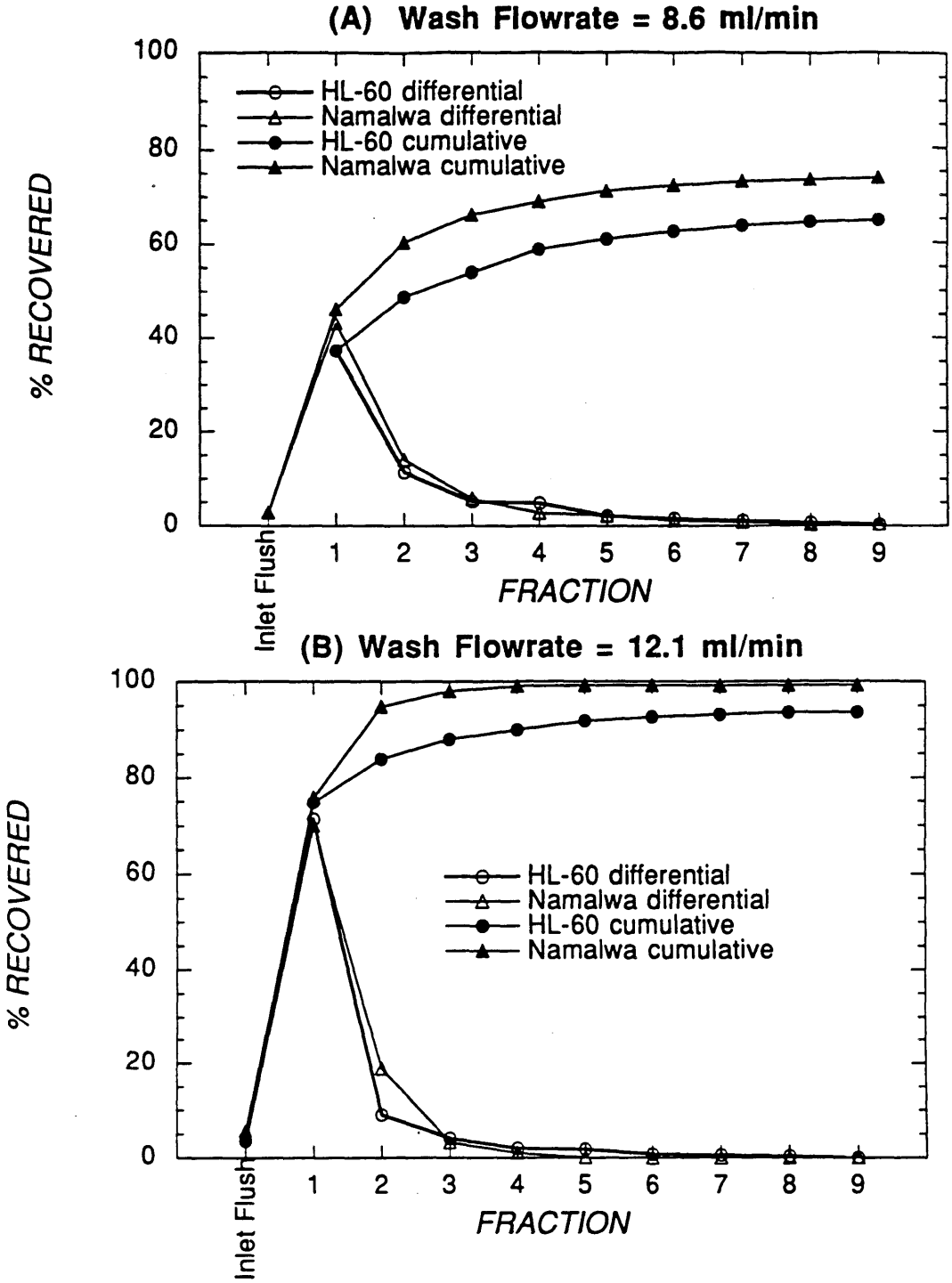

Figure 4.7 Results of shell-side cell number balance experiments for wash flowrates of 8.6 ml/min (A) and 12.1 ml/min (B). Cells recovered in each fraction are plotted as a percentage of the total cells injected into the module. Circles indicate data for HL-60, and triangles Namalwa. Open symbols show the percentage recovered in each fraction (differential), and solid symbols show the cumulative recovery. Each point represents the average of duplicate cell counts.

shear stress at the inner surface (R_1) of 0.3 dynes/cm^2, a pressure drop through the module of 0.007 mmHg, a Reynolds number of 33.5, and an entrance length of 2.3 mm, which is about 6 % of the total flow path length. Each fraction collected had a volume of about 2 ml representing a wash time of about 10 sec per fraction for 12.1 ml/min wash flowrates and about 14 sec per fraction for 8.6 ml/min flowrates. The results indicate that only 65 % of injected HL-60 cells and 74 % of Namalwa cells were recovered. Nearly all of the cells which were recovered were recovered in fractions 1 to 5. Figure 4.7 (B) shows equivalent results for a wash flowrate of 12.1 ml/min. This flowrate yields a calculated wall shear stress at the inner surface of 0.45 dynes/cm^2, a pressure drop through the module of 0.010 mmHg, a Reynolds number of 47, and an entrance length of 3.3 mm, which represents about 8 % of the total flow path. In this case, 94 % of the HL-60 cells were recovered, and over 99 % of the Namalwa cells. Again nearly all of the cells were collected in the first five fractions. Based on these results, for subsequent experiments with hollow fibers, wash shear stress prior to elution was at least 0.45 dynes/cm^2, and at least five fractions, of similar or longer duration, were collected during the wash step.

4.5.3.2 Cell Adsorption and Elution Experiments Using Type B and Type C Outside Retentive Surface Fibers

The results from cell adsorption and elution experiments using outside "skinned" Type B hollow-fiber modules are shown in figures 4.8 and 4.9. For figure 4.8 (A) and figure 4.9 (A), the results are expressed in an identical format as that used previously in figure 4.7 for shell-side cell number balance experiments. However, because the surface area of the fiber available for binding cells is small compared to the total shell volume, only a relatively small fraction of the cells injected into the module can be loaded by filtration onto the fiber in a monolayer (about 10 to 20 %), and, therefore, we have also presented the data for the elution

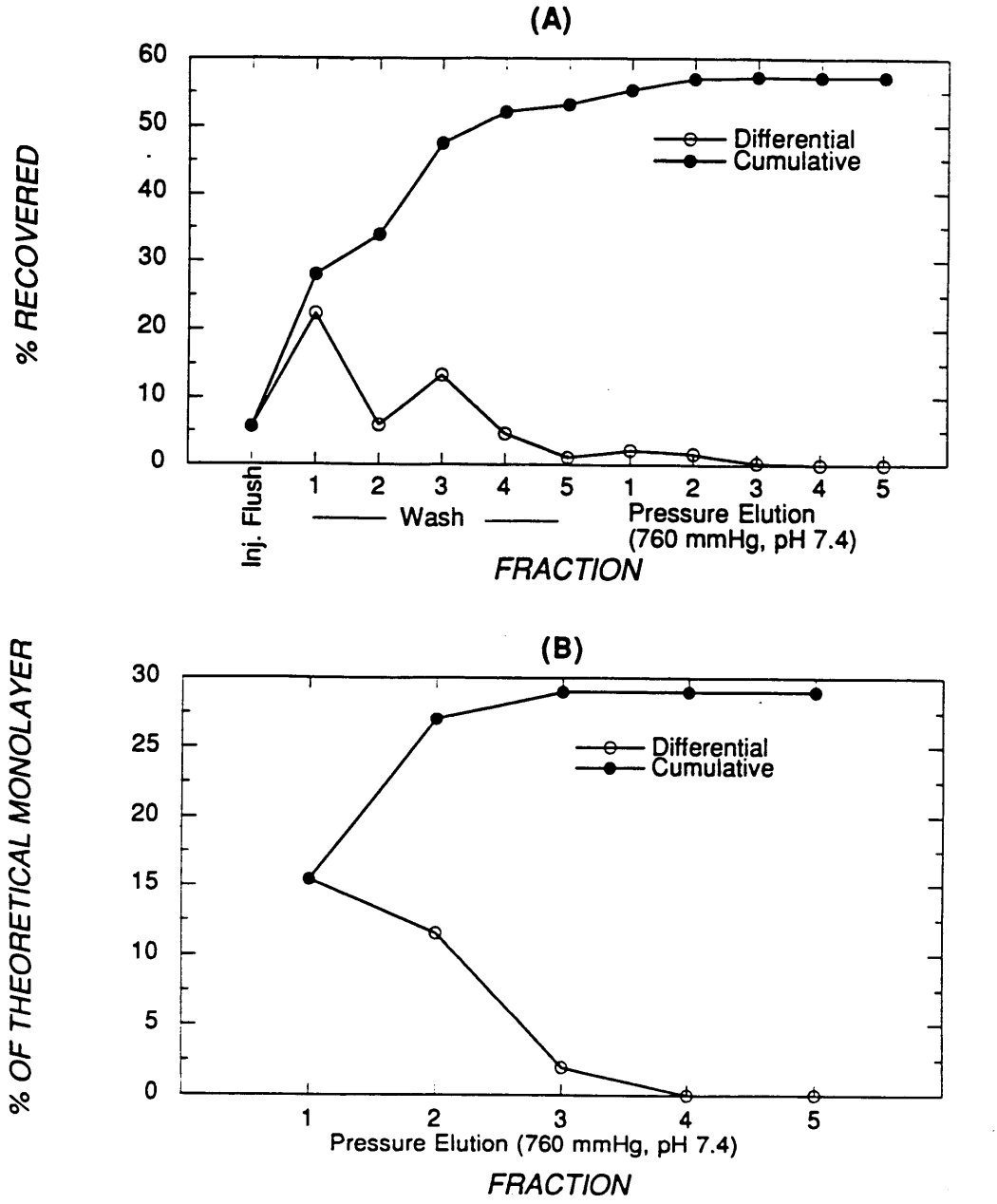

Figure 4.8 Cell attachment/detachment results using Type B hollow fiber with HL-60 cells pre-incubated with a 1:500 dilution of anti-CD33 ascites loaded onto the outside surface of the fiber via shell to lumen filtration at about 260 mmHg. Wash flowrate pumped through the shell-side was 12.1 ml/min during wash step and 4.4 ml/min during pressure elution. Cells were eluted with DPBS (pH 7.4) filtered from lumen to shell at a back-pressure of 760 mmHg. (A) Cells recovered in each fraction as a percentage of the total cells injected into the module. Open symbols show the percentage recovered in each fraction (differential), and solid symbols show the cumulative recovery. (B) Replot of cells recovered in elution fractions as percentage of a calculated theoretical monolayer of cells loaded onto the hollow-fiber surface. See text for details of calculation. Each point represents the average of duplicate cell counts.

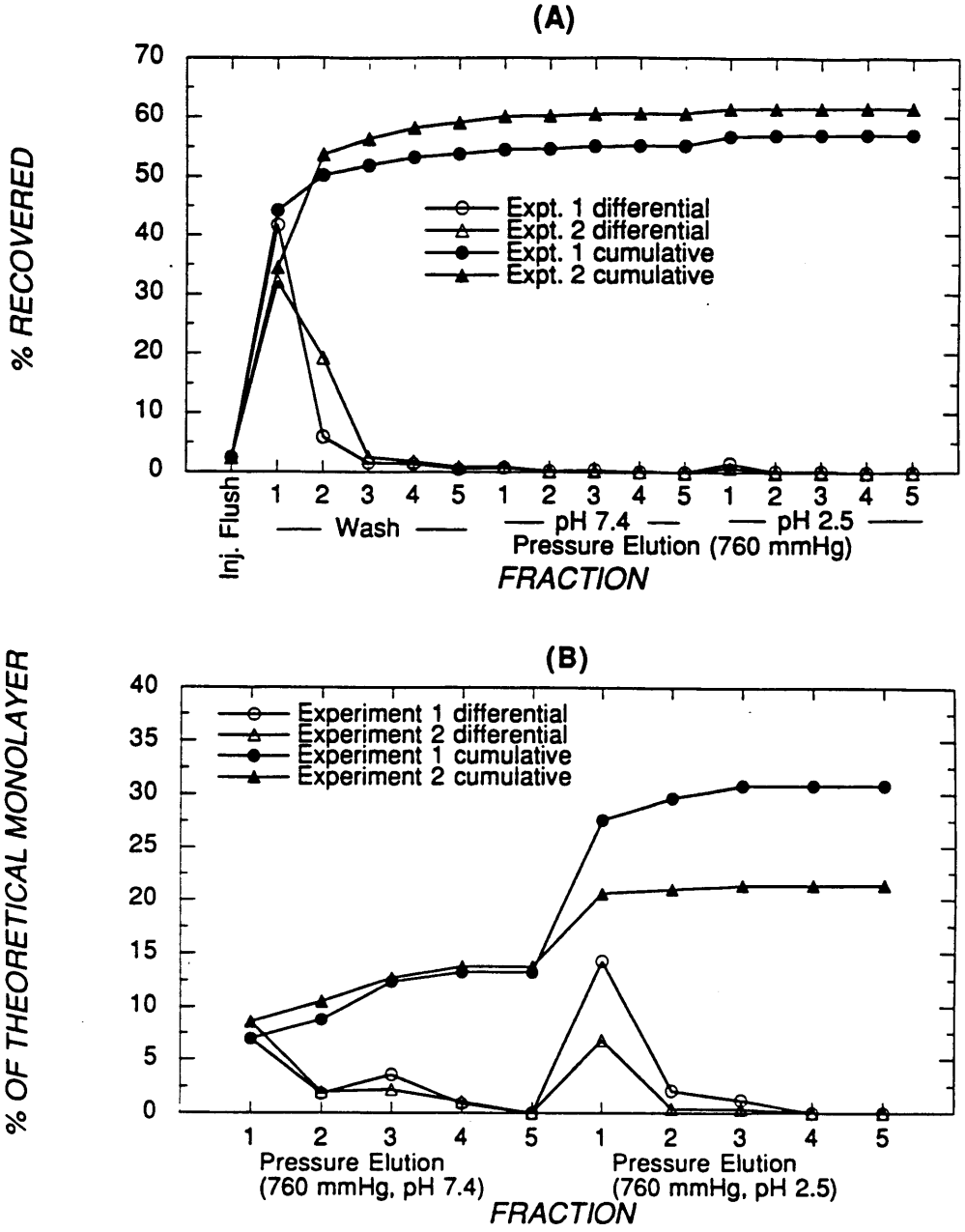

Figure 4.9 Cell attachment/detachment results using Type B hollow fibers with HL-60 cells, pre-incubated with a 1:500 dilution of anti-CD33 ascites. Loading and wash steps were as described in figure 4.8 caption. Cells were eluted first with DPBS (pH 7.4), then with 10 mM glycine-saline (pH 2.5) filtered from lumen to shell at a back-pressure of 760 mmHg. (A) Cells recovered in each fraction as a percentage of the total cells injected into the module for two equivalent experiments. (B) Cells recovered in elution fractions as percentage of a calculated theoretical monolayer of cells loaded onto the hollow-fiber surface. Each point represents the average of duplicate cell counts.

profiles during pressure elution (fractions collected after the washing steps) in the form of cells recovered in each fraction as a percentage of one theoretical monolayer of cells on the active fiber surface (figure 4.8 (B) and figure 4.9 (B)). The number of cells in a theoretical monolayer was estimated as follows. Cells attached to the membrane were assumed to have an average diameter of 12 μm (see morphometric analysis in section 4.9). Cells in a monolayer were assumed to be in contact with each other and arranged in a square array. For such a configuration, the packing efficiency, or the surface area of the cells divided by the surface area of the fiber, will be equal to the ratio of a circle of diameter d, divided by a square of side length d. This ratio is equal to $\pi/4 \approx 0.785$. So, the number of cells in a theoretical monolayer was determined by multiplying the active surface area of the fiber by $\pi/4$ and dividing by the area of a circle of 12 μm diameter ($\pi DL/(144 \times 10^{-12})$) where D and L are the hollow-fiber diameter and length in meters respectively.

Figure 4.8 shows results for a module containing a Type B fiber, onto which anti-CD33-pre-incubated HL-60 cells (Target cells) were loaded by filtration and eluted by reverse filtration of a neutral pH buffer (DPBS, pH 7.4). The total number of cells initially injected into the shell side of the module was 4.8×10^{6} in about 1.3 ml of solution. The number of cells per theoretical monolayer for this fiber was about 6.8×10^{5} cells, or about 14 % of the total cells in the module. Cells were loaded onto the fiber by filtration from the shell to the lumen (at about 260 mmHg) until about 0.5 ml of permeate was collected (about 15 min loading time) ensuring that about 1.8×10^{6} cells representing about 2.7 theoretical monolayers had been brought to the surface. Excess cells were washed from the module with a buffer flowrate of 12.1 ml/min (wall shear stress at the inner surface of 0.45 dynes/cm^2) and collected in the wash fractions. Cells on the fiber were eluted at a back-pressure of 760 mmHg. During the elution, cells were flushed from the shell with a supplemental shell-side

wash of 4.4 ml/min. The maximum flowrate in the shell during elution (supplemental wash plus permeate was about 5 ml/min). Figure 4.8 (A) indicates that the vast majority of the cells which are removed from the module are removed during the first 4 wash steps. There was a small increase in the number of cells collected at the onset of pressure elution (fractions 1 and 2). The total number of cells collected was only about 57 % of those initially injected into the module. This indicates that about 2.1×10^{6} cells were unaccounted for. Since this number is greater than a theoretical monolayer, some cells could have been attached to other surfaces such as the tubing or shell, been lysed or destroyed during the loading or detachment process, been lost during the collection process, or alternatively, could have been attached to the fiber in multiple layers. The exact location or fate of the missing cells is unknown. Figure 4.8 (B) shows that the total number of cells collected during pressure elution represented about 30 % of a theoretical monolayer. Viability of cells collected in wash fractions, determined by Trypan Blue dye exclusion, was 96 %, and in eluted fractions was 97 %. Direct observation of the cells along the edges of the fiber with an inverted microscope suggested that the fiber was still densely coated with cells even after the elution steps; however, because of optical distortion due to the glass module, the image quality was poor and coverage was difficult to determine with certainty.

Figure 4.9 (A) and (B) presents results for two additional experiments with Type B fiber modules and HL-60 target cells. Experimental conditions were similar to the experiment just described, except that an additional elution step was performed using back-filtration at 760 mmHg of 10 mM glycine-saline (pH 2.5) with a 4.4 ml/min supplemental shell-side wash. The results of both experiments were very similar. As before, figure 4.9 (A) indicates that only about 60 % of the cells initially injected into the module were recovered during the experiment. Unlike the previous result, however, for these experiments there was no increase

in the number of cells collected at the onset of pressure elution at neutral pH, but there was a small increase at the onset of the low pH elution. This is more clearly indicated in figure 4.9 (B) which shows that about 12 % of a theoretical monolayer of cells were collected during the entire neutral pH elution, which increases abruptly to 20 % (experiment 1) or 30 % (experiment 2) at the onset of low pH elution. Viability of cells collected in wash fractions was 94 % (experiment 1) and 99 % (experiment 2), in neutral pH eluted fractions was 100 % (experiment 1) and 94 % (experiment 2), and in low pH eluted fractions was 82 % (experiment 1) and 90 % (experiment 2). As before, direct observation of the cells along the edges of the fibers with an inverted microscope suggested that the fibers were still densely coated with cells even after the elution steps; however, because of optical distortion due to the glass module, the image quality was poor and coverage was difficult to determine with quantitative certainty.

Figure 4.10 (A) and (B) presents equivalent results for experiments performed with Type C fibers which had a hydraulic permeability over 10 times greater than Type B fibers. In addition, for one of the experiments, non-specific adsorption behavior was analyzed by using non-target HL-60 cells which had not been pre-incubated with anti-CD33. Experimental conditions were similar to those described previously except that the pressure during cell loading was only about 20 mmHg and the loading time was about 5 min. Wash flowrates before elution and supplemental wash flow rates during elutions were the same, but since the fiber was much more permeable, the maximum combined permeate/supplemental wash flow in the shell during elutions was about 9.5 ml/min versus 5 ml/min for Type B experiments. Figure 4.10 indicates that the results for target cells were very similar to those for Type B fibers. Only about 70 % of the total cells initially injected into the module were recovered leaving almost 2×10^6 cells (about 2.8 theoretical monolayers) unaccounted for.

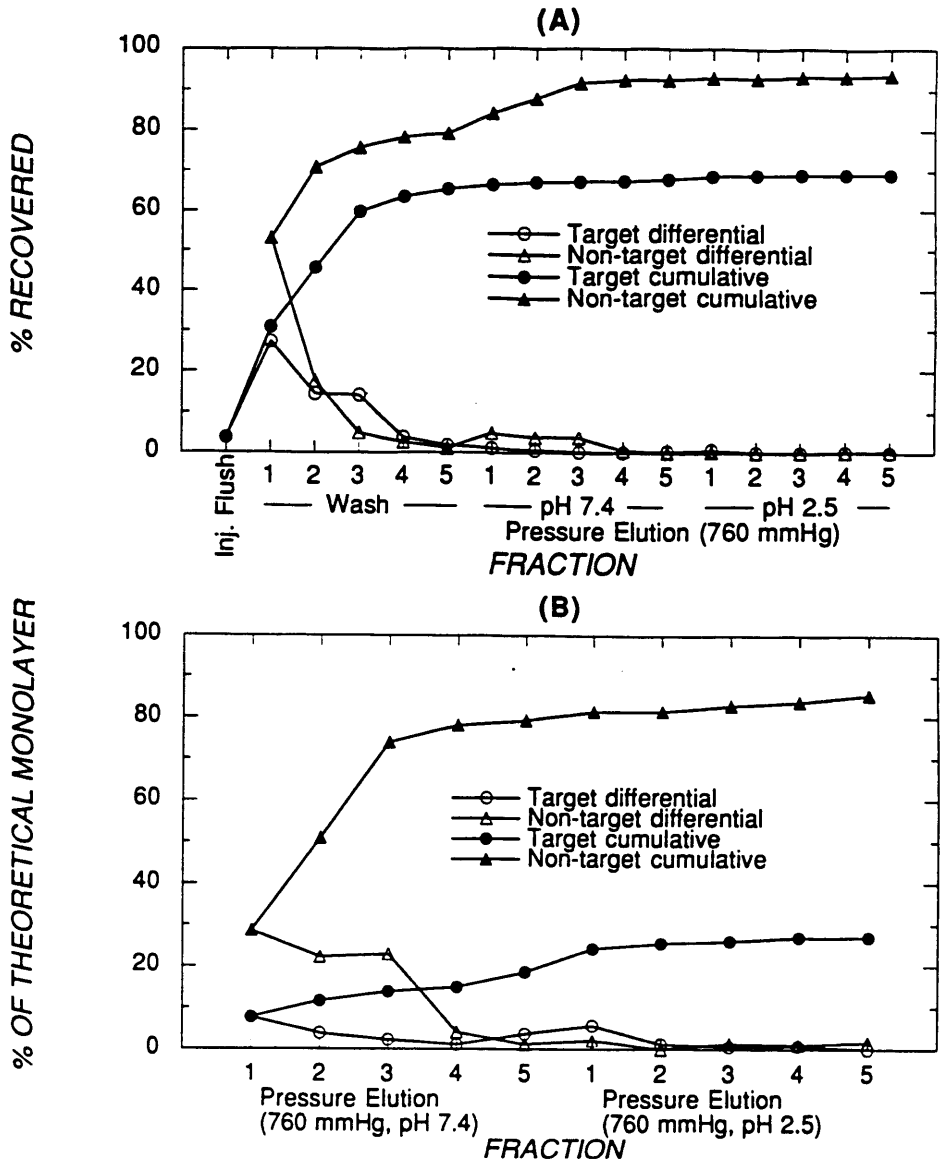

Figure 4.10 Cell attachment/detachment results using Type C hollow fibers with HL-60 cells loaded onto the outside surface of the fiber via shell to lumen filtration at about 20 mmHg. One experiment was performed with cells which were pre-incubated with a 1:500 dilution of anti-CD33 ascites (Target), while the other experiment was designed as a non-specific adsorption control using HL-60 which had not been pre-incubated with anti-CD33. (A) Cells recovered in each fraction as a percentage of the total cells injected into the module. (B) Cells recovered in elution fractions as a percentage of a calculated theoretical monolayer of cells loaded onto the hollow-fiber surface. Each point represents the average of duplicate cell counts.

Nearly all of the target cells recovered were recovered in the wash steps, with only a very slight increase in cells collected upon commencement of low pH elution and no increase observed with neutral pH elution. The total target cells collected during both elutions was less than 30 % of a theoretical monolayer. By contrast the behavior of non-target cells was quite different. Almost 94 % of the cells initially injected into the module were recovered leaving only about 3×10^5 (less than half a theoretical monolayer) unaccounted for. Also, a significant portion (about 15 % of the total injected) were collected during the first three fractions of the neutral pH back-pressure elution, but few additional cells were collected upon switching to low pH. The total eluted fractions of non-target cells amounted to about 86 % of a theoretical monolayer. This result suggests that the non-target cells are more easily removed, but that they may have sufficient affinity or mechanical attachment to the fiber to resist a wash flow which was previously shown to be effective in removing cells from the module. Viability of cells collected in wash fractions was 92 % and 91 %, in neutral pH elution fractions was 69 % and 90 %, and in low pH elution fractions was 84 % and 100 %, for target and non-target cells, respectively. Direct observation of the cells along the edges of the fibers with an inverted microscope suggested that the fiber loaded with target cells was still densely coated with cells even after the elution steps; however, the fiber loaded with non-target cells had very few cells attached to one edge of the two observed, while the other edge had several regions of dense cell coverage. Again, because of optical distortion due to the glass module, the image quality was poor and coverage was difficult to determine with quantitative certainty.

4.5.3.3 Cell Adsorption and Elution Experiments Using Type E Lumen Retentive Surface Fibers

Figure 4.11 (A) and (B) presents adsorption and elution results for experiments

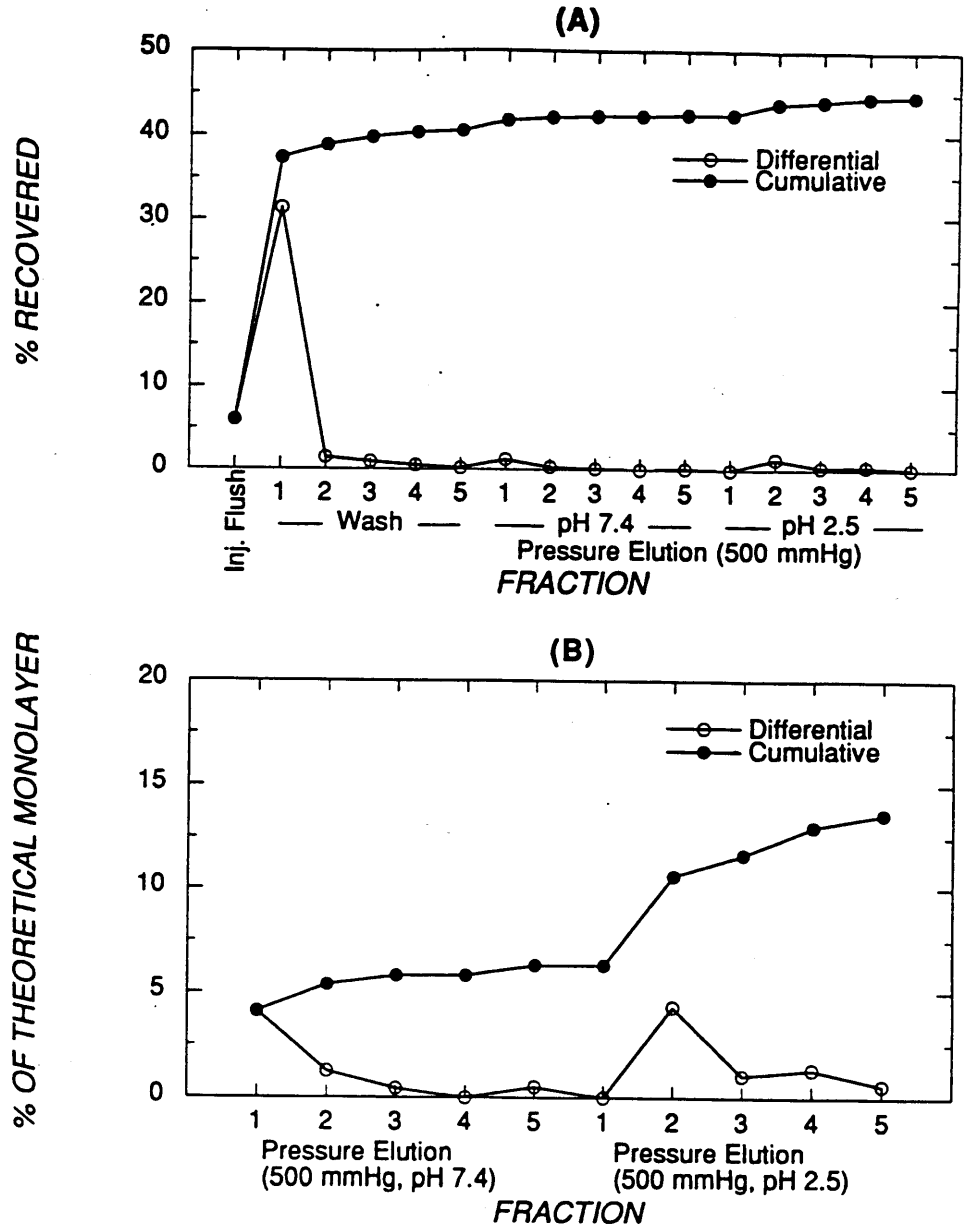

Figure 4.11 Cell attachment/detachment results using Type E hollow fibers with HL-60 cells, pre-incubated with a 1:500 dilution of anti-CD33 ascites, loaded onto the lumen surface of the fiber via lumen to shell filtration at about 15 mmHg. Flowrate in lumen was 0.8 ml/min during wash step and during pressure elutions the maximum induced permeate flow was 1.5 ml/min. Cells were eluted first with DPBS (pH 7.4), then with 10 mM glycine-saline (pH 2.5) filtered from shell to lumen at a back-pressure of 500 mmHg. (A) Cells recovered in each fraction as a percentage of the total cells injected into the fiber. (B) Cells recovered in elution fractions as a percentage of a calculated theoretical monolayer of cells loaded onto the hollow-fiber surface. Each point represents the average of duplicate cell counts.

performed with Type E fibers which had a hydraulic permeability similar to Type C fibers, but whose retentive surface is the lumen, or inside, surface. For experiments with these fibers, cells were loaded onto the inside fiber surface using the apparatus shown in figure 4.2 (B) via filtration from the lumen to the shell. HL-60 target cells pre-incubated with a 1:500 dilution of anti-CD33 were used in the experiment shown in figure 4.11. Experimental conditions were as follows. Cells were injected into the lumen side of the apparatus and loaded onto the fiber at a load flowrate of about 0.15 ml/min yielding a maximum shear stress exposure of cells during loading of about 0.25 dynes/cm^2; the pressure during cell loading was about 15 mmHg and the loading time to filter 2.5 × 10^6 onto the surface (about 3 theoretical monolayers) was about 10 min. Unloaded cells remaining behind in stopcocks 3 and 4 in figure 4.2 were flushed out with buffer and collected into an "injection flush" fraction before fiber washing. The wash flowrate before elution was 0.8 ml/min yielding a maximum shear stress of about 1.3 dynes/cm^2 with a Reynolds number of 18, an entrance length of 0.6 mm, and a pressure drop from one end of the fiber to the other of 0.14 mmHg. Elution was performed using two stages of back-pressure generated by filtration from the module shell to the fiber lumen. The back-pressure generated during each stage was 500 mmHg which induced a maximum permeate flow in the fiber of about 1.5 ml/min yielding a maximum shear stress at the fiber outlet of about 2.5 dynes/cm^2 . The first stage of elution used DPBS (pH 7.4) while the second stage used 10 mM glycine-saline (pH 2.5) as with the previous experiments described. Figure 4.11 indicates that the results for this experiment with HL-60 target cells was similar to that for Type B and C fibers. Only about 45 % of the total cells initially injected were recovered leaving almost 1.4 × 10^6 cells (about 1.8 theoretical monolayers) unaccounted for. Nearly all of the target cells recovered were recovered in the wash steps, with only a small increase in cells collected upon commencement of neutral pH

elution and low pH elution. The total number of target cells collected during both elutions was less than 15 % of a theoretical monolayer which was about 8×10^5 cells for Type E fibers. Viability of cells collected in wash fractions was 93 % , and in neutral pH elution fractions was 78 %. The viability of cells collected during low pH elution was not determined for this experiment.

Figure 4.12 (A) and (B) presents equivalent results for experiments performed with Type E fibers using HL-60 cells pre-treated in a fashion designed to reduce specific affinity for the fiber surface. Target cells for the experiments shown in figure 4.12 were pre-incubated with a 1:50,000 dilution of anti-CD33 instead of the 1:500 dilution previously used. In addition, non-specific adsorption behavior was analyzed by using non-target HL-60 cells which had not been pre-incubated with anti-CD33. Experimental conditions were similar to those described for the previous experiment with Type E fibers, except that the flowrate during loading was about 0.2 ml/min (maximum shear stress 0.16 dynes/cm^2 at each end) creating a transmembrane pressure drop during cell loading of about 20 mmHg for target cells and about 60 mmHg for non-target cells. The average loading time to filter about 2×10^6 cells onto the fibers was 4.2 min. Wash flowrates were the same as in the previous experiment. Because these fibers were less permeable than the Type E fiber used for the previous experiment, the maximum permeate flowrate induced in the lumen during elutions was about 0.85 ml/min versus 1.5 ml/min for the previous experiment (1.4 versus 2.5 dynes/cm^2 maximum shear stress).

Figure 4.12 indicates that the results for target cells incubated with a hundred-fold lower specific antibody concentration (circular symbols) were similar to those for the previous experiment using target cells and a Type E fiber. In this case, a somewhat higher fraction, about 60 % of the total cells initially injected were recovered (versus 45 % for the previous

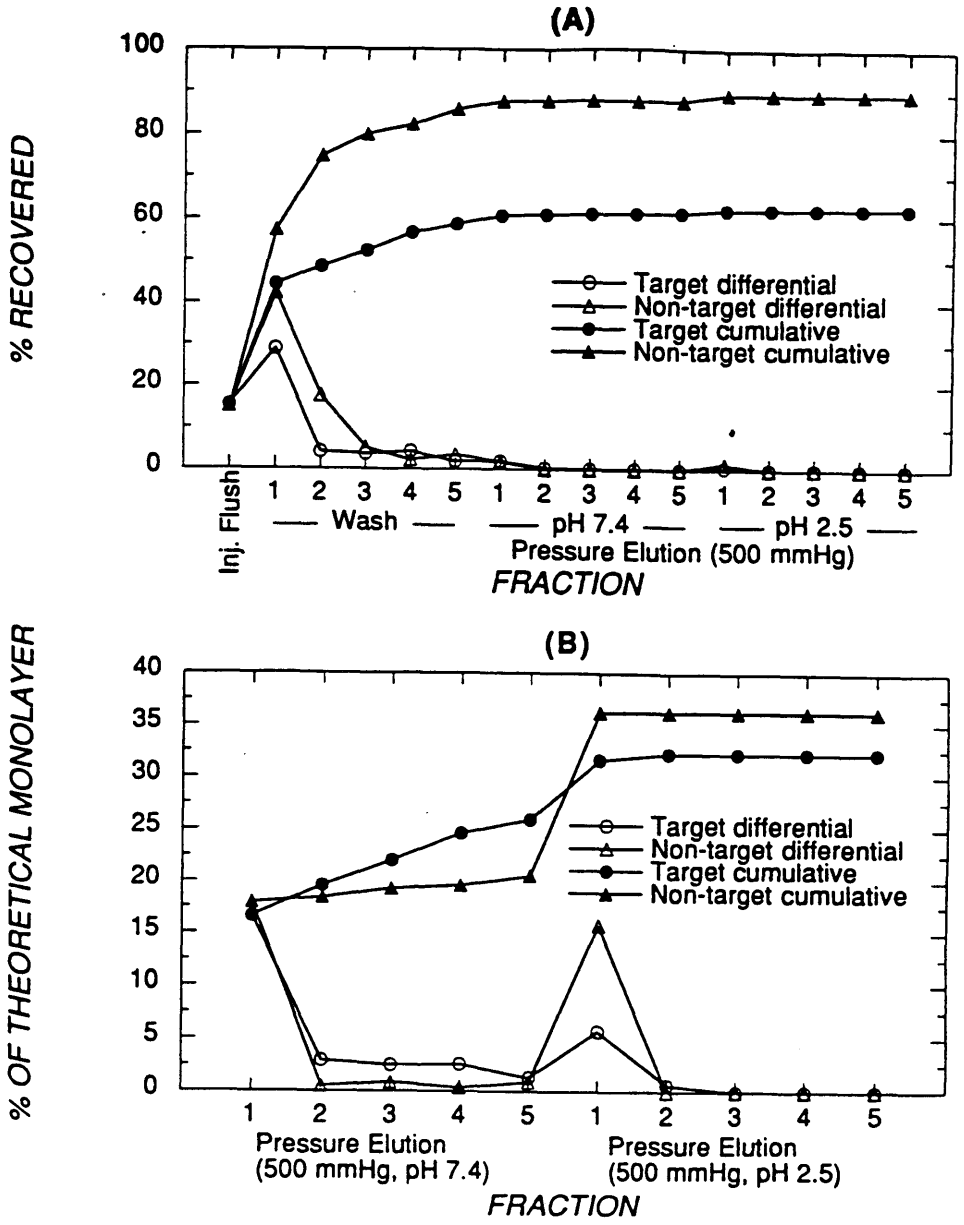

Figure 4.12 Cell attachment/detachment results using Type E hollow fibers with HL-60 cells loaded onto the lumen surface of the fiber via lumen to shell filtration. Maximum flowrate in lumen was 0.8 ml/min during wash step and pressure elutions. One experiment was performed with cells which were pre-incubated with a 1:50, 000 dilution of anti-CD33 ascites (Target), while the other experiment was designed as a non-specific adsorption control using HL-60 which had not been pre-incubated with anti-CD33. (A) Cells recovered in each fraction as a percentage of the total cells injected into the fiber. (B) Cells recovered in elution fractions as a percentage of a calculated theoretical monolayer of cells loaded onto the hollow-fiber surface. Each point represents the average of duplicate cell counts.

case) still leaving more than a theoretical monolayer of cells unaccounted for. Nearly all of the target cells recovered were recovered in the wash steps, with only a slight increase in cells collected upon commencement of neutral and low pH elution. The total target cells collected during both elutions was 32 % of a theoretical monolayer, more than twice that collected for the previous Type E experiment. As before with Type C fibers, the behavior of non-target cells was different. Almost 90 % of the cells initially injected were recovered leaving about 7 $\times 10^5$ (less than a theoretical monolayer) unaccounted for. Unlike the results with Type C fibers and non-target cells, nearly all of the cells were collected during the washes, with less than 2 % of the total collected being in the elution fractions. It should be kept in mind, however, that the shear stress during the wash step was about a factor of three higher for experiments with Type E fibers compared to Type C or Type B fiber experiments. Also dissimilar was the increase in the number of non-target cells eluted upon commencement of low pH elution (compare figures 4.12 (B) and 4.10 (B)). This result may be due to substantially increased exposure of the cells in the fiber to low pH for Type E fibers. Unlike experiments with Type B and C fibers where a neutralizing buffer flow was established in the shell during low pH elution, for Type E fibers, cells in the lumen were completely immersed in the low pH buffer until they reached the fraction collector. The total number of non-target cells in the eluted fractions amounted to only about 36 % of a theoretical monolayer versus 86 % of a theoretical monolayer for Type C fiber with non-target cells. These results again suggest that the non-target cells were more easily removed than target cells and that missing target cells are more likely to be remaining attached to the fiber, or destroyed by detachment due to their greater affinity for the surface, than remaining non-specifically attached to tubing or the module. Viability of cells collected in wash fractions was 87 % and 99 %, in neutral pH elution fractions was 89 % and 100 %, and in low pH elution fractions was 89 % and 100

%, for target and non-target cells, respectively. Direct observation of target and non-target cells on the fiber lumen after loading, washing and fixation with transmission electron microscopy (see section 4.9 and chapter 5) suggested that the fibers remain coated with many cells which were more or less evenly distributed over the length of the fibers.

4.5.3.4 Cell Adsorption and Elution Experiments Using Type A Lumen Retentive Surface Fibers with Elution by Laminar Shear Stress

Figures 4.13 - 4.16 present results for experiments performed with Type A lumen-retentive fibers with various experimental conditions. As with Type E fibers, cells were loaded onto the inside fiber surface via filtration from the lumen to the shell. For experiments with Type A fibers; however, cells were removed with laminar shear stress instead of back-filtration. Type A fibers had a smaller internal diameter than Type E fibers (0.6 vs 1.0 mm) so that a theoretical monolayer on a typical fiber used in experiments was about 5 to 6.5 $\times$ 10^5 cells. Figure 4.13 (A) and (B) shows results for HL-60 cells pre-incubated with a 1:500 dilution of anti-CD33, and anti-CD33-free HL-60. Cells were injected into the lumen side of the apparatus shown in figure 4.2 (B) and loaded onto the fibers at a load flowrate of 0.15 ml/min (maximum shear stress at each end of 0.6 dynes/cm^2) which created a back-pressure of 74 mmHg for each experiment. The time required to filter about 1.8 $\times$ 10^6 cells (about 2.8 monolayers) onto the surface was about 5.5 min. After injection of cells and before washing, the stopcocks on the lumen-side tubing were flushed out with buffer into an "injection flush" fraction as Type E fiber experiments. Wash flowrate before elution was 0.2 ml/min yielding a maximum shear stress of 1.5 dynes/cm^2 with a Reynolds number of 1.8, an entrance length of 0.04 mm, and a pressure drop from one end of the fiber to the other of 0.3 mmHg. Because the flowrate during the wash step was low, only two fractions were collected (5 min each) instead of 5. Elution was performed in three stages with shear stress.

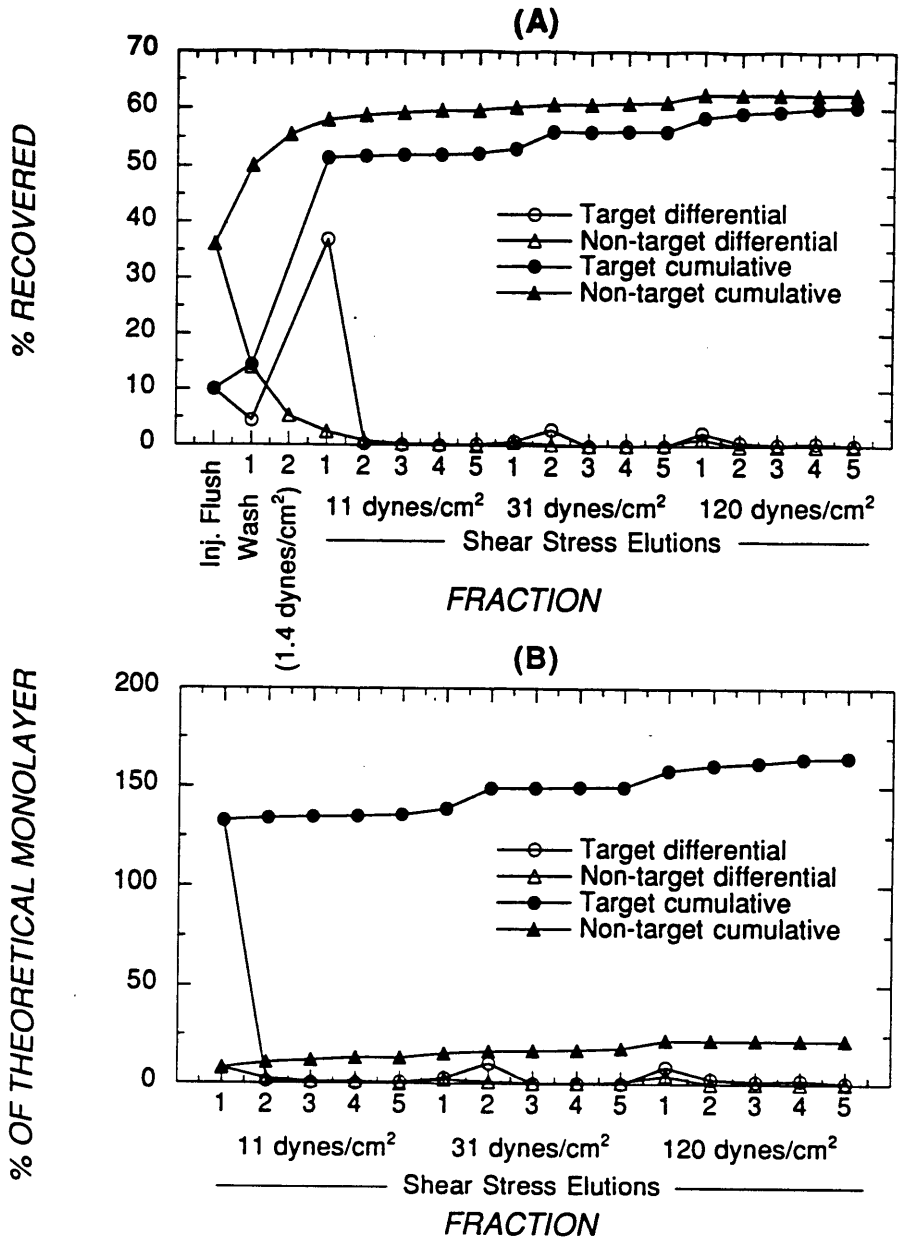

Figure 4.13 Cell attachment/detachment results using Type A hollow fibers with HL-60 cells loaded onto the lumen surface of the fiber via lumen to shell filtration at about 70 mmHg. Cells were eluted with shear stress using DPBS + 1% w/v BSA (pH 7.4). Target cells were pre-incubated with a 1:500 dilution of anti-CD33 ascites .Non-target cells were not pre-incubated with anti-CD33. (A) Cells recovered in each fraction as a percentage of the total cells injected into the fiber. (B) Cells recovered in elution fractions as percentage of a calculated theoretical monolayer of cells loaded onto the hollow-fiber surface. Each point represents the average of duplicate cell counts.

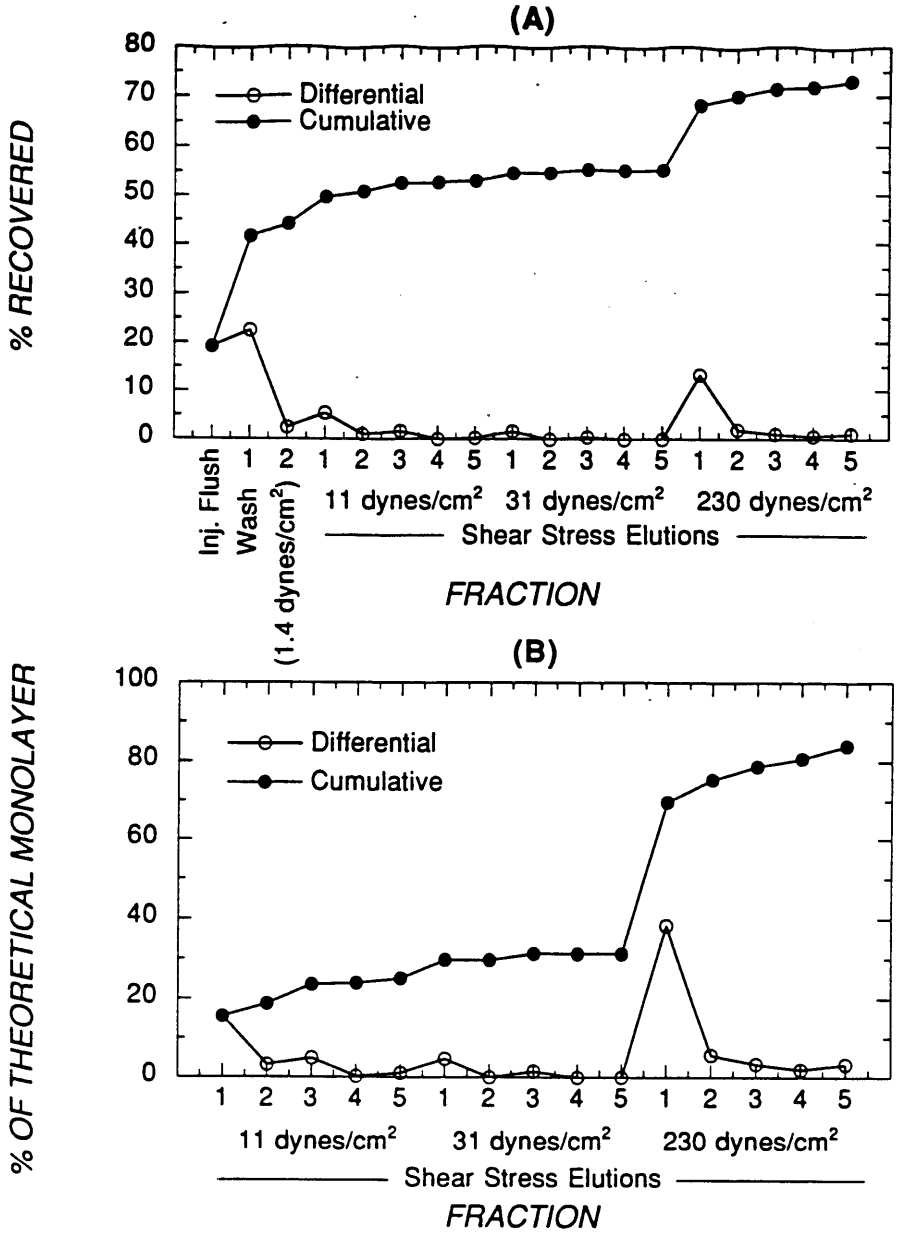

Figure 4.14 Cell attachment/detachment results using Type A hollow fibers with HL-60 cells loaded onto the lumen surface of the fiber via lumen to shell filtration. Cells used in this experiment were non-target cells (not pre-incubated with anti-CD33). (A) Cells recovered in each fraction as a percentage of the total cells injected into the fiber. (B) Cells recovered in elution fractions as a percentage of a calculated theoretical monolayer of cells loaded onto the hollow-fiber surface. Each point represents the average of duplicate cell counts.

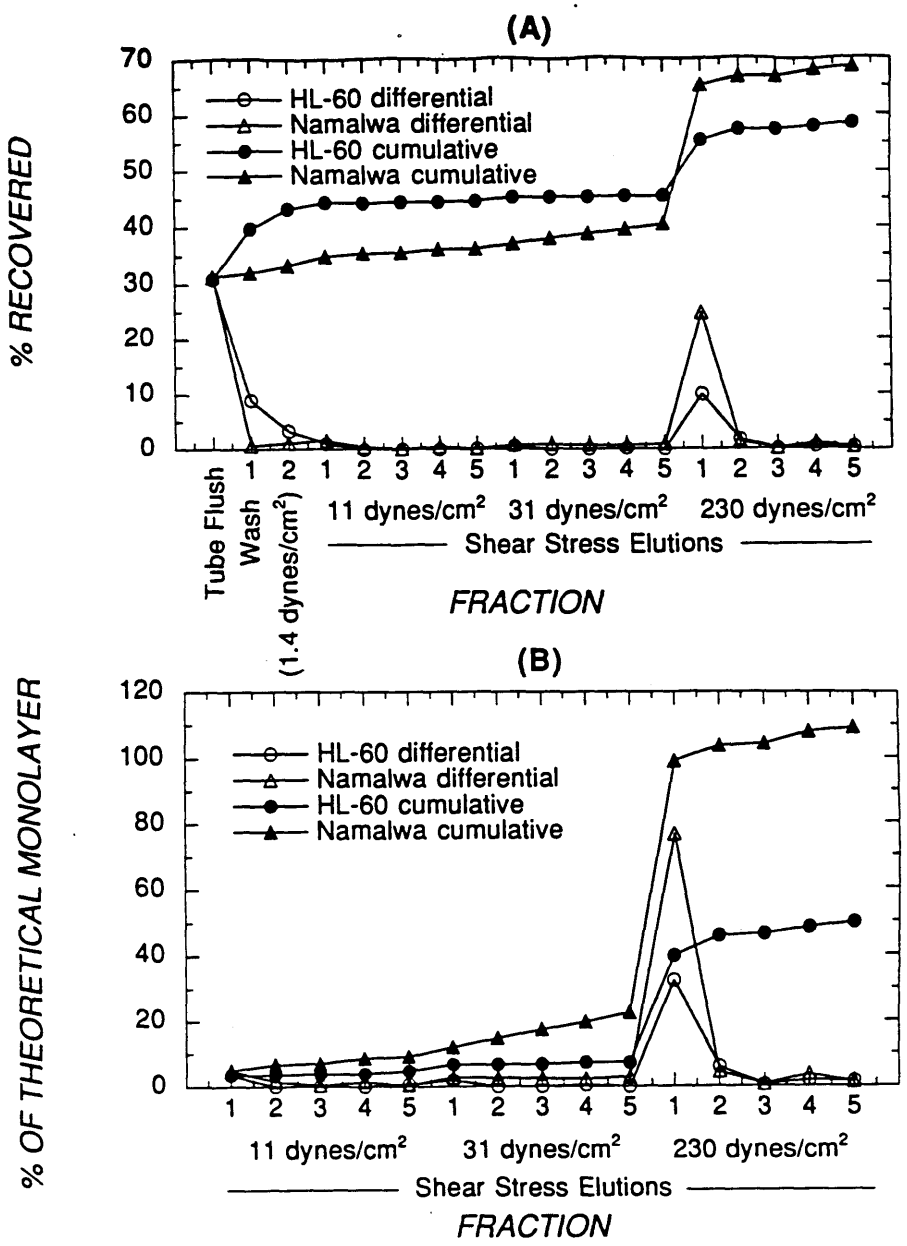

Figure 4.15 Cell attachment/detachment results using Type A hollow fibers with HL-60 non-target cells (circles) or Namalwa cells (triangles) loaded onto the lumen surface of the fiber via lumen to shell filtration. Tubing used during cell loading was replaced before wash and elutions to eliminate artifact. The removed tubing used for cell loading and the injection ports were flushed and cells were collected in the "Tube Flush" fraction. (A) Cells recovered in each fraction as a percentage of the total cells injected into the fiber. (B) Cells recovered in elution fractions as a percentage of a calculated theoretical monolayer of cells loaded onto the hollow-fiber surface. Each point represents the average of duplicate cell counts.

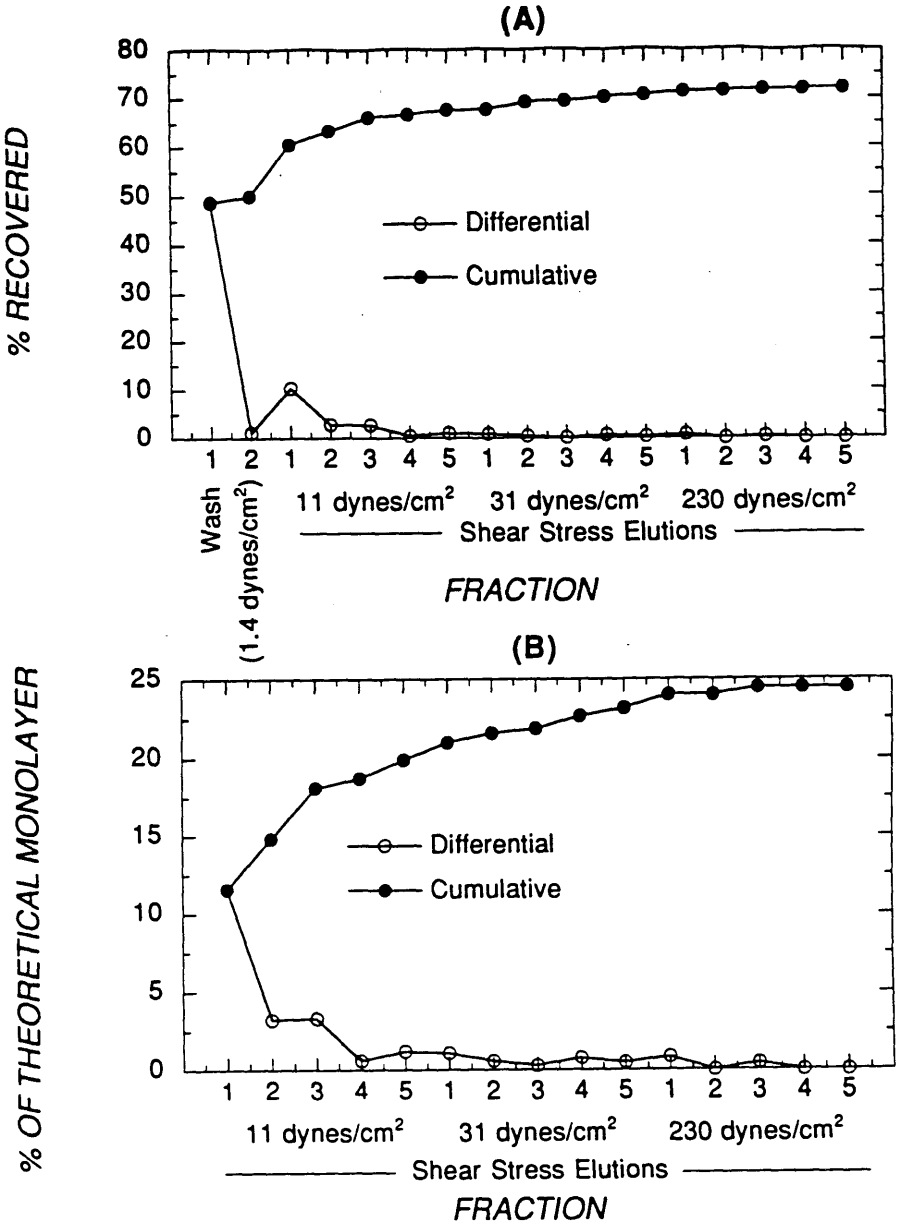

Figure 4.16 Cell attachment/detachment results using Type A hollow fibers with HL-60 non-target cells loaded onto the lumen surface of the fiber by gravity. Tubing used during cell loading was replaced before wash and elutions to eliminate artifact. (A) Cells recovered in each fraction as a percentage of the total cells injected into the fiber. (B) Cells recovered in elution fractions as a percentage of a calculated theoretical monolayer of cells settled onto the hollow-fiber surface. Each point represents the average of duplicate cell counts.

Step 1: 1.5 ml/min flowrate, 11 dynes/cm^2 maximum shear stress, Reynolds number of 14, entrance length of 0.3 mm, and pressure drop of 2.2 mmHg. Step 2: 4 ml/min flowrate, 31 dynes/cm^2 maximum shear stress, Reynolds number of 36, entrance length of 0.8 mm, and pressure drop of 6 mmHg. Step 3: 16 ml/min flowrate, 120 dynes/cm^2 maximum shear stress, Reynolds number of 146, entrance length of 3.1 mm, and pressure drop of 23 mmHg. Figure 4.13 (A) indicates that, unlike experiments with Type C and Type E fibers, the total fraction of cells initially injected which were recovered was similar for target and non-target cells. The total number of recovered cells was about 60 to 65 % of those initially injected into the apparatus leaving about 7.5×10^5 cells (about 1.2 monolayers) unaccounted for. Nearly all of the recovered non-target cells were recovered before the first shear elution (55 %) compared to only 14.5 % of target cells. In contrast, most target cells were recovered during the first shear elution (52 % recovered by end of first shear elution). Relatively few cells were eluted by higher shear elutions. Figure 4.13 (B) indicates that over 150 % of a theoretical monolayer of target cells was recovered during shear elutions versus about 22 % for non-target cells. This corresponds to an equivalent selectivity (defined as 100% × target/(target + non-target) cells recovered in elutions) of about 87 % for a hypothetical separation. Viability of the eluted cells was 99 % and 100 % for step 1, 100 % and 100 % for step 2, and 73 % and 88% for step 3 for target and non-target cells respectively. These results suggest that target cells may be more strongly adsorbed to the fiber, that cells may be more tightly packed on the fiber than our calculated theoretical monolayer (since 150% of a theoretical monolayer of target cells recovered during shear stress elutions), and that a substantial fraction of both target and non-target cells which are not recovered may be very tightly attached to the fiber or apparatus.

Figure 4.14 presents the results from an additional experiment with Type A fibers and

HL-60 non-target cells where the final elution was performed using a shear stress of 230 dynes/cm^2 (30 ml/min, Re = 273, Le = 5.7 mm, Δp = 43 mmHg) instead of 120 dynes/cm^2. Comparing figure 4.14 to figure 4.13 shows that the elution behavior of the non-target cells was similar for wash steps and the first two shear elution steps, but that an additional large peak (18 % of total) was eluted by 230 dynes/cm^2 but not by 120 dynes/cm^2 shear stress. In this case, almost 75 % of injected cells were recovered, and the cells recovered by shear elutions represented almost 85 % of a theoretical monolayer. The majority of the cells recovered in shear elutions were recovered at 230 dynes/cm^2 (about 63 %). The viability of eluted cells was 94 %, 100 %, and 98 % for steps 1, 2, and 3 respectively. This result indicates that there probably were a significant number of cells remaining in the fiber or tubing after shear exposure of cells in the fiber to 120 dynes/cm^2.

The experiments whose results are given in figure 4.15 were designed to determine the origin of the cells which resist elution except at the highest shear stress. In order to eliminate the possibility that cells which may adhere to Tygon tubing during the loading step dislodge during the final elution step and cause an artifactual peak, for these experiments, after loading by filtration as before, the inlet and outlet tubing and stopcocks connected to the fiber lumen were replaced with new tubing. The load tubing and stopcocks were rinsed into a collected fraction (labeled "Tube Flush" in figure) with elution buffer at a flowrate of 30 ml/min. This fraction will contain the cells remaining behind in the injection ports (collected in "injection flush" fractions in previous experiments) as well as additional cells dislodged from the inside surface of the Tygon tubing used for cell loading. Cells were then eluted from the lumen of the hollow fiber using the replacement tubing in three stages with shear stresses of 11, 31, and 230 dynes/cm^2. Two different types of non-target cells were used in these experiments. HL-60 cells without anti-CD33 and Namalwa cells. Elution patterns were similar to the

previous experiments with few cells eluting during the first two shear elution steps, but a large bolus of cells eluting at 230 dynes/cm^2. The number of cells eluted by shear was about 50 % of a theoretical monolayer for HL-60, and over 100 % for Namalwa (figure 4.15 (B)). The vast majority of these cells were recovered during elution at 230 dynes/cm^2. The viability of cells recovered was in all cases > 98 %. This result indicates that the origin of the cells which were recovered only at 230 dynes/cm^2 shear stress was the hollow fibers and not the load tubing. In fact, the percent of the total cells injected which were recovered by flushing the load tubing (about 30%) was within the range previously recovered by flushing only the injection ports (10-35 %, see figures 4.13 and 4.14). Figure 4.16 suggests that the elution peak at 230 dynes/cm^2 may depend upon the way in which the cells were loaded onto the membrane. Figure 4.16 shows the results from an equivalent experiment with HL-60 non-target cells loaded onto the lumen of the fiber by gravity settling. In this case, nearly all of the cells which were recovered were collected during the wash or lowest shear elution. There was no dramatic increase in the number of cells collected upon application of 230 dynes/cm^2 shear stress as with cells loaded onto the fiber by filtration under pressure. For this experiment, the determination of the total percent of cells recovered (about 73%) of those initially injected was based on a calculated estimate of the number of cells injected (based on the dimensions of the fiber see table 4.1) and not a precise measurement of the injected volume of cell suspension as for previous experiments. Because of this, the determination may have been less accurate.

4.5.3.5 Cell Adsorption and Elution Experiments Using Type B Fibers and Direct Observation of Adsorbed Cells

Figure 4.17 shows a typical photograph of cells bound to the edge of a Type B fiber, and figures 4.18 and 4.19 present the results from cell attachment and detachment experiments

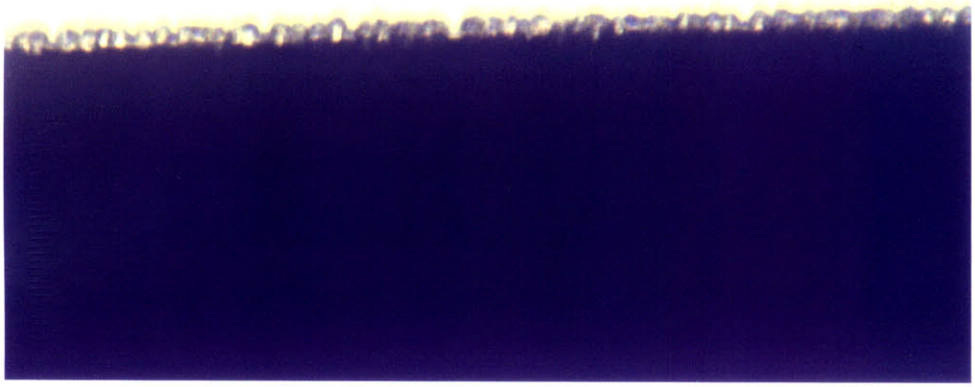

Figure 4.17 Photograph of HL-60 cells adsorbed to the edge of a Type B hollow fiber in a module with a viewing "window" photographed in brightfield.

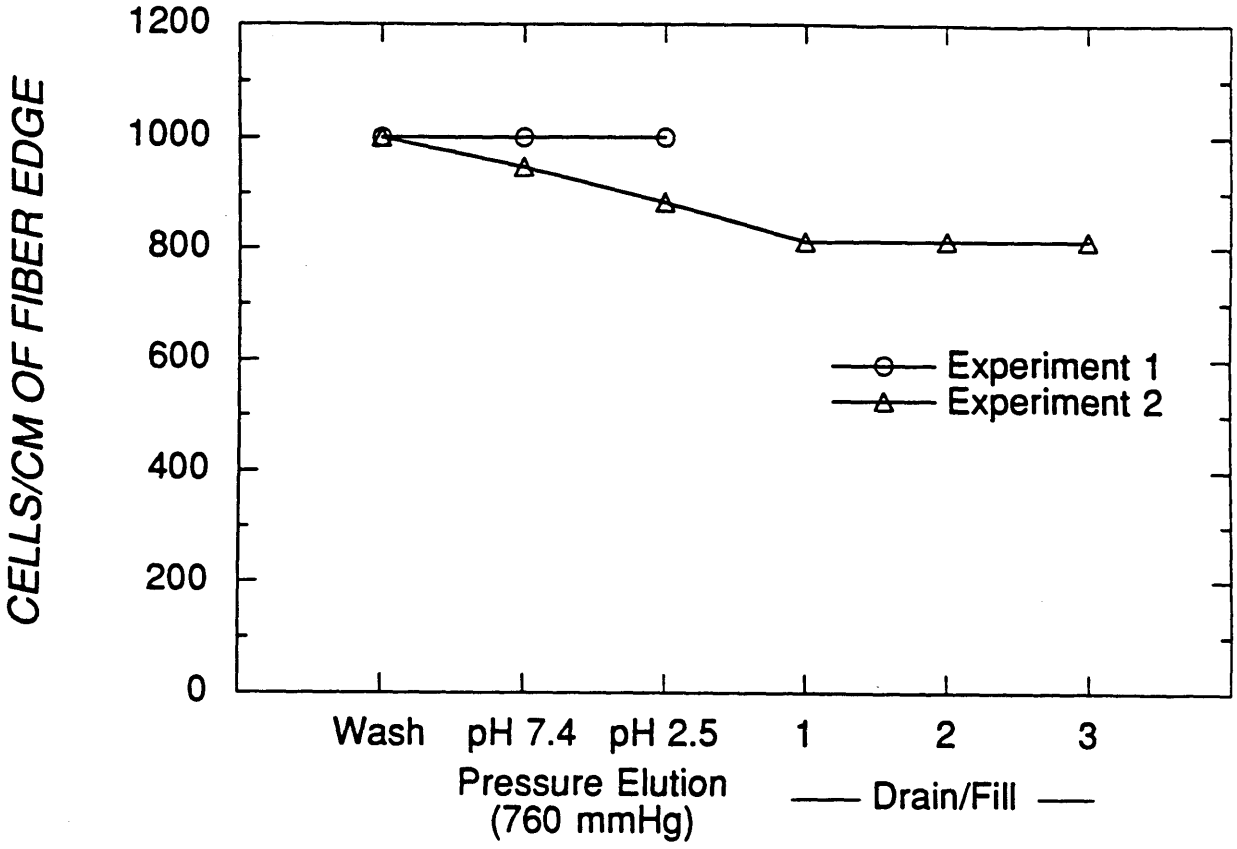

Figure 4.18 Cell attachment/detachment results using Type B hollow fiber with HL-60 cells pre-incubated with a 1:500 dilution of anti-CD33 ascites loaded onto the outside surface of the fiber via shell to lumen filtration. Wash flowrate was 12.1 ml/min during wash step and pressure elution. Cells were eluted with DPBS (pH 7.4) and 10 mM glycine-saline (pH 2.5) filtered from lumen to shell at a back-pressure of 760 mmHg. For experiment 2, cells were also eluted by draining, then refilling and flushing the module (12.1 ml/min). Cell adsorption was quantified by counting cells bound to the edges of the fiber visible under the viewing window (see figure 4.1 (C)).

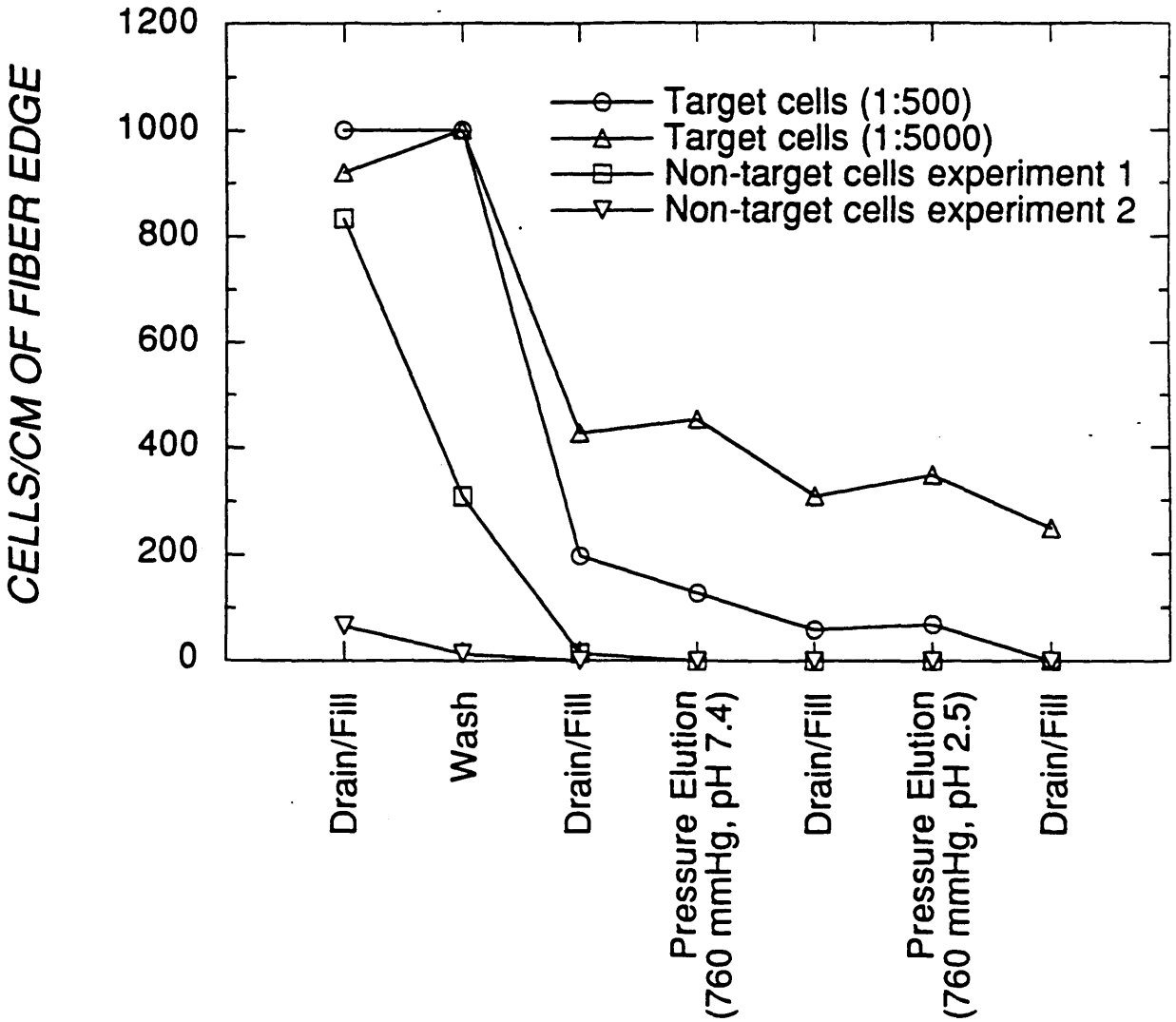

Figure 4.19 Cell attachment/detachment results using Type B hollow fiber with target HL-60 cells pre-incubated with a 1:500, or 1:5000 dilution of anti-CD33 ascites or with non-target anti-CD33-free HL-60 cells loaded onto the outside surface of the fiber via shell to lumen filtration. Procedures were performed in the order indicated on the x axis.

using Type B fibers, with cell loading by filtration, and quantification of cell attachment and removal by direct observation of cells bound to the edges of the fiber under the viewing window in modified modules (see figure 4.1 (C) and 4.17). Cell loading, module washing, and elutions by back-filtration were performed in an identical fashion as previous experiments with Type B fibers already described except that the maximum shell-side wash flowrate during pressure elutions was 12 ml/min versus 5 ml/min. Figure 4.18 shows results from two experiments with HL-60 target cells (pre-incubated with a 1:500 dilution of anti-CD33). In experiment 2, cells were also eluted from the fiber by draining the module, exposing the fiber to air for about 5 sec, and then refilling and flushing the shell with about 3 ml of wash buffer at 12 ml/min. These elution steps are designated by the label "Drain/Fill" in the figure. Results are presented as cells/cm of fiber edge, where 1000 cells/cm represents maximum coverage (no space between cells bound to edge). Figure 4.18 indicates that no detachment was observed for cells in experiment 1. Maximum cell coverage was observed after wash and neutral and low pH pressure elutions. By contrast, for experiment 2 there was a modest removal of cells during the elution steps (about 19 %). The percent of the initial cells bound which were removed from the fiber was 5.3 %, 6.4 %, and 7 % for neutral pH pressurization, low pH pressurization, and the first air exposure respectively. Two additional air exposure steps did not remove any additional cells. Viability of cells collected during each step was > 90%

Experiments were also performed where air exposure elution steps were interspersed between other steps in a manner designed to better simulate the bare fiber experiments performed and summarized in chapter 3. The order of the procedure used in these experiments was as follows. After loading of the cells by filtration as usual, there was an air exposure elution step followed by washing of the module shell, a second air exposure, neutral

pH pressure elution, a third air exposure, low pH pressure elution, and a final air exposure step. Each step was performed as previously described. The results for target and non-target HL-60 cells are shown in figure 4.19. Results indicated that target cells pre-incubated with both a 1:500 and a 1:5,000 dilution of anti-CD33 ascites behaved in a similar fashion with maximum cell coverage observed through the wash step, a large drop in cell density after the post-wash air exposure, and a much lower degree of cell removal with subsequent elution steps. For target cells pre-incubated at the 1:500 dilution, about 80 % of the cells present on the fiber after the wash step were removed during the subsequent air exposure, 35 % of the remaining cells were removed by pressure elution at pH 7.4, 54 % of the remaining cells were removed by the following air exposure, no cells were removed during the low pH pressurization, and all of the remaining cells were removed by the final air exposure. For target cells pre-incubated at the 1:5,000 dilution, about 57 % of the cells present on the fiber after the wash step were removed during the subsequent air exposure, no cells were removed by pressurization at pH 7.4, 32 % of the remaining cells were removed by the air exposure step following the pressure elution at pH 7.4, no cells were removed during the low pH pressurization, and 28 % of the remaining cells were removed by the final air exposure for a total removal of 75 %. Viability of all eluted cells was > 90 %. Both experiments performed with non-target HL-60 cells indicated that these cells were more easily detached. For the first experiment most of the cells were removed during the wash step (63 %) with the remaining cells removed by the subsequent air exposure. For experiment 2, very few cells were observed attached to the fiber after the initial air exposure (66 cells/cm), and nearly all of these were removed during the wash step (80 %). For both experiments with non-target cells, complete removal of cells was observed during the experiment. These results indicate that exposure to an air/liquid interface or to air seem to be an effective means of removing a

substantial fraction of cells loaded onto these fibers by filtration. Comparing target cell behavior in figures 4.18 and 4.19, results also indicate that the specific order in which elution steps are performed may be significant, or that cell elution from fibers is not reproducible from fiber to fiber. In addition to the observations summarized in the figures, some fibers were observed by light microscopy after removal from modules after experiments, and it was observed that the distribution of residual cells was not homogeneous. Typically there would be regions with high cell density, and other regions which were cell-free. Lack of reproducibility from fiber to fiber in these experiments could, therefore, be due, at least in part, to inhomogeneities in attachment/detachment behavior along the length of the fiber combined with observation of only a single small region of the fiber edge (less than 3 % of the total edge length).

4.6 Discussion

In contrast to our previous work with Type B rpA-coated hollow-fiber microporous membranes, with cell loading by gravity settling, where the majority of target cells could be easily removed from the fiber surface (we observed 56 % target cell removal by handling and manipulation of control fibers, 73 % target cell removal with supplemental pH 7.4 back-filtration and 96 % target cell removal with supplemental pH 2.5 back-filtration), and where non-target cell binding was very low (see chapter 3), in the present chapter, for cells loaded by filtration under the influence of hydrostatic pressure onto Type B, C or E fibers, results suggested that cells were more difficult to remove. Back-pressure and back-filtration did not elute a substantial fraction of the cells initially loaded onto the fiber (< 33% of a theoretical monolayer was removed, see figures 4.8-4.12). Also, the use of fibers with higher hydraulic permeabilities than Type B fibers (Types C and E) and lumen retentive surfaces (Type E) did

not improve target cell recovery, contrary to expectations.

Total recovery of target cells for experiments with back-pressure elution was lower (< 70 %, see figures 4.8 to 4.12) than for non-target cells (up to 93 %, see figures 4.10 and 4.12) indicating that non-target cells may be more easily dislodged from the fibers; however, a considerable fraction of these cells (from about 35 - 85 % of a theoretical monolayer) were removed during the elution procedure indicating that they were able to resist shear forces during washing sufficient to recover > 93 % of cells in our cell number balance experiments (see figure 4.7). This suggests that even non-target cells may be strongly attached to the fibers. Typically, only about 60 % of the target cells initially loaded into modules or fibers were recovered during the experiments utilizing elution with back-pressure (figures 4.8-4.12). The number of target cells which were unaccounted for ranged from 1.5 to 3 $\times$ 10^6, representing at least 1.5 to 3 times a calculated theoretical monolayer. This suggests that the one or more of the following was occurring: that cells were able to cover the fiber much more densely than we estimated, that target cells were somehow destroyed during the loading or detachment process, or that target cells may have a greater tendency to adhere to other surfaces or to each other than non-target cells. Direct visual observation of Type B and Type C hollow fibers after completion of experiments indicated that the fibers remain covered with many target cells and a lower, but still substantial, number of non-target cells.

Experiments undertaken with lumen-retentive Type A fibers using laminar shear stress for elution investigated the degree and nature of non-specific cell adsorption in the fiber and to the apparatus. Unlike the experiments using back-pressure for elution, cell recoveries were generally lower for non-target cells (about 60 to 70 %, see figures 4.13 to 4.15) and were not significantly different from recovery of target cells. Non-target cells were recovered mainly during the low shear wash (1.4 dynes/cm^2), while target cells were primarily recovered at

higher shear (11 dynes/cm^2) (see figure 4.13). This level of shear stress is substantially lower (by about an order of magnitude) than that observed by other investigators as necessary to remove specifically adsorbed cells from a modified glass substrate (Nordon et al., 1994) or cellulosic hollow-fiber dialysis membranes (Nordon et al., 1996). Possibly the cells removed during the 11 dynes/cm^2 shear elution were only loosely bound by few bonds or with small contact areas. Such may be the case if a secondary layer of cells were to form on the fiber during loading by filtration which have extruded into spaces between the primary monolayer of cells on the surface and are in contact with the membrane over only a small, irregular contact area. Such cells may also be more sensitive to shear forces than back-filtration since the cell profile would be exposed to streamlines of higher flow velocity with less shielding from surrounding cells. This may also partially explain why over a monolayer of target cells were removed from Type A fiber by shear stress elution (see figure 4.13) compared to much lower fractions removed from Type B, C, and E fibers by back-filtration. Even so, for experiments with both target and non-target cells, at least 7.5×10^5 cells (about 125 % of a calculated theoretical monolayer) were unrecovered after exposure of shear up to 120 dynes/cm^2 (see figure 4.13), a level in excess of that which has been previously used to recover specifically adsorbed cells (Nordon et al., 1994). Increasing the shear stress to 230 dynes/cm^2 during the final elution step resulted in a significant increase in the number of non-target cells recovered (see figures 4.14 and 4.15). Experiments utilizing a modified protocol, in which the tubing used to load cells was replaced with cell-free tubing prior to elution steps, indicated that the origin of these cells was the hollow fiber not the Tygon tubing used for cell loading (compare figures 4.14 and 4.15). This elution peak at 230 dynes/cm^2 was eliminated when non-target cells were loaded by gravity suggesting that the high resistance of non-target cells to shear removal was directly related to loading by filtration.

In order to eliminate cell collection artifacts, cell loss, and effects of non-specific/non-fiber binding, experiments were performed with specially modified modules with viewing ports through which the outside edges of the fiber could be directly observed and photographed. Less than 10 % of the total fiber edge length was visible through the viewing port. The lack of quantitative reproducibility of the results may be due to this limited observation area coupled with non-homogeneous binding along the length of the fiber. Back-pressure and back-filtration with either a pH 7.4 buffer or a pH 2.5 buffer removed from 0 % to 35 % of the adsorbed cells along the visible fiber edges (see figures 4.18 and 4.19). More effective for most experiments was exposure to an air-liquid interface and 5 - 10 sec air exposure which removed from about 0 % to 80 % of the previously bound cells from the visible fiber edges. Consistent with cell recovery experiments, non-target cells were more easily removed than target cells.

Taken together, our results suggest that cells loaded by filtration onto hollow-fiber membranes under the conditions studied were more difficult to remove by shear and back-pressure than those loaded by gravity settling. Further visual evidence that cells were more resistant to removal when loaded by filtration than by gravity was provided by transmission electron microscopy (TEM) of Type E and Type A fibers after cell loading and washing (section 4.9 and chapter 5). TEM photomicrographs showed that for both target and non-target cells, the lumen of these fibers were covered with many cells after loading by filtration and washing using the same protocols described earlier. However, when non-target cells were loaded by gravity onto Type E fibers, no cells could be found along the entire length of the fiber after washing and TEM preparation. Morphometric analysis presented in section 4.9 of adsorbed target cells loaded by filtration onto Types B, C, and E fibers indicated that the shape, contact area size, and minimum separation distance was not significantly different than

that observed for gravity settled cells in chapter 3.

The analysis performed in section 4.10 compared experimental conditions to estimated forces and pressures necessary for target cell removal using the methods, assumptions, and simplifications described in chapter 2. The analysis suggested that the forces on adsorbed cells due to the experimentally applied back-pressures should have been sufficient to detach the cells and that the pressure necessary for cell detachment should decrease for Type C and Type E fibers assuming they are sufficiently anisotropic. These predictions were not supported by our experimental observations. While it is possible that Type C and Type E fibers are substantially less anisotropic in morphology than Type B fibers, and thus more inefficient in transmitting applied back-pressure to the cell contact area, this does not explain the lack of significant cell removal from Type B fibers with back-pressure. In chapter 3 using Type B (Lot 2) fibers and fibers with even lower hydraulic permeabilities (Lot 1), we demonstrated that when cells were loaded by gravity that elution with back-pressure removed significantly more adsorbed cells than for controls.

Two substantial differences between the cell recovery experiments in the present study and previous experiments using unpotted hollow fibers with gravity settling were the application of static pressure to cells on fibers during loading in the present study, and the handling and brief air exposure of cells on fibers during previous experiments with unpotted fibers. The effect of an air interface and brief air exposure was analyzed in this study by direct observation of cells on Type B fibers potted in specially modified modules. We found the effect of air exposure on removal of target cells to be substantial, in fact, more effective than back-pressure alone for the majority of experiments. With previous results obtained with unpotted fibers and cells settled by gravity onto similarly prepared fibers, while air exposure and handling alone was able to remove about 56 % of cells, it was significantly less effective

than a combination of air exposure and back-pressure at pH 7.4 (73 % removal) or back-pressure at pH 2.5 (96 % removal), suggesting that a reduced effectiveness of back-pressure as an elution technique for target cells may be correlated to the loading of cells by filtration under applied pressure.

The TEM analysis shown in section 4.9 suggests a potential explanation which fits well with observed results. We observed that cells loaded by filtration, but not gravity, onto fibers using the conditions employed in this study displayed a tendency to infiltrate into the pore structure of all of the hollow fiber membranes used (see figures 4.B.4, 4.B.6, and chapter 5). By penetrating under the surface of the hollow fiber, the cells may more irreversibly anchor themselves to the substrate (as if by hooks as in figure 4.B.4), especially if these infiltrations are stabilized by specific bonds. This behavior could greatly increase non-specific mechanical attachment of non-target cells and make infiltrated target cells difficult or impossible to remove in a viable state by back-pressure. Because the hollow fiber matrix is very irregular and tortuous, and because forces would be applied directly to cellular infiltrations during back-pressure, there could be a tendency for back-filtration to actually further entangle and enmesh these infiltrations in the fiber matrix by extruding some infiltrations back up into different, previously unblocked, flow channels. For target cells, the infiltrations may also have specific affinity for the internal surfaces of the hollow-fiber membrane and a tendency to adhere. The effect of this mechanical anchoring may overwhelm the force on the contact area due to the back-pressure, and may eliminate the ability to detach the cell without lysis especially for target cells. Body forces applied to the cell exterior, such as shear or the passage of an air-liquid interface, may be more effective in removing infiltrated cells since such forces would tend to create a cell membrane tension tending to pull out the infiltrations along the paths upon which they entered. The tendency towards

infiltration would also occur more frequently with filtration membranes having larger surface pores, as was the case for the membranes with higher hydraulic permeability than Type B in this study. Infiltration could also explain the tendency of cells remaining on the surface after experiments where cells were loaded by filtration to be non-homogeneously distributed on fibers like Type B. Cells may tend to remain preferentially in regions of the surface with relatively larger pores or surface damage.

We believe that in order to successfully use porous membranes to separate cell populations and recover viable cells, infiltration of cells into membrane pores during cell attachment should be understood and prevented as much as possible. Loading cells by gravity settling is a viable option; however, this method is slow and inefficient. Also, gravity settling results in a large variation in cell residence times, poorer cell distribution on curved surfaces, and is difficult to perform and automate. Our TEM observations indicated that target cells loaded by gravity onto the lumen of Type E hollow fibers only adhered in a narrow band (about 8 cells abreast) on the surface to which the cells were initially allowed to settle. This coverage represents less than 4 % of a theoretical monolayer based on the surface area of the entire fiber. It is just as difficult, if not more so, to load cells with even distribution onto the outside surface of fibers. If gravity were to be used as a primary means of cell loading, a flat sheet device with a minimal settling depth may be a more appropriate design geometry than hollow-fibers. Unfortunately, flat sheet devices are more difficult to scale up for handling large, clinical scale, cell loads than hollow-fiber devices. Because loading of cells onto membranes by filtration has so many practical advantages, it is important to more thoroughly investigate and understand cell infiltration into small pores during cell loading by filtration to determine operating conditions and/or membrane morphologies where it can be prevented or minimized. This task is the subject of the remaining two chapters.

4.7 Acknowledgements

Experimental hollow-fiber membranes were kindly provided by Dr. Sam Williams at Sepracor (Marlborough, MA). Special thanks as well to Dr O.D. Holton and Dr. Abdul Azad at Sepracor for assistance with membrane modification. Scanning electron microscopy was performed in the EM facility of the Center for Materials Science and Engineering at MIT, a Materials Science and Engineering Center supported by the National Science Foundation under grant number DMR 9400334. Special thanks to Dr. David C. Bell, and Mr. Michael Frongillo for assistance with sample coating and microscopy. Transmission electron microscopy was performed in the Biomedical Electron Microscopy Laboratory at MIT. The JEOL 1200 EX II was purchased through an NIH multi-user instrumentation program, BRS Shared Instrumentation Grant number S10 RR05734-01. Special thanks to Ms. Patricia Reilly for assistance with sample preparation and microscopy.

4.8 Appendix A: Estimation of Surface Area Available for Specific Bond Formation for Type B, C, and E Hollow Fiber Membranes.

In this appendix, we present an estimate of the fraction of the retentive surface available for specific bond formation between the cell and the fiber surface. The available fractional surface area for bond formation was defined as 100 % minus the percentage of the surface area occupied by pores. The fractional surface area occupied by pores was determined as described previously (section 3.10). Briefly, high-resolution photocopies were made of SEM photomicrographs of two independent samples of the retentive surface of each fiber. The pores from each image were carefully dissected using a surgeon's scalpel. The dissected pores and the remaining pore-free image were independently weighed with an analytical balance (Model BA210S, Sartorius Corporation, Edgewood, NY). The weight of

each fraction was converted to an equivalent area by multiplying the weight by the average weight of three samples of known size of the paper upon which the photocopies were made (see section 3.10, for details). The results of the analysis are shown in table 4.A.1. Photomicrograph image magnifications for the samples used were 50, 000× and 40, 000× yielding a total surface area analyzed of about 10 μm^2 for Type B, 50, 000× and 10,000× yielding a total surface area analyzed of about 105 μm^2 for Type C, and 20, 000× and 5,000× yielding a total surface area analyzed of about 430 μm^2 for Type E.

Table 4.A.1 *Percentage of Hollow-Fiber Surface Area Available For Specific Bond Formation*

Hollow-Fiber	Percent of Retentive Surface Available For Bond Formation
Type B	87.6 ± 1.2
Type C	80.1 ± 3.8
Type E	79.0 ± 3.9

Results are expressed as mean ± SD.

4.9 Appendix B: Morphometric Analysis of Filtration-Loaded HL-60 Target Cells Adsorbed to Hollow-Fiber Membranes.

HL-60 target cells (pre-incubated with a 1:500 dilution of anti-CD33 ascites) loaded by filtration onto Type B, C, and E fibers under identical conditions as described previously for cell attachment and recovery experiments, were observed with transmission electron microscopy (TEM) using methods previously described (chapter 3). Briefly, after loading by filtration, the unbound cells were washed out of the shell or lumen under identical conditions as for the cell attachment and recovery experiments, and the cells adsorbed on the fiber were fixed for 1 hr at room temperature with 1 % w/v glutaraldehyde in PBS (pH 7.4), post fixed

with 2 % w/v osmium tetroxide, dehydrated through a series of graded ethanol/water washes, infiltrated with Spurr's resin (Polysciences, Warrington, PA), cured, sectioned, post stained with 1 % w/v potassium permanganate, 2 % w/v uranyl acetate, and Reynolds lead citrate (Reynolds, 1963), then observed at 80 kV on a JEOL 1200 EX II TEM (JEOL, Peabody, MA). Typical results for Type B and E fibers are shown in figures 4.B.1-4.B.6. Figure 4.B.1 shows a typical cell on Type B fibers with a semi-hemispherical shape showing a distinct flattened contact region whose diameter is a substantial fraction of the cell diameter. This morphology was nearly identical to that observed for the same cells loaded onto Type B fibers by gravity settling (see chapters 3 and 5). A close up of the cell-fiber contact area at higher magnification is shown in figure 4.B.2 for Type B fibers. Some cells displayed a more irregular contact area morphology. This is evident for the cell shown in figure 4.B.3 on a Type B fiber which has a very irregular, villous contact area. Figure 4.B.4 shows part of a cell which has infiltrated beneath the surface of a Type B fiber. This infiltration was never observed for cells loaded by gravity (see chapter 3 and 5) and may explain in part the difficulty observed in removing and recovering cells loaded by filtration. Figures 4.B.5 and 4.B.6 show similar results for cells on Type E fibers. The cell in figure 4.B.6 has also infiltrated beneath the surface of the membrane. The infiltration visible in figure 4.B.6 has come from a portion of the cell outside the plane of the section, and, therefore, is not directly attached to the contact region visible in the figure. Infiltration was more common with the more open fibers such as Types C, E, and A (see chapter 5 results).

Quantitative measurements were taken from photographic enlargements of TEM photomicrographs with high-precision calipers (Mitutoyo Corporation, Tokyo, Japan) of cell diameters both parallel and perpendicular to the plane of the fiber membrane surface, cell contact area diameters, and minimum separation distances (taken from photomicrographs with

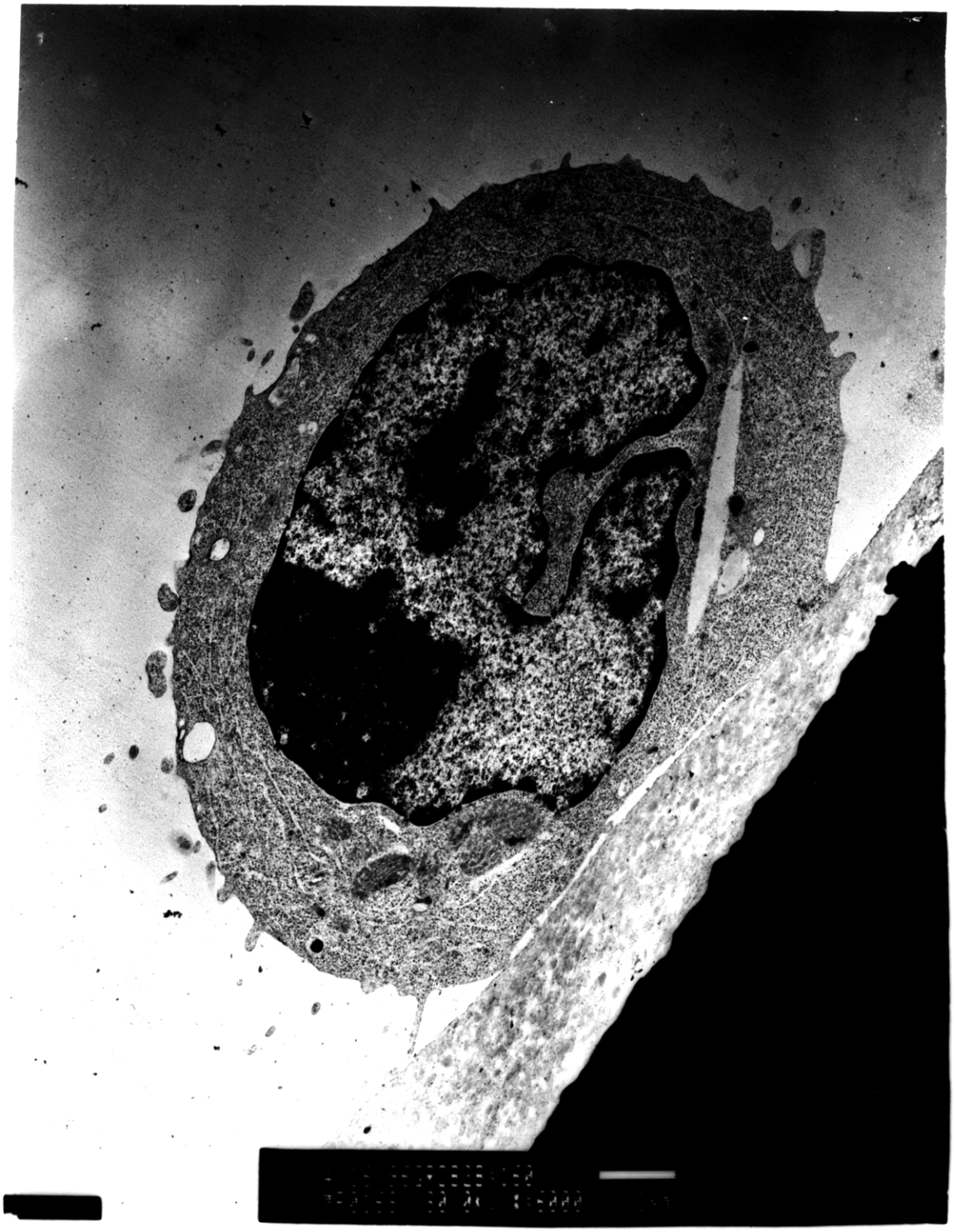

Figure 4.B.1

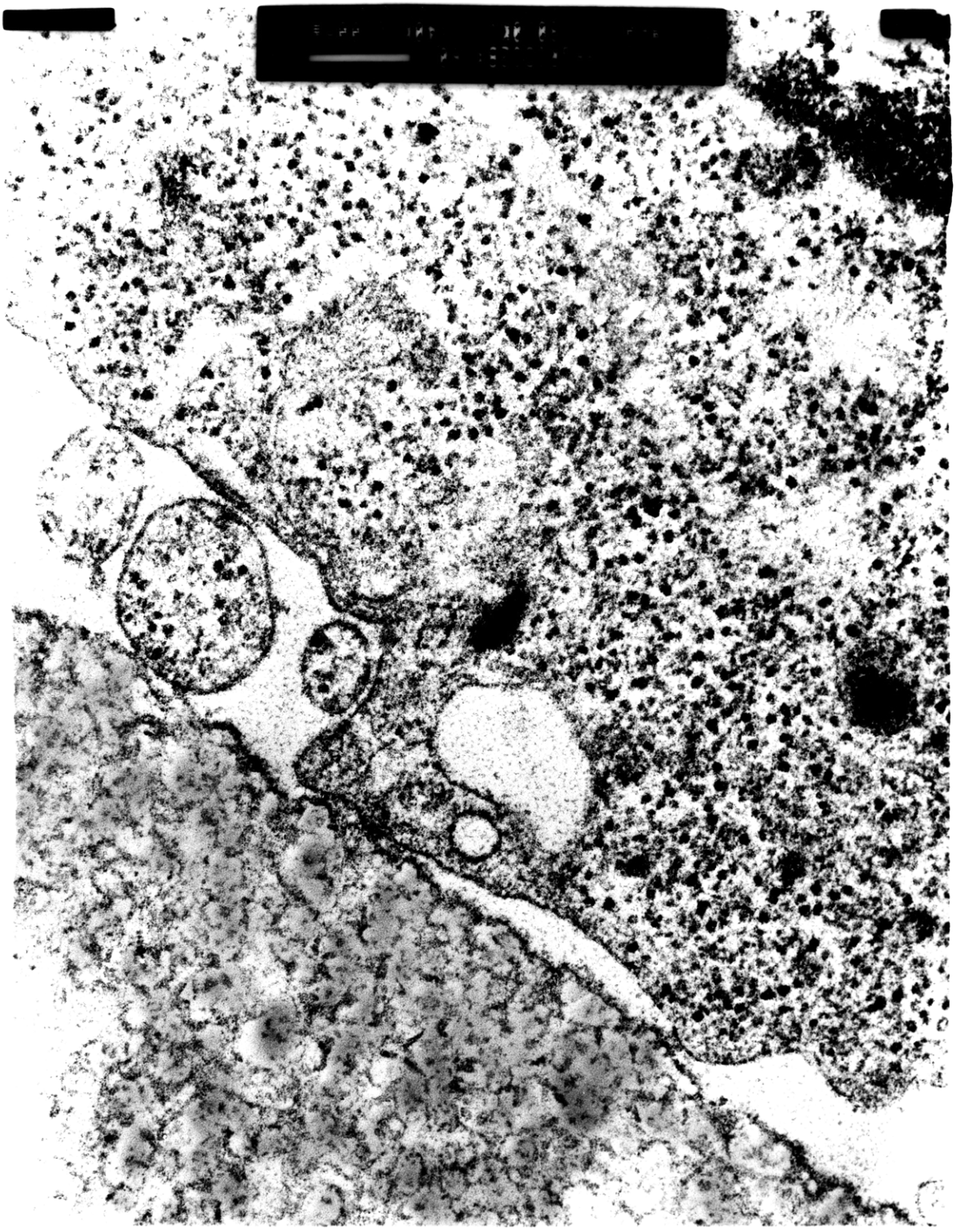

Figure 4.B.2

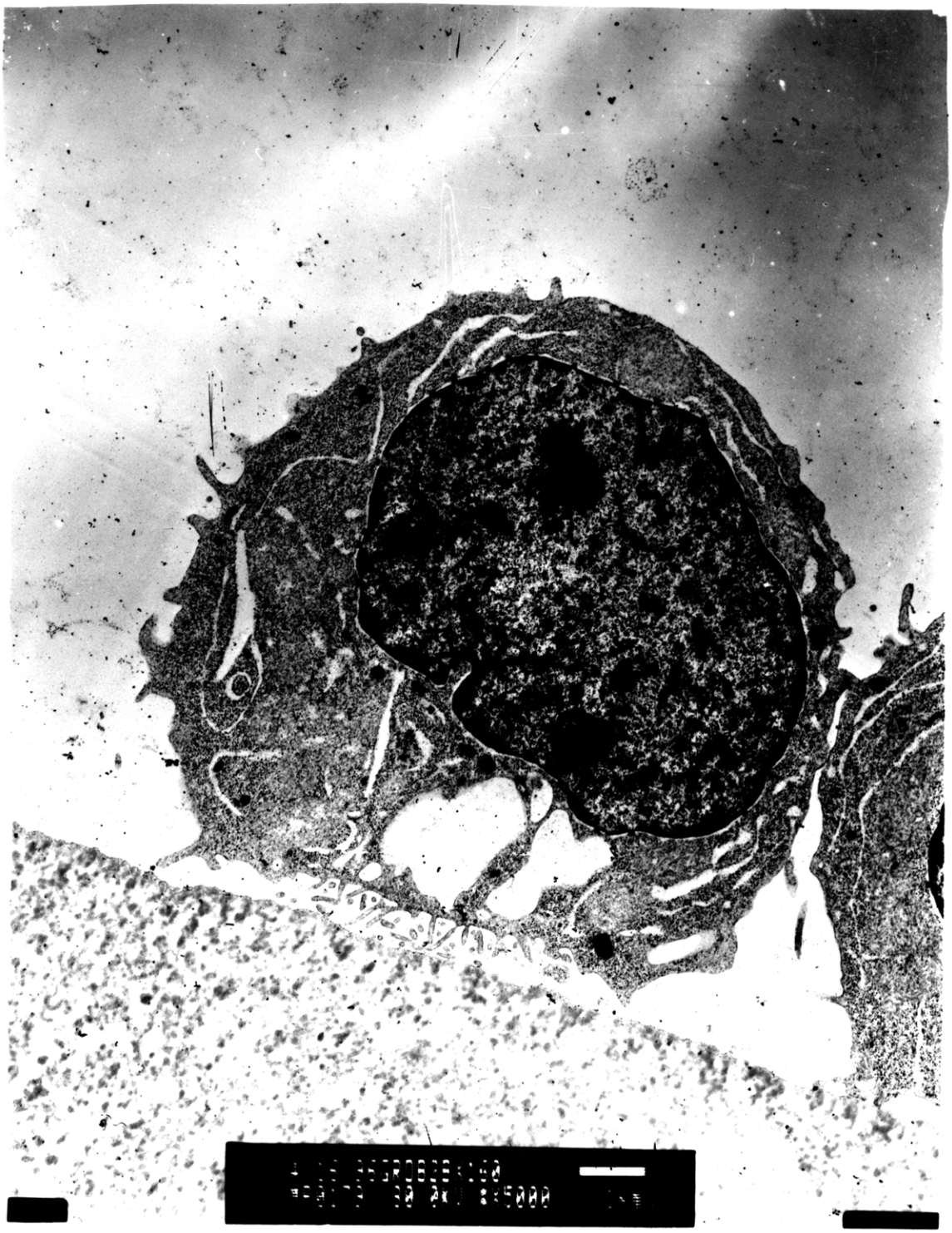

Figure 4.B.3

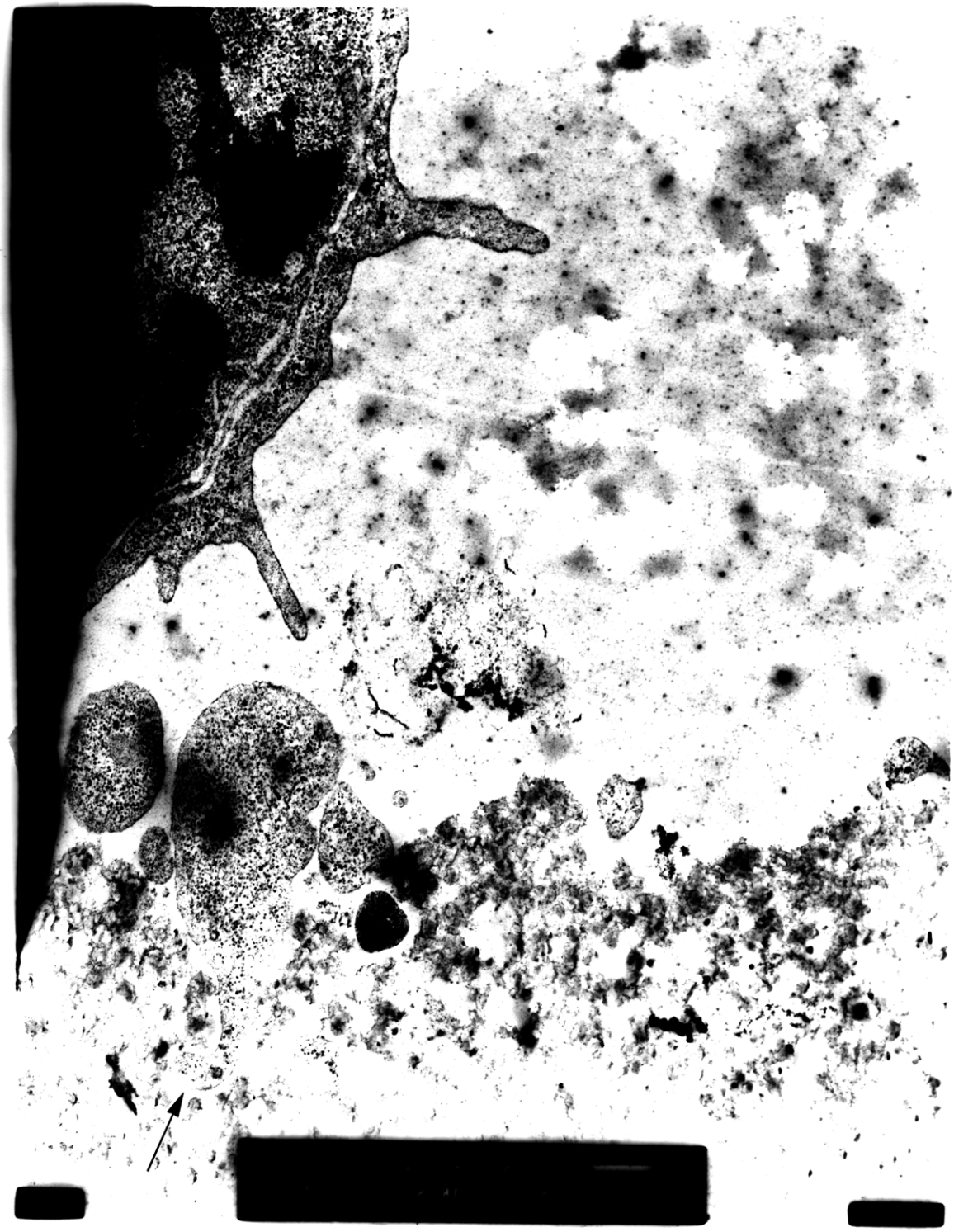

Figure 4.B.4

Figure 4.B.5

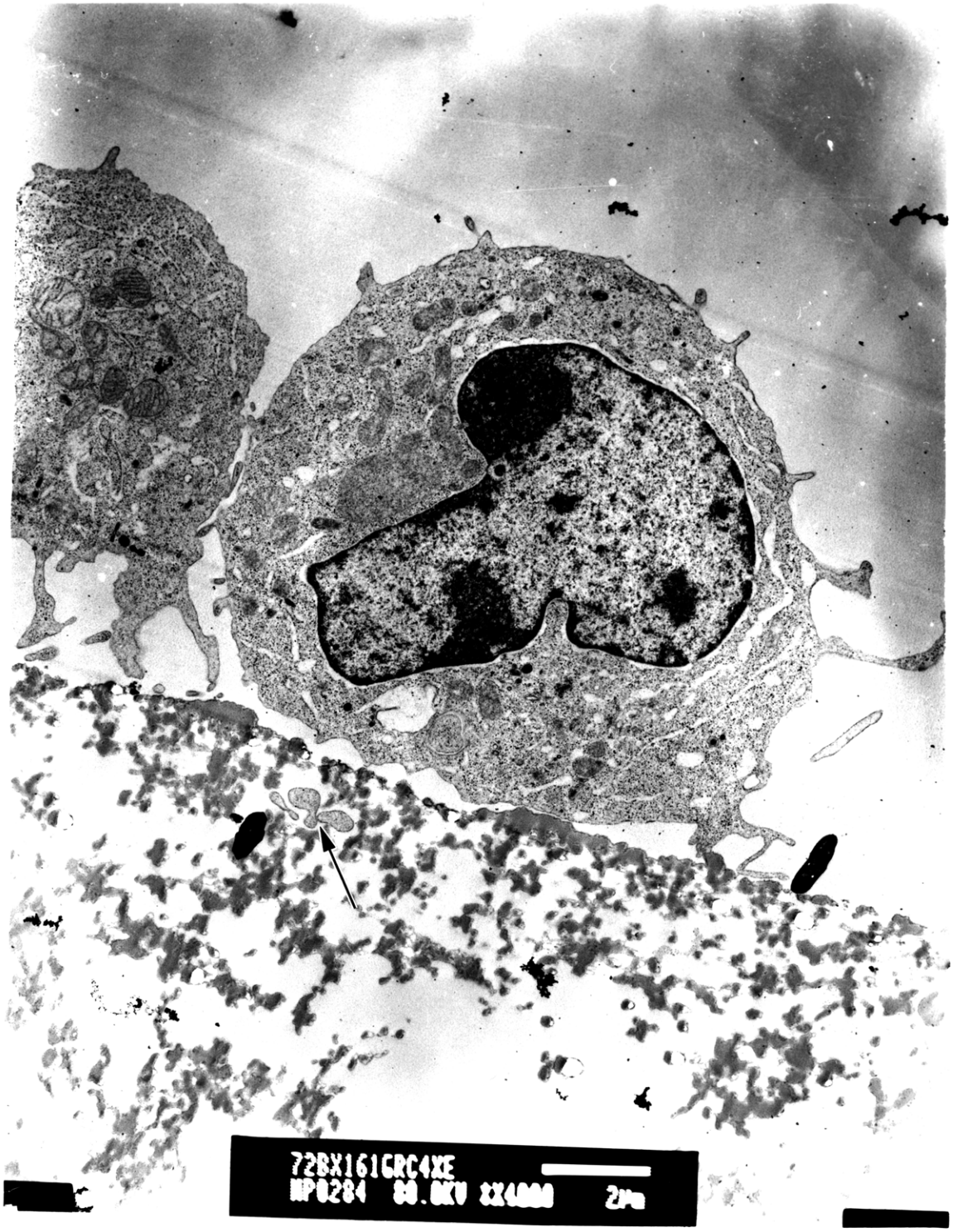

Figure 4.B.6

Captions for Figures 4.B.1 to 4.B.6

Figure 4.B.1 TEM photomicrograph of an HL-60 cell, preincubated with anti-CD33, loaded by filtration onto a Type B fiber showing typical flattened contact area morphology. Bar in legend represents 1 μm. Black area is a grid bar on the sample holder.

Figure 4.B.2 TEM photomicrograph of an HL-60 cell, preincubated with anti-CD33, loaded by filtration onto a Type B fiber showing close up of region of close contact between cell and fiber. Bar in legend represents 200 nm.

Figure 4.B.3 TEM photomicrograph of an HL-60 cell, preincubated with anti-CD33, loaded by filtration onto a Type B fiber displaying an irregular, villous contact area morphology. Bar in legend represents 1 μm.

Figure 4.B.4 TEM photomicrograph of an HL-60 cell, preincubated with anti-CD33, loaded by filtration onto a Type B fiber. Cell has infiltrated membrane at site of large pore or defect (arrow). Bar in legend represents 500 nm.

Figure 4.B.5 TEM photomicrograph of an HL-60 cell, preincubated with anti-CD33, loaded by filtration onto a Type E fiber showing typical flattened contact area morphology. Bar in legend represents 1 μm.

Figure 4.B.6 TEM photomicrograph of an HL-60 cell, preincubated with anti-CD33, loaded by filtration onto a Type E fiber where the cell has infiltrated the membrane (arrow). Bar in legend represents 2 μm.

magnification from 20,000× to 100,000×). The results for HL-60 target cells loaded by filtration onto Type B, C, and E fibers are shown in table 4.B.1. Measured values for maximum cell and contact area diameters were corrected to reflect the true three dimensional maximum diameters using morphometric analysis as described in section 3.10. Average measured diameters were multiplied by $4/\pi$ to obtain the true average maximum diameters (Weibel, 1969). The values shown in table 4.B.1 were very similar from fiber to fiber, and were also similar to those previously determined for HL-60 target cells loaded onto Type B rpA-coated fibers by gravity (see section 3.10).

Table 4.B.1 *Morphometric Analysis of Filtration-Loaded HL-60 Cells Specifically Adsorbed To Hollow-Fiber Membranes*

	Corrected Diameters (μm)			
	Cell			
Hollow-Fiber	// to Surface	⊥ to Surface	Contact Region	Min. Separation (Å)
Type B	12.6 ± 2.4 (n=29)	10.3 ± 2.0 (n=29)	10.5 ± 3.9 (n=28)	212 ± 60 (n=26)
Type C	12.0 ±3.1 (n=8)	11.7 ± 2.3 (n=8)	11.1 ± 4.5 (n=28)	209 ± 50 (n=4)
Type E	12.1 ± 1.7 (n=11)	11.2 ± 2.7 (n=11)	8.7 ± 2.5 (n=11)	215 ± 74 (n=3)

Results expressed mean ± SD for n cells.

4.10 Appendix C. Theoretical Estimates of Attachment Strength and Critical Removal Pressures

4.10.1 Purpose

The purpose of this appendix is to compare the magnitude of the experimentally applied pressure to the critical pressures predicted for cell removal by the methods discussed

in chapter 2.

4.10.2 Methods

The theoretical models presented in chapter 2 were used to determine the equilibrium number of bonds/cell, the critical detachment force/bond, the critical transmembrane pressure drop for anisotropic fibers, the minimum transmembrane pressure drop for isotropic membranes, and the critical shear stress necessary for cell removal. In addition, a calculation of the minimum critical transmembrane pressure drop was performed assuming that the transmembrane pressure drop occurs over the thin region of lowest porosity near the retentive surface of the fiber and that this region is isotropic in structure. Some parameters were assumed, while the majority were derived from measurements. The total number of target cell surface markers was assumed to be 50,000 per cell. Calculations were made both for fixed and freely mobile cell surface markers. For the indirect binding of cells to rpA-coated fibers, the affinity constant for reaction in solution was taken as 6.25×10^6 M^{-1} which has been previously measured for a protein A-mouse IgG bond at pH 7.4 (Kuo and Lauffenburger, 1993). This is most likely a high estimate since it has been determined that for bonds in series, such as with our experimental system, the specific adhesion strength of the linkage is considerably less than for single bonds (Saterbak and Lauffenburger, 1996). For rpA-coated fibers, the active ligand density was determined from the capacity of the fiber to bind mouse IgG2b (from table 4.3) and the specific surface area of the fiber. The hydraulic permeability of the membranes was determined as discussed in the materials and methods section and the permeability constant was determined from the average value by multiplying by the viscosity of water at 25 °C (0.9 cp). The average cell diameter was determined by light scattering (see section 3.9), and the average contact area diameter, minimum separation distance, fiber porosity, and fiber thickness from electron microscopic measurements discussed in the text

and appendices A and B. The "skin" thickness is the thickness of the low porosity region near the retentive surface observed in electron microscopic cross-sections.

4.10.3 Results

4.10.3.1 Indirect Binding of anti-CD33 Coated HL-60 Cells to rpA-Coated Fibers

Measured Parameter	Type B	Type C	Type E
Ligand density	8.4×10^{11} cm^{-2}	9.2×10^{11} cm^{-2}	9.4×10^{11}cm^{-2}
Permeability constant	5.0×10^{-13} m	6.5×10^{-12} m	6.9×10^{-12} m
Cell diameter	14 μm	14 μm	14 μm
Contact area diameter	10.5 μm	11.1 μm	8.7 μm
Separation distance	212 Å	209 Å	215 Å
Porosity	0.124	0.199	0.210
Fiber thickness	200 μm	200 μm	250 μm
"Skin" thickness	2.5 μm	10 μm	7.5 μm

The results of the simulation are shown in table 4.C.1. The simulation predicts the critical levels for which an average cell would be detached. In actuality, for each condition, only a fraction of the cells are likely to be removed because of cell and fiber heterogeneities (see chapter 3). Heterogeneities will be present in both the cells and the fibers. Examples of parameters which are likely to be sources of significant heterogeneity are cell surface marker expression, contact area size and morphology (especially with respect to separation distance), as well as fiber porosity, morphology and surface characteristics. Because it would be very difficult to accurately determine the distribution of these and other properties for a given experiment, simulation results should be considered as only a semi-quantitative prediction of average behavior and the effect of experimental parameters.

Transmembrane pressure differences applied for cell detachment were 760 mmHg for

Type B and C fibers, and 500 mmHg for Type E fibers. The simulation results shown in table 4.C.1 suggest that for anisotropic membrane morphology, the experimentally applied pressures should be in excess of those required to detach cells with typical size and morphology, and with at least 50,000 fixed or mobile cell surface markers, from all of the fibers. If the fiber morphology is closer to isotropic, the simulations suggest that for mobile surface markers, it is unlikely that removal would occur with Type C and Type E fibers because of their thicker "skin" region. Experimentally, however, pressure appeared ineffective at removing a significant fraction of target cells from any fiber. While the membrane morphology may be a detrimental factor for Type C and E fibers, it does not explain the lack of correlation with the results predicted for and observed with Type B fibers using experiments with gravity settling (see chapter 3 results for Lot 2 (Type B) fibers and section 3.12) suggesting the cause of the irreversible attachment may be another factor such as infiltration of the cell into the pores. The predicted critical shear stresses for cell detachment are very high, especially for cells with freely mobile markers, higher than any to which the cells were exposed during experiments.

Table 4.C.1. *Critical Detachment Pressures and Shear Stress from Theoretical Predictions For HL-60 Binding to rpA-Coated Hollow Fibers in Small Modules*

	Attachment (Fixed/Mobile)	Detachment (Fixed/Mobile)				
Fiber	# Bonds	F_b^{crit} (μdynes)	τ (dynes/cm^2)	ΔP Anisotropic Membrane (mmHg)	ΔP_{min} Isotropic Membrane (mmHg)	ΔP_{min} Isotropic Skin Region (mmHg)
Type B	6,200/49,990	6.1/6.0	560/4,500	56/450	3,800/30,000	90/720
Type C	6,300/49,990	6.1/6.1	600/4,800	34/270	3,300/26,000	200/1,600
Type E	3,800/49,980	6.2/6.1	290/3,800	35/450	5,100/67,000	200/2,500

4.11 References

Azad, A.R.M.,and R.A. Goffe. 1990. Process for the covalent surface modification of hydrophobic polymers and articles made therefrom. Patent Cooperation Treaty Publication No. WO 90/04609.

Bird, R.B., W.E. Stewart, and E.N. Lightfoot. 1960. Transport Phenomena. John Wiley & Sons, New York, NY.

Collins, S. J., R. C. Gallo, and R. E. Gallagher. 1977. Continuous growth and differentiation of human myeloid leukaemic cells in suspension culture. *Nature.* 270:347-349.

Folkman, J., and A. Moscona. 1978. Role of cell shape in growth control. *Nature.* 273:345-349.

Granger, J., J. Dodds, and N. Midoux. 1989. Laminar flow in channels with porous walls. *The Chemical Engineering Journal.* 42:193-204.

Holton, O.D., and J.J. Vicalvi, Jr. 1991. Optimization of monoclonal antibody immobilization on hydrazide-preactivated hollow fiber membrane. *BioTechniques* 11:662-665.

Klein, E., E. Eichholz, and D.H. Yeager. 1994. Affinity membranes prepared from hydrophilic coatings on microporous polysulfone hollow fibers. *Journal of Membrane Science* 90:69-80.

Kuo, S.C., and D.A. Lauffenburger. 1993. Relationship between receptor/ligand binding affinity and adhesion strength. *Biophysical Journal.* 65:2191-2200.

Nadkarni, J.S., J.J. Nadkarni, P. Clifford, G. Manolov, E.M. Fenyö, and E. Klein. 1969. Chacterization of new cell lines derived from Burkitt lymphomas. *Cancer.* 23:64-79.

Ngo, T.T. 1986. Facile activation of sepharose hydroxyl groups by 2-fluoro-1 methylpyridinium toluene-4-sulfonate: Preparation of affinity and covalent chromatographic matrices. *Bio/Technology.* 4:134-137.

Nordon, R.E., B.K. Milthorpe, K. Schindhelm, and P.R. Slowiaczek. 1994. An experimental model of affinity cell separation. *Cytometry.* 16:25-33.

Nordon, R.E., D.N. Haylock, L. Gaudry, and K. Schindhelm. 1996. Hollow-fiber affinity cell separation system for $CD34^+$ cell enrichment. *Cytometry.* 24:340-347.

Reynolds, E. S. 1963. The use of lead nitrate at high pH as an electron opaque stain in electron microscopy. *Journal of Cell Biology.* 17:208.

Saterbak, A., and D.A. Lauffenburger. 1996. Adhesion mediated by bonds in series. *Biotechnology Progress.* 12:682-699.

Stich, T. 1990. Determination of protein covalently bound to agarose supports using bicinchoninic acid. *Annals of Biochemistry.* 159:138-142.

Weibel, E.R. 1969. Stereological principles for morphometry in electron microscopic cytology. *International Review of Cytology.* 26:235-302.

Chapter 5. Infiltration of HL-60 and Namalwa Cells Into Pores of Microporous, Hollow-Fiber Membranes Under Conditions of Positive-Pressure Filtration.

5.1 Abstract

In this chapter, we investigated the ability of HL-60 leukemic leukocytes and Namalwa lymphoma cells to infiltrate into the pores of a variety of hollow-fiber microporous membranes with effective pore diameters ranging from 0.01 μm to 2.1 μm during loading of cells onto the fiber surface by filtration induced by positive hydrostatic pressure. The hollow-fiber membranes employed were chemically modified to provide a hydrophilic surface with low non-specific binding, but with specific affinity for a subset of the cells tested. The fibers had a heterogeneous pore size distribution, irregular pore shapes, and tortuous flow paths within the membrane. Transmission electron microscopy was employed for determination of cellular infiltration into pores. Cells could infiltrate into the pores of all the membranes tested at pressures as low as 13 mmHg. Cell infiltration into porous membranes did not occur when cells were loaded by gravity, and specific affinity between the cell and the substrate was not required. Infiltration was not prevented or reduced by inhibiting cytoskeletal rearrangement with cytochalasin-D or cellular metabolism with a combination of sodium azide and 2-deoxy-D-glucose, but was drastically reduced by pre-fixing the cells with glutaraldehyde. We conclude that the observed cellular infiltration was not caused by active cell motility, but was due primarily to passive deformation or aspiration of parts of the cell into the porous membrane during filtration. Our results suggest that membranes with a homogeneous pore size distribution may be more ideally suited for applications where it is desired to load

leukocytes onto the surface by filtration for subsequent recovery. This study provides insights into leukocyte mechanical properties and has practical relevance in applications employing filtration for cell loading onto porous substrates such as affinity membrane-based cell separation.

5.2 Introduction

Recent work in our laboratory has demonstrated the utility of using hollow-fiber membranes and physical detachment forces for selective leukemic white blood cell binding and detachment when the cells are loaded onto the membranes by gravity (see chapter 3). Cell deposition by filtration is faster, more efficient, easier to control, and yields more uniform cell contact times than gravity settling. However, we have noticed in previous experiments (see chapter 4) that cells deposited by gravity can be removed more easily than cells deposited by filtration. Analysis of target cells loaded onto membranes by filtration with transmission electron microscopy (TEM) indicated that portions of the cell membrane and cytoplasm of some cells observed had infiltrated into the porous structure of the membrane (see chapter 4, appendix B). In this chapter, we will investigate the mechanism of infiltration of leukemic white blood cells into hollow fiber membranes in detail.

Cell infiltration can be an active or a passive process. White blood cells such as leukocytes and lymphocytes commonly marginate from the bloodstream into tissue through tight junctions between cells such as endothelial cells (Lin et al., 1995; Noris and Remuzzi, 1995; Hunt et al., 1996). The process typically occurs when the leukocytes adhere to the substrate via adhesion receptors, project pseudopods into intercellular junctions widening them sufficiently so that the cell can move between the cells by a process of active locomotion (Bakowski and Tschesche, 1992; Lin et al., 1995; Noris and Remuzzi, 1995). Active cell

migration can also occur through substrates such as reconstituted basement membranes *in vitro* by motile cells such as leukocytes and metastatic tumor cells (Terranova et al., 1986). In all cases, active migration requires the ability of the cell to adhere to the substrate, and requires the cell to move via a process involving active cell metabolism and cytoskeletal rearrangement. Substances which inhibit metabolism or prevent cytoskeletal rearrangement are effective at inhibiting active cell migrations and other forms of cell motility (Carter, 1967; Zigmond and Hirsch, 1972; Horvath and Kellie, 1990; Haug et al., 1993; Stracke et al., 1993).

Cells can also undergo passive deformations under the influence of external forces. Such deformation is what enables red blood cells and leukocytes to traverse small capillaries which are typically somewhat smaller than the undeformed cell diameter. Previous work has studied the passive mechanical behavior of leukocytes by several methods, including analyzing filtration of cells through capillary sized pores (5 - 10 μm in diameter) in synthetic membranes (Lichtman and Kearney, 1976; Hallows and Frank, 1992), and complete or partial aspiration of cells with micropipets (Evans and Yeung, 1989; Needham and Hochmuth, 1992; Zhelev et al., 1994; Ting-Beall et al., 1995; Tsai et al., 1996). Micropipet experiments have shown that leukocyte membranes and cytoplasm can be aspirated into pipets with diameters as small as 0.48 μm (Zhelev et al., 1994).

Models proposed to explain the passive mechanical properties of leukocytes view the cell as a liquid-like object having a persistent surface tension supplied by a cytoskeletal "cortex" underlying and supporting the plasma membrane (Evans and Kukan, 1984; Yeung and Evans, 1989) which has been observed to be as thick as 0.05 - 0.1 μm in TEM micrographs (Bray et al., 1986; Esaguy et al., 1989). This model, which has proven very successful at interpreting experimental micropipet aspiration data (eg. Evans and Yeung, 1989; Needham and Hochmuth, 1992; Tsai et al., 1993) predicts that a leukocyte will not enter a

pore until a pressure is applied to the membrane above a critical threshold which is a function of the surface "cortical" tension of the cell, the pore size, and, for small pores (< 2.4 μm in diameter), the cortex thickness and bending modulus (Zhelev et al., 1994). Once the critical pressure is exceeded, the cell will flow into the pore continuously within the constraints of its excess plasma membrane surface area. However, these models have been developed for, and the experiments have utilized, cylindrical channels with well defined, uniform geometry and negligible frictional resistance to cell entry. The hollow-fiber membranes we have utilized for cell separation, and with which we have observed cell infiltration have irregularly shaped pores and highly tortuous flow paths which may greatly restrict the ability of cells to passively deform. In addition, the typical surface pore dimensions on these membranes are often smaller than the channel diameters used previously by other investigators studying leukocyte deformation into small holes.

Our purpose in this study was to investigate infiltration of leukemic leukocytes into hollow-fiber membranes with a microporous morphology in a systematic way. We used the same hollow-fiber membranes used previously in chapter 4. Cells loaded by filtration were loaded at constant flowrates with transmembrane pressure drops similar to those used in chapter 4. TEM analysis was employed to determine the effect of pore size and loading pressure on infiltration. We also determined the effect on infiltration of cell-fiber affinity by using both target and non-target cells with affinity membranes. We determined whether infiltration requires active cell motility by performing experiments where cell metabolism was poisoned and ATP levels depleted with sodium azide and 2-deoxy-D-glucose (Popov and Margolis, 1988; Horvath and Kellie, 1990), and by performing experiments where cytoskeletal rearrangement was inhibited with cytochalasin-D (Schliwa, 1982; Stracke et al., 1993). Our results strongly suggest that infiltration is a passive process which depends on the membrane

pore size and applied loading pressure.

5.3 Materials and Methods

5.3.1 Functionalized Fibers

The same four lots of polyethersulfone/polyethylene oxide hollow-fiber microporous membranes (kindly provided by Sepracor Inc., Marlborough, MA) designated by the manufacturer as lots A3194A4 (Type A), X3257B2 (Type B), X3257C2 (Type C), and XE3182A (Type E) were used in this study as were used in chapter 4, . The preparation, characterization, and properties of the hollow-fiber membranes were described previously in chapter 4.

5.3.2 Cell Lines

Two human cell lines, Namalwa and HL-60 were used for experiments. Namalwa is a Burkitt's lymphoma cell line (Nadkarni et al., 1969), and HL-60 is a pro-myelocyte leukemia cell line (Collins et al., 1977) which expresses CD33 markers on its surface. Cell lines were grown in continuous suspension culture in tissue culture flasks at 37° C in a humidified air atmosphere containing 5% CO_2 in RPMI media supplemented with 25 mM HEPES buffer, 10% fetal bovine serum (FBS), 4 mM L-glutamine, 50 IU/ml penicillin and 50 μg/ml streptomycin (BioWhittaker, Walkersville, MD). Cell cultures were passaged approximately every 48 hr. Cells were used for experiments while in their log growth phase.

5.3.3 Experimental Apparatus For Loading Cells Onto Fibers by Filtration

Figure 5.1 (A) shows a schematic diagram of the FMP-functionalized hollow fibers used in this study. Small (1 to 1.5 cm) lengths of 1/16 " inner diameter Tygon tubing (Tygon S-50-HL, Norton Performance Plastics Corporation, Akron, OH) were glued with hot-melt glue (Surebonder®, FPC Corporation, Wauconda, IL) to each end to facilitate handling and

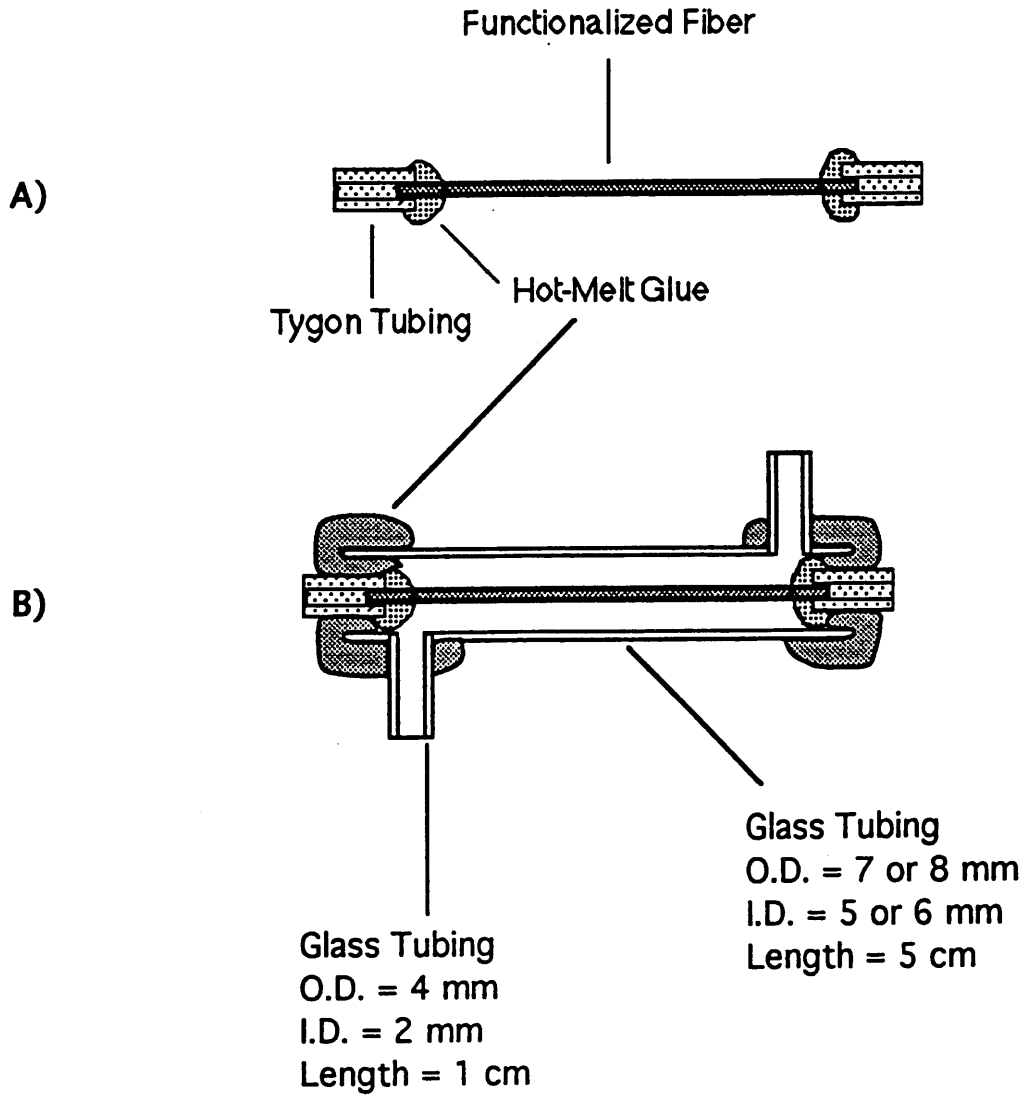

Figure 5.1 Schematic diagram of cross-section of functionalized fiber as prepared for cell infiltration experiments. A) Fiber alone. B) Fiber in module.

pressurization. After the plastic tubing was attached, the active length of the fiber available for cell loading by filtration was 3 to 4 cm. The fibers were then coated with rpA as previously described in chapter 4. The shell side of the small modules was constructed from Pyrex glass tubing (Corning Inc., Corning, NY) by the MIT glass blower (see figure 5.1 (B)). The main tube was 5 cm in length with an inner diameter of 5 or 6 mm and an outer diameter of 7 or 8 mm. The side tubes for cross-flow through the shell were 1 cm in length with an inner diameter of 2 mm and an outer diameter of 4 mm, and were located 0.5 cm from each end in the configuration shown in cross-section in figure 5.1 (B). The rpA-coated fiber was placed into the shell and each end was sealed with hot-melt glue in such a way that the active length of the fiber was kept submerged at all times in PBSA. Figure 5.2 (A) and (B) shows a schematic diagram of the set up used for measurement of hydraulic permeability, and cell loading experiments for flow into the shell (A) and lumen (B). The apparatus was constructed using 1/16 " or 5/32 "I.D. Tygon tubing for the shell-side configuration shown in figure 5.2 (A), and 1/16 " I.D. Tygon tubing for the lumen-side configuration shown in figure 5.2 (B). Positive pressure and flow was generated using a two-channel syringe pump with a synchronous, surge-less motor (Model 975, Harvard Apparatus, South Natick, MA), and pressure was measured with a stainless steel test gauge (0 to 760 mmHg, Ashcroft, Stratford, CT) or a digital pressure monitor (Model SP1405, Gould Statham, Oxnard, CA). In addition, short lengths (2 to 10 cm) of 1/16 " I.D. Tygon tubing with 3-way Luer stopcocks ((3) and (4) in figure 5.2) were attached to the fiber with small polypropylene fittings, and short lengths (2 to 3 cm) of 5/32 " I.D. Tygon tubing were attached to the shell with a 3-way Luer stopcock (1) at the inlet, and a 1-way Luer stopcock at the outlet (2). The module and tubing was pressure tested for leaks at 15 psig in the lumen side, and 10 psig in the shell side. The module was stored filled with PBSA until use.

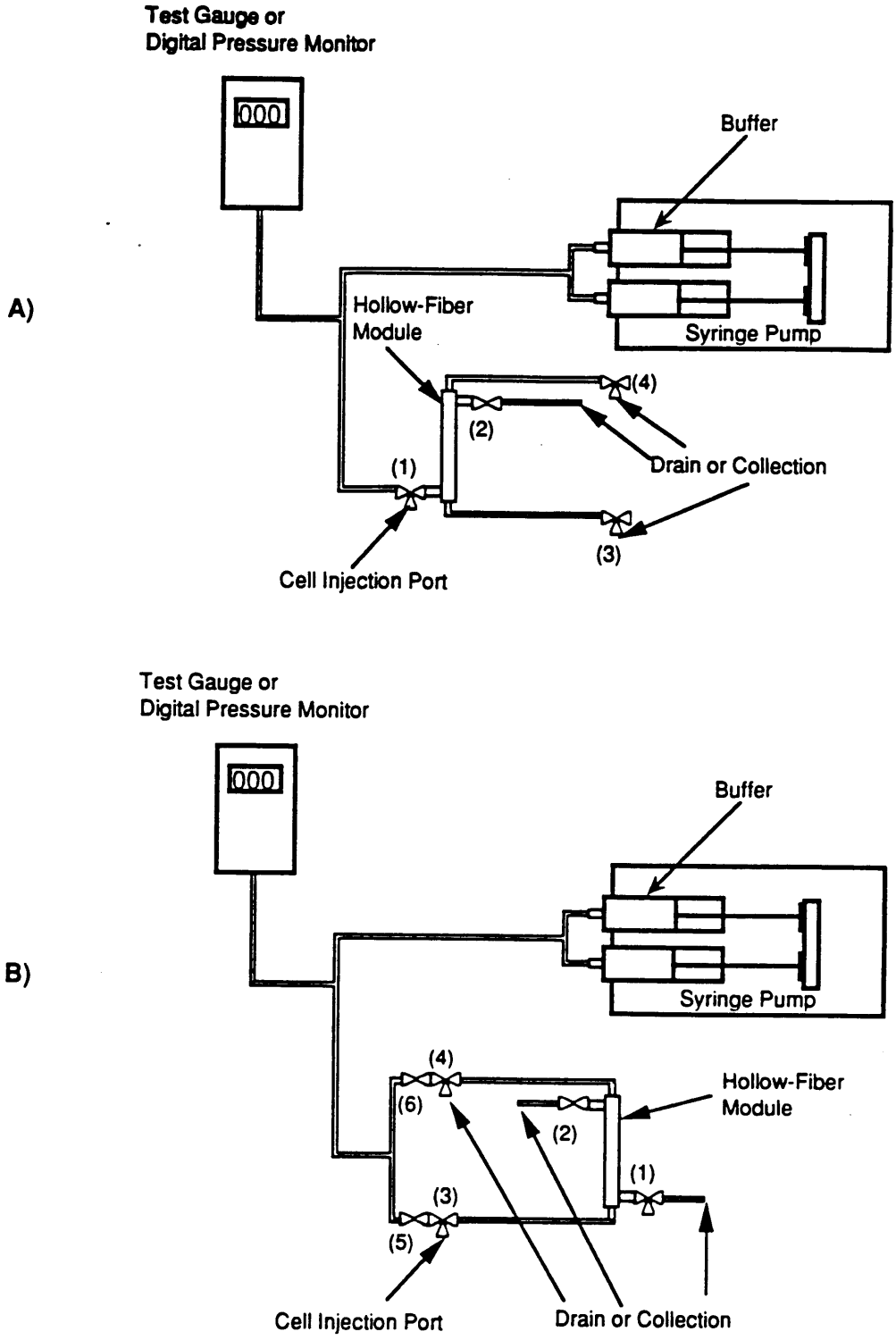

Figure 5.2 Schematic diagram of experimental apparatus as set up for loading cells from the shell side of the module onto the outside surface of fibers as in A), or loading cells onto the lumen of fibers as in B). Numbers in parentheses refer to stopcocks (see text).

5.3.4 Procedure for Cell Loading onto Fibers by Filtration

Prior to use, the fibers in modules were washed extensively with Dulbecco's phosphate buffered saline without calcium and magnesium (DPBS, Sigma, St. Louis, MO) to remove the sodium azide in the storage buffer. An aliquot of cells from culture was added to a test tube containing Trypan Blue dye, and live and dead cells were counted with a hemacytometer (Reichert Scientific Instruments, Buffalo, NY). A sufficient number of cells to perform the experiment were centrifuged (400 × g, 4°C, 10 min) and the pellet was resuspended in cold DPBS (pH 7.4) for washing. The cells were centrifuged and washed once more with cold DPBS. For some experiments, HL-60 cells were made to have affinity for the rpA fiber by resuspending the pellet from the first centrifugation in cold RPMI media containing 10 % FBS and a 1:500 dilution of ascites containing approximately 5 mg/ml anti-CD33 mAb at a concentration of 5 to 10 × 10^6 cells/ml and incubating on ice for 30 min. These cells were subsequently washed twice with cold DPBS as above. Finally, the cells were centrifuged and resuspended at 2 to 5 × 10^6 cells/ml in cold DPBS supplemented with 1 % w/v BSA which had been pre-filtered through a 0.1 μm membrane. Cell suspensions were kept on ice until immediately prior to use.

For experiments with Type B or Type C fibers, cells were loaded onto the retentive outer surface of the fiber via filtration from the shell to the lumen. The shell was initially drained of buffer by opening stopcocks (1) and (2) in figure 5.2 (A). The cell suspension was then injected into stopcock (1) to fill the shell. Stopcock (2) was closed, and stopcock (1) was set to receive flow of DPBS from the pump. Stopcock (4) was opened and the pump was turned on and set for a constant flowrate (about 0.2 ml/min) which was maintained until a sufficient volume of permeate was collected to ensure that 1 to 2 × 10^6 cells were filtered onto the fiber. The maximum pressure attained during filtration was recorded. The pump

was then stopped, stopcock (4) was closed, stopcock (2) was opened, and excess cells were washed out of the shell by gently pumping DPBS through the shell (wall shear at fiber surface < 1 dyne/cm^2). After washing, the module was drained and immediately refilled with fixative (1 % w/v glutaraldehyde in PBS pH 7.4), and the cells were fixed in the module for 60 min. All procedures were carried out at room temperature.

For experiments with Type E or Type A fibers, cells were loaded onto the retentive lumen surface of the fiber via filtration from the lumen to the shell. The lumen was initially drained of buffer by opening stopcocks (3) and (4) in figure 5.2 (B). The cell suspension was then injected into stopcock (3) to fill the lumen of the fiber and attached tubing. For some experiments the cells were loaded into both sides of the lumen simultaneously with the module in a horizontal position. In such cases, stopcocks (3) and (4) were set to receive flow od DPBS from the pump. Stopcock (2) was opened and the pump is turned on and set for a constant flowrate (about 0.2 ml/min) which was maintained until a sufficient volume of permeate was collected to ensure that 1 to 2 × 10^6 cells were filtered onto the fiber. For other experiments, cells were loaded into one end of the lumen for half the time, and into the alternate end for the other half. In such cases, stopcock (3) or (4) was set to receive flow of DPBS from the pump and flow to the other end of the fiber was prevented by closing stopcock (5) or (6). After one half the desired volume of permeate was collected through stopcock (2), stopcocks were adjusted to allow flow to the alternate end of the lumen. These measures were taken to ensure even distribution of the cells on the fibers. The maximum pressure attained during filtration was recorded. The pump was then stopped; stopcock (2) was closed; stopcock (4) was opened to drain, and excess cells were washed out of the fiber by gently pumping DPBS through the lumen (wall shear in fiber < 1.5 dyne/cm^2). After washing, the shell was drained and immediately refilled with fixative (1 % w/v glutaraldehyde

in PBS pH 7.4). Fixative was pumped into the lumen at the same flowrate used for washing, and the cells were fixed in the module for 60 min. All procedures were carried out at room temperature.

For some experiments cells were loaded by gravity onto the fibers instead of by filtration. For cells loaded onto the outer surface of type B fibers, fibers were not placed in modules but were used as shown in figure 5.1 (A). In this case, 5 ml of cell suspension containing 25×10^6 cells was added to a T25 tissue culture flask (Falcon, Beckton Dickinson, Franklin Lakes, NJ). The fiber was added to the flask, and the flask was tilted at a 45° angle to maximize the number of cells which settle onto the surface. The cell suspension was incubated with the fiber for 30 min at 4 °C and then at room temperature for an additional 45 min. The suspension was very gently agitated every 15 min to resuspend nonadsorbed cells. After incubation, the supernatant was gently aspirated, leaving enough liquid to cover the fiber. The fiber was gently washed three times with 25 ml DPBS dispensed at about 25 ml/min from a pipet into the flask, but away from the fiber, and the wash fluid was aspirated each time. After the final wash, 5 ml of fixative was added to the flask and the cells were fixed for 60 min at room temperature. For cells loaded onto the lumen surface by gravity (in type E fibers), the fiber was contained in a module and a cell suspension containing 3.5×10^7 cells/ml was injected into the fiber lumen. The module was placed in a horizontal position, and the cells were allowed to settle for 15 min. The module was then rotated 180°, and the cells were allowed to settle onto the opposite side for an additional 15 min. The excess cells were then washed out, and the cells were fixed for 60 min as previously described. All steps were performed at room temperature.

5.3.4.1 Experiments to Investigate the Role of the Cytoskeleton and Active Metabolism on Infiltration.

Three separate experiments were performed to investigate the effect of the cytoskeleton and active metabolism on infiltration of cells into membranes during filtration. In the first experiment, the cytoskeletal proteins were stabilized by pre-fixing the cells before loading and filtration. Cells were counted and washed before except washes were performed at room temperature, and 10^7 cells were re-suspended in 10 ml of 1 % w/v glutaraldehyde in PBS and fixed at room temperature for 60 min. The fixed cells were then washed twice with room temperature DPBS, resuspended in DPBS with 1 % w/v BSA at 5×10^6 cells/ml, filtered onto a Type E fiber, and fixed after loading as previously described except that the load flow rate was about 0.8 ml/min.

In the second experiment, cytoskeletal F-actin was disrupted with cytochalasin-D prior to loading and fixation using a protocol similar to Ting-Beall et al. (Ting-Beall et al., 1995). Cells were counted, washed at room temperature, and re-suspended at 5×10^6 cells/ml in 2 ml of DPBS supplemented with 25 mM HEPES, 1 % w/v BSA and a 1:100 dilution of 2 mM cytochalasin-D (Sigma, St. Louis, MO) in dimethylsulfoxide (DMSO) yielding a final concentration of 10μM cytochalasin-D and 0.5 % v/v DMSO. The cell suspension was incubated for 15 min in this solution before loading and filtration onto a Type E fiber. Loading, filtration, washing, and fixation were performed as previously described except that all DPBS buffer used for loading and washing also contained 10μM cytochalasin-D and 0.5 % v/v DMSO.

In the third experiment, active metabolism was inhibited and ATP levels depleted with sodium azide and 2-deoxy-D-glucose (DOG) prior to loading and fixation using a protocol adapted from those of Popov and Margolis and Horvath and Kellie (Popov and Margolis,

1988; Horvath and Kellie, 1990). Cells were counted and centrifuged (200 × g, 15 min) at room temperature, and cells were re-suspended at 3.3×10^6 cells/ml in 6 ml of Dulbecco's Modified Eagle Medium without glucose (Gibco BRL, Life Technologies Inc., Grand Island, NY) supplemented with 27 mM DOG, and 20 mM sodium azide (DOGA). The cell suspension was incubated for 90 min in this solution at 37 °C in an incubator with a humidified air environment containing 5 % CO_2. After incubation, cells were washed twice with cold DOGA and resuspended in DOGA supplemented with 1 % w/v BSA at 4 °C. For loading onto Type C fibers, filtration, washing, and fixation were performed as previously described except that all DPBS buffer used for loading and washing contained 27 mM DOG, and 20 mM sodium azide and the fixative was supplemented with 20 mM sodium azide.

5.3.5 Preparation of Samples for Transmission Electron Microscopy.

Samples of cells adhered to fibers were prepared for analysis by transmission electron microscopy (TEM) as follows. Glutaraldehyde-fixed cells adhered to fibers were washed three times with cold 0.1 M cacodylate buffer (pH 7.4) and post-fixed with 2 % w/v osmium tetroxide in 0.1 M cacodylate buffer for 1 hr at 4°C. Fibers were then washed with the cacodylate buffer and dehydrated through a graded series of ethanol/water mixtures. During the dehydration step with 70 % w/v ethanol, 0.5 % w/v uranyl acetate was added for en bloc staining. The dehydrated samples were then infiltrated with Spurr's low viscosity resin (Polysciences, Inc., Warrington, PA) in three steps through a graded series of propylene oxide/Spurr's resin mixtures. After infiltration and curing of the resin, thin sections (70 nm) were made in a direction normal to the surface of the fiber yielding cross-sectional views through the cells and fibers. Thin sections were collected on 200 mesh copper grids (Polysciences, Inc., Warrington, PA) and post-stained with 1 % w/v potassium permanganate for 5 min, 2 % w/v uranyl acetate for 30 min, and Reynolds lead citrate (Reynolds, 1963) for

5 min before observation at 80 KV with the TEM (JEOL 1200 EX II, JEOL, Peabody, MA).

5.4 Results

5.4.1 Surface Pore Diameter Range of Hollow-Fiber Membranes

Figures 4.4 and 4.5 (see chapter 4) showed SEM photomicrographs of the retentive surfaces of the hollow-fiber membranes. The surface pore diameter range measured for the membranes is summarized in table 5.1.

Table 5.1 *Surface Pore Diameter Range of Hollow-Fiber Membranes*

Fiber Type	Surface Pore Diameter Range (μm)
B	0.01 - 0.26
C	0.02 - 1.3
E	0.14 - 2.1
A	0.04 - 1.5

Figures 4.4 and 4.5 showed that the surface morphology and pore size and shape for the membranes was very heterogeneous. Type B (figure 4.4 (A)) and Type A (figure 4.5 (B)) membranes had long, narrow pores aligned axially along the fiber length. Type C (figure 4.4 (B)) and Type E (figure 4.5 (A)) had more randomly oriented and shaped pores. For all membranes, the pore structure and flow path of permeate (see also cross-sections in figure 4.6) appeared irregular and tortuous in dimension and direction. Type B fibers had the smallest pore diameters of the membranes used (0.01 - 0.26 μm). Table 5.1 indicates that Type A and Type C fibers were similar in pore diameter range (although not in shape as previously discussed) with the largest pores observed having an effective diameter of 1.3 to 1.5 μm for Type C and Type A respectively. Type E fibers had the largest pores with a pore diameter range of 0.14 to 2.1 μm.

5.4.2 Cell Filtration Experiments

Sections of cells observed on fiber samples by TEM were placed into two categories, those which have infiltrated the hollow-fiber membrane as evidenced by the appearance of cytoplasm beneath the surface of the membrane, and cells whose section did not show evidence of infiltration. Consecutive cells on a minimum of two sections from different parts of the fiber were included for each analysis. Only cells whose contact area and region of the hollow-fiber membrane below the cell were visible and free of obstruction (eg. by grid bars) were considered. In addition, no cell visible on the section whose diameter was less than about 50 % of the largest visible was considered (so that cells sectioned close to the center of their contact area were preferentially considered), nor were cells separated from the membrane by a distance of more than 25 % of their cell diameter. Determinations were judged at a minimum magnification of 10,000×. TEM photomicrographs were taken of a significant fraction of the cells included in the analysis. Maximum infiltration depth for each condition was measured from enlargements of the photomicrographs using precision calipers. Table 5.2 summarizes the results of the TEM analysis for each condition. Figures 5.3 to 5.14 show representative TEM photomicrographs for the conditions presented in table 5.3. The observations summarized in table 5.2 and shown in figures 5.3 to 5.6 clearly indicate that HL-60 cells treated in an identical manner as for the cell separation experiments of chapters 3 and 4 (pre-incubation with anti-CD33 (designated αCD33 in table 5.2)), will infiltrate all of the hollow fibers tested when loaded by filtration at the flowrates used previously in cell attachment/detachment studies (see chapter 4). Infiltrations typically appeared as tongues or balls of material at various depths beneath the surface of the fiber with a granularity and appearance consistent with cell cytoplasm surrounded by a plasma membrane. In many cases, infiltrations increased in diameter as they expanded into interstices within the fibers (e.g.

Figure 5.3

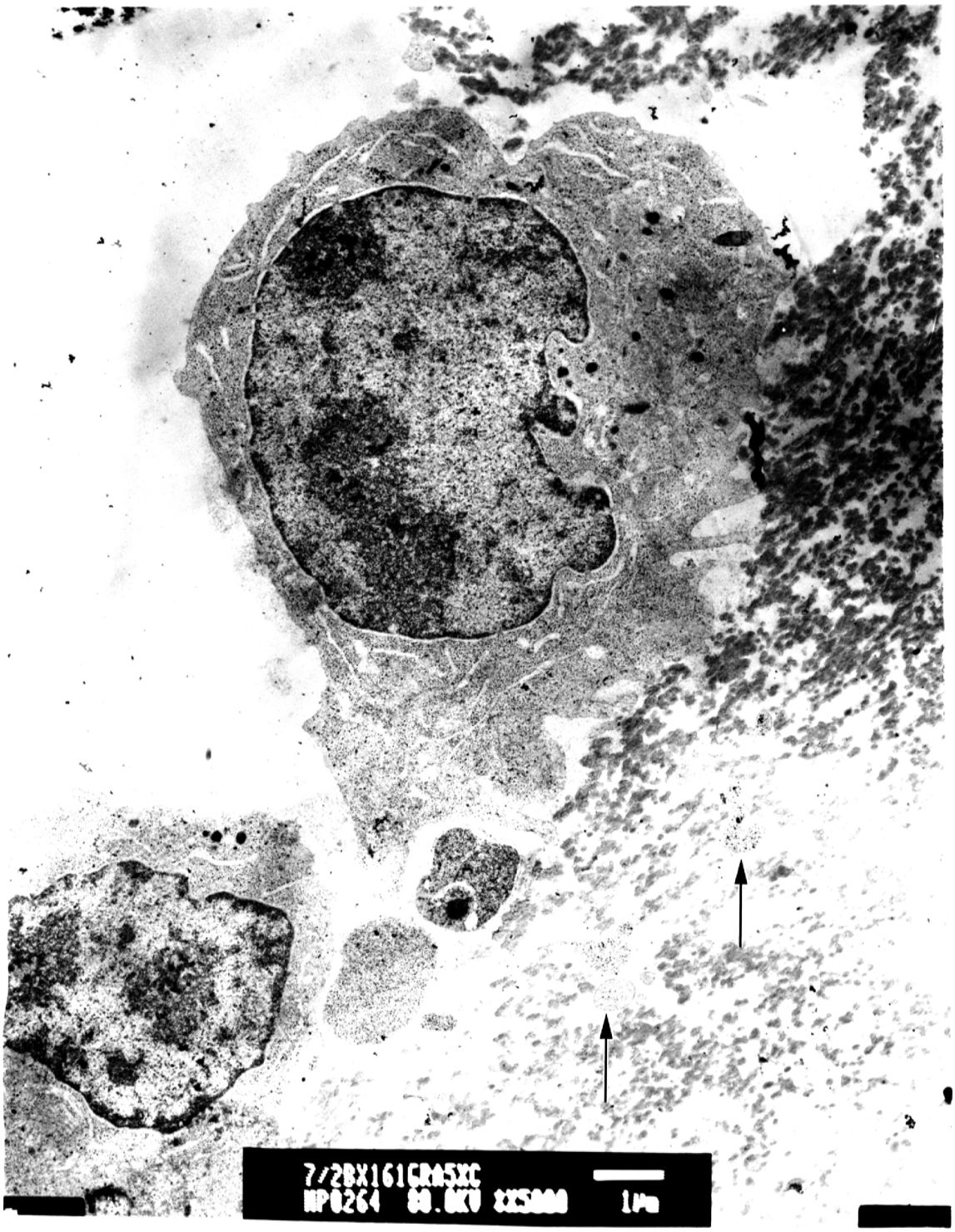

Figure 5.4

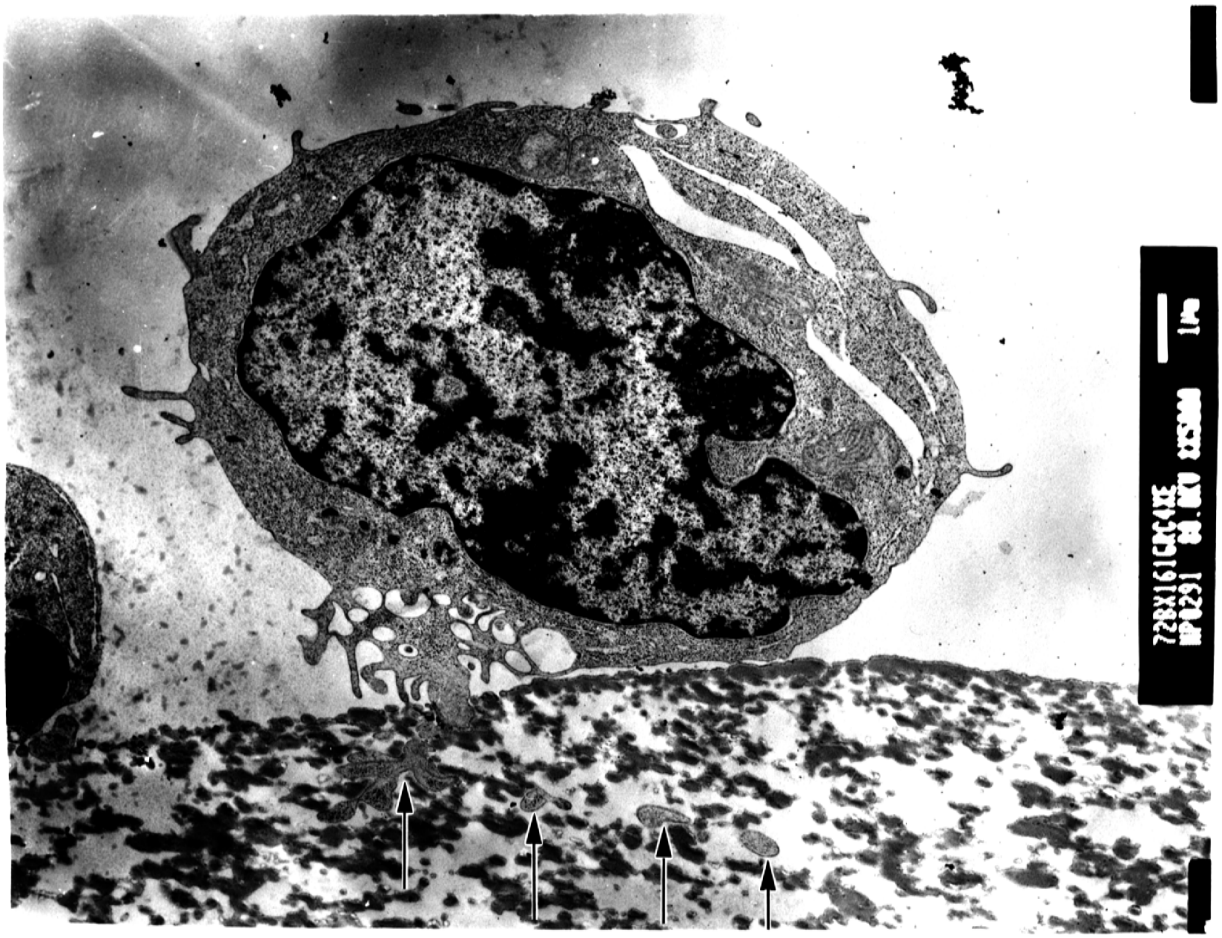

Figure 5.5

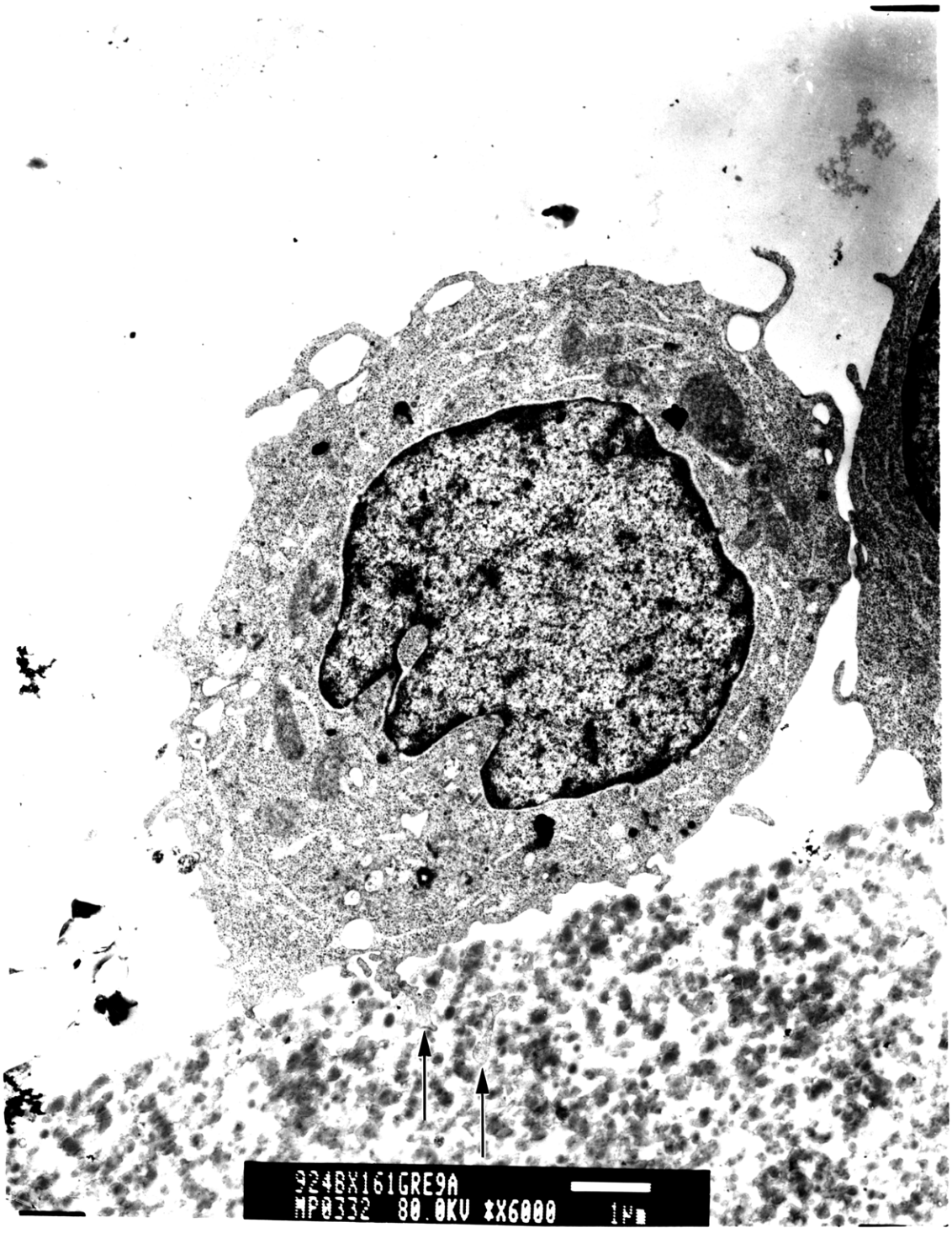

Figure 5.3

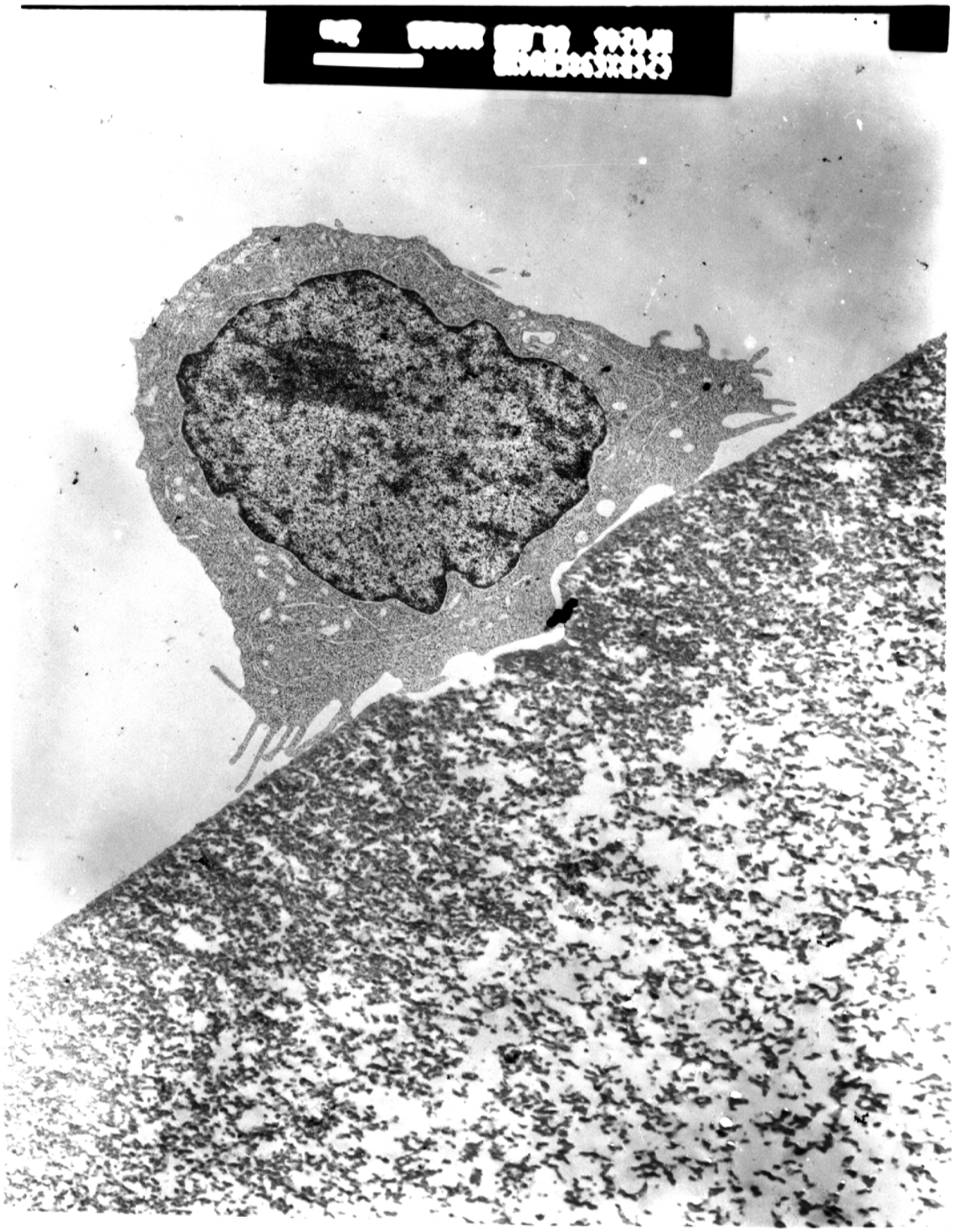

Figure 5.7

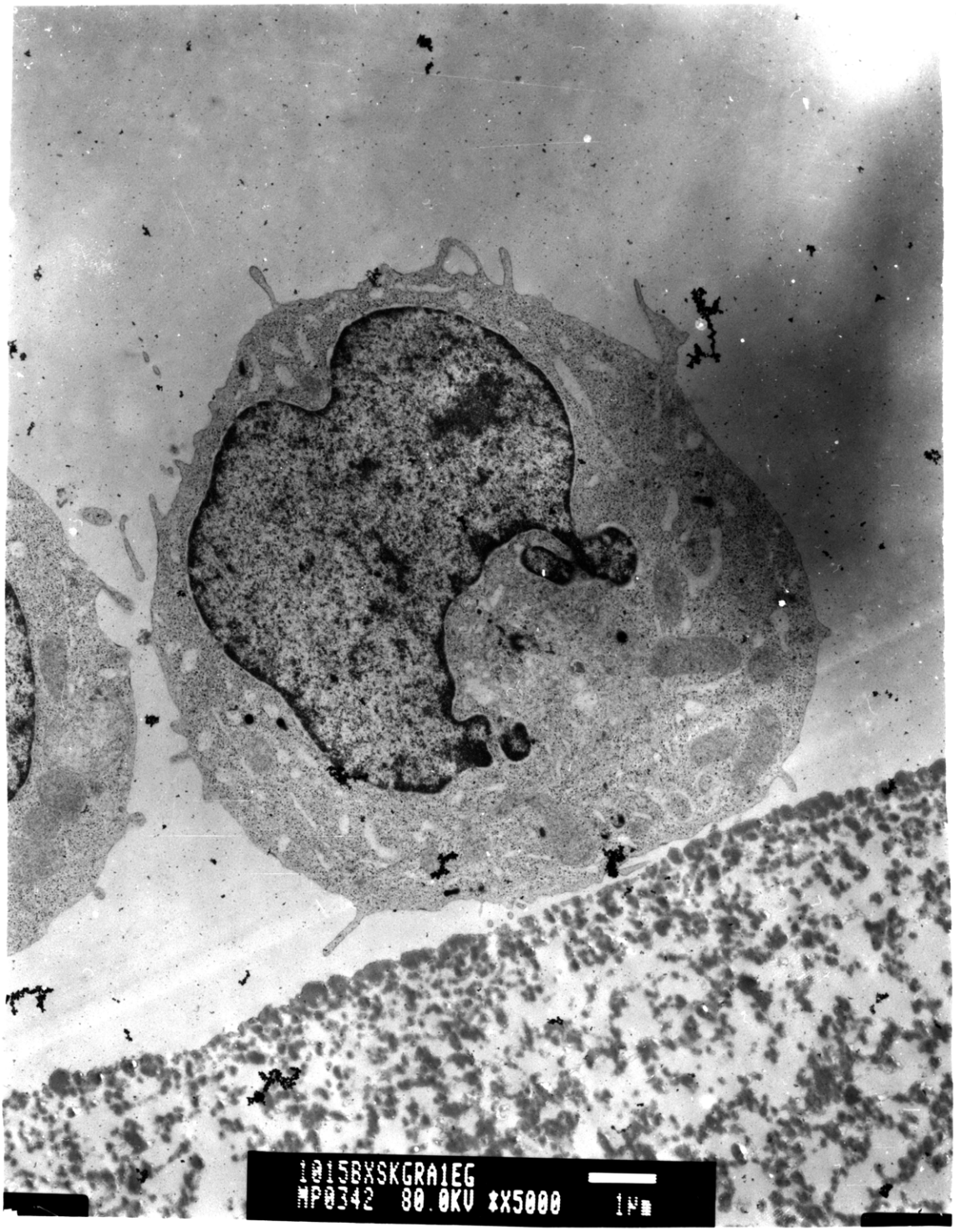

Figure 5.8

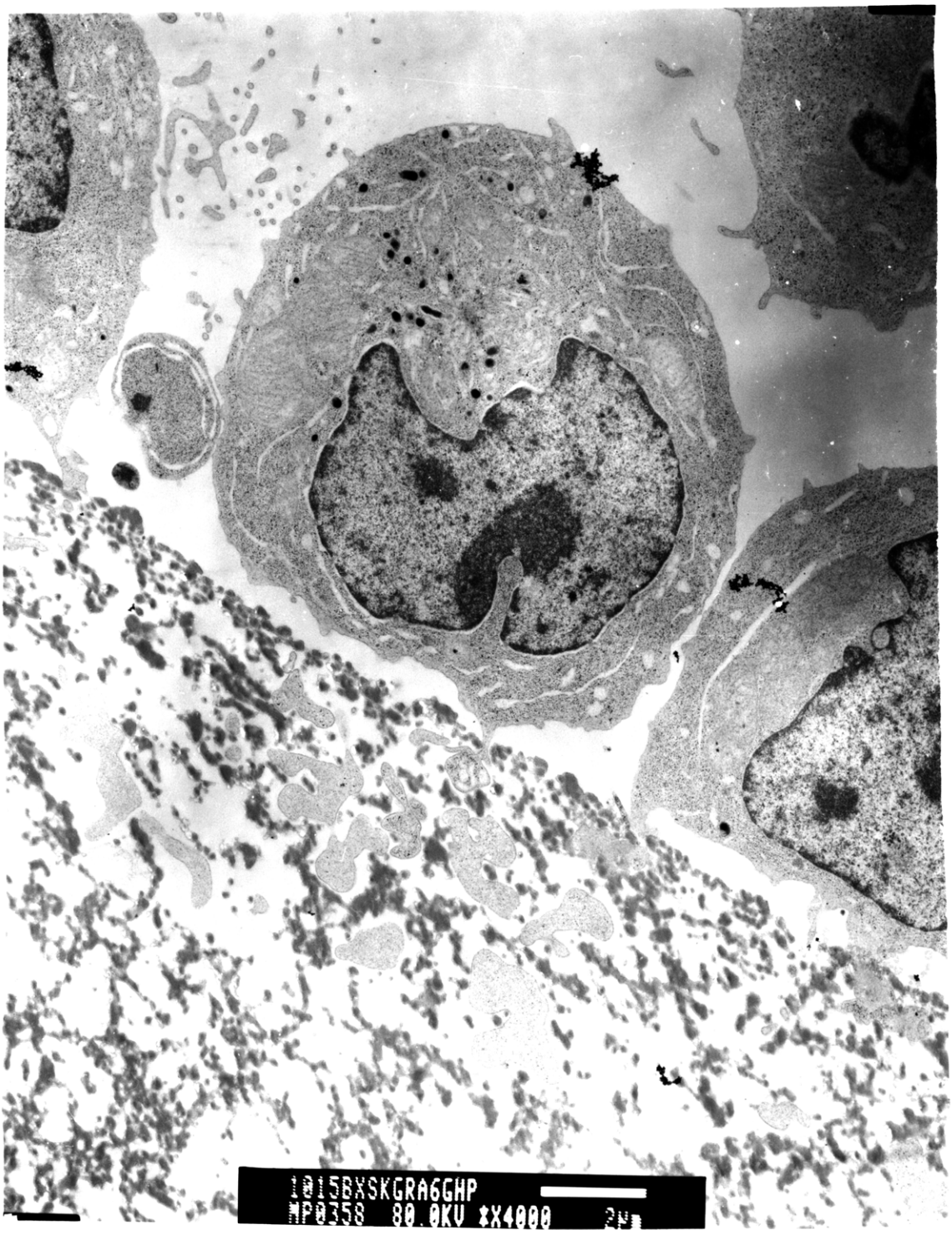

Figure 5.9

Figure 5.10

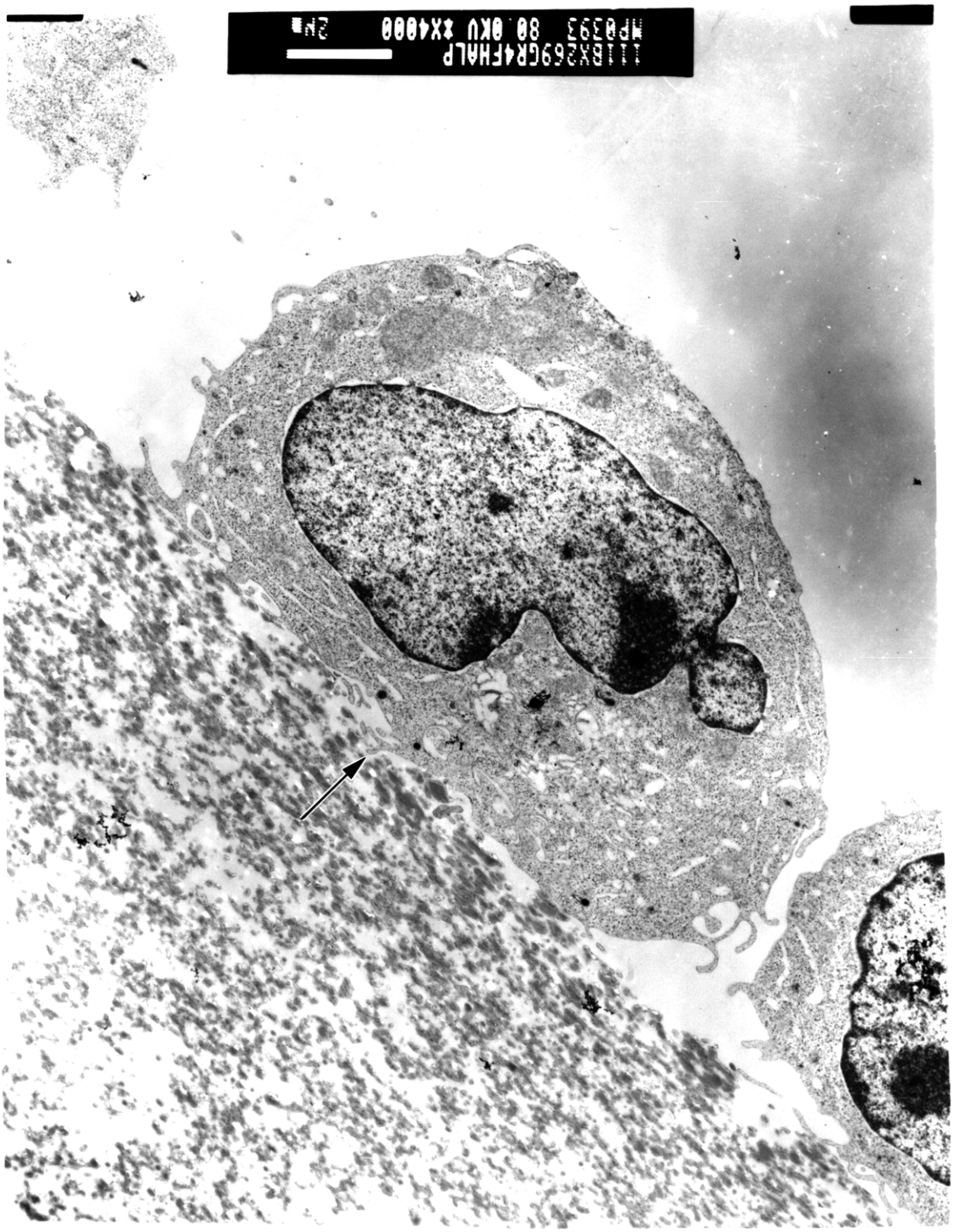

Figure 5.11

Figure 5.12

Figure 5.13

Figure 5.14

Captions for Figures 5.3 to 5.12

Figure 5.3 TEM photomicrograph of an HL-60 cell, pre-incubated with anti-CD33, loaded by filtration onto a Type B fiber. Cell has infiltrated membrane at site of large pore or defect (arrows). Bar in legend represents 2 μm. Black region is a grid bar.

Figure 5.4 TEM photomicrograph of an HL-60 cell, pre-incubated with anti-CD33, loaded by filtration onto a Type C fiber. Cell appears to be sitting on and infiltrating (arrows)a region of surface with a possible defect. Bar in legend represents 1 μm.

Figure 5.5 TEM photomicrograph of an HL-60 cell, pre-incubated with anti-CD33, loaded by filtration onto a Type E fiber which has infiltrated the membrane (arrows). Bar in legend represents 1 μm.

Figure 5.6 TEM photomicrograph of an HL-60 cell, pre-incubated with anti-CD33, loaded by filtration onto a Type A fiber which has infiltrated the membrane (arrows). Type A fibers show a tighter, denser pore structure under the surface than fibers with similar surface pore size (Types C and E) and infiltrations appear more narrow with fewer balls of cytoplasm seen under the surface. Bar in legend represents 1 μm.

Figure 5.7 TEM photomicrograph of an HL-60 cell, pre-incubated with anti-CD33, loaded by gravity onto a Type B fiber. No evidence of infiltration was observed for this condition. Notice cell is sitting on a defect with larger surface pores but has not penetrated the surface. Bar in legend represents 2 μm.

Figure 5.8 TEM photomicrograph of an HL-60 cell, pre-incubated with anti-CD33, loaded by gravity onto a Type E. No evidence of infiltration was observed for this condition. Bar in legend represents 1 μm.

Figure 5.9 TEM photomicrograph of an HL-60 cell, not pre-incubated with anti-CD33, loaded by filtration onto a Type E fiber which has infiltrated the membrane. Bar in legend represents 2 μm.

Figure 5.10 TEM photomicrograph of a Namalwa cell loaded by filtration onto a Type E fiber which has infiltrated the membrane (arrows). Bar in legend represents 1 μm.

Figure 5.11 TEM photomicrograph of an HL-60 cell, pre-incubated with anti-CD33, loaded by filtration, under reduced pressure conditions, onto a Type A fiber, which has infiltrated the membrane (arrow). Infiltration for this condition was less common, deep and extensive than for cells loaded onto the same fibers at higher pressure (see figure 5.6). Bar in legend represents 2 μm.

Figure 5.12 TEM photomicrograph of an HL-60 cell, not pre-incubated with anti-CD33, and pre-fixed prior to loading by filtration onto a Type E fiber. Infiltration (arrow) for this condition was rare (only this single observation) and superficial. Bar in legend represents 1 μm.

Captions for Figures 5.33 and 5.14

Figure 5.13 TEM photomicrograph of an HL-60 cell, not pre-incubated with anti-CD33, and treated with cytochalasin-D prior to loading by filtration onto a Type E fiber, which has infiltrated the membrane. Cells appeared smoother in contour than for similar loading conditions without pre-treatment with cytochalasin-D (see figure 5.9). Bar in legend represents 1 μm.

Figure 5.14 TEM photomicrograph of an HL-60 cell, not pre-incubated with anti-CD33, and treated with sodium azide and 2-deoxy-D-glucose prior to loading by filtration onto a Type C fiber, which has infiltrated the membrane (arrows). Cells appeared smoother in contour than for other, similar loading conditions without pre-treatment with metabolic inhibitors. Also, mitochondria stained more intensely. Bar in legend represents 2 μm.

figures 5.3, 5.5, 5.9, and 5.13).

Table 5.2 *Summary of Filtration Conditions and Infiltration Results*

	Cell Loading Conditions				TEM Observation Results		
Fiber Type	**Max. Pressure (mmHg)**	**Time of Filtration (min)**	**Cell Type**	**Pre-Treatment**	**% Infiltrated**	**Max. Depth (μm)**	**# of Cells**
B	266	17.5	HL-60	αCD33	7	3.3	28
C	21	7	HL-60	αCD33	41	5.3	22
E	13	13	HL-60	αCD33	20	3.8	54
A	86	6	HL-60	αCD33	69	6.4	35
B	Gravity	n.a.	HL-60	αCD33	0	n.a.	100
E	Gravity	n.a.	HL-60	αCD33	0	n.a.	20
E	61	6.5	HL-60	None	78	9.9	18
E	61	6.75	Namalwa	None	80	15.7	15
A	13	11.5	HL-60	αCD33	38	0.8	53
E	60	3	HL-60	Fixation	3	0.2	32
E	80	6	HL-60	Cytochalasin	90	12.7	103
C	78	3.5	HL-60	DOGA	97	20.8	59

The degree of infiltration was a function of the surface pore size. Only 7 % of the pressure-loaded cells observed on Type B fibers showed evidence of infiltration when exposed to 266 mmHg loading pressure during filtration whereas 20 to 69 % of identically prepared cells on Types C, E, and A fibers displayed infiltrations even though the loading pressures were much lower (13 to 86 mmHg). In addition, cells with infiltrations on Type B fibers were always associated with regions of the fiber surface which appeared to have larger than typical pores or damage (see figure 5.3). This was also the case for many cells on Type C fibers as well (figure 5.4). Maximum infiltration depths under these conditions ranged from 3.3 μm for Type B fibers to 6.4 μm for Type A fibers.

Infiltration could be completely prevented by loading the cells onto the fibers under the influence of gravity (0 mmHg loading pressure) for fibers with relatively small pores (Type B) and large pores (Type E) (table 5.2 and figures 5.7 and 5.8). Cells with reduced affinity for the fiber surface (HL-60 without anti-CD33 pretreatment and Namalwa) were also able to infiltrate Type E fibers (table 5.2 and figures 5.9 and 5.10). For a maximum loading pressure of 61 mmHg , 78 to 80 % of such cells observed by TEM showed evidence of infiltration with maximum infiltration depths of 9.9 μm for HL-60 without anti-CD33, to 15.7 μm for Namalwa. The effect of loading pressure on infiltration can be seen by comparing the results of the two experiments using Type A fibers in table 5.2. For both experiments HL-60 pre-incubated with anti-CD33 were loaded by filtration. In the first experiment, maximum loading pressure was 86 mmHg with a filtration time of 6 min, and for the second experiment, maximum loading pressure was only 13 mmHg with a filtration time of 11.5 min. Despite the increased exposure time to loading pressure in the second experiment, the fraction of cells observed with infiltrations was almost twice as much for the higher loading pressure (69 % vs. 38 %). In addition, the infiltrations observed for the cells loaded at lower pressure were more superficial (figure 5.11) with a maximum depth of 0.7 μm vs. 6.4 μm for cells loaded at the higher pressure.

Stabilizing the cytoskeleton by cross-linking F-actin with glutaraldehyde fixation dramatically reduced the degree of cell infiltration during loading by filtration onto Type E fibers (table 5.2 and figure 5.12). Load flowrates had to be increased by a factor of four to yield the same loading pressure (about 60 mmHg) with pre-fixed cells as with untreated cells of the same type on the same fiber. The percentage of observed pre-fixed cells with infiltration was only 3 % versus 78 % for non-prefixed cells under similar conditions. Also, the infiltrations observed were very superficial (maximum depth of 0.2 μm) and may be the

result of pre-formed cell surface features coincidentally lying in a surface pore of sufficient size (see figure 5.12). In contrast to results obtained for cells with stabilized cytoskeletons, HL-60 cells whose cytoskeletons were disrupted by pre-treatment with cytochalasin-D, showed no decrease in the extent and degree of infiltration compared to untreated cells loaded under similar conditions (table 5.2, compare rows 11 and 7 also see figure 5.13). Ninety percent of cells pre-treated with cytochalasin-D were observed to have infiltrated Type E fibers with a maximum infiltration depth of 12.7 μm. The extent of infiltration was high for this condition with a considerable quantity of cytoplasm under the membrane surface for most cells with infiltrations. HL-60 cell surface morphology was also typically smoother than with most other conditions. Similarly, poisoning cellular metabolism by pre-treatment of HL-60 with a combination of 20 mM sodium azide and 27 mM 2-deoxy-D-glucose (DOG) did not prevent or inhibit cell infiltration (table 5.2 and figure 5.14). Cells observed for this condition displayed very deeply stained mitochondria compared to cells which were not metabolically poisoned, and the extent of infiltration and cell morphology was similar to cells pre-treated with cytochalasin-D. Almost all cells (97 %) observed on Type C fibers loaded by filtration at a maximum loading pressure of 78 mmHg after metabolic poisoning showed evidence of infiltration (maximum depth 20.8 μm). These results, in addition to the results with pre-treatment with cytochalasin-D and glutaraldehyde, indicate that infiltration can occur in a completely passive manner without cell motility, and that the rigidity of the cytoskeleton seems to be an important factor.

5.5 Discussion

Our results have demonstrated that HL-60 leukemic leukocytes are able to infiltrate all of the hollow-fiber membranes tested when loaded by filtration at flowrates and pressures

previously used for cell binding and detachment studies (chapter 4). Cells in TEM photomicrographs with infiltrations appeared intact, and infiltrations below the surface of the hollow-fiber membrane typically appeared as tongues or balls of cytoplasm surrounded by a plasma membrane. The fraction of cells on sectioned samples which had infiltrated the fiber was related to the maximum surface pore size of the fiber. Less than 10 % of cells observed on sections had infiltrated Type B fibers when loaded with a loading pressure of 266 mmHg. In contrast, 20 to 69 % of similar cells had infiltrated the other fiber types with larger maximum pore diameters even though loading pressures were typically an order of magnitude lower. Also, cell infiltrations on Type B fibers (and to a lesser extent Type C fibers) were commonly associated with areas of the fiber surface showing atypically large pores or damage. The fraction of cells on sections with infiltrations and the extent and maximum observed depth of infiltrations was a function of loading pressure. No evidence of infiltration was observed when cells were loaded by gravity, even onto Type E fibers with the largest surface pores. In addition, the fraction of cells on sections with infiltrations which had been loaded onto Type A fibers at a maximum loading pressure of 86 mmHg was almost twice that for cells loaded at only 13 mmHg, and the maximum observed depth of the infiltrations was almost nine times as great.

Our results also indicate that cells need not have specific affinity for the fiber for infiltration to occur. HL-60 cells which had not been coated with anti-CD33 mouse IgG2b and Namalwa cells, both of which have been shown previously to have low affinity for the rpA-coated fibers (see chapter 3), infiltrated Type E fibers when loaded by filtration. This observation argues against infiltration by a mechanism where cell processes crawl into the porous fiber by active motility. An increased tendency toward infiltration for cells with less affinity for the porous substrate may be related to a decrease in the frictional resistance to

passive aspiration into pores.

Further evidence that active cell motility is not required for cell infiltration comes from the results of our metabolic inhibition and cytoskeletal rearrangement experiments. Active metabolism and cytoskeletal integrity were not prerequisites for cell infiltration. Cells pre-treated with cytochalasin-D, or a combination of sodium azide and DOG, underwent extensive infiltration. Cytochalasins, such as cytochalasin-D, at the concentrations used prevent active motility; however, they decrease resistance to passive deformation by disrupting the cytoskeletal support structure (Ting-Beall et al., 1995; Tsai et al., 1996). This is consistent with our observation of a somewhat higher fraction of infiltrated cells and higher degree of membrane fouling during loading by filtration as evidenced by an increased pressure during cell loading for cytochalasin treated cells compared to untreated non-target cells on the same fiber. Sodium azide in combination with DOG inhibit both oxidative phosphorylation and glycolysis and thus drastically reduce cellular ATP levels. Exposure to metabolic inhibitors under similar conditions has previously been observed to also disrupt the cytoskeleton (Kuhne et al., 1993). Nearly all cells we observed (97 %) had infiltrated when pre-treated with metabolic inhibitors. The appearance, by TEM, of the cells which had been pre-treated with cytochalasin-D or metabolic inhibitors was different than for cells of the same type which had not been pre-treated. The surface morphology was smoother, and infiltrations were very deep and numerous (maximum depth over 20 μm). Cells pre-treated with metabolic poisons also showed unusually intense staining of mitochondria (see figure 5.14). Stiffening the cells and increasing their resistance to passive deformation by cross-linking the cytoskeleton with glutaraldehyde before loading, drastically reduced the fraction of cells observed with infiltrations and required a four fold increase in loading flowrate to supply the same loading pressure as similar experiments with untreated cells indicating a reduced

tendency of pre-fixed cells to foul membranes. All of these results implicate a passive pressure-driven process as the mechanism of infiltration.

The experimental protocol and method of quantification of cell infiltration were designed to be used to make relative comparisons between different cell loading conditions. There are several limitations of the methods which must be considered, especially if trying to extrapolate observations to come to absolute conclusions about cell population behavior. Both fiber pore sizes and the mechanical properties of individual HL-60 cells in a continuous cell culture are heterogeneous (Tsai et al., 1996), so that individual observations cannot be extrapolated to the population at large. The preparation procedure may cause a tendency to overestimate the fraction of the original population which had infiltrated the membrane because cells without infiltrations may be preferentially dislodged during washing, fixation, and embedding steps. This is especially true for experiments with non-target cells with little intrinsic affinity for the fibers. Conversely, the loading and fixation procedure may cause an underestimation of cells with short infiltrations because the pressure was not maintained during fixation, and short infiltrations may be able to retract into the cell before they are fixed. Observation of thin sections of cells by TEM will tend to underestimate the actual fraction of cells on the fiber with infiltrations because only a small fraction of the total contact area was being observed in a given section. For example, for Type B fibers, assuming that infiltrations were due to the largest pores (d = 0.26 μm), and that a typical contact area was about 8 μm in diameter, there were about 114, sections, each 70 nm thick, per contact area. For infiltrations oriented in the same plane as the plane of the section, each infiltration occupied only 4 sections. So, for a given cell observed on a section, there would be a probability of 4/114, or about 3.5 % for seeing a single such infiltration in its contact area by looking at a single section. Thus, if every cell on the fiber had a single such

infiltration, only about 3.5 % of the total cells observed on the sections would show evidence of infiltration. So the 7 % of cells that we observed which had infiltrated the fiber could conceivably be consistent with 100 % of the cells on the fiber having two such infiltrations. In actuality, this analysis exaggerates the error because the photomicrographs suggest that once beneath the surface, the infiltrations appear to increase in size as they expand into larger interstices (see figures 5.3, 5.5, 5.9, and 5.13). Also it is probable that many infiltrations penetrated the fiber at a non zero angle with respect to the slicing plane and/or changed directions once in the membrane so that they would extend across many section planes depending on their length. By similar reasoning, infiltrations due to larger pores would have a higher probability of being observed on a given section than infiltrations originating from small pores; thus, this may inflate somewhat the relative fraction of cells with infiltrations on large pore size fibers (Types C, E and A) compared to the Type B fiber results. Therefore, caution should be used in making comparisons for conditions using different fiber morphologies; however, relative comparisons for conditions employing the same fiber are more unambiguous. Finally, TEM only provides 2-D information. It is impossible to make conclusions about the exact shape or size of infiltrations, or determine the three dimensional shape of the pore responsible without observing a large number of serial sections. These fibers, with their heterogeneous pore structure and size, are thus not ideally suited for gaining a quantitative understanding the effects of pressure and pore size on infiltration.

For passive flow of cells into cylindrical holes or pipets whose radius is much larger than the thickness of the membrane-cortex, and with negligible friction at the pipet wall and negligible flow of liquid between the pipet wall and cell surface, the critical pressure required before the cell membrane will enter the hole is related to the cortical surface tension by the law of Laplace for an interface with two principle curvatures such as a liquid drop:

$$\Delta P_{cr} = 2T\left(\frac{1}{R_p} - \frac{1}{R_{cell}}\right) \quad (1)$$

where R_p is the hole radius, R_{cell} is the radius of the cell external to the hole, and T is the cortical tension (Evans and Skalak, 1980). The cortical tension for neutrophils (the cell most similar to HL-60 for which data is published) has been measured in several laboratories and was found to be quite small, ranging from 0.024 to 0.035 mN/m (Evans and Yeung, 1989; Needham and Hochmuth, 1992). The assumptions made in applying the law of Laplace to cell deformation into pores will not be valid as the pore size is reduced to the point where the membrane and cortical thickness are not a negligible fraction of the pore radius. As the pore size becomes small, the bending resistance and molecular size of the membrane/cortex will increase the pressure necessary to deform the cell into the pore. At the limit where the membrane/cortical thickness become equal to the pore radius, it would become impossible for a cell with an intact cortex to penetrate the pore. This behavior has been investigated by Zhelev and coworkers by aspirating neutrophils into micropipets with very small diameters (0.48 to 2 μm) (Zhelev et al., 1994). Their results indicate that for pipets with diameters smaller than 2.4 μm, Laplace's law underpredicts the critical pressure required for cell aspiration. For example for a 1.2 μm diameter pipet they found the measured critical pressure was 230 Pa compared to 140 Pa predicted from Laplace's law. The authors demonstrated that the cause of this excess pressure was the bending stiffness of the cortex, and proposed a model which successfully predicted the critical pressure over the range of pipet sizes tested. Their proposed model equates the total free energy change in the membrane undergoing a small displacement into the pipet with the work that produces the displacement. The critical pressure predicted by their analysis is

$$\Delta P_{crit} = f_0\left(\frac{R_{cell}}{R_p'}, \frac{r}{R_p'}\right) \cdot \frac{k_c}{R_p'^3} + f_1\left(\frac{R_{cell}}{R_p'}, \frac{r}{R_p'}\right) \cdot \frac{T}{R_p'} \quad (2)$$

where T is the cortical tension, k_c is the bending modulus of the membrane-cortex. The functional coefficients f_0 and f_1 are defined elsewhere (Zhelev et al., 1994; see chapter 6 appendix) and are functions of R_{cell}, the radius of the cell, R_p', the radius of the pore minus half the thickness of the membrane-cortex, and r, the radius of curvature of the small torus region where the cell bends into the pore (see figure 6.A.1). The authors were able to fit their aspiration data with values of k_c ranging from 1 to 2×10^{-18} J for typical cortical tensions and for a cortical thickness ranging from 0.1 μm down to an infinitely small thickness (0 μm) . Table 5.3 presents the predictions for the critical pressures required to enable cells (with mechanical properties similar to neutrophils) to enter the pores of the membranes in this study as calculated by the law of Laplace (column 2), and the model of Zhelev et al. for an intact membrane-cortex (column 3). In order to give an estimate of the critical pressure based on typical parameters, T was assumed to be 0.03 mN/m, k_c used for the membrane-cortex was 2×10^{-18} J, and the cell diameter outside the pore was 10 μm. The thickness of the membrane-cortex was assumed to be zero (negligibly thin) and r was varied, up to a maximum value of 0.2 μm (see Zhelev et al., 1994) so that ΔP_{crit} was minimized for each pore size. The predictions in table 5.3 should be considered low estimates. In actuality, the tortuous pore structure and irregular pore shape of the membranes in our study will most likely provide greater resistance to entry than the uniform cylindrical pipet apertures for which these models were derived. In addition, it is probable that leukemic cells such as HL-60 are somewhat stiffer than neutrophils (Tsai et al., 1996).

Table 5.3 *Predicted critical pressures to form infiltrations into hollow-fiber membrane pores*

Fiber Type	Equivalent Pore Diameter Range (min/max) (μm)	ΔP_{crit} (mmHg) for min/max Pore Diameter	
		Law of Laplace	Zhelev et al., 1994 Membrane-Cortex
B	0.01 / 0.26	64 / 3.4	2.8×10^5 / 50
C	0.02 / 1.3	37 / 0.6	5.5×10^4 / 1.1
E	0.14 / 2.1	6.5 / 0.3	312 / 0.5
A	0.04 / 1.5	24 / 0.5	1.4×10^4 / 0.9

From table 5.3, the model of Zhelev et al. for small pores predicts that the critical pressure beyond which infiltration would occur was 50, 1.1, 0.5, and 0.9 mmHg for Type B, C, E, and A fibers respectively. It is clear from the predictions that according to these models the pressures applied in this study were sufficient to deform cells into straight cylindrical pores of equivalent effective diameter. The analysis suggests that since the maximum allowable loading pressure will be limited by the largest pores on the membrane, the most ideal membranes for loading cells by filtration would have a uniform pore size.

The hollow fiber membranes used in this study, because of their relatively wide pore size range and low hydraulic permeability to maximum pore size ratio, place limitations on certain operating parameters when cells are loaded by filtration for cell separation. The maximum allowable pressures during cell loading must be maintained below those which will result in cell infiltration into the largest pores on the surface. By using membranes of similar hydraulic permeability with a smaller, but more homogeneous pore size, load pressures may be higher which can reduce loading time. By reducing loading time, one of the primary advantages of loading by filtration, namely bringing all the cells to the surface quickly to

reduce processing time, cell-substrate affinity, and heterogeneity due to differences in contact times could be better realized. As an example of operating constraints with current membranes, consider our Type E fibers. Assuming that the maximum allowable loading pressure is 0.5 mmHg, hydraulic permeability is about 5 L/hrm^{2}mmHg, and the active length in the module is 4 cm, the time required to load 1×10^6 cells (about 80 % of a theoretical monolayer) from a cell suspension containing 5×10^6 cells/ml would be at least 39 min. This time period is longer than the time required for cells to simply settle by gravity. Increasing the total available surface area by a factor of 10 (eg. using 10 fibers or a 40 cm long fiber) would reduce the time to a minimum of about 4 min but would yield only about 8 % of maximum surface coverage, a relatively inefficient use of fiber surface area. A reduction in loading time could also be gained by increasing the cell density of the load solution and reducing dead volume in the apparatus to a minimum. The absolute minimum volume of load solution which could be used in this case would be the internal volume of the fiber itself (about 30 μl for a 4 cm fiber length). A cell concentration of about 3.3×10^7 cells/ml would be required to provide 1×10^6 cells (about 1 theoretical monolayer) in such a small volume. Loading the cells by filtration of this minimum volume within the pressure constraints to prevent infiltration would require at least 5 min (at a load flowrate of 6 μl/min) , similar to the loading times in this chapter and previously used in chapter 4.

In conclusion, we have demonstrated that cells infiltrated into hollow-fiber membranes over the range of filtration rates and applied pressures examined in this study. The membrane morphology of the fibers used in this study, because of its heterogeneous pore-size distribution, creates limitations in operability for cell separations where cells are loaded by filtration, and limits the utility of the fibers for studying the effects of pore size and pressure on cell infiltration. Future work should focus on the development and use of high-

permeability/small pore size membranes with a more homogeneous pore size distribution. In addition, the relationship between pressure, pore size, and cell infiltration should be investigated in a more systematic way for very small pores.

5.6 Acknowledgements

Experimental hollow-fiber membranes were kindly provided by Dr. Sam Williams at Sepracor (Marlborough, MA). Special thanks as well to Dr O.D. Holton and Dr. Abdul Azad at Sepracor for assistance with membrane modification. Scanning electron microscopy was performed in the EM facility of the Center for Materials Science and Engineering at MIT, a Materials Science and Engineering Center supported by the National Science Foundation under grant number DMR 9400334. Special thanks to Dr. David C. Bell, and Mr. Michael Frongillo for assistance with sample coating and microscopy. Transmission electron microscopy was performed in the Biomedical Electron Microscopy Laboratory at MIT. The JEOL 122 EX II was purchased through an NIH multi-user instrumentation program, BRS Shared Instrumentation Grant number S10 RR05734-01. Special thanks to Ms. Patricia Reilly for assistance with sample preparation and microscopy.

5.7 References

Azad, A.R.M.,and R.A. Goffe. 1990. Process for the covalent surface modification of hydrophobic polymers and articles made therefrom. Patent Cooperation Treaty Publication No. WO 90/04609.

Bakowski, B., and H. Tschesche. Migration of polymorphonuclear leukocytes through human amnion membrane--a scanning electron microscopic study. *Biological Chemistry Hoppe-Seyler.* 373:529-546.

Bray, D., J. Heath, and D. Moss. 1986. The membrane-associated "cortex" of animal cells: its structure and mechanical properties. *Journal of Cell Science Supplement.* 4:71-88.

Carter, S.B. 1967. Effects of cytochalasins on mammalian cells. *Nature.* 213:261-264.

Collins, S. J., R. C. Gallo, and R. E. Gallagher. 1977. Continuous growth and differentiation of human myeloid lukaemic cells in suspension culture. *Nature.* 270:347-349.

Esaguy, N., A. P. Aguas, and M. T. Silva. 1989. High-resolution localization of lactofeffin in human neutrophils: labling of secondary granules and cell heterogenity. *Journal of Leukocyte Biology.* 46:51-62.

Evans, E. A., and R. Skalak. 1980. Mechanics and thermodynamics of biomembranes. CRC Press Inc., Boca Raton, FL.

Evans, E. A., and B. Kukan. 1984. Passive material behavior of granulocytes based on large deformation and recovery after deformation tests. *Blood.* 64:1028-1035.

Evans, E. A., and A. Yeung. 1989. Apparent viscosity and cortical tension of blood granulocytes determined by micropipet aspiration. *Biophysical Journal.* 56:151-160.

Hallows, K. R., and R. S. Frank. 1992. Changes in mechanical properties with DMSO-induced differentiation of HL-60 cells. *Biorheology.* 29:295-309.

Haug, I.J., E.M. Siebke, I.A. Grimstad, and H.B. Benestad. 1993. Simultaneous assessment of migration and proliferation of murine fibrosarcoma cells, as affected by hydroxyurea, vinblastine, cytochalasin B, Razoxane and interferon. *Cell Proliferation.* 26:251-261.

Holton, O.D., and J.J. Vicalvi, Jr. 1991. Optimization of monoclonal antibody immobilization on hydrazide-preactivated hollow fiber membrane. *BioTechniques.* 11:662-665.

Horvath, A.R., and S. Kellie. 1990. Regulation of integrin mobility and cytoskeletal association in normal and RSV-transformed chick embryo fibroblasts. *Journal of Cell Science.* 97:307-315.

Hunt, S.W., E.S. Harris, S.A. Kellermann, and Y. Shimizu. 1996. T-lymphocyte interactions with endothelium and extracellular matrix. *Critical Reviews in Oral Biology and Medicine.* 7:59-86.

Klein, E., E. Eichholz, and D.H. Yeager. 1994. Affinity membranes prepared from hydrophilic coatings on microporous polysulfone hollow fibers. *Journal of Membrane Science* 90:69-80.

Kuhne, W., M. Besselmann., T. Noll, A. Muhs, H. Watanabe, and H.M. Piper. 1993. Disintegration of cytoskeletal structure of actin filaments in energy-depleted endothelial cells. *American Journal of Physiology.* 264:H1599-H1608.

Lichtman, M.A., and E.A. Kearney. 1976. The filterability of normal and leukemic human leukocytes. *Blood Cells.* 2:491-506.

Lin, Y., L. Xia, J.D. Turner, and X. Zhao. 1995. Morphologic observation of neutrophil diapedesis across bovine mammary gland epithelium in vitro. *American Journal of Veterinary Research.* 56:203-207.

Nadkarni, J.S., J.J. Nadkarni, P. Clifford, G. Manolov, E.M. Fenyö, and E. Klein. 1969. Chacterization of new cell lines derived from Burkitt lymphomas. *Cancer.* 23:64-79.

Needham, D., and R. M. Hochmuth. 1992. A sensitive measure of surface stress in the resting neutrophil. *Biophysical Journal.* 61:1664-1670.

Ngo, T.T. 1986. Facile activation of sepharose hydroxyl groups by 2-fluoro-1 methylpyridinium toluene-4-sulfonate: Preparation of affinity and covalent chromatographic matrices. *Bio/Technology.* 4:134-137.

Noris, M., and G. Remuzzi. 1995. New insights into circulating cell-endothelium interactions and their significance for glomerular pathophysiology. *American Journal of Kidney Disease.* 26:541-548.

Popov, S.V., and L.B. Margolis. 1988. Formation of cell outgrowths by external force: a model study. *Journal of Cell Science.* 90:379-389.

Reynolds, E. S. 1963. The use of lead nitrate at high pH as an electron opaque stain in electron microscopy. *Journal of Cell Biology.* 17:208.

Schliwa, M. 1982. Action of cytochalasin D on cytoskeletal networks. *The Journal of Cell Biology*. 92:79-91.

Stich, T. 1990. Determination of protein covalently bound to agarose supports using bicinchoninic acid. *Annals of Biochemistry*. 159:138-142.

Stracke, M.L., M. Sorousch, L.A. Liotta, and E. Schiffmann. 1993. Cytoskeletal agents inhibit motility and adherence of human tumor cells. *Kidney International*. 43:151-157.

Terranova, V.P., E.S. Hujanen, D.M. Loeb, G.R. Martin, L. Thornburg, and V. Glushko. 1986. Use of a reconstituted basement membrane to measure cell invasiveness and select for highly invasive tumor cells. *Proceedings of the National Academy of Sciences USA*. 83:465-469.

Ting-Beall, H.P., A.S. Lee, and R.M. Hochmuth. 1995. Effect of cytochalasin D on the mechanical properties and morphology of passive human neutrophils. *Annals of Biomedical Engineering*. 23:666-671.

Tsai, M. A., R. S. Frank, and R. E. Waugh. 1993. Passive mechanical behavior of human neutrophils: power-law fluid. *Biophysical Journal*. 65:2078-2088.

Tsai, M.A., R. E. Waugh, and P. C. Keng. 1996. Cell cycle-dependence of HL-60 cell deformability. *Biophysical Journal*. 70:2023-2929.

Yeung, A., and E. Evans. 1989. Cortical shell-liquid core model for passive flow of liquid-like sherical cells into micropipets. *Biophysical Journal*. 56:139-149.

Zhelev, D. V., D. Needham, and R. M. Hochmuth. 1994. Role of the membrane cortex in neutrophil deformation in small pipets. *Biophysical Journal*. 67:696-705.

Zigmond, S.H., and J.G. Hirsch. 1972. Effects of cytochalasin B on polymorphonuclear leukocyte locomotion, phagocytosis and glycolysis. *Experimental Cell Research*. 73:383-393.

Chapter 6. Deformation of HL-60 Cells Into Pores as Small as 0.1 μm in Diameter on Polycarbonate, Track-Etched Membranes Under Conditions of Positive-Pressure Filtration.

6.1 Abstract

The simplest and most successful models for large deformations of leukocytes are based on the notion that the cell consists of a liquid-like cytoplasmic core surrounded by a thin membrane-cortex which imparts to the cell its shape and many of its mechanical properties. The cortex, believed to be from 0.05 - 0.1 μm in thickness for leukocytes, is composed of a structural meshwork of F-actin and is anchored to the plasma membrane, thereby giving the membrane mechanical strength and a constant isotropic surface tension. For small curvature deformations, there exists a critical suction pressure below which a cell will not enter a small hole and which can be determined from the cortical "surface" tension by the law of Laplace. For cell deformation into very small holes, the law of Laplace underpredicts the critical pressure, and the bending resistance of the membrane-cortex must be considered. Zhelev and coworkers have proposed such a model and successfully used it to predict critical pressures for neutrophil aspiration into pipets with internal diameters as small as 0.48 μm (Zhelev et al, 1994a).

In this study, we investigate the ability of HL-60 leukemic leukocytes to deform into pores with internal diameters from 0.2 μm down to 0.05 μm using polycarbonate track-etched membranes, filtration by positive hydrostatic pressure, and field-emission scanning and transmission electron microscopy for determination of cellular infiltration into pores. We demonstrate that HL-60 can infiltrate into pores as small as 0.1 μm in diameter at pressures

far below those predicted by models which account for cortical bending resistance. We found the critical pressure for cell infiltration to be from 2 to 5 mmHg for 0.2 μm diameter pores and 5 to 20 mmHg for 0.1 μm diameter pores. Evidence for infiltration into 0.05 μm diameter pores was inconclusive even for pressures as high as 200 mmHg, suggesting that this may be close to an effective cut-off size for cell penetration. The mechanism for cell penetration into such small pores at such low pressures is unclear. Our data suggest that it is unlikely that intact membrane-cortex is deforming into pores, and we speculate based on our observations several possible mechanisms for cell aspiration. This study has relevance both in the study of cell mechanics and also in practical applications employing filtration for cell loading onto porous substrates.

6.2 Introduction

Recent work in our laboratory (see chapters 2 to 4) and by other investigators (Mandrusov et al., 1995; Nordon et al., 1996; Nordon and Schindhelm 1997) has focused on the design and use of permeable membranes for affinity cell separation. In our application, microporous, or ultrafiltration membranes are utilized for cell separations involving leukemic white blood cells, and forces generated by convection of fluid through the membrane are utilized for cell deposition and removal. Cell deposition by filtration is faster and more efficient than gravity settling, however, we have noticed in previous experiments (chapter 3 and 4) a difference in the ability to remove cells from membranes depending on the way in which they were deposited onto the membrane. Cells deposited by gravity settling were detached more easily than cells deposited by filtration. Analysis of cells loaded onto membranes by transmission electron microscopy (TEM) indicated that portions of the cell membrane and cytoplasm of many cells loaded by filtration had infiltrated into the porous

structure of the membrane. None of the cells observed loaded by gravity had infiltrated (chapter 5). Pore diameters of the various membranes used ranged from less than 0.15 μm to several tenths of a micron. Unfortunately, because the surface pore size and shape of these membranes was not homogeneous, they were not ideally suited for gaining a systematic understanding of the effects of pore size and applied pressure for filtration on the infiltration phenomenon.

In the current study, we utilize polycarbonate track-etched (PCTE) membranes with small pore diameters together with an apparatus designed to deposit and chemically fix cells under conditions of constant pressure. PCTE membranes are ideally suited for understanding the effect of pore size on cell infiltration. They are flat, smooth membranes which have cylindrically shaped straight-through pores that are very uniform in pore diameter. PCTE membranes with pore diameters ranging from 0.6 to 1.0 μm have been used previously to characterize the mechanical properties of red blood cell membranes by aspiration, fixation, and measurement of infiltration dimensions, and results have correlated well with similar properties measured by other means such as micropipette aspiration (Brailsford et al., 1977; Missirlis and Brain, 1979; Baker, 1981; Saul et al.; 1984; Reinhart et al., 1987). Analysis of infiltration dimensions is accomplished by removal of the PCTE membrane from the cell by dissolution in a solvent or by mechanical means and observation of the cells by electron microscopy. In the current study, we employ similar methods to study the effects of pore size and filtration pressure on the tendency of HL-60 leukemia cells to infiltrate into membrane pores. HL-60 is a human leukemic cell line with characteristics similar to promyleoblasts and promyelocytes (Collins et al., 1977). This cell line has been used extensively in our laboratory as a model cell system for cell separations. The cell line also has been used previously as a model system to characterize the mechanical behavior of immature leukemic

leukocytes and its mechanical properties have been compared to those of neutrophils, one of the most extensively studied leukocytes (Hallows and Frank, 1992; Tsai et al, 1996). The primary reason why we want to better understand the infiltration phenomenon is to devise strategies to prevent or minimize its occurrence.

Leukocyte morphology and rheology, as typified by that of the neutrophil, is very different from that of the more extensively studied red blood cell. Much of the understanding of the mechanical properties of the neutrophil comes from experiments involving micropipet aspiration (e.g., Needham and Hochmuth, 1992; Hochmuth et al., 1993; Tsai et al, 1993; Tsai et al, 1994; Zhelev et al, 1994a; Evans and Yeung 1989; Yeung and Evans 1989). Passive leukocytes are spherical but their membrane morphology, unlike the red blood cell, is not smooth but folded, villous, and irregular. These features form a supply of excess surface area which allows the cell to undergo large area deformations before the membrane is pulled taut (Needham and Hochmuth, 1992, Ting-Beall et al., 1993, Evans and Yeung, 1989). A conceptual model which has great utility for understanding the mechanical properties of leukocytes undergoing large deformations is the cortical shell-liquid core model (Yeung and Evans, 1989). In this model, the cell cytoplasm behaves as a viscoelastic liquid rather than a solid, and the spherical shape is maintained by a persistent interfacial "cortical" surface tension (Needham and Hochmuth, 1992; Evans and Kukan, 1984; Dong et al., 1988; Yeung and Evans, 1989). The "cortex" is viewed as a thin structure forming a shell adjacent to the cell surface (Yeung and Evans, 1989). This model explains successfully the observation that a passive leukocyte will flow continuously into a small micropipette (within the constraints of its total plasma membrane surface area) as long as the aspiration pressure exceeds a critical level ΔP_{crit} which is the pressure necessary to form a static, hemispherical projection in the micropipet. For flow into pipets whose radius is much larger than the thickness of the

membrane-cortex with negligible friction at the pipet wall and negligible flow of liquid between the pipet wall and cell surface, this critical pressure is related to the cortical surface tension by Laplace's law for an interface with two principle curvatures such as a liquid drop:

$$\Delta P_{crit} = 2T\left(\frac{1}{R_p} - \frac{1}{R_{cell}}\right) \quad (1)$$

where R_p is the micropipette radius, R_{cell} is the radius of the cell external to the pipet, and T is the cortical tension (Evans and Skalak, 1980). The cortical tension has been measured for neutrophils in several laboratories and was found to be quite small, ranging from 0.024-0.035 mN/m (Needham and Hochmuth; 1992, Evans and Yeung, 1989). The cortical tension was also found to have a very small apparent area expansion modulus (change in the tension with changes in surface area), on the order of 0.04 mN/m (Needham and Hochmuth, 1992), when the membrane is not taut. This mechanical behavior is in stark contrast to that observed for red blood cells. The membrane of red blood cells, which is smooth, displays shear elasticity, so that the cells do not flow continuously into pipets above a threshold pressure, but rather the length of the projection inside the pipet is a linear function of the aspiration pressure. (e.g. Evans and Skalak, 1980).

The rheological properties of HL-60 have also been successfully described with the liquid drop model described above (Hallows and Frank, 1992; Tsai et al., 1996). Results from these studies indicate that the flow behavior of HL-60 through small capillary sized pores is very similar to that of neutrophils. Both cells exhibited power-law fluid behavior (Tsai et al., 1996); however, the HL-60 cells were considerably less deformable with apparent cytoplasmic viscosities two to three times higher than those for neutrophils measured at similar shear rates (Tsai et al., 1993; Tsai et al., 1996). Deformability was dependent on the position in the cell growth cycle (S phase cells were stiffer than G1 cells) but in all cases the

cells were less deformable than neutrophils. As with neutrophils, the deformability was a strong function of the state of the cytoskeleton, and cytoskeleton-disrupting agents such as cytochalasins significantly softened both cell types (Tsai et al., 1996).

The cortical shell is believed to be composed of cytoskeletal scaffolding of F-actin under the plasma membrane. Transmission electron micrographs from some investigators have suggested that this layer is approximately 0.05 to 0.1 μm thick (Bray et al., 1986; Esaguy et al., 1989). The assumptions made in applying the law of Laplace to cell deformation into pores will not be valid as the pore size is reduced to the point where the membrane and cortical thickness are not a negligible fraction of the pore radius. As the pore size becomes small, the bending resistance and molecular size of the membrane/cortex will increase the pressure necessary to deform the cell into the pore. At the limit where the membrane/cortical thickness become equal to the pore radius, it would become impossible for a cell with an intact cortex to penetrate the pore. This behavior has been investigated by Zhelev and coworkers by aspirating neutrophils into micropipets with very small diameters (0.48 to 2 μm) (Zhelev et al., 1994a). Their results indicate that for pipets with diameters smaller than 2.4 μm, Laplace's law underpredicts the critical pressure required for cell aspiration. For example for a 1.2 μm diameter pipet they found the measured critical pressure was 230 Pa compared to 140 Pa predicted from Laplace's law. The authors demonstrated that the cause of this excess pressure was the bending stiffness of the cortex, and proposed a model which successfully predicted the critical pressure over the range of pipet sizes tested. Their proposed model equates the total free energy change in the membrane undergoing a small displacement into the pipet with the work that produces the displacement (see discussion and appendix). The model predicts a $1/R_p$ dependence on the cortical tension and a $1/R_p^3$ dependence on the bending modulus. Thus as pore size decreases, the contribution of

bending becomes more important and eventually overwhelms the contribution of the cortical tension. The bending elastic modulus of 10 to 20 × 10^{-19} J they deduced for the neutrophil cortex is about an order of magnitude larger than those measured for phospholipid bilayers or red cell membranes. Because of the limits of the resolving power of the light microscope used to observe cell penetration into the pipet, the authors were not able to investigate pore sizes approaching the proposed dimensions of the cortex.

In the present study, we investigated the tendency of HL-60 to infiltrate PCTE membranes with nominal pore diameters of 0.2, 0.1, and 0.05 μm, significantly smaller than for any previous study and approaching the proposed dimensions of the cortical layer. We studied a variety of hydrostatic pressures for each membrane ranging from values near or below the critical pressure predicted by Laplace's law, to values at least an order of magnitude higher. Our results indicated that cells will infiltrate 0.2 and 0.1 μm pores at pressures far below those predicted by the theory proposed by Zhelev et al. discussed above, but were probably unable to penetrate the 0.05 μm diameter pores. Based on our TEM images and analysis we speculate that the first step of infiltration may be the aspiration of pre-formed surface features, and that subsequent elongation may be due to dissociation of the supporting cytoskeletal structure.

6.3 Materials and Methods

6.3.1 HL-60 Cell Suspensions

HL-60 cells were grown in continuous suspension culture in tissue culture flasks at 37° C in a humidified atmosphere containing 5% CO_2 in RPMI media supplemented with 25 mM HEPES buffer, 10% fetal bovine serum, 4 mM L-glutamine, 50 IU/ml penicillin and 50 μg/ml streptomycin (BioWhittaker, Walkersville, MD). Cell cultures were passaged approximately

every 48 hr, and cells were harvested for use in cell aspiration experiments while in their log growth phase.

Before use in cell aspiration experiments, the concentration of cells in suspension culture was determined by counting the cells contained in a diluted aliquot with a hemacytometer (Reichert Scientific Instruments, Buffalo, NY). Viability was determined by Trypan Blue dye exclusion. A fraction of the cell suspension, containing a number of cells sufficient to perform the cell aspiration experiment, was centrifuged at 200 × g and 4° C for 15 min to pellet cells. The supernatant was discarded and the cells were resuspended in Dulbecco's Phosphate Buffered Saline without calcium and magnesium pH 7.4 (DPBS, Sigma Chemical Company, St. Louis, MO) at 4° C for washing. The cells were centrifuged and washed once more with cold DPBS. Finally, the cells were centrifuged and resuspended at 2 × 10^6 cells/ml in cold DPBS supplemented with 1% w/v bovine serum albumin (BSA, Miles Inc., Kankakee, IL) which had been pre-filtered through a 0.1μm or 0.05 μm membrane. Cell suspensions were kept on ice until immediately prior to use in cell aspiration experiments. For one experiment, cells were prepared in an identical fashion except that all procedures were performed at room temperature instead of 4° C.

6.3.2 Polycarbonate Track-Etched Membranes

Polycarbonate track-etched (PCTE) membranes with nominal pore diameters of 0.05 (Lot #AE86AX12A), 0.1 (Lot #AE84AH11C) and 0.2 μm (Lot #AG83CD11D) and a diameter of 25 mm were purchased from Osmonics, Livermore, CA. The PCTE membranes have cylindrical, straight through pores, normal within ± 34° to the surface. Nominal thickness of the membranes is 10 μm for the 0.2 μm nominal pore diameter, and 6 μm for the 0.05 and 0.1 μm nominal pore diameters. The membranes are coated with polyvinylpyrrolidone to increase hydrophilicity and allow thorough wetting of even the

smallest pore sizes.

Actual pore density, pore size distribution, and the frequency of pore overlaps was determined by observing samples of the membranes with a field emission scanning electron microscope (JEOL 6320F, JEOL, Peabody, MA). Samples of each membrane were mounted on aluminum stubs using conductive graphite paint (Ted Pella, Inc., Redding, CA) with the shiny side up. The membranes were then coated with 30 to 40 Å of gold/palladium using a high resolution ion beam coater (Model 681, Gatan Inc., Warrendale, PA). Coated samples were observed and photographed at 1.0 kV with an 8 mm working distance and angle of observation of 0°. Pore density, and the frequency of occurrence of pore overlaps, was determined by counting the pores visible on photomicrographs of two different areas of the sample taken at 10,000× for 0.2 and 0.1 μm membranes (101 μm^2 area for each photomicrograph) and 20,000× for 0.05 μm membranes (25 μm^2 area). Pore size distribution was determined by measuring two, orthogonal diameters of single pores visible on photomicrographs taken at 20,000× for 0.2 and 0.1 μm membranes and 40,000× for 0.05 μm membranes with a high-precision dial caliper (Mitutoyo Corporation, Tokyo, Japan). The actual pore size was determined as the geometric mean of the two orthogonal diameters for each pore. The total number of pores measured was 42, 51, and 34 for 0.2 μm, 0.1μm, and 0.05 μm membranes respectively.

6.3.3 Filter Aspiration Procedure

The experimental set up for application of constant pressure to HL-60 cells on PCTE membranes is shown schematically in figure 6.1. The PCTE membranes were placed horizontally, with the glossy face on the upstream side, in a polycarbonate "Swin-Lok" filter holder (Nuclepore Corporation, Pleasanton, CA). The apparatus was constructed using 1/16" I.D. flexible plastic tubing (Tygon S-50-HL, Norton Performance Plastics Corporation, Akron,

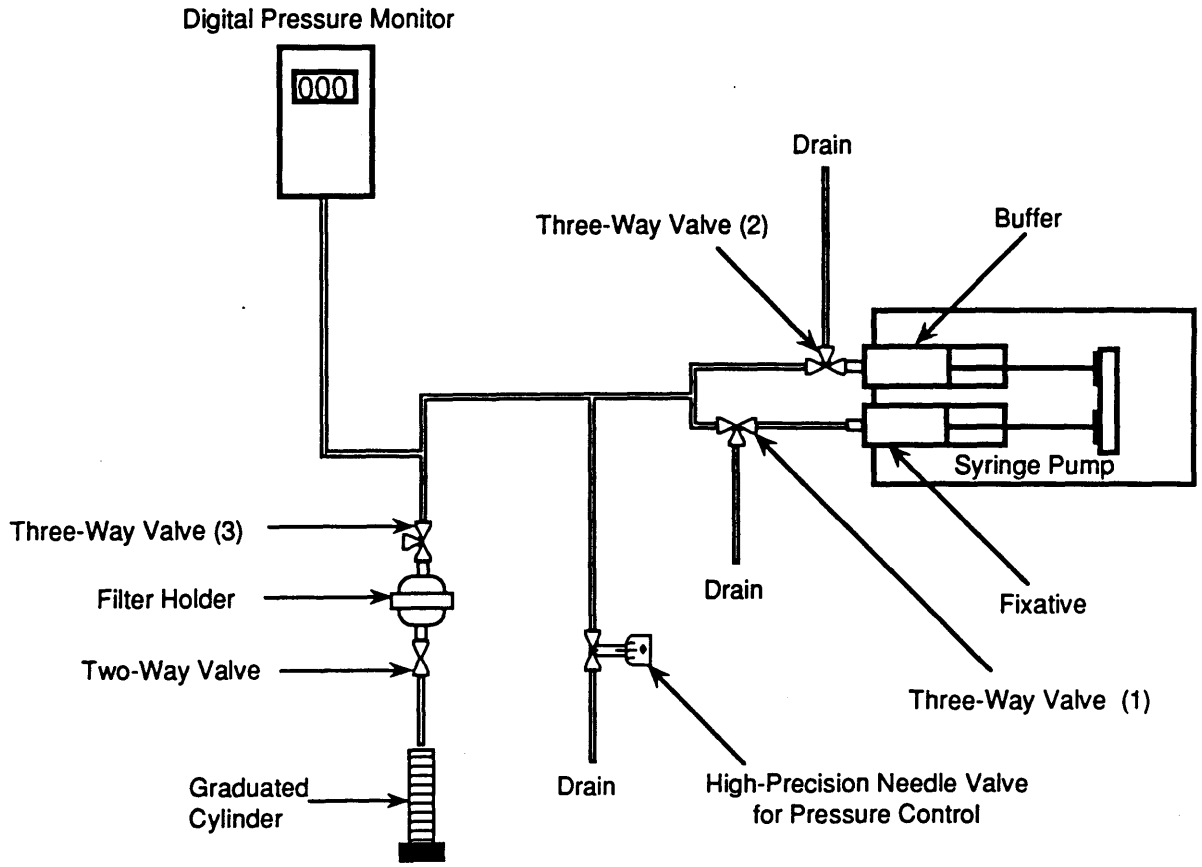

Figure 6.1 Experimental apparatus for application of constant pressure to HL-60 cells.

OH) and lengths were minimized to minimize hold up volume in the system. Positive pressure was generated using a two channel syringe pump with a synchronous, surge-less motor (Model 975, Harvard Apparatus, South Natick, MA), and measured with a digital pressure monitor (Model SP1405, Gould Statham, Oxnard, CA).

After assembly of the apparatus, the digital pressure monitor was checked for accuracy with air in the system using an open-ended mercury manometer connected in series with the pressure monitor. The system was also leak-tested with both air and buffer solution (DPBS) in the system prior to the start of the experiment. Before cells were loaded into the filter holder, the PCTE membrane was thoroughly wetted by pumping a small volume of DPBS through the membrane at high pressure (200 to 250 mmHg). After wetting the membrane, the one-way stopcock downstream of the filter holder was closed and the filter holder was removed from the system by disconnecting it from three-way stopcock (3) shown in figure 6.1. The buffer was manually shaken out of the upstream side of the filter holder which was then slowly filled with the HL-60 cell suspension. Care was taken to completely fill the upstream portion of the holder to eliminate bubbles (about 0.95 ml). The filter holder was carefully reattached with three-way stopcock (3) filled with DPBS and adjusted so that the outlet was vented to atmospheric pressure. Three-way stopcock (3) was then adjusted so that the filter holder could receive flow from the system, the one-way stopcock was opened and buffer was pumped through at a very slow rate (previously determined to create a pressure drop well below the target pressure drop for the experiment) until the first drop of buffer appeared at the outlet of the one-way stopcock. The flow was stopped, and, after allowing the pressure reading to equilibrate, the digital pressure monitor was zeroed. During the first phase of the experiment, three-way stopcocks (1) and (2) shown in figure 6.1 were adjusted so that buffer flowed to the filter holder and the fixative (2% w/v glutaraldehyde in PBS pH

7.2) was diverted to drain, and the pressure was maintained at the desired level by diverting a portion of the flow through a high-precision needle valve (Nuclear Products Co., Cleveland, OH). After all cells had been loaded onto the membrane (after one load volume, about 0.95 ml, of permeate had been collected) the desired pressure was maintained for 5 min (30 min for one experiment) before fixation. In order to fix the cells at constant pressure, three-way stopcocks (1) and (2) were simultaneously adjusted so that fixative flowed to the filter holder and buffer to drain. A fixation time of 10 min at constant pressure was determined to start when a volume of permeate had been collected equal to the hold-up volume in the system from three-way stopcock (1) to the PCTE membrane (1.3 ml). The cells were then fixed in the 2% glutaraldehyde for an additional 60 min at ambient pressure.

For experiments performed with no applied pressure, the filter holder and PCTE membrane was assembled and the membrane was wetted as described above. The DPBS was manually shaken out of the upstream part of the filter as previously described and then filled with DPBS supplemented with 1 % BSA. After a period of 10 or more minutes, the DPBS with BSA was shaken out of the filter holder and 0.7 ml of an HL-60 suspension at 2×10^6 cells/ml in DPBS was slowly injected. This injected volume was sufficient to cover the 2.4 cm^2 membrane area to a depth of 3 mm. The cells were allowed to settle and attach to the membrane for 30 min with the filter holder inlet open to the atmosphere. After 30 min, 1 ml of 2 % glutaraldehyde fixative was added dropwise (about 10 µl at a time) over a period of about two minutes. The cells were then fixed in the 2% glutaraldehyde for an additional 60 min at ambient pressure. All procedures were carried out at room temperature.

6.3.4 Preparation of Cells for Electron Microscopy

Samples of cells adhered to PCTE membranes were prepared for analysis by transmission electron microscopy (TEM) and field-emission scanning electron microscopy

(SEM). For TEM, cells adhered to membranes were washed three times with cold 0.1 M cacodylate buffer (pH 7.4) and post-fixed with 2 % w/v osmium tetroxide in 0.1 M cacodylate buffer for 1 hr at 4°C. Membranes were then washed with the cacodylate buffer and dehydrated through a graded series of ethanol/water mixtures. During the dehydration step with 70 % w/v ethanol, 0.5 % w/v uranyl acetate was added for en bloc staining. The dehydrated samples were then infiltrated with Spurr's low viscosity resin (Polysciences, Inc., Warrington, PA) in three steps through a graded series of propylene oxide/Spurr resin mixtures. After infiltration and curing of the resin, thin sections (40 to 90 nm) were made in a direction normal to the plane of the PCTE membrane yielding cross-sectional views through the cells and membranes. Thin sections were collected on 200 mesh copper grids (Polysciences, Inc., Warrington, PA) and post-stained with 1 % w/v potassium permanganate for 5 min, 2 % w/v uranyl acetate for 30 min, and Reynolds lead citrate (Reynolds, 1963) for 5 min before observation at 80 KV with the TEM (JEOL 1200 EX II, JEOL, Peabody, MA). The HL-60 cells were prepared for SEM using a modified version of the method described by Brailsford, et al. for red blood cells (figure 6.2.) (Brailsford et al., 1977). Briefly, the PCTE membranes with adherent cells were washed in 0.1 M cacodylate and post-fixed with 2 % osmium tetroxide as described above, dehydrated through a series of graded ethanol/water mixtures, and immersed in two changes of hexamethyldisilazane (HMDS) (Polysciences, Inc., Warrington, PA) for 5 min each. A small square of the filter was cut with a razor blade and while still wet with HMDS was placed cell side down on a 12 mm round glass coverslip. The membrane was gently patted flat with a piece of dry filter paper to absorb excess HMDS and cause the cells to adhere to the coverslip. Before the HMDS dried under the membrane, the coverslip was placed very gently into a watch glass containing chloroform by slipping it carefully under the chloroform/air interface. The coverslip was immersed in three changes of

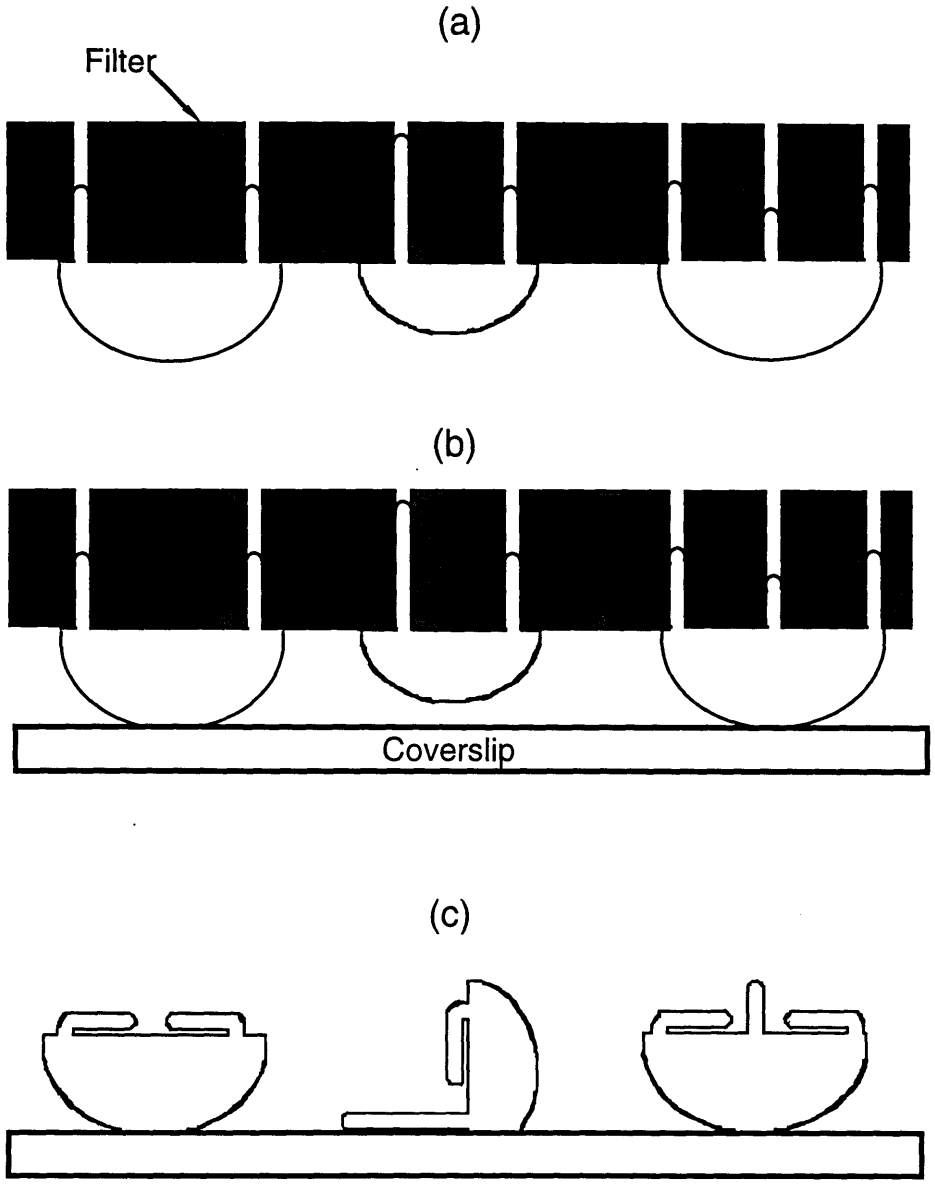

Figure 6.2 Schematic illustration showing preparation procedure for SEM. (a), Filter with attached cells after fixation and dehydration. (b), After transfer to glass cover slip. (c), Some observed *orientations of cells and infiltrations* after dissolving PCTE membrane with chloroform.

chloroform for 5 min each to ensure complete dissolution of the PCTE membrane, transferred to HMDS for an additional two changes of 5 min each and air-dried in a desiccator. The completely dried coverslip was mounted onto an aluminum stub with conductive graphite paint and coated with 100-300 Å of gold/ palladium using an evaporative coater (Model E306A, Edwards High Vacuum International, Manor Royal, England) The samples were analyzed on the SEM at 5 KV, a working distance of 8 mm and a viewing angle of 0° to 90°.

Results are expressed as mean ± one standard deviation. Statistical comparisons of some data were made using a two-tailed Student's t test for unpaired data, and results were considered significant for $p \leq 0.05$.

6.4 Results

6.4.1 Morphology of PCTE Membranes as Observed by SEM

Figure 6.3 presents SEM photomicrographs of the PCTE membranes used in this study. The pore diameter and pore density measurements are presented in table 6.1 along with the measured hydraulic permeability. The actual pore diameter was found to be very close to the nominal pore diameter with a narrow pore size distribution. The percentage of single pores at the surface ranged from 78.6 % for 0.2 μm to 96.8 % for 0.05 μm membranes.

6.4.2 Cell Filtration Experiments

The pressure displayed by the digital pressure monitor was in agreement to that read by the mercury manometer to ± 1 mm Hg at the desired target pressure for all experiments. Pressures were recorded at six times during the course of an experiment. Pressure was easily controllable to ± 1 to 2 mmHg for target pressures up to 10 mmHg and ± 2 to 3 mmHg for higher target pressures. Pressures were most unstable during the periods of initial pressure

(a)

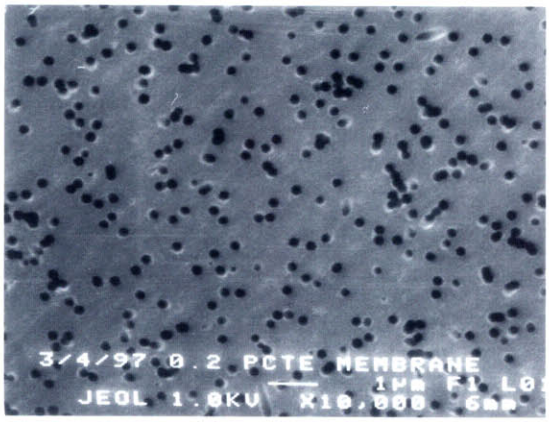

(b)

(c)

Figure 6.3 SEM Photomicrographs of PCTE membranes used for cell infiltration studies. (a) 0.2 μm, (b) 0.1 μm, and (c) 0.05 μm nominal pore diameters. Bars on photomicrographs represent 1 μm.

Table 6.1 *Morphology of PCTE Membranes and Measured Hydraulic Permeability*

Nominal pore diameter (μm)	0.05	0.1	0.2
Pore Density (10^8/cm^2)	7.7 ± 0.2	4.263 ± 0.007	3.85 ± 0.04
Singles (%)	96.8 ± 0.7	91 ± 1	78.6 ± 0.7
Doubles (%)	3.2 ± 0.7	8.3 ± 0.5	15.9 ± 0.7
Triples (%)	0	0.4 ± 0.5	5.0 ± 0.3
>Triples (%)	0	0	0.5 ± 0.2
Pore Diameter (μm)	0.048 ± 0.006	0.10 ± 0.01	0.19 ± 0.02
Surface Porosity (%)	1.4 ± 0.4	3.3 ± 0.7	11 ± 2
Hydraulic Permeability [L/(hr m^{2}mmHg)$^{-1}$]	0.86	7.81	36.8

adjustment and cell loading, and for a brief period after the switch from buffer to fixative during which brief excursions (< 5 sec and below target pressure) outside the above mentioned ranges sometimes occurred before readjustment could be made. Table 6.2 presents the actual mean pressures recorded during the course of the experiments along with the maximum pressure to which cells were exposed. Total exposure time of cells to pressure was a function of pressure and pore size since cell loading and the exchange of fixative for buffer in the system depends on filtration rate. Figure 6.4 summarizes exposure times for all conditions studied. The data points represents the median time of exposure for the cell population (represents exposure time for a cell which comes into contact with the membrane half way through the time required to load all cells), and the error bars reflect the full range of exposure times for cells in the device. The median time of exposure includes: one half of the full loading time, 5 min of time at pressure before the switch to fixative, and the time

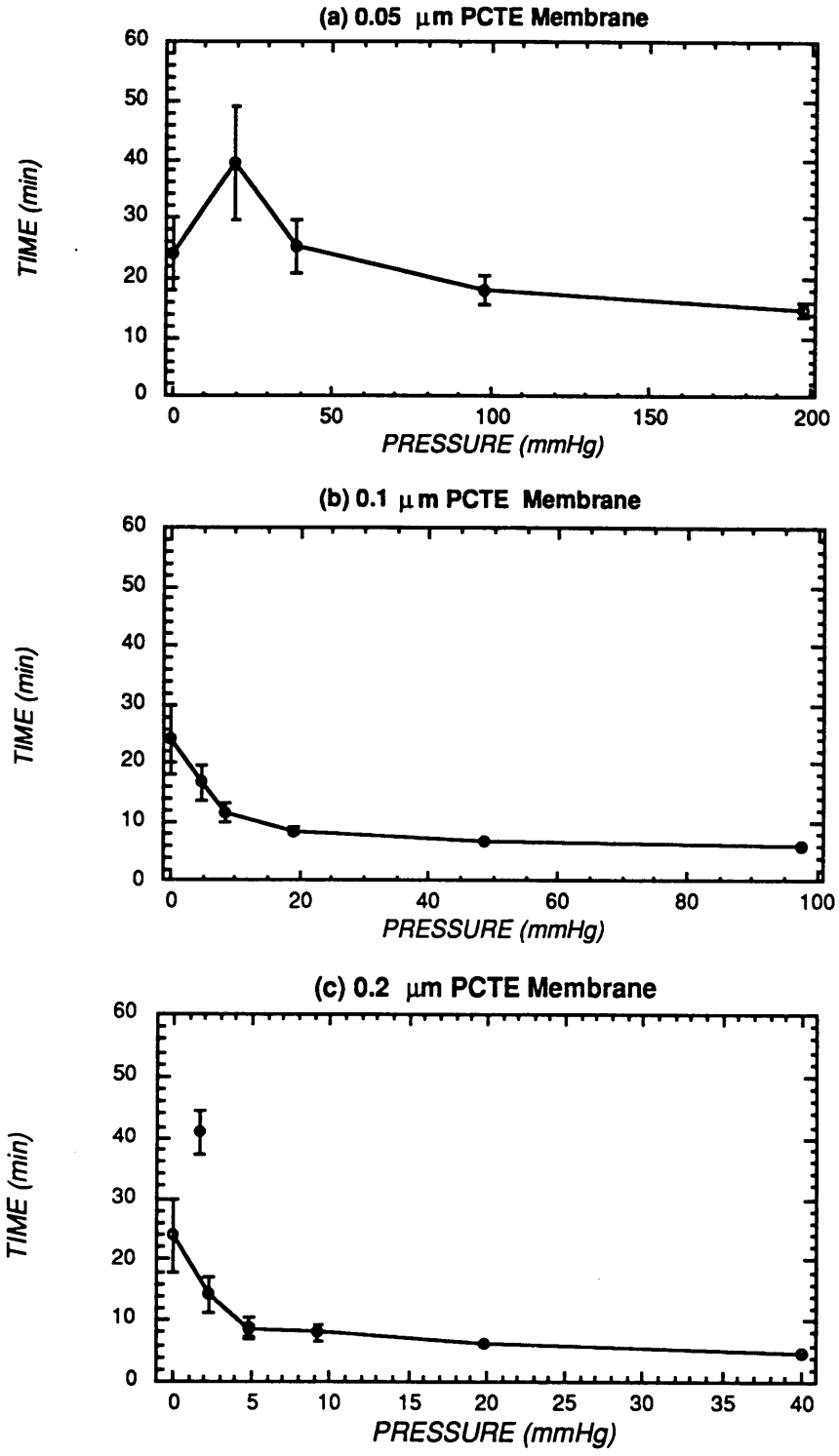

Figure 6.4 Total exposure time of cells to pressure before fixation for experiments performed with: (a) 0.05 mm, (b) 0.1 mm and (c) 0.2 mm PCTE membranes. Error bars reflect deviation in exposure time due to time required to bring all cells into contact with the membrane surface by filtration.

required for the fixative to displace the buffer in the system and reach the cells on the membrane. The minimum time for infinite flowrate would be 5 min. Differences in exposure times for 0 pressure condition reflects the settling rate of the cells. Figure 6.4 (b) and (c) shows that exposure times are fairly constant and close to 5 min for high pressure conditions for the 0.1 (≥ 20 mmHg target pressure)and 0.2 μm membranes (≥ 5 mmHg) but rise more sharply for lower pressures.

Table 6.2 *Actual and Maximum Pressures Recorded During Experiments*

Membrane	Target Pressure (mmHg)	Actual Pressure (mmHg)	Maximum Pressure (mmHg)
0.2 μm	2	2.2 ± 0.5	4
	2 (30 min exposure)	1.7 ± 0.5	3
	5	4.8 ± 0.4	7
	5 (Room Temp)	4.8 ± 0.4	6
	10	9 ± 1	12
	20	20 ± 3	23
	40	40 ± 1	43
0.1 μm	5	4.8 ± 0.4	6
	10	8.5 ± 0.8	10
	20	19 ± 1	21
	50	49 ± 2	53
	100	97.4 ± 0.6	108
0.05 μm	20	19.7 ± 0.5	23
	40	39 ± 2	42
	100	98 ± 2	107
	200	197 ± 4	218

Figure 6.4 (a) shows that exposure times for 0.05 μm membranes were significantly higher than for the other membranes for most conditions tested, and are a stronger function of pressure over the range studied. The data point which is off the curve in figure 6.4 (c) indicates the exposure time for the cells which were exposed to pressure for 30 min before fixation instead of 5 min.

6.4.2.1 TEM Observations of Cells Exposed to Pressure on PCTE Membranes.

Figures 6.5 to 6.10 show TEM photomicrographs of typical observations. Because of the variable angle of incidence of the pores with the membrane, very few pores were observed to pass all the way through the membrane in the sections. However, also because of the angle of the pores, many of the infiltrations visible in a single section will originate from regions of the contact area outside the plane of the section. Infiltrations appeared typically as tongues of material at various depths in the membrane with a granularity and appearance consistent with cellular cytoplasm surrounded by a plasma membrane (see figures 6.5 to 6.6 and 6.9 and 6.10), sometimes containing ribosomes (about 200 Å diameter black granules, see figures 6.5, 6.6, and 6.9). Most infiltrations were not continuously visible from the cell contact area to their terminus because of the angle of the pores with respect to the section. Many infiltrations appeared to be small pieces or discontinuous. It is not possible to say for certain whether, in fact, the pieces have become separated from the cell or if instead they are a part of a continuous infiltration which is not parallel to the plane of the section.

Figures 6.5 and 6.6 show results typical for cells exposed to higher pressures on 0.2 and 0.1 μm PCTE membranes (figure 6.5: 0.2 μm PCTE membrane and 40 mmHg, figure 6.6: 0.1 μm PCTE membrane and 50 mmHg) . The cells with infiltrations typically displayed a flattened contact area and a relatively smooth contour outside the contact area. Some cells as in figure 6.6 were observed to penetrate the membrane completely. This was evident from

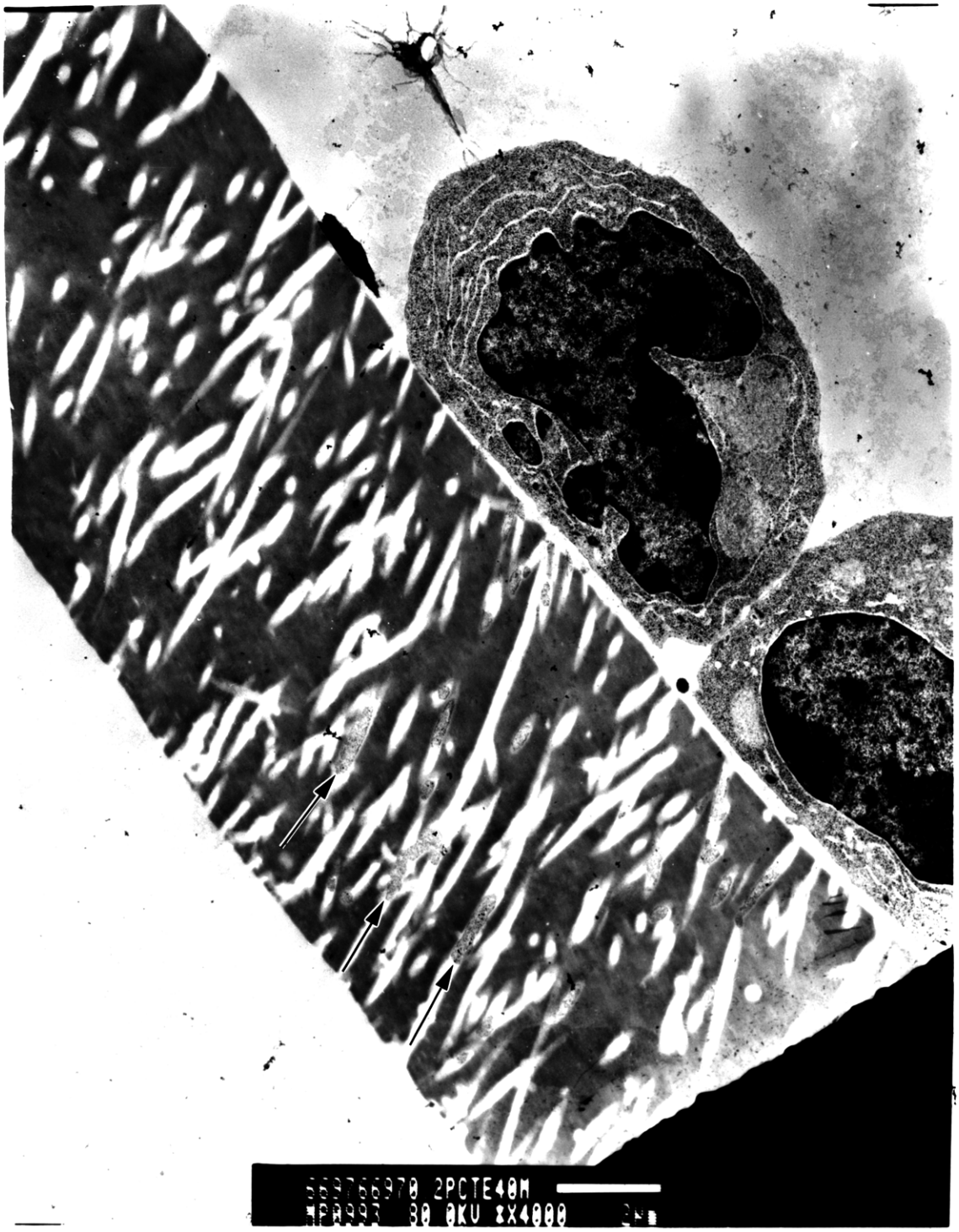

Figure 6.5

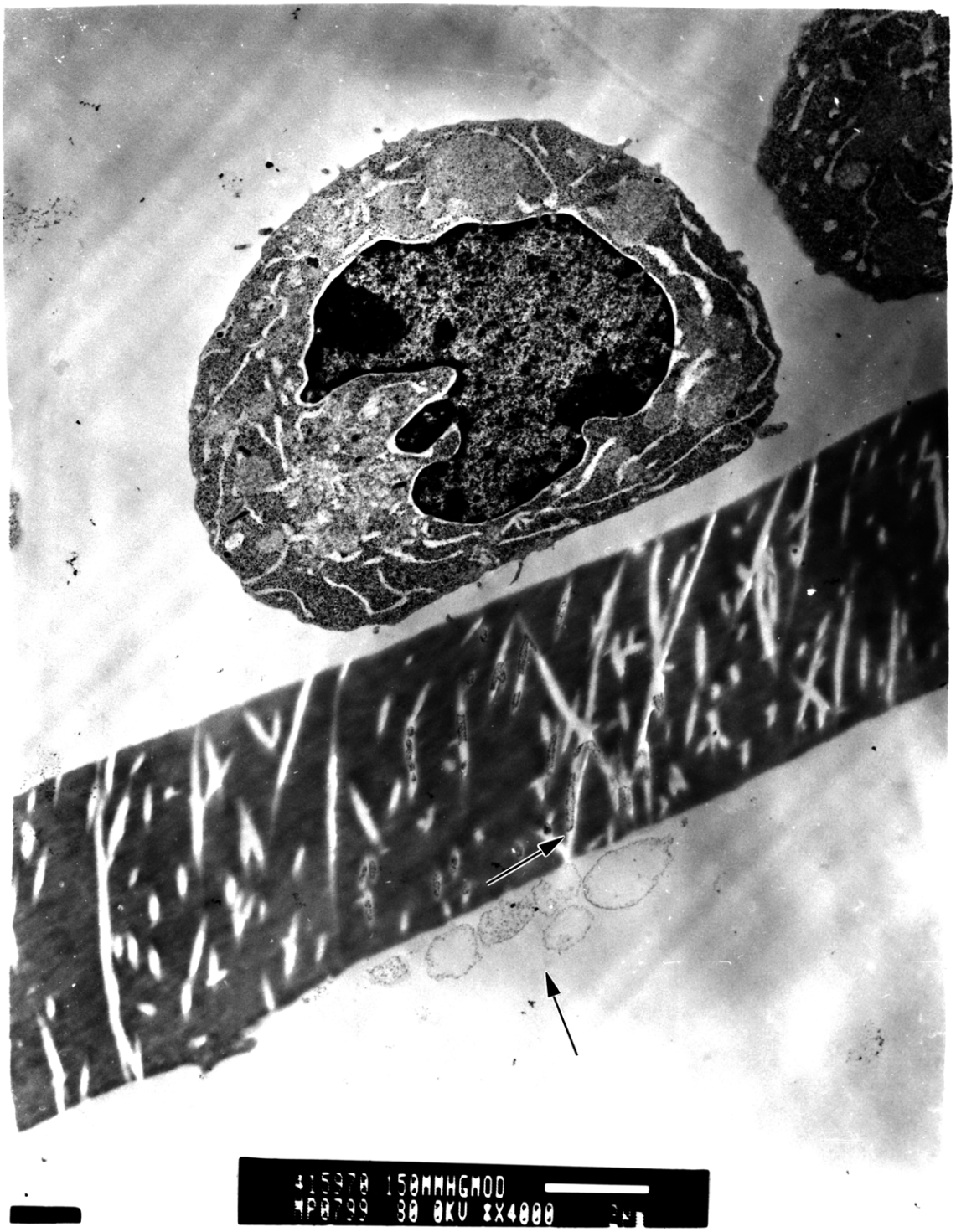

Figure 6.6

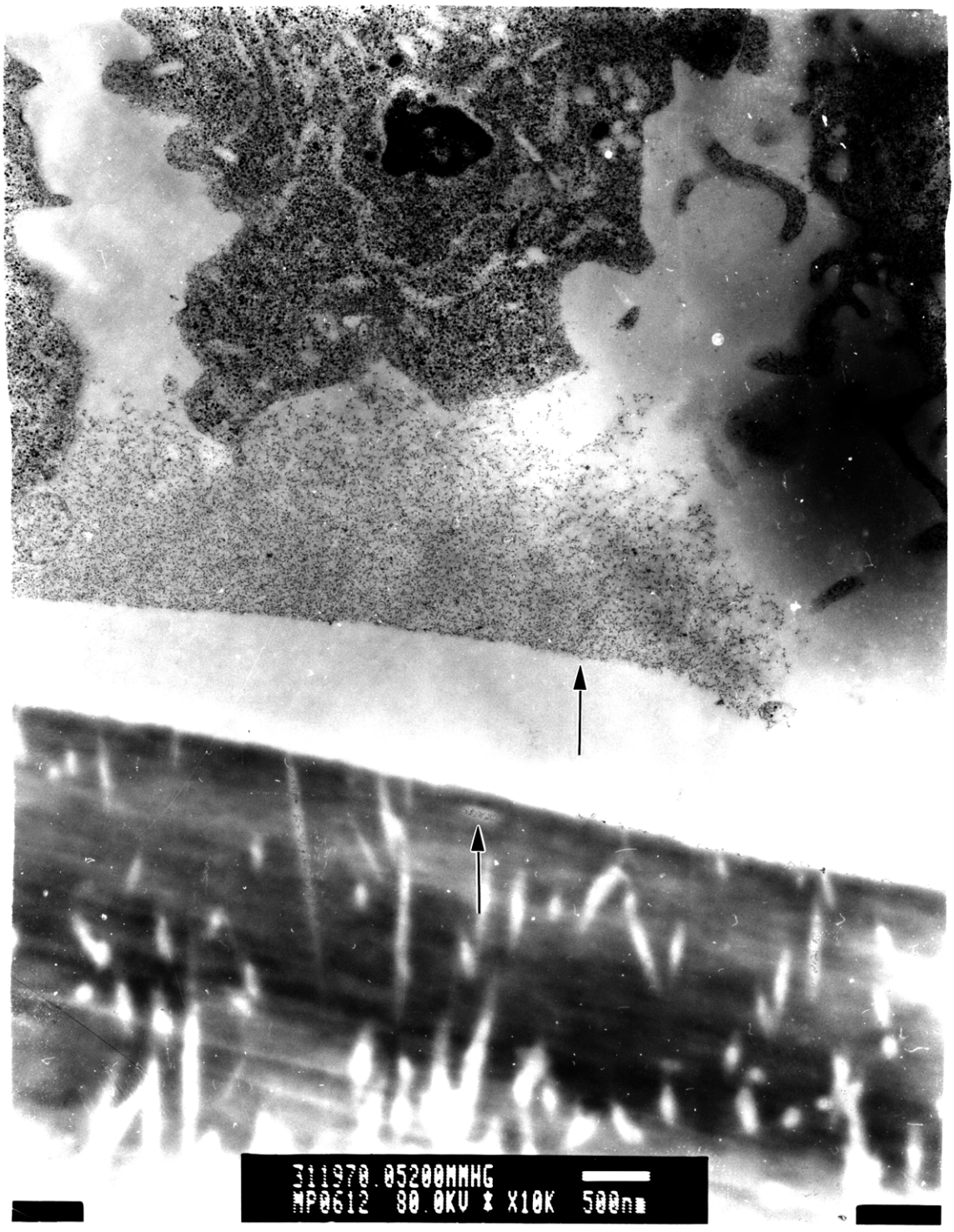

Figure 6.7

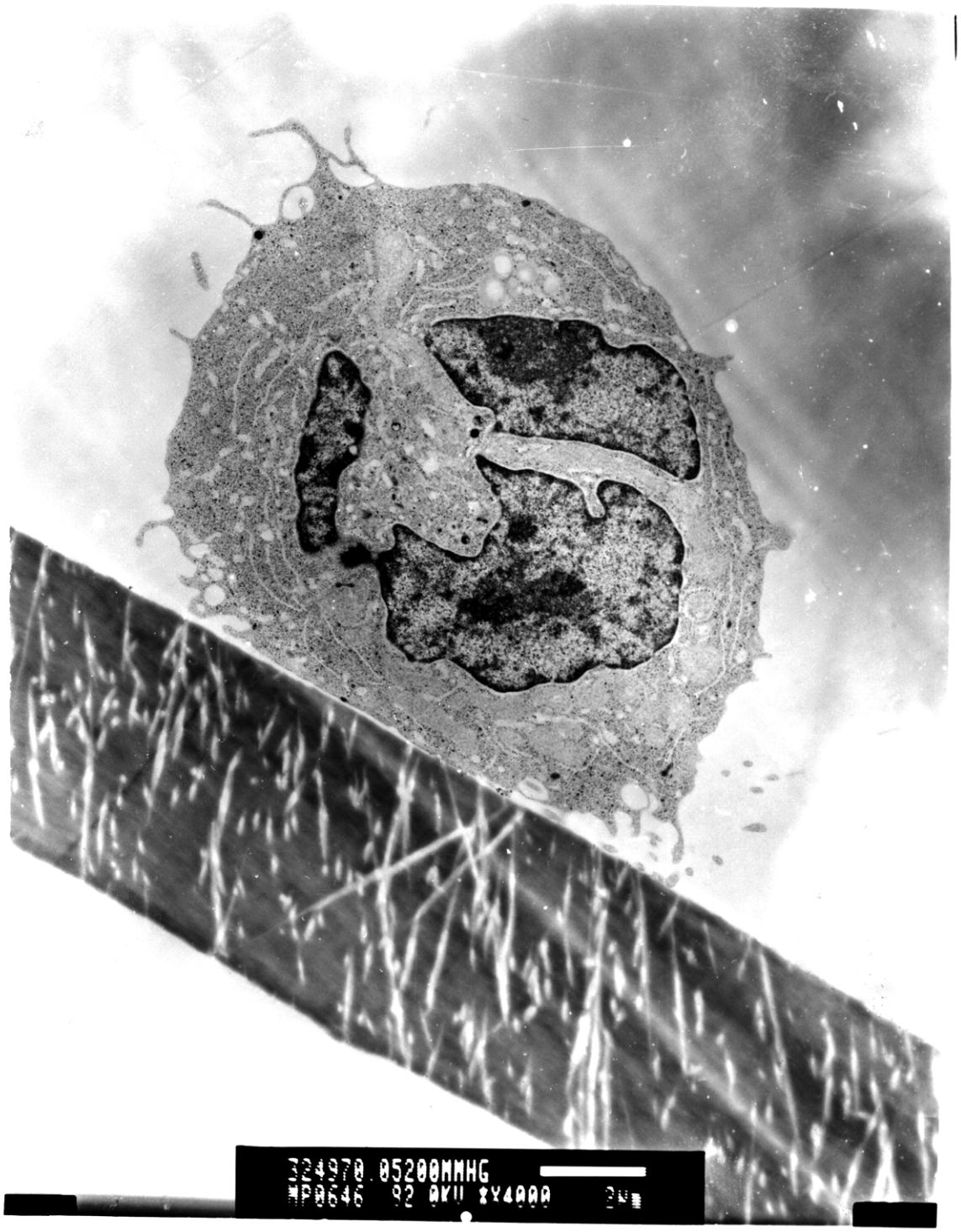

Figure 6.8

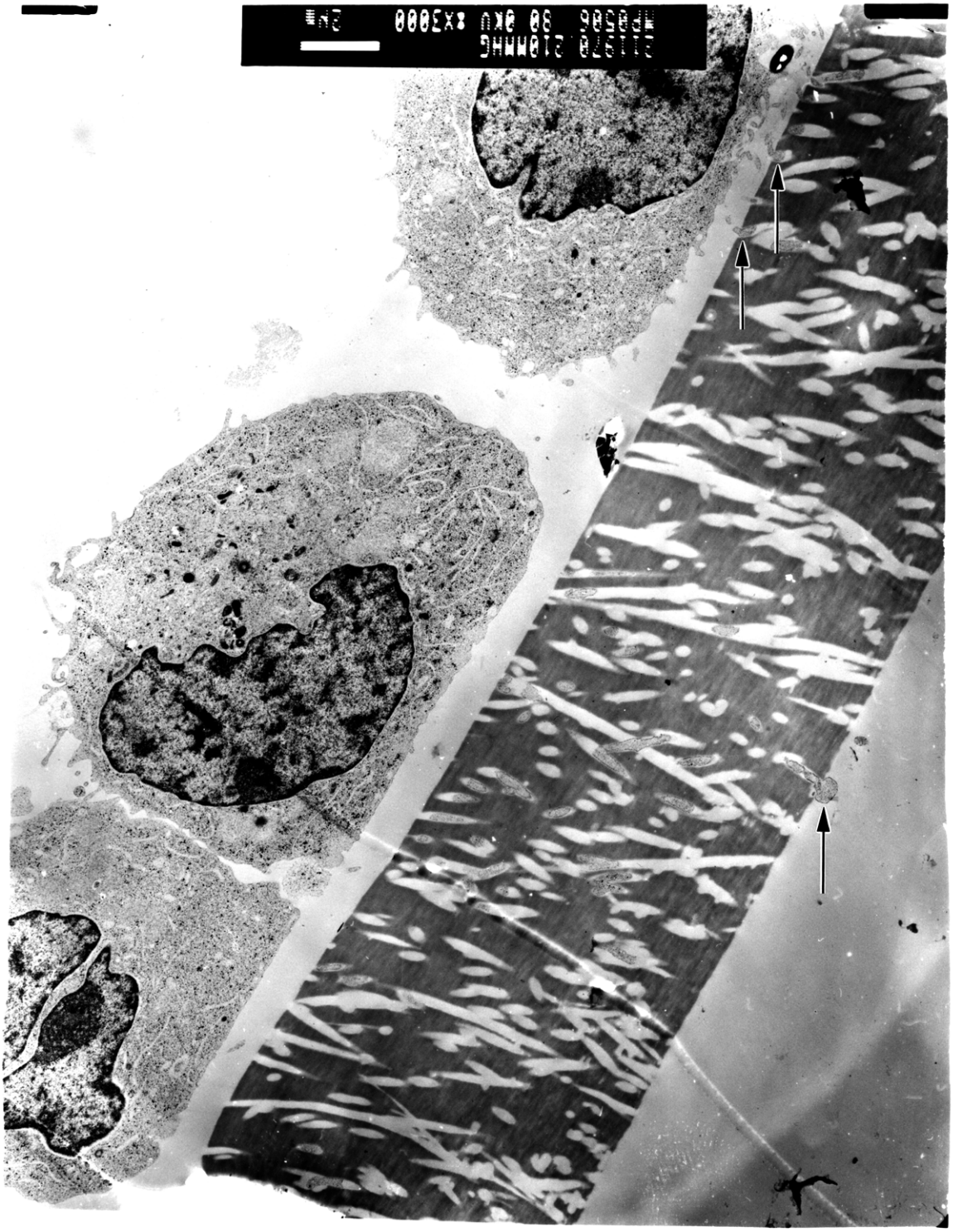

Figure 6.9

Figure 6.10

Captions for Figures 6.5 to 6.10

Figure 6.5 TEM photomicrograph showing a cell exposed to 40 mmHg pressure which has infiltrated a 0.2 μm PCTE membrane (arrows) but has not penetrated completely through. Small bar in legend is 2 μm.

Figure 6.6 TEM photomicrograph showing a cell exposed to 50 mmHg pressure which has infiltrated a 0.1 μm PCTE membrane and has penetrated completely through (arrows). Small bar in legend is 2 μm.

Figure 6.7 TEM photomicrograph showing a cell exposed to 200 mmHg pressure on a 0.05 μm PCTE membrane. Photo shows extracellular artifact observed in association with about 30% of cells at this experimental condition (top arrow). Some cellular or artifactual material has infiltrated into membrane (bottom arrow). Small bar in legend is 500 nm.

Figure 6.8 TEM photomicrograph showing a cell exposed to 200 mmHg pressure on a 0.05 μm PCTE membrane with no infiltrations visible. Small bar in legend is 2 μm.

Figure 6.9 TEM photomicrograph showing 3 cells exposed to 10 mmHg pressure on a 0.2 μm PCTE membrane. Center cell has infiltrated completely through membrane (bottom arrow) and top cell suggests aspiration of cellular microvilli often apparent at lower pressures (top two arrows). Small bar in legend is 2 μm.

Figure 6.10 TEM photomicrograph showing a cell exposed to 10 mmHg pressure which has infiltrated a 0.1 μm PCTE membrane (arrow). Photo suggests aspiration of cellular microvilli often apparent at lower pressures. Small bar in legend is 2 μm.

infiltrations which were visible at or near the side of the membrane opposite the cell, and by balls of material, resembling the infiltrations in consistency, on this same side.

In contrast to cells pressurized on 0.2 and 0.1 μm PCTE membranes, cells pressurized on 0.05 μm PCTE membranes were overwhelmingly free of visible infiltrations. Only for the highest pressure tested (200 mmHg) was there any suggestion of infiltration, and the observations were not conclusive. Figure 6.7 shows a cell on a 0.05 μm PCTE membrane which was exposed to 200 mmHg pressure. The photo shows an artifact which was associated with about 30 % of the cells observed on 0.05 μm PCTE membranes which were exposed to 200 mmHg pressure, and with two thirds of the cells which appeared to have infiltrated the membrane. The artifact consists of a diffuse granular material under the cell which does not appear to be contained by a membrane or to have an appearance consistent with cellular cytoplasm. It was unclear in such cells if the infiltration (visible in two pores near the top of membrane in figure 6.7) consists of cellular material, or is part of the artifact. Figure 6.8 shows a more typical cell which has also been exposed to 200 mmHg which is free of artifact and infiltrations.

In contrast to cells exposed to the higher pressures tested, some cells exposed to lower pressures on 0.2 and 0.1 μm PCTE membranes had a more irregular or microvillous appearance (see figures 6.9 and 6.10 which cells on a 0.2 μm PCTE membrane exposed to 10 mmHg pressure and 0.1 μm PCTE membrane exposed to 10 mmHg respectively). In many cases it appears that the microvilli on the cells are being aspirated into the pores of the membrane (top cell in figure 6.9 and cell in figure 6.10).

6.4.2.2 SEM Observations of Cells Exposed to Pressure on PCTE Membranes.

Cells from which the PCTE membrane to which they were attached has been removed are shown in figures 6.11 to 6.14 for various experimental conditions. Samples were viewed

(a)

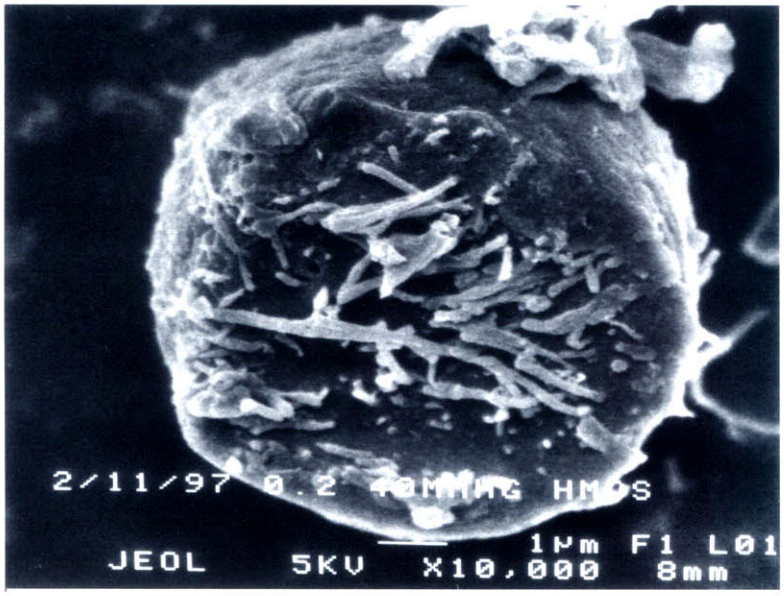

(b)

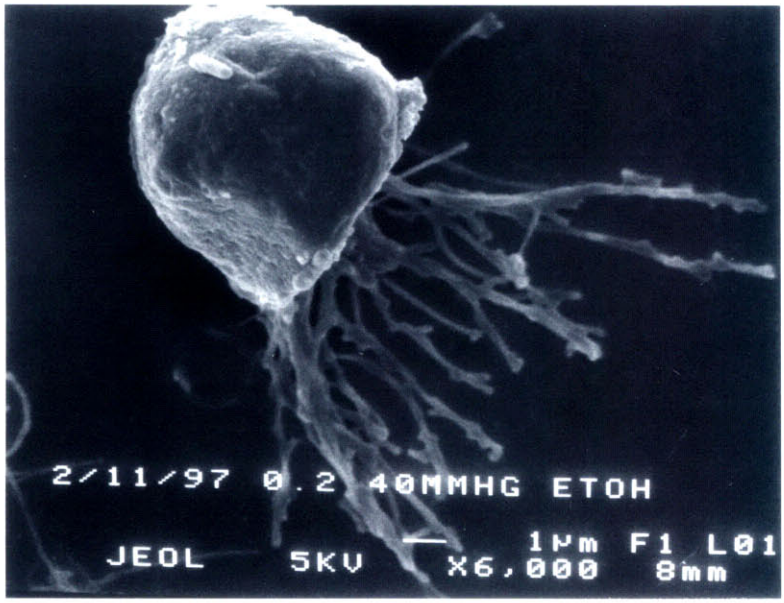

Figure 6.11 SEM photomicrographs showing cells exposed to 40 mmHg pressure on a 0.2 µm PCTE membrane after dissolving away the PCTE membrane. The cell in photo (a) shows the most typical orientation with the contact area nearly co-planar with the photographic plane. The cell displays numerous infiltrations many of which are lying approximately flat on the contact area. The cell in photo (b) is lying on the coverslip so that its contact area is approximately normal to the plane of the photograph with the infiltrations extended and supported by the coverslip. Smooth morphology is typical of cells showing extensive infiltration. Small bars in legends are 1 µm.

(a)

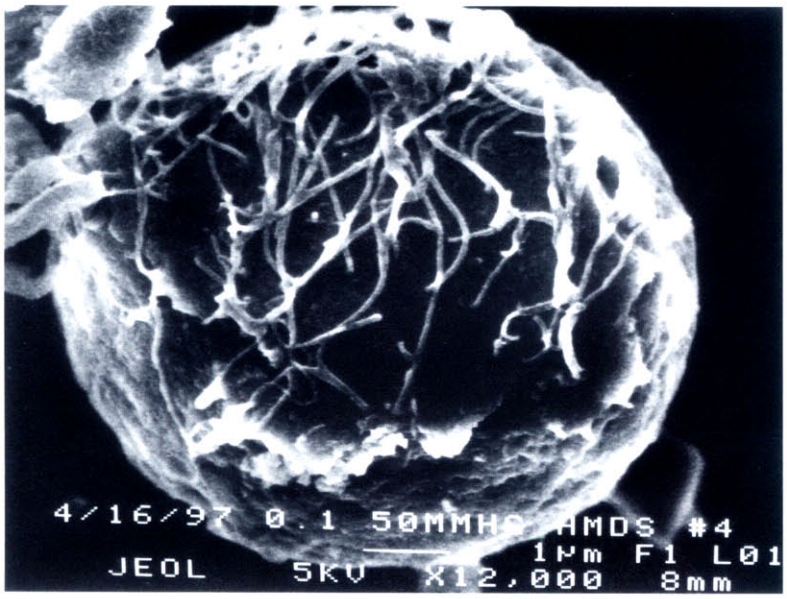

(b)

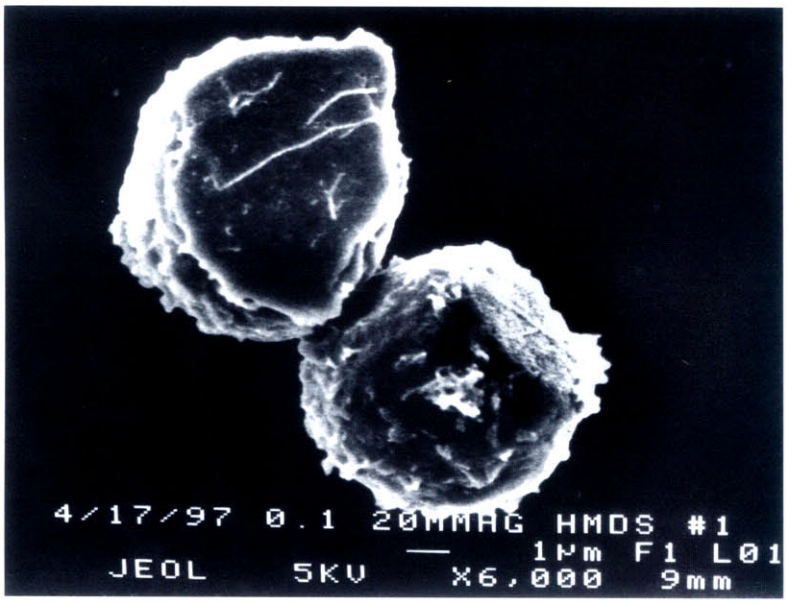

Figure 6.12 SEM photomicrographs showing cells exposed to 50 mmHg pressure (a) or 20 mmHg pressure (b) on a 0.1 μm PCTE membrane after dissolving away the PCTE membrane. The cell in photo (a) displays numerous infiltrations, many of which are lying approximately flat on the contact area, and a smooth morphology outside the contact area. The cells in photo (b) have fewer infiltrations and a rougher, more irregular morphology outside the contact area. Small bars in legends are 1 μm.

(a)

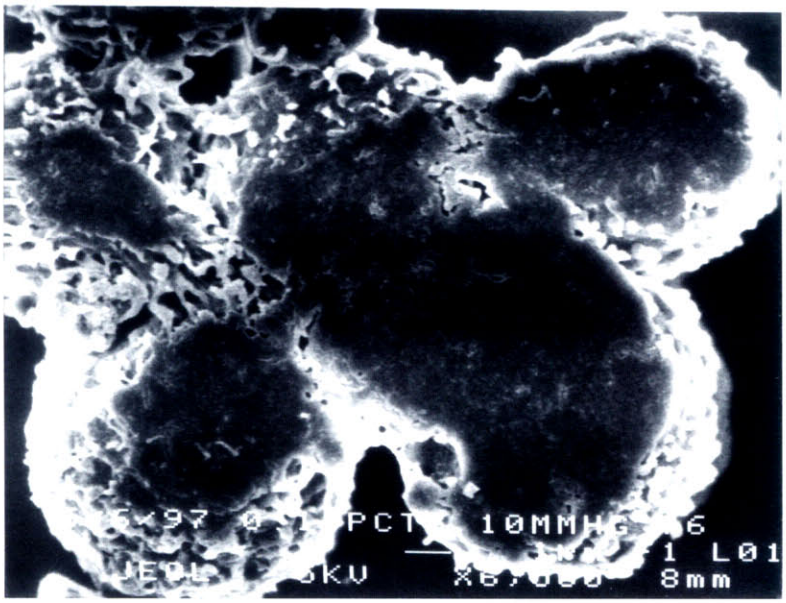

(b)

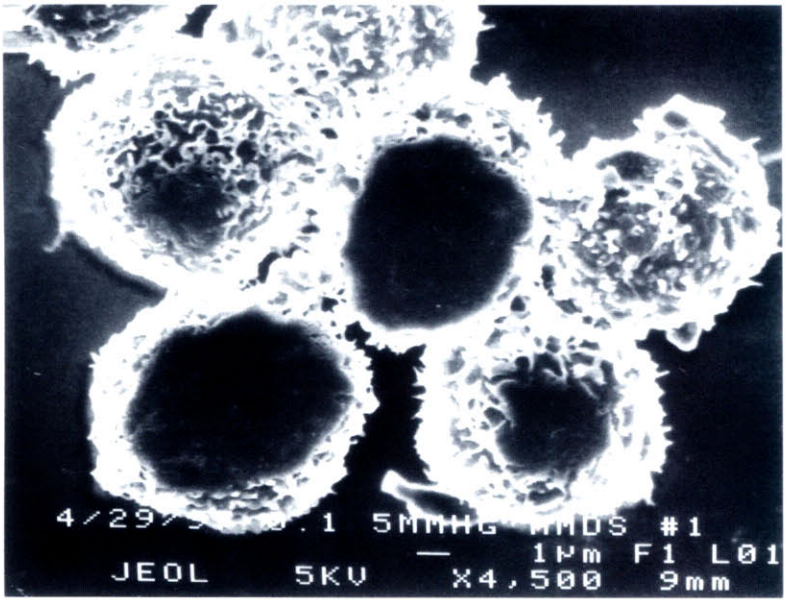

Figure 6.13 SEM photomicrographs showing cells exposed to 10 mmHg pressure (a) or 5 mmHg pressure (b) on a 0.1 μm PCTE membrane after dissolving away the PCTE membrane. Photo (a) shows a group of cells whose contact areas are oriented approximately co-planar with the photographic plane. The cells at the top right and bottom left have a few short infiltrations (≤ 1 μm). The other cells have no visible infiltrations. Photo (b) displays a group of cells with no visible infiltrations. Microvillous morphology is common for cells with few or no infiltrations Small bars in legends are 1 μm.

(a)

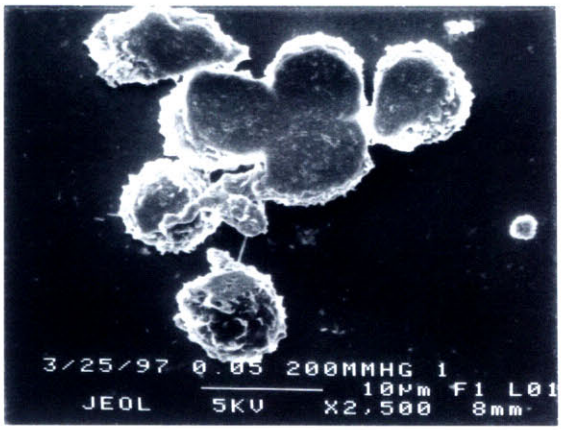

(b)

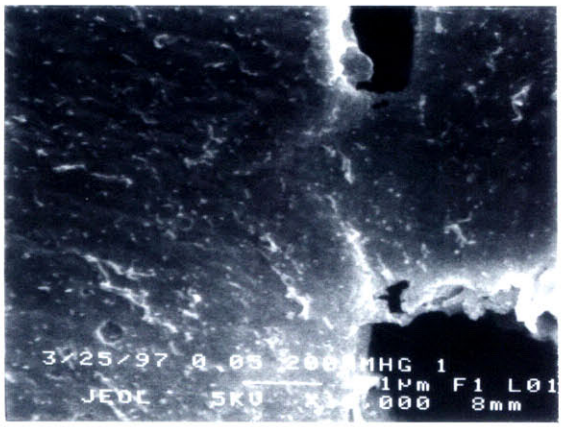

(c)

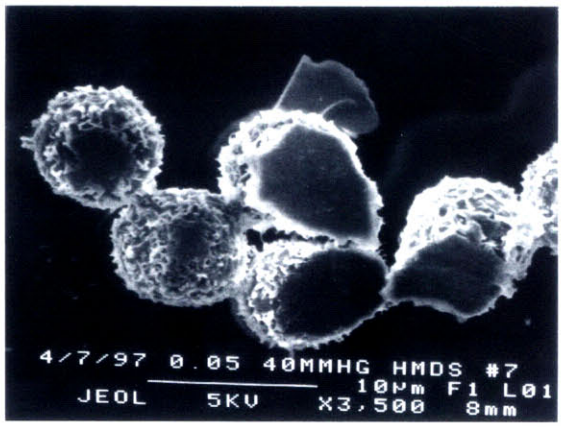

Figure 6.14 SEM photomicrographs showing cells exposed to 200 mmHg pressure (a) and (b) or 40 mmHg pressure (c) on a 0.05 µm PCTE membrane after dissolving away the PCTE membrane. Photo (a) shows a group of cells with contact areas possessing irregularities counted as infiltrations in characterizing the cells. (b) is a high magnification photo of part of the contact area in (a). Irregular shape and diameter of features in contact area was in contrast to most of the infiltrations observed with other pore sizes. Photo (c) shows a typical group of cells with no visible infiltrations. Microvillous morphology was observed for nearly all cells on 0.05 µm PCTE membranes. Small bar in legend: (a) and (c) 10 µm, (b) 1 µm.

on the microscope from a viewing direction normal to the plane of the glass cover slip (photographic plane and coverslip were co-planar). Figure 6.11 (a) shows a typical orientation of the cells with the flattened area which had been in contact with the PCTE membrane nearly co-planar with the viewing plane. A significant fraction of cells, however, appeared with their contact areas at other angles between 0° and 90°. Figure 6.11 (b) shows a cell with a contact area approximately normal to the viewing plane. Cells such as those in figure 6.11 (b) and 6.12 (b) which appear to have fallen over to some degree before making contact with the coverslip were probably not in firm contact with the coverslip when the PCTE membrane was dissolved (similar to center cell in figure 6.2). The cells shown in figure 6.11 were both subjected to 40 mmHg pressure on a 0.2 μm membrane. Infiltrations appeared as extended tube-like projections from the contact area with a diameter close to the nominal pore diameter of the PCTE membrane (almost all had diameters between 75 to 150 % of the nominal pore diameter). Infiltrations were generally not self-supporting and tended to lie flat on a supporting surface. Such a surface was typically the flattened contact area of the cell for cells with contact areas nearly co-planar with the coverslip (figure 6.11 (a)), or the supporting surface for the infiltrations was the glass coverslip for cells where the plane of the contact area was at a large angle to the coverslip (figure 6.11 (b)). Both cells in figure 6.11 possess many infiltrations, many whose length is comparable to or exceeding the cell diameter. The cells in the figure also demonstrate that the length of the infiltrations is variable even for a single cell. The morphology of cells showing extensive infiltration is typically smooth outside the contact area as shown in figure 6.11 and figure 6.12 (a).

Typical cells subjected to pressure on 0.1 μm membranes for 50 and 20 mmHg pressure conditions are shown in figure 6.12 (a) and (b), respectively. The cell in figure 6.12 (a) is similar to those seen in figure 6.11. The cells in figure 6.12 (b), however, have fewer

infiltrations and a rougher, more irregular morphology outside the contact area. Figure 6.13 shows cells subjected to pressure on 0.1 μm membranes at 10 mmHg pressure (a) and 5 mmHg pressure (b). Figure 6.13 (a) shows a group of cells whose contact area is oriented approximately parallel to the plane of the photo. Two of the cells (top right and bottom left) have a few short infiltrations (≤ 1μm) as well as a few bumps with a diameter consistent with the membrane pore size. The other cells in the photo, and the cells in (b) have no visible infiltrations. The cells also possess a microvillous or highly folded surface morphology (with spike-like, but not straight, projections or narrow surface ridges typically about 0.1 to 0.2 μm in diameter) common for cells having few or no infiltrations. For some cells exposed to the lower pressures on 0.2 and 0.1 μm membranes, and for cells subjected to only gravity, the contact areas were often difficult to distinguish and/or had features present which were difficult to categorize as infiltrations or surface features.

Cells subjected to pressure on 0.05 μm PCTE membranes were essentially infiltration-free or possessed short, more irregularly shaped features in their contact areas as shown the contact areas of a cells pressurized at 200 mmHg in figure 6.14 (a) and (b). Figure 6.14 (c) shows a group of cells subjected to 40 mmHg pressure which have flat, smooth contact areas without any evidence of infiltration. A microvillous morphology outside of the contact area was typical for cells subjected to all pressures on this membrane.

6.4.2.3 Quantitative Characterization of Cell Populations by On-Scope Categorization of Cells in TEM and SEM Samples

To quantify the tendency of pressure to cause HL-60 cells to infiltrate membranes of different pore sizes, cells in samples were assigned to one of three categories during observation of samples directly on the microscope (referred to as "on-scope" measurements as opposed to measurements made from the photographs of a portion of the cells observed). For

samples observed by TEM, cells were placed into the following categories: 1) no visible infiltration (eg. figure 6.8); 2) infiltration into, but not completely through membrane (eg. figure 6.5); or 3) infiltration completely through membrane (eg. figure 6.6). From 2 to 6 individual sections were analyzed for each condition depending on the cell density. Each section analyzed came from a different region of the PCTE membrane. Only cells where the contact area and the PCTE membrane below the cell were completely visible and free of obstruction (e.g. by grid bars) were included. In addition, no cell visible on the section whose diameter was less than about 5 μm was considered (so that cells sectioned close to the center of their contact area were preferentially considered), nor were cells separated from the membrane by a distance of more than about 25% of their cell diameter. Determinations were made at minimum magnifications of 10,000× for 0.2 μm membrane samples, 20,000× for 0.1 μm membrane samples and 40,000× for 0.05 μm membrane samples.

For samples observed directly on the SEM, cells were placed into the following categories: 1) no visible infiltration (eg. figures 6.13 (b) and 6.14 (b)), 2) infiltration less than or equal to 1 μm in length (eg. figure 6.13 (a)), or 3) infiltration exceeding 1 μm in length (eg. figures 6.11 and 6.12). Only cells with well defined and flattened contact areas were included. Only features possessing the following characteristics were counted as infiltrations: 1) shape and size distinct from the morphology of the rest of the contact area; 2) substantially straight and with relatively constant diameter over the length of the feature, and 3) diameter of feature between 75 % and 150 % of the nominal pore diameter. For cells exposed to lower pressures where a microvillous morphology was common, it was sometimes difficult to distinguish between infiltrations and flattened surface features. In such cases, cells were not included. Even with the above criteria, because of the similarity in appearance between morphological features of some cells and infiltrations as described by the criteria above, there

was inevitably some judgement involved in categorizing some cells. Measurements were made with a transparent ruler and high precision calipers directly from the SEM screen for cells with clearly visible contact areas, and were not corrected for cell contact area angles with respect to the plane of the screen. This invariably leads to some underestimation of the length of infiltrations on cells with contact areas oriented at large angles with respect to the plane of the viewing screen (see section 6.4.3.1). Therefore, the fraction of cells categorized as having infiltrations ≤ 1 μm may have been somewhat exaggerated at the expense of the fraction with infiltrations ≥ 1 μm. Determinations were made at minimum magnifications of 10,000× for 0.2 μm membrane samples, 20,000× for 0.1 μm membrane samples and 40,000× for 0.05 μm membrane samples. Cells satisfying the above criteria from at least 3 different locations on the sample were included.

Results of the on-scope cell categorization are shown in figure 6.15 (a), (b), and (c) for cells pressurized on 0.05, 0.1, and 0.2 μm PCTE membranes respectively. The results are presented as the percentage of the total number of cells observed which fell into the categories described in the figure legends as a function of applied pressure. The number of cells represented by each data point is shown in table 6.3, columns 3 and 4. Figure 6.15 (b) and (c) show that with 0.1 and 0.2 μm pore sizes, the cell suspensions display a threshold-like behavior with respect to infiltration with the percentage of cells displaying infiltrations rising rapidly to a plateau over a fairly narrow range of pressure. Results from TEM and SEM observations are in good qualitative agreement. For cells pressurized on 0.1 μm pore size membrane this transition occurs between the pressures of 5 mmHg, where cell populations resemble cells exposed to gravity, except for a modest increase in primarily short infiltrations, and 20 mmHg where more than 80 % of cells have infiltrated the membrane (TEM observations). The situation is similar for cells pressurized on 0.2 μm pore size membranes,

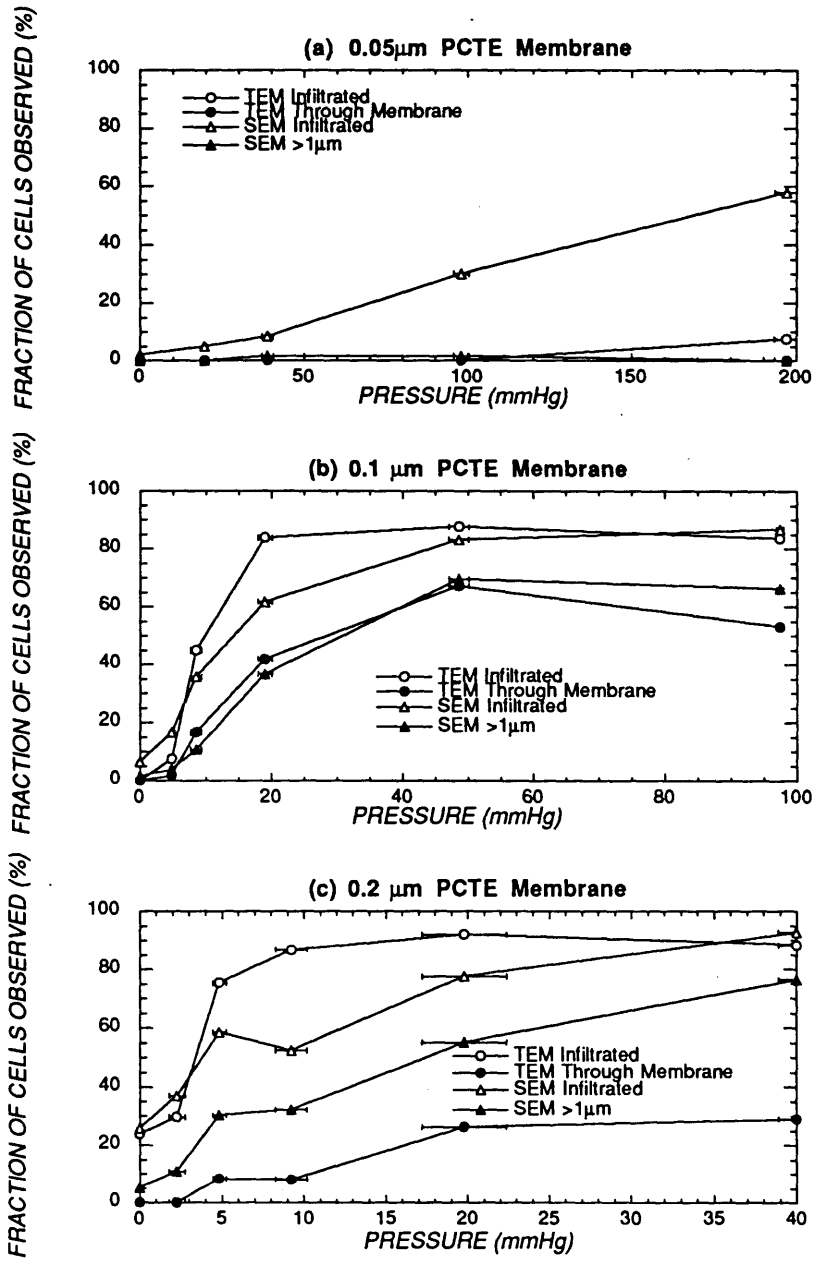

Figure 6.15 Results of on-scope categorization of cells pressurized on (a) 0.05 μm pore size PCTE membranes, (b) 0.1 μm pore size PCTE membranes, and (c) 0.2 μm pore size PCTE membranes. Open circles show the total percentage of cells in the observed TEM samples where infiltration into the membrane was evident. Closed circles show the total percentage of cells whose infiltrations completely penetrated the membrane. Open triangles show the total percentage of cells in the observed SEM samples where infiltrations were observed in the cell contact area. Closed triangles show the total percentage of cells whose infiltrations were more than 1 μm long as measured in the photo plane. Error bars in the *x* direction represent one standard deviation of the average applied pressure (see table 6.2).

except that the transition occurs between 2 mmHg and 5 mmHg. Also, for cells on 0.2 μm pore size membranes, even exposure to only gravity induced some primarily superficial infiltration in a small fraction of cells (20 to 25 %). In addition, a substantially higher fraction of cells completely penetrated the 0.1 μm pore size membranes as opposed to 0.2 μm pore size membranes. This is no doubt due, in part, to the thinner dimensions of the 0.1 μm pore size membranes.

Figure 6.15 (a) shows very different results for cells pressurized on 0.05 μm pore size membranes. There is no threshold pressure, and only a gradual but steady rise (above 40 mmHg) in the percentage of cells which displayed primarily short features in their contact areas which were counted as infiltrations (see figure 6.14 (a) and associated discussion). None of the cells was observed to infiltrate the membrane by TEM analysis except for a small percentage (< 10 %) at 200 mmHg primarily associated with the artifact shown in figure 6.7 and discussed previously. It cannot be determined with certainty if there was any infiltration at all into the 0.05 μm pore size PCTE membrane at any of the pressures studied.

Table 6.3 *Number of Cells Analyzed for On-Scope Categorization of Infiltration and Categorization of Cellular Morphology*

		Number of Cells Analyzed		
		On-scope Categorization of Infiltration		
Membrane	Target Pressure (mmHg)	TEM	SEM	Categorization of Morphology from SEM Photos
0.05 μm	0	17	50	15
	20	46	60	18
	40	51	59	54
	100	25	60	25
	200	40	52	36
0.1 μm	0	28	62	17
	5	55	78	42
	10	78	84	46
	20	43	60	22
	50	64	59	27
	100	79	68	23
0.2 μm	0	38	58	31
	2	71	65	26
	2 (30 min)	27	55	21
	5	73	53	16
	5 (Room Temp)	121	65	16
	10	136	59	18
	20	38	58	53
	40	76	55	36

6.4.2.4 Cell Morphology as Observed by SEM

The morphology of cells observed by SEM was analyzed from photomicrographs, and the cells were assigned to three categories based on the appearance of the plasma membrane outside of the contact area: 1) smooth (see figures 6.11 and 6.12 (a)); 2) rough (broad ruffles or ridges, large diameter blebs, but no microvilli or narrow surface ridges, eg. figure 6.12 (b)), or 3) microvillous for spike-like, or narrow ridge-like surface features (see figures 6.13 and 6.14 (b)). Results are shown in figure 6.16 for cells pressurized on 0.05 μm (figure 6.16 (a)), 0.1 μm (figure 6.16 (b)), and 0.2 μm (figure 6.16 (c)) pore size membranes. Results are expressed as percentage of the total cells observed on the photomicrographs displaying the morphology indicated in the figure legend. Each data point represents the number of cells indicated in table 6.3. The results are entirely consistent with the hypothesis that the cell becomes smoother as the degree of infiltration increases. More than 80 % of the cells pressurized on 0.05 μm membranes retain their microvillous morphology, and almost none are smooth. Morphology also is independent of pressure for this membrane. In contrast, for cells pressurized on 0.1 and 0.2 μm membranes, there is a transition from a primarily microvillous morphology at low pressures to a rough and then primarily smooth morphology at higher pressures where most cells infiltrated the membrane as shown in figure 6.15. The transition occurs over the same range of pressure as for infiltration in figure 6.15.

6.4.3 Detailed Measurements of Infiltrations from TEM and SEM Photomicrographs

Photomicrographs were taken at a variety of magnifications (figures 6.5 to 6.14 for examples) of a significant fraction of the cells analyzed during the on-scope TEM and SEM observations as well as others present on the samples. Photos of cells possessing infiltrations were used to analyze the infiltrations in detail for cells pressurized on 0.1 and 0.2 μm pore size membranes. Parameters measured included: the number of infiltrations per cell,

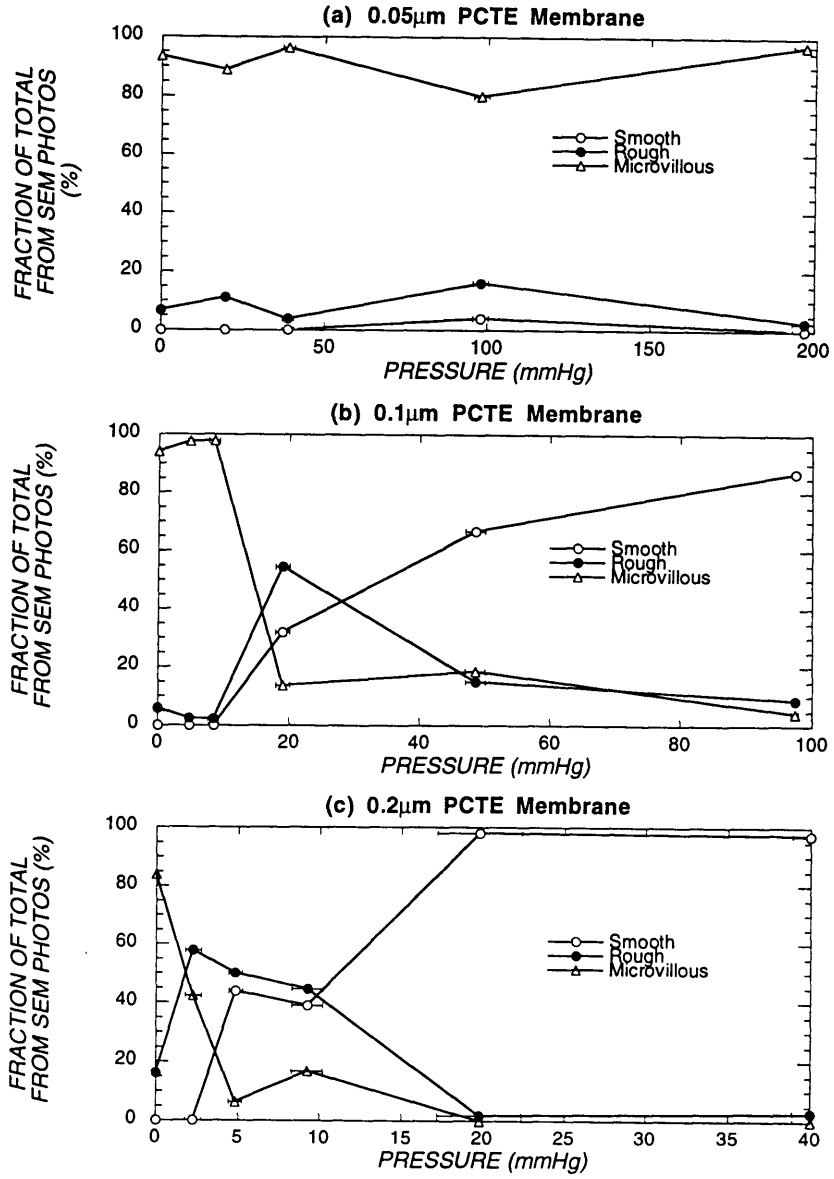

Figure 6.16 Results of categorization of cellular morphology from SEM photomicrographs for cells pressurized on (a) 0.05 μm pore size PCTE membranes, (b) 0.1 μm pore size PCTE membranes, and (c) 0.2 μm pore size PCTE membranes. See text for discussion of categorization criteria and table 6.3 for the number of cells represented by each data point. Error bars in the x direction represent one standard deviation of the average applied pressure (see table 6.2).

diameter of infiltrations, length of infiltrations from SEM photos, or depth of infiltrations below the surface of the PCTE membrane from TEM photos. Measurements were made directly from photos of appropriate magnification using the same precision calipers used to measure membrane pore size. For TEM photos, the number of infiltrations counted was all of those visible in a region of the PCTE membrane directly below the cell diameter on a single section for each cell. Depth was measured as the maximum depth below the surface of the membrane to which the cell is attached in a direction normal to the plane of the membrane. The diameter was measured at the terminus of each infiltration. For SEM photos, the number of infiltrations was counted for cells whose entire contact area was visible, and for which the infiltrations were individually distinguishable to the point where they could be counted. For measurements of length and diameter, only infiltrations which had a shape and diameter suggesting they originated from single pores were included. In addition, no clumped or grossly entangled infiltrations were included, only those which were individually distinguishable over their length. This unavoidably reduced the fraction of infiltrations on any given cell which could be measured in detail, especially for cells with many infiltrations. In addition, since longer infiltrations are more likely to overlap and/or clump, the measured population may be skewed to shorter infiltrations. Length was measured as much as possible along the contour of the infiltration shape from the cell contact area to the terminus. Infiltrations which appeared to have broken (jagged or irregularly shaped terminal end) were not included. Diameter was measured as close as possible to the origin of the infiltration where the pore size of the membrane is most accurately known). Length measurements were corrected for the angle which the contact area makes with the photo plane as discussed below.

In order to accurately reflect the composition and behavior of the HL-60 population observed in the on-scope measurements summarized in figures 6.15 and 6.16, the cells

included in the analysis of the photomicrographs were randomly selected so that the fraction of cells having infiltrations >1 μm vs. ≤ 1 μm for SEM photos, or having infiltrations which pass completely through vs. not completely through the membrane for TEM photos was the same as for the cell population at large. Figure 6.17 shows a comparison of infiltration length/depth for the cells included for this analysis vs. the population at large for TEM photos ((a) and (b)) and SEM photos ((c) and (d)). Table 6.4 shows the number of cells and infiltrations included in the measurements for each condition. The numbers are smaller for conditions where only a small fraction of the cells possessed infiltrations.

6.4.3.1 Correction of Infiltration Length for Infiltrations Measured from SEM Photomicrographs

The infiltration lengths measured for infiltrations lying approximately flat on contact areas which were nearly co-planar with the plane of the photo (eg. figure 6.5 (a) and figure 6.6 (a)), and for infiltrations oriented perpendicular to the contact area for cells whose contact area was perpendicular to the plane of the photo (eg. figure 6.5 (b)) reflected the actual length of the infiltration. For infiltrations present on contact areas with other orientations with respect to the plane of the photo, correction must be made to the measured length (M) so that the actual length (L) will not be underestimated. Figure 6.18 (a) shows a general case of a two-dimensional object of actual length L co-planar with a contact area plane with coordinate directions (x, y). The object is oriented with angle ϕ in the contact area plane and has coordinate components L_x and L_y (figure 6.18 (b)). The plane of the photograph (x', y') is oriented perpendicular to the line of sight (z' axis) and at angles θ_x and θ_y in the coordinate directions with respect to the contact area plane (figure 6.18 (a),(c),(d)). The measured length, M, is the projection of the actual object along the line of sight onto the photo plane (figure 6.18 (a)). This projection is oriented at a measurable angle ϕ' in the

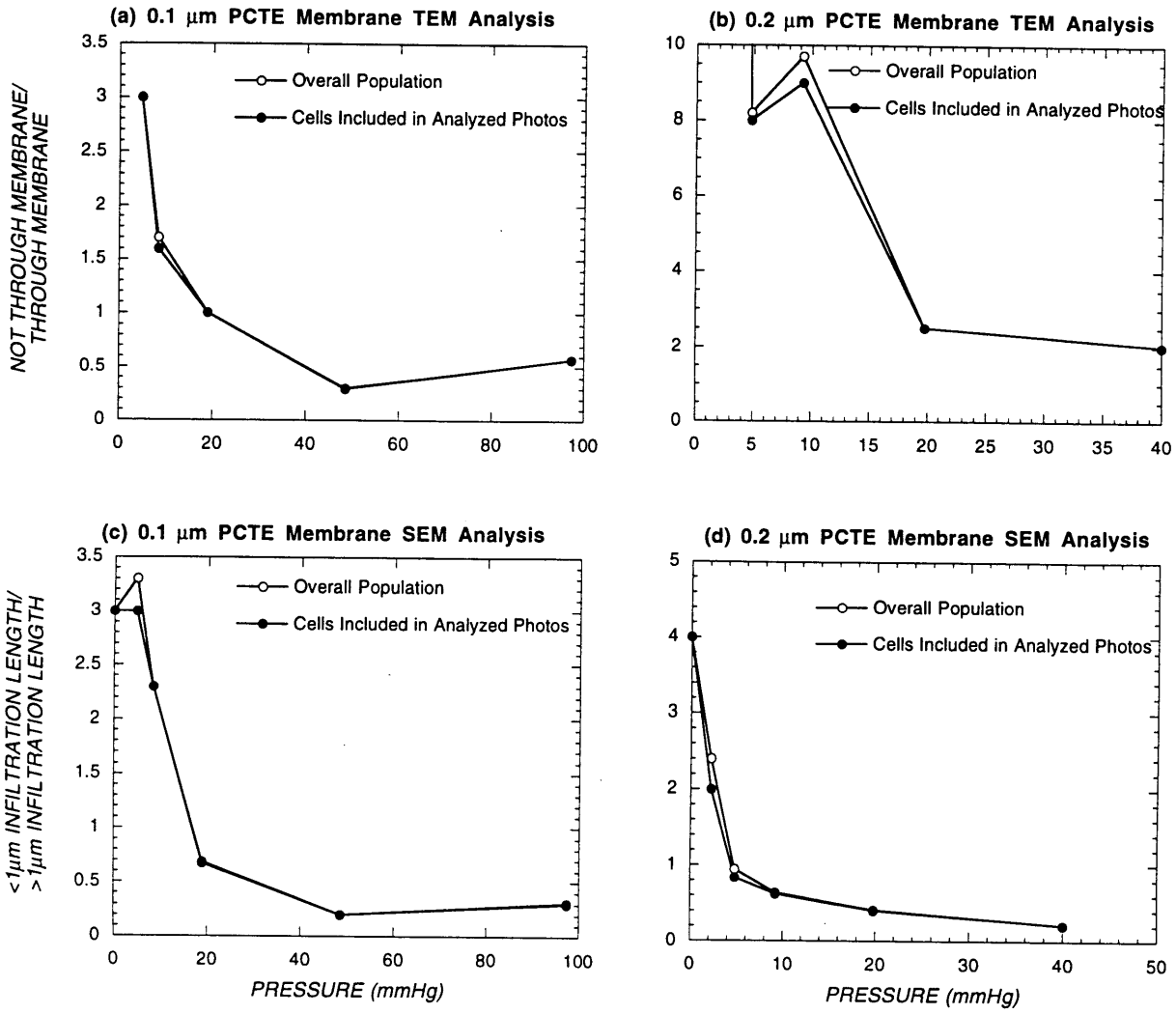

Figure 6.17 Comparison of distribution of cell populations included from TEM and SEM photomicrographs for detailed analysis of infiltrations to the overall cell population as determined from on-scope categorization. (a) and (b) show the ratio of cells with infiltrations which do not pass completely through the PCTE membrane to cells with infiltrations which do, as determined by TEM for the overall cell population (open circles) and the cells from photomicrographs included in the detailed analysis and measurement of infiltrations (closed circles). (c) and (d) show the ratio of cells with infiltrations whose infiltrations exceed 1μm in length to those whose do not as determined by SEM for the overall cell population (open circles) and the cells from photomicrographs included in the detailed analysis and measurement of infiltrations (closed circles).

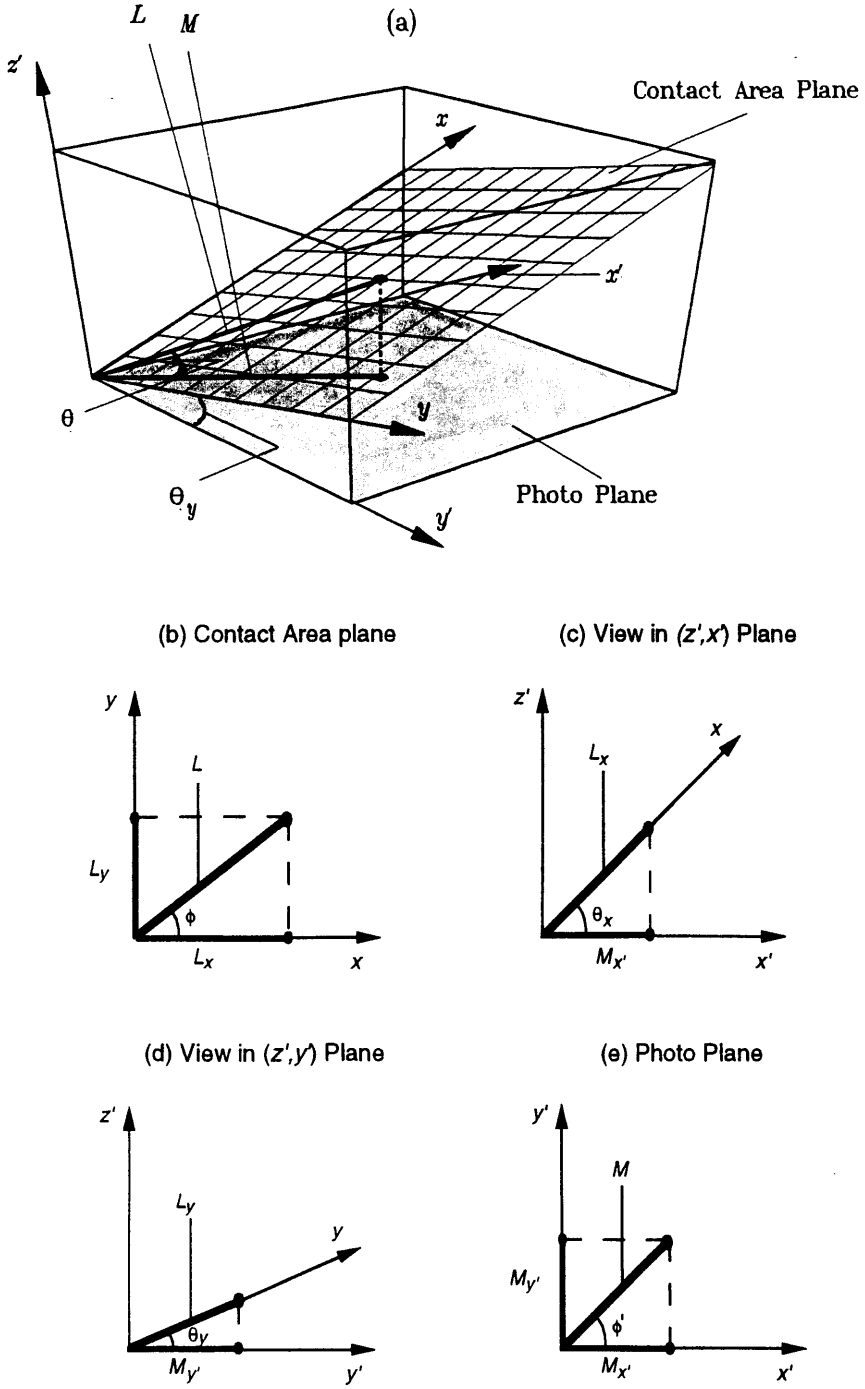

Figure 6.18 Schematic diagram showing an object co-planar with the plane of the contact area (x,y) (lying flat on contact area). The line of sight is in the z' direction, normal to the plane of the photo (x',y'). (a) shows a three dimensional diagram showing the orientation of the contact area (yellow) with respect to the photo plane (blue). The observed and measured projection of the object onto the photo plane is M, and the actual object in the contact area is L. θ is the angle between the L and M in the z' direction. (b) shows the orientation of L in the contact area plane (x,y). (c) and (d) are two dimensional views of the (z',x') plane (c), or (z',y') plane (d) showing the projections of L and M in the coordinate directions. (e) shows the orientation of M in the photo plane (x',y').

Table 6.4 *Number of Cells With Infiltrations, and Number of Infiltrations Analyzed, for Detailed Measurements of Infiltration Number and Dimensions from TEM and SEM Photomicrographs*

Membrane	Target Pressure (mmHg)	Number of Cells Analyzed		Number of Infiltrations Analyzed	
		TEM	SEM	TEM	SEM
0.1 μm	0	0	4	0	12
	5	4	8	4	23
	10	13	10	47	25
	20	6	10	91	52
	50	9	6	215	35
	100	11	13	157	87
0.2 μm	0	7	5	14	12
	2	17	6	56	51
	2 (30 min)	10	7	34	32
	5	18	11	115	67
	5 (Room Temp)	21	14	148	113
	10	10	13	95	81
	20	7	7	41	27
	40	15	17	182	108

photo plane and has coordinate components M_x, and M_y,(figure 6.18 (e)). The actual angle between the contact area plane and the photo plane along the direction of the object is shown in figure 6.18 (a) as θ. L and θ were determined from the measurable quantities M, ϕ', θ_x, and θ_y as follows:

$$L = \frac{M}{\cos\theta} = [(L_x)^2 + (L_y)^2]^{\frac{1}{2}} \tag{2}$$

thus,

$$\frac{M}{\cos\theta} = \left[\left(\frac{M\cos\phi'}{\cos\theta_x}\right)^2 + \left(\frac{M\sin\phi'}{\cos\theta_y}\right)^2\right]^{\frac{1}{2}} \tag{3}$$

so that,

$$\theta = \cos^{-1}\left[\left(\frac{\cos\phi'}{\cos\theta_x}\right)^2 + \left(\frac{\sin\phi'}{\cos\theta_y}\right)^2\right]^{-\frac{1}{2}} \tag{4}$$

Equation (4) is used to determine θ and then equation (2) can be used to determine L. The reason for calculating θ explicitly rather than calculating L directly by combining equations (2) and (3) is that knowing θ becomes necessary for determining the actual length of three-dimensional objects as discussed below.

Only certain cells whose contact areas were at non-zero or non-perpendicular angles with respect to the photo plane were considered in the analysis. In order to estimate the orientation between the contact area and the photo plane, one of the component angles of orientation θ_x or θ_y between the contact area and the viewing plane must be known, and an assumption must be made about the shape of the contact area in order to calculate the other. For cells which were included for analysis (eg. figure 6.12 (b) lower cell) the contact area must appear to be co-planar with the photo plane along some directional axis, typically in the direction of maximum contact area diameter. This axis was chosen as the x' and x direction so that θ_x was 0° (For the cell in figure 6.12 (b), this direction becomes horizontal when the photo is rotated about 45° counterclockwise). In addition, cells which were included had

contact areas which appeared to be symmetrical. It was assumed that such contact areas were roughly circular and θ_y was calculated by taking the inverse cosine of the ratio of the contact area diameter measured in the y' direction to the diameter measured in the x' direction. These angles, along with the measured orientation of the object in the (x', y') plane, ϕ', were used with equation 4 to determine the actual orientation of the object with respect to the viewing plane, θ.

For objects with a finite thickness, such as the infiltrations observed by SEM, on a contact area which is not co-planar with the plane of the photo, some additional corrections must be made to the measured length in order to determine the actual length. Only infiltrations oriented perpendicular to, or lying flat on, the contact area were included in the measurements. Figure 6.19 shows a two dimensional view of an infiltration oriented perpendicular to the contact area and of thickness $2Rp$. The contact area is at an angle θ to the viewing plane in the y' direction. The direction of view is along the z' axis, the true length of the infiltration is L, and the measured length is M. The shape of the infiltration is assumed to be cylindrical with a hemispherical terminus. L can be related to M by considering triangle ABC in the figure.

$$\sin\theta = \frac{AB}{AC} = \frac{M - Rp - Rp\cos\theta}{L - Rp} \tag{5}$$

$$L - Rp = \frac{M - Rp}{\sin\theta} - \frac{Rp}{\tan\theta} \tag{6}$$

$$L = Rp(1 - \cot\theta) + \frac{M - Rp}{\sin\theta} \tag{7}$$

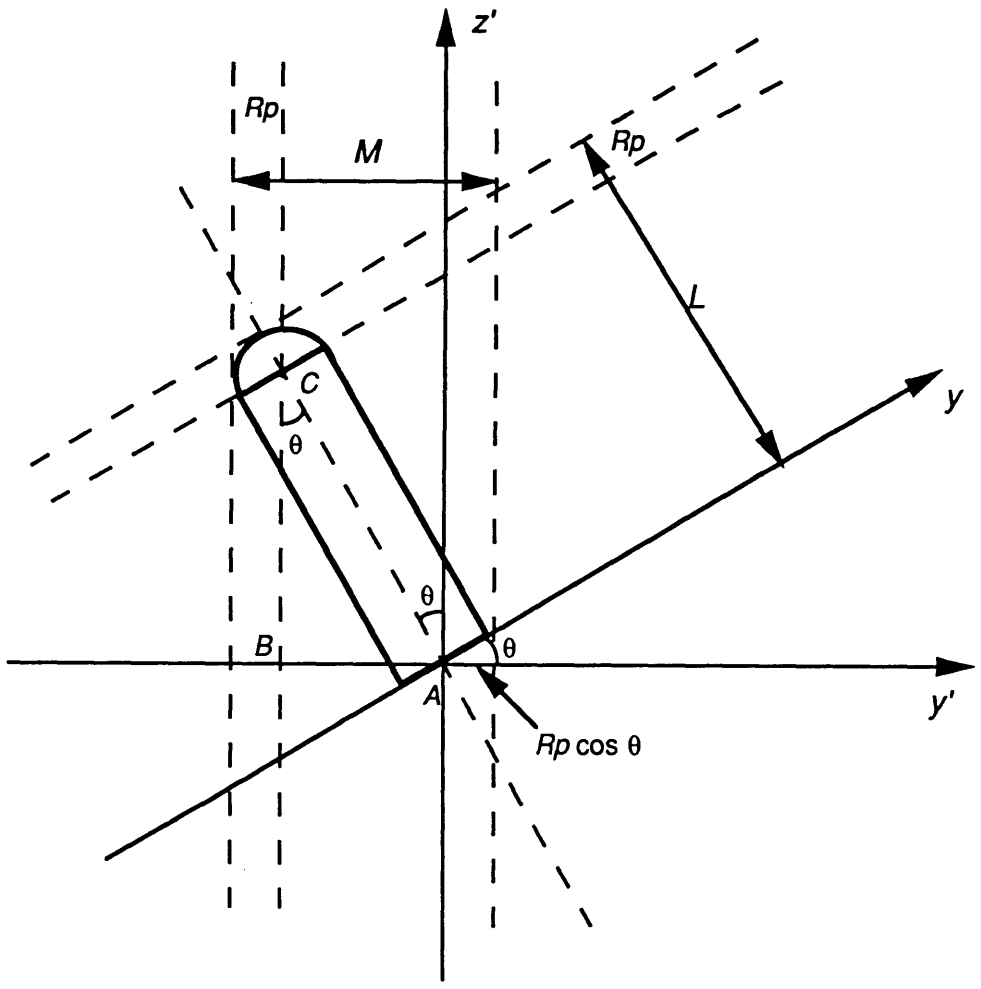

Figure 6.19 Schematic diagram of infiltration oriented normal to the plane of the contact area (x,y), showing the relationship between actual length (L) and observed length (M) when y is oriented at an angle θ to the plane of photo (x',y').

The case for infiltrations which lay flat on the contact area is shown in figure 6.20. Again considering the triangle ABC we relate L to M as follows:

$$\cos\theta = \frac{AB}{AC} = \frac{M - Rp}{L - Rp + Rp\tan\theta} \tag{8}$$

$$L = \frac{M - Rp}{\cos\theta} + Rp(1 - \tan\theta) \tag{9}$$

For the general case of an infiltration lying on the contact area whose projection of length M is oriented in the photo plane with a measured angle ϕ'; θ is first calculated as outlined previously using equations 2 to 4, then L is determined with equation 9 using this θ.

6.4.3.2 Infiltration Measurements from TEM and SEM Photomicrographs

Figures 6.21-6.24 summarize the data derived from the measurements of infiltration dimensions. Figure 6.21 shows the average infiltration diameters for cells pressurized on 0.1 μm pore size (figure 6.21 (a)) and 0.2 μm pore size (figure 6.21 (b)) membranes. The measured pore diameters were very close to the average membrane pore diameter (shown as a bold line in the figure), and was, for the most part, invariant with pressure. For the 0.2 μm pore size membrane, infiltration diameters measured for cells exposed to gravity were lower than for other pressure conditions, especially as measured from TEM images. Larger standard deviations for TEM diameter measurements are expected due to the variability in the location of the cross-section with respect to the center of the infiltration.

Figure 6.22 presents the average number of infiltrations per cell for cells with infiltrations. The number of infiltrations as measured by SEM tended to be only modestly higher than the number measured by TEM. This is surprising since in SEM images the

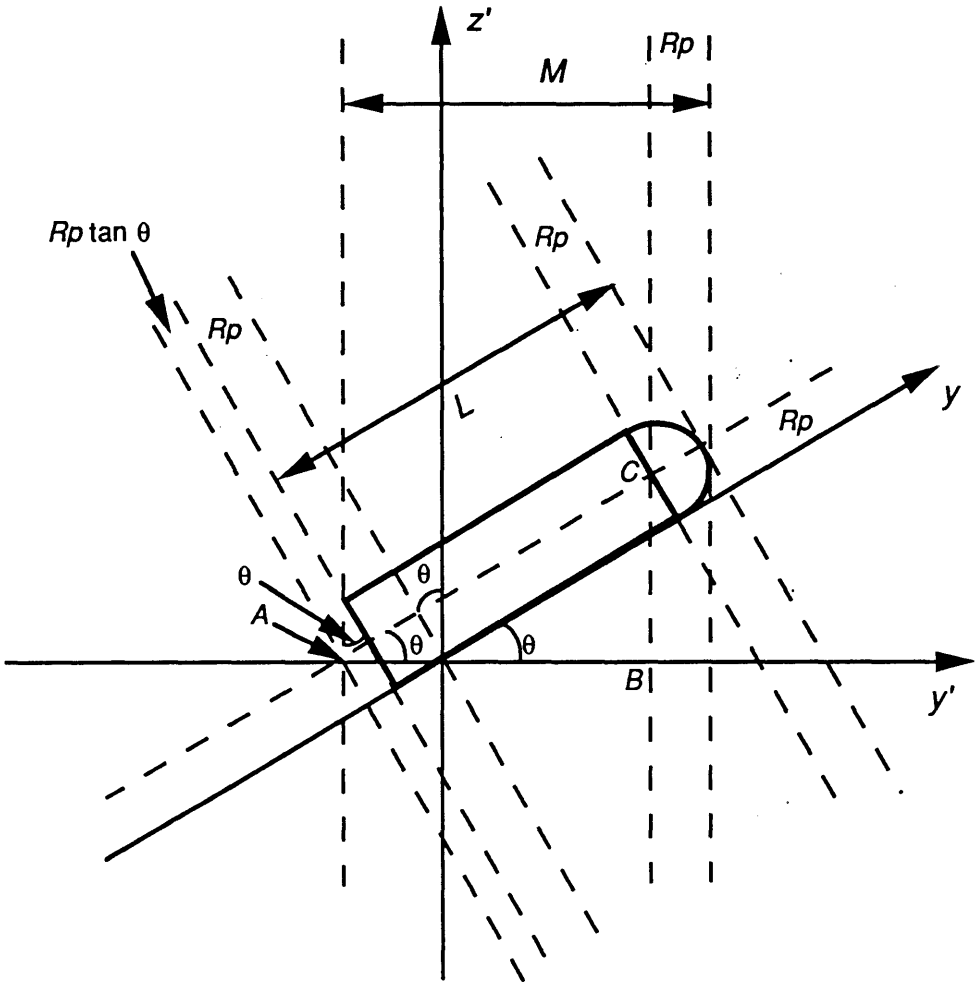

Figure 6.20 Schematic diagram of infiltration oriented parallel to the plane of the contact area (x,y) (lying flat on contact area), showing the relationship between actual length (L)and observed length (M) when y is oriented at an angle θ to the plane of view (x',y').

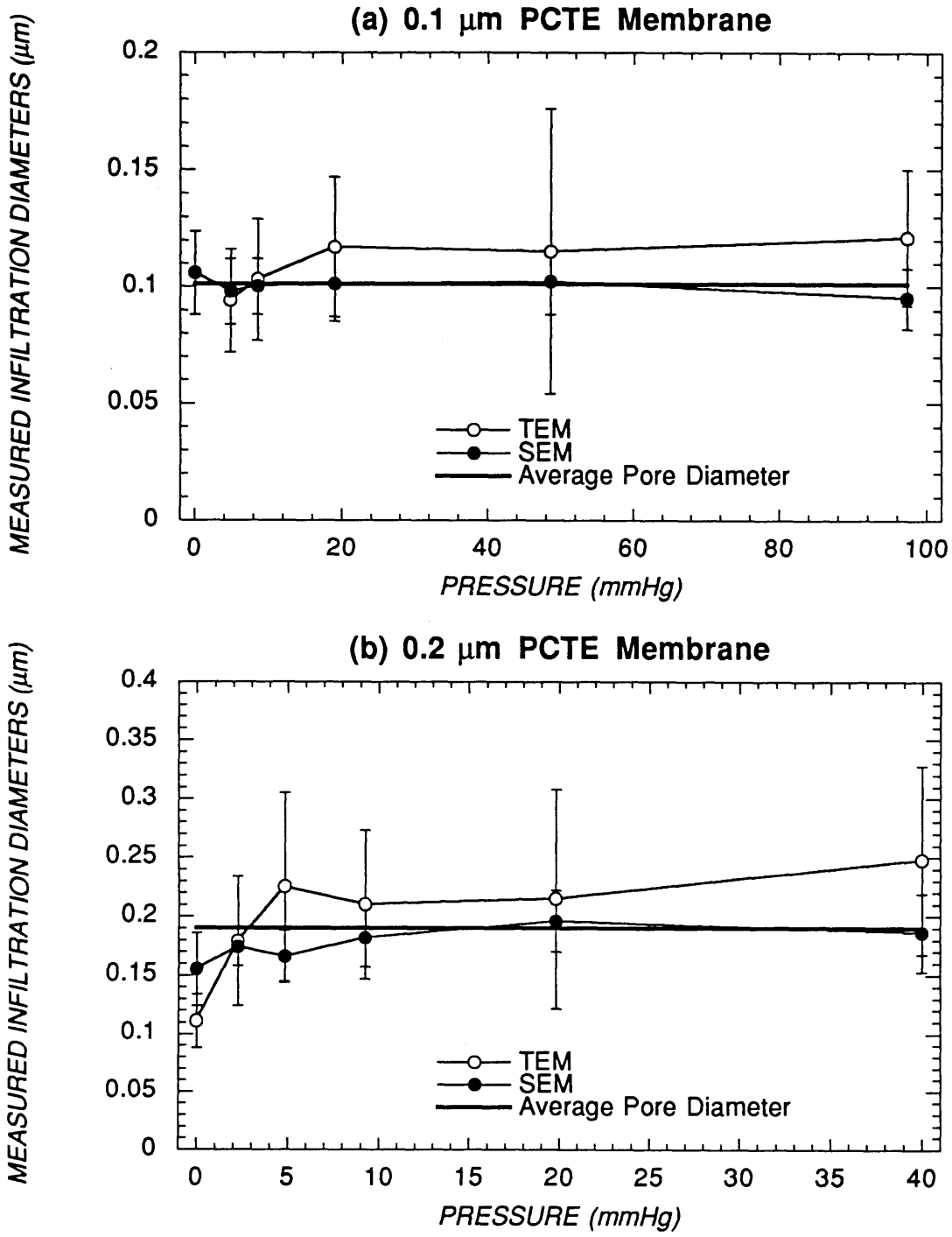

Figure 6.21 Average measured infiltration diameter for cells pressurized on 0.1 μm pore size membranes (a) and 0.2 μm pore size membranes (b) for TEM measurements and SEM measurements. Error bars represent one standard deviation. Error bars in the x direction have been omitted for clarity. Bold lines show the mean pore diameter for each membrane. The number of measurements for each data point is shown in table 6.4.

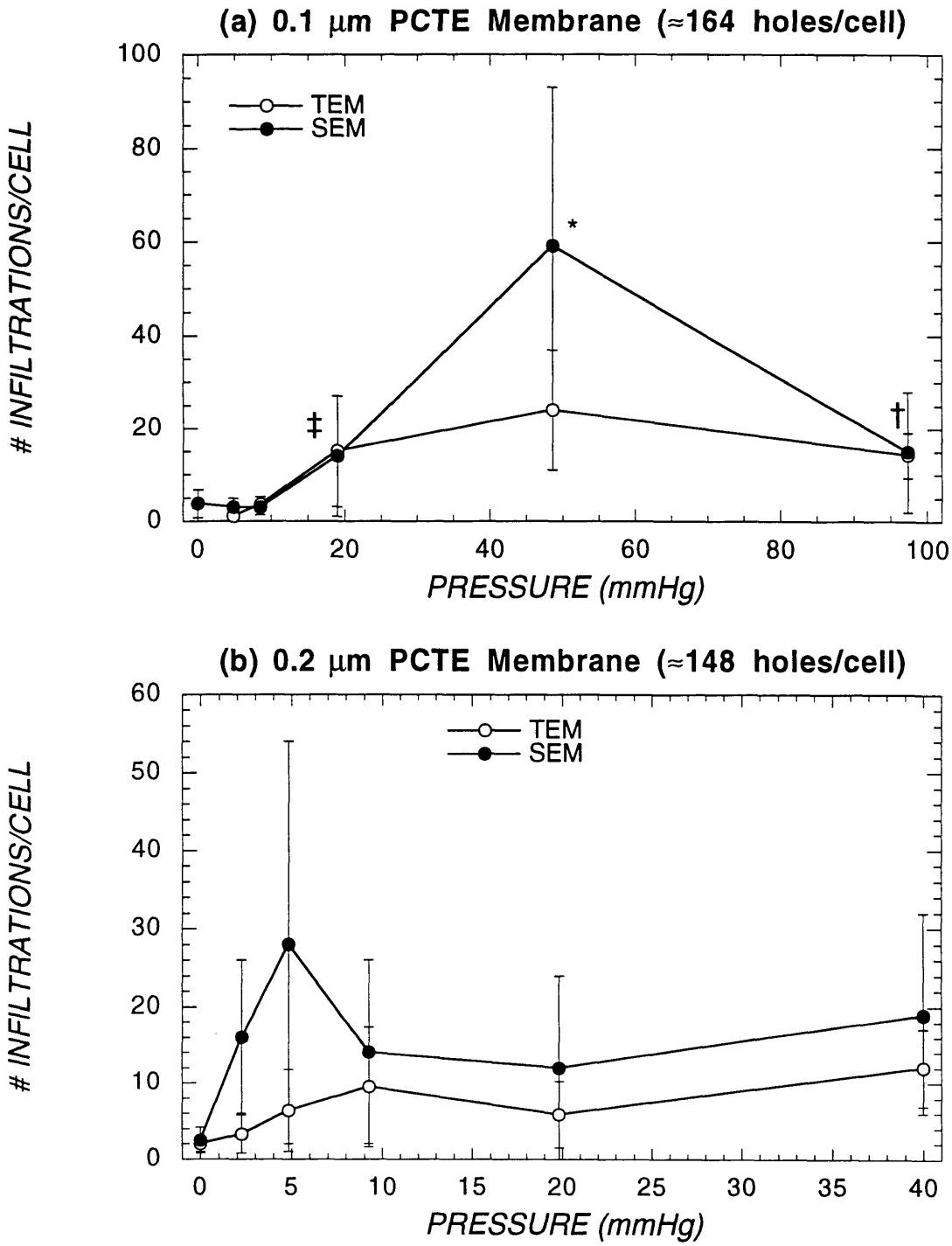

Figure 6.22 Average number of infiltrations per cell for cells with infiltrations for cells pressurized on 0.1 μm pore size membranes (a) and 0.2 μm pore size membranes (b) for TEM measurements and SEM measurements. Error bars represent one standard deviation. Error bars in the x direction have been omitted for clarity. Titles indicate approximate number of holes below a cell contact area of typical size (contact area diameter of about 7 μm) based on the measured pore density of the membranes. In (a), * is significantly different from adjacent ‡ ($p=0.003$) and † ($p=0.007$). The number of measurements for each data point is shown in table 6.4.

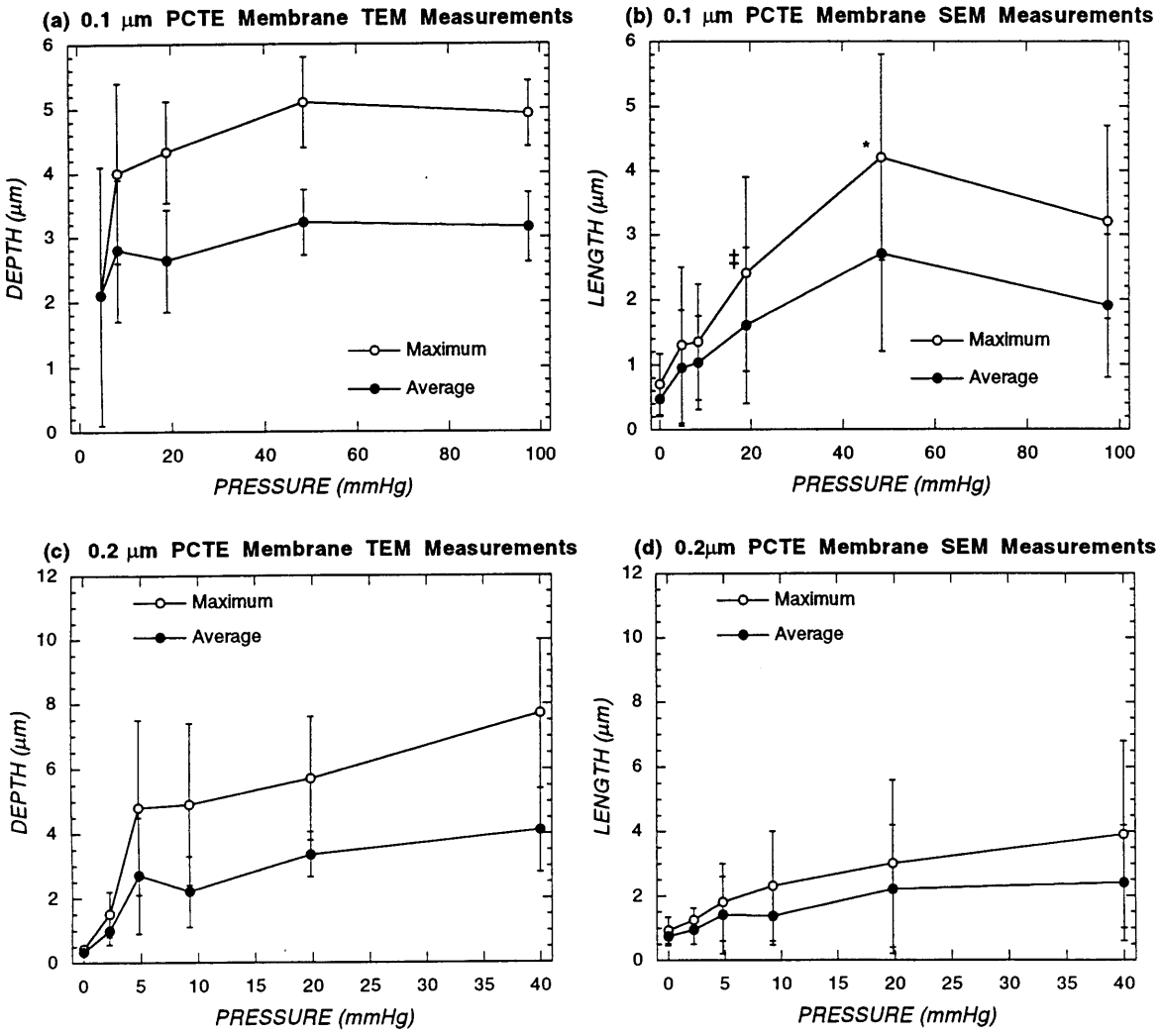

Figure 6.23 Measured infiltration depths or corrected lengths for cells with infiltrations for TEM images (a) and SEM images (b) for cells pressurized on 0.1 μm pore size membranes, and TEM images (c) and SEM images (d) for cells pressurized on 0.2 μm pore size membranes. Open circles represent the maximum depth or length per cell and closed circles the average depth or length per cell. Error bars represent one standard deviation. Error bars in the x direction have been omitted for clarity. In (b), * differs significantly from neighboring ‡ ($p=0.04$). The number of measurements for each data point is shown in table 6.4.

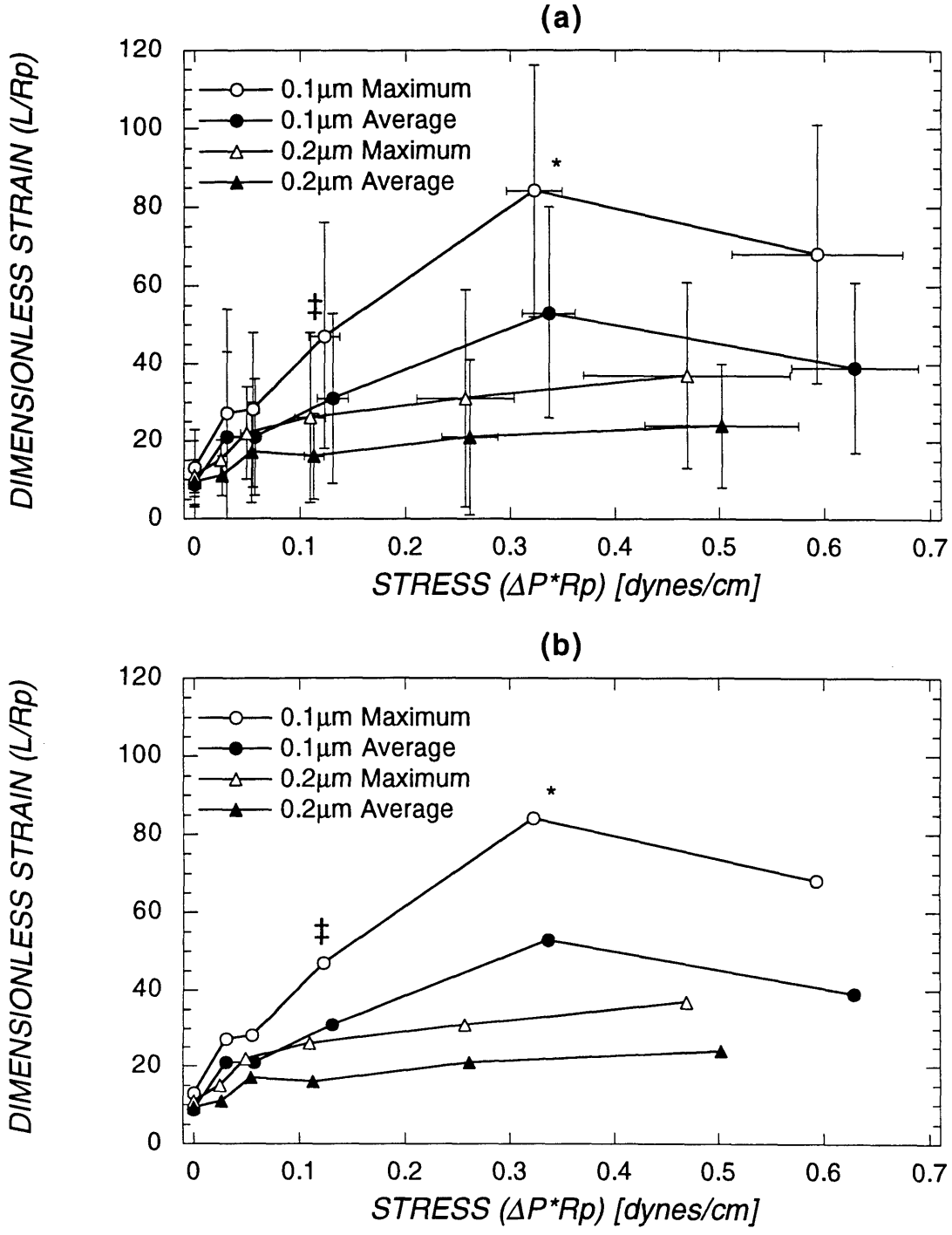

Figure 6.24 Stress-strain relationship for cells pressurized on 0.1 μm pore size membranes (circles) and 0.2 μm pore size membranes (triangles) from SEM measurements. Open symbols represent the maximum strain, and closed symbols the average strain per cell. Error bars represent one standard deviation. The data is replotted in (b) without error bars for clarity. Value indicated by * differs significantly from neighboring ‡ (p=0.03). The number of measurements for each data point is shown in table 6.4.

entire contact area is visible, while for TEM, only the infiltrations which intersected the plane of a single section were counted for each cell. This observation may indicate that a substantial number of infiltrations were lost during the SEM preparation procedure. The qualitative dependence of the number of infiltrations on pressure was similar for both TEM and SEM measurements. The data show an initial rise at low pressures (between 10 and 50 mmHg for the 0.1 μm pore size membrane, and between 0 and 5 to 10 mmHg for the 0.2 μm pore size membrane) before decreasing or becoming flatter at higher pressures. The behavior was qualitatively similar to the trends observed previously in figure 6.15. For 0.1 μm membranes, there was a peak in the number of infiltrations as measured by SEM at 50 mmHg which was significantly higher than neighboring values at 20 mmHg ($p=0.003$) and 100 mmHg ($p=0.007$). The small peak in the number of infiltrations for cells on 0.2 μm membranes as measured by SEM was not significantly different from adjacent points ($p>0.05$). The maximum average number of infiltrations per cell ranges from about 15 to 60 for 0.1 μm pore size membranes and about 10 to 30 for 0.2 μm pore size membranes as measured by SEM compared to the approximately 164 pores/typical cell (with a 7 μm diameter contact area) for 0.1 μm pore size membranes and 148 pores/typical cell for 0.2 μm pore size membranes predicted from the measured membrane pore densities.

Average infiltration depth from TEM measurements and length from SEM measurements are presented in figure 6.23 for both maximum depth/length per cell and average depth/length per cell. The dependence of the depth and length of infiltrations on pressure was similar to the dependence of the number of infiltrations per cell on pressure seen in figure 6.22. Infiltration depths and lengths rise over a narrow pressure range between 5 mmHg and 10 to 50 mmHg for 0.1 μm and between 0 and 5 to 10 mmHg for 0.2 μm pore size membranes. This behavior is more pronounced from TEM measurements (figure 6.23 (a)

and (c)) than from SEM measurements (figure 6.23 (b) and (d)). SEM measurements suggest a possible maximum in infiltration length at 50 mmHg for 0.1 μm membranes (value for maximum length at 50 mmHg differs significantly from adjacent value at 20 mmHg ($p=0.04$), but not from value at 100 mmHg ($p>0.05$)) and display a more gradual rise over the entire pressure range compared to TEM measurements for 0.2 μm membrane data. The average and maximum lengths as determined by TEM and SEM measurements are similar in magnitude as are the overall maximum values of length and depth for the two different membranes (about 3 to 7 μm). The length data from SEM measurements was transformed into stress ($\Delta P \times Rp$)-dimensionless-strain (L/Rp) data in figure 6.24. The data for the 0.2 μm pore size membrane now more clearly show the tendency for an initial rise and plateau compared to the length-pressure data of figure 6.23. The range of stress over which the steepest increase in strain occurs is nearly the same for both pore sizes, and the observed strains are at least an order of magnitude greater than that seen for elastic membranes (eg. red cells, Brailsford et al., 1977; Missirlis and Brain, 1979; Reinhart et al., 1987) or for elastic behavior of white blood cells subjected to rapid deformation by micropipette (Chien et al., 1984) at similar stresses.

6.4.3.3 Effect of Time of Exposure to Pressure, and Temperature History of Cells on Infiltration

Figures 6.25 to 6.30 summarize results from experiments performed to examine the effect of exposure time and preparation and handling temperature on infiltration of cells into 0.2 μm pore size PCTE membranes. To examine the effect of exposure time, an additional membrane was prepared at a target pressure of 2 mmHg (1.7 mmHg actual average pressure) where the cells were pressurized for 30 min after loading before switching from buffer to fixative. The total average exposure time of cells to pressure before contact with fixative for this case was 41 min versus 14 min for the same target pressure condition (2.25 mmHg actual

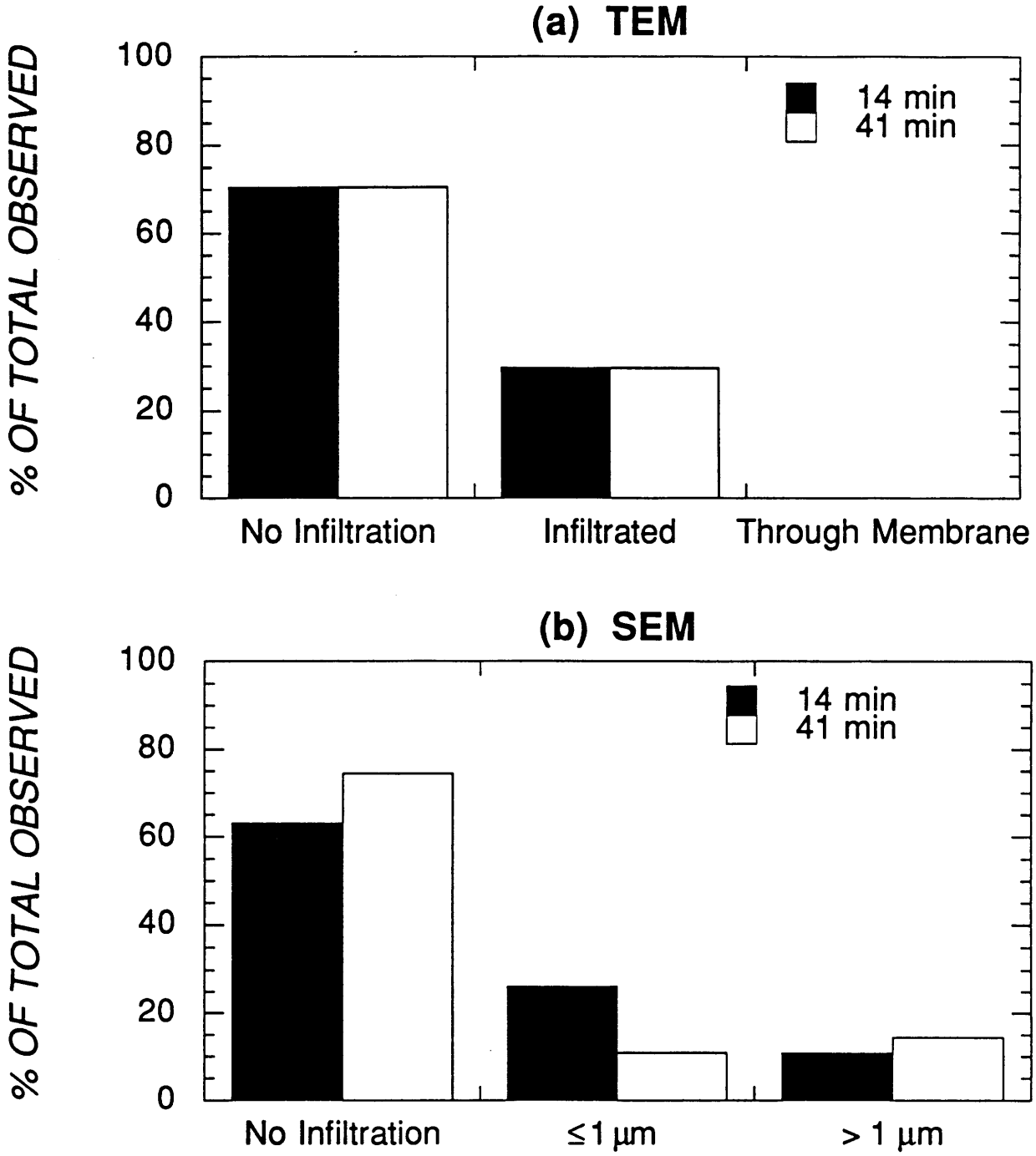

Figure 6.25 Results of on-scope characterization of cells pressurized on 0.2 μm pore size PCTE membranes for two different exposure times before fixation from (a) TEM and (b) SEM observations. Results are presented as the total percentage of cells observed in samples showing no infiltration (column 1 both plots); infiltration into but not through membrane (TEM data column two), or infiltration less than 1 μm in length (SEM data column 2); and infiltration through the membrane (TEM data column 3), or infiltrations longer than 1 μm (SEM data column 3) for cells pressurized at 2 mmHg target pressure conditions for an average exposure time of 14 min (5 min from start to valve switch to fixative) and 41 min (30 min from start to valve switch to fixative).

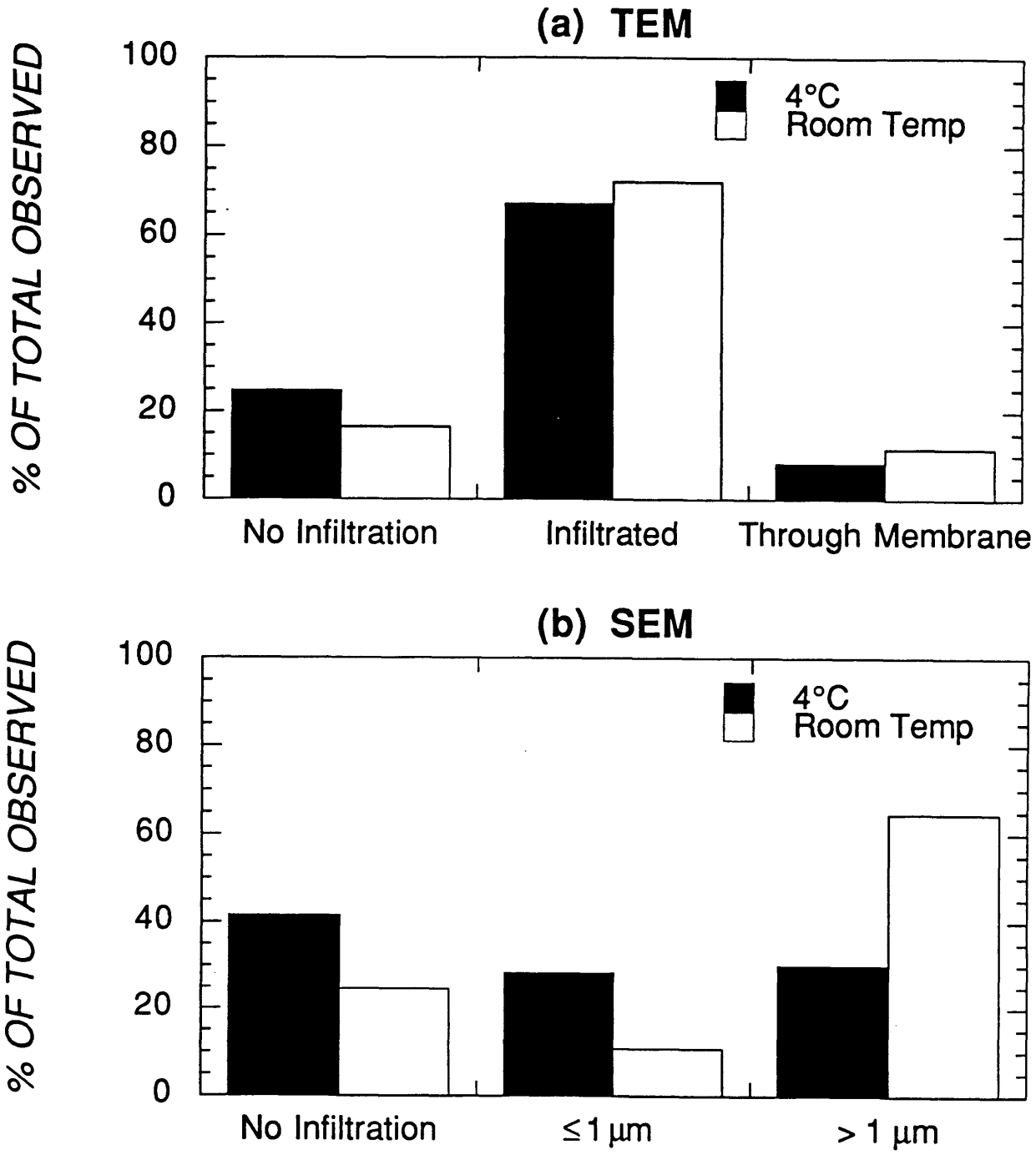

Figure 6.26 Results of on-scope characterization of cells pressurized on 0.2 μm pore size PCTE membranes which had been prepared and handled at two different temperatures prior to pressurization: (a) TEM and (b) SEM observations. Results are presented as the total percentage of cells in samples showing no infiltration (column 1 both plots); infiltration into but not through membrane (TEM data column two), or infiltration ≤ 1 μm in length (SEM data column 2); and infiltration through the membrane (TEM data column 3), or infiltration ≥ 1 μm (SEM data column 3) for cells pressurized at 5 mmHg target pressure which had been prepared and handled at 4° C (standard protocol) and room temperature (about 22° C).

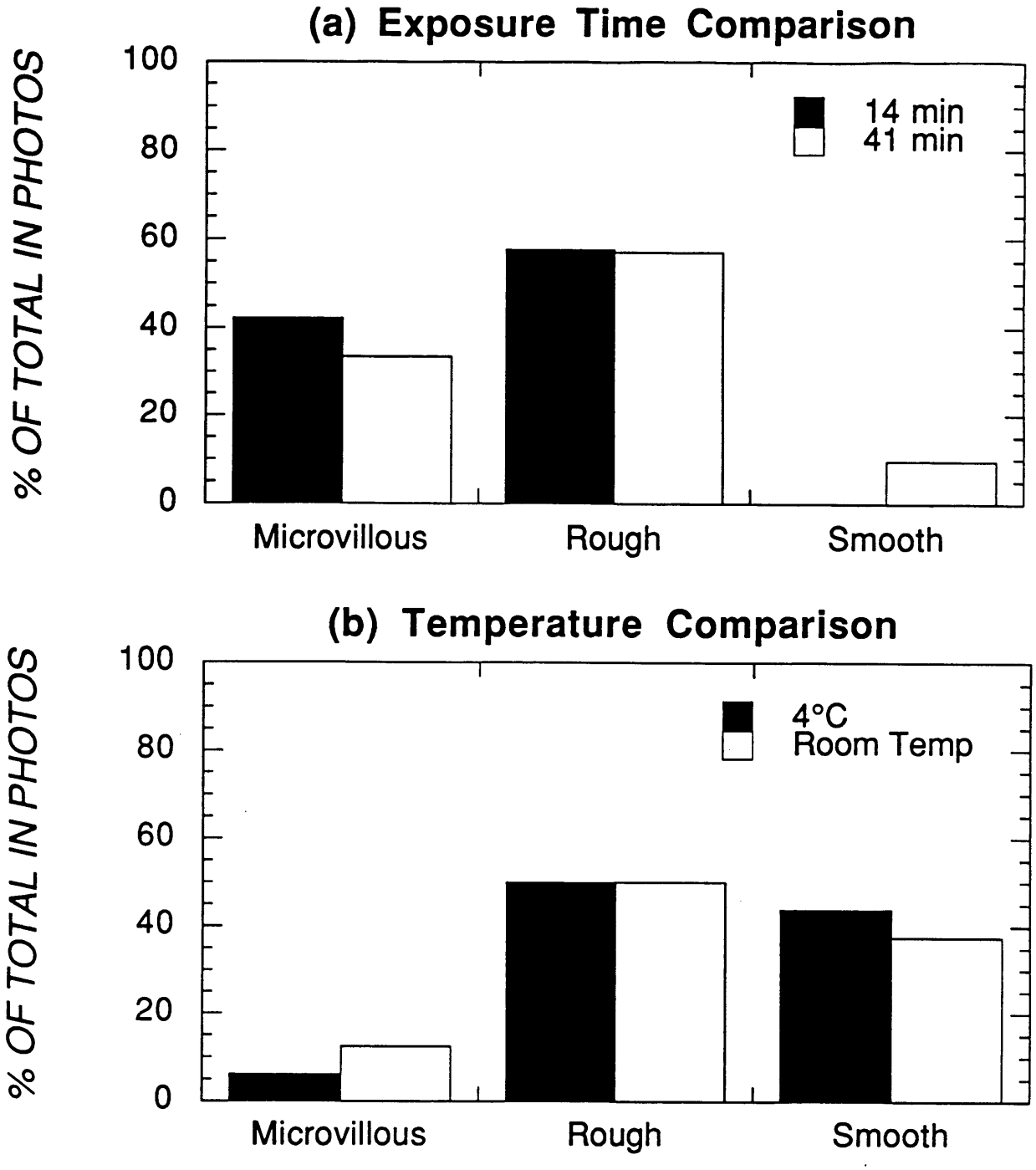

Figure 6.27 Results of chacterization of cellular morphology from SEM photomicrographs for cells pressurized on 0.2 μm PCTE membranes for: (a), two different exposure times (14, min solid bars; 41 min, hollow bars) at a target pressure of 2 mmHg, or (b) cells exposed to two different preparation and handling conditions (4° C, solid bars; room temp, hollow bars) at a target pressure of 5 mmHg. Results are presented as the total percentage of cells observed in photomicrographs having a microvillous (column 1), rough (column two), or smooth (column 3) morphology.

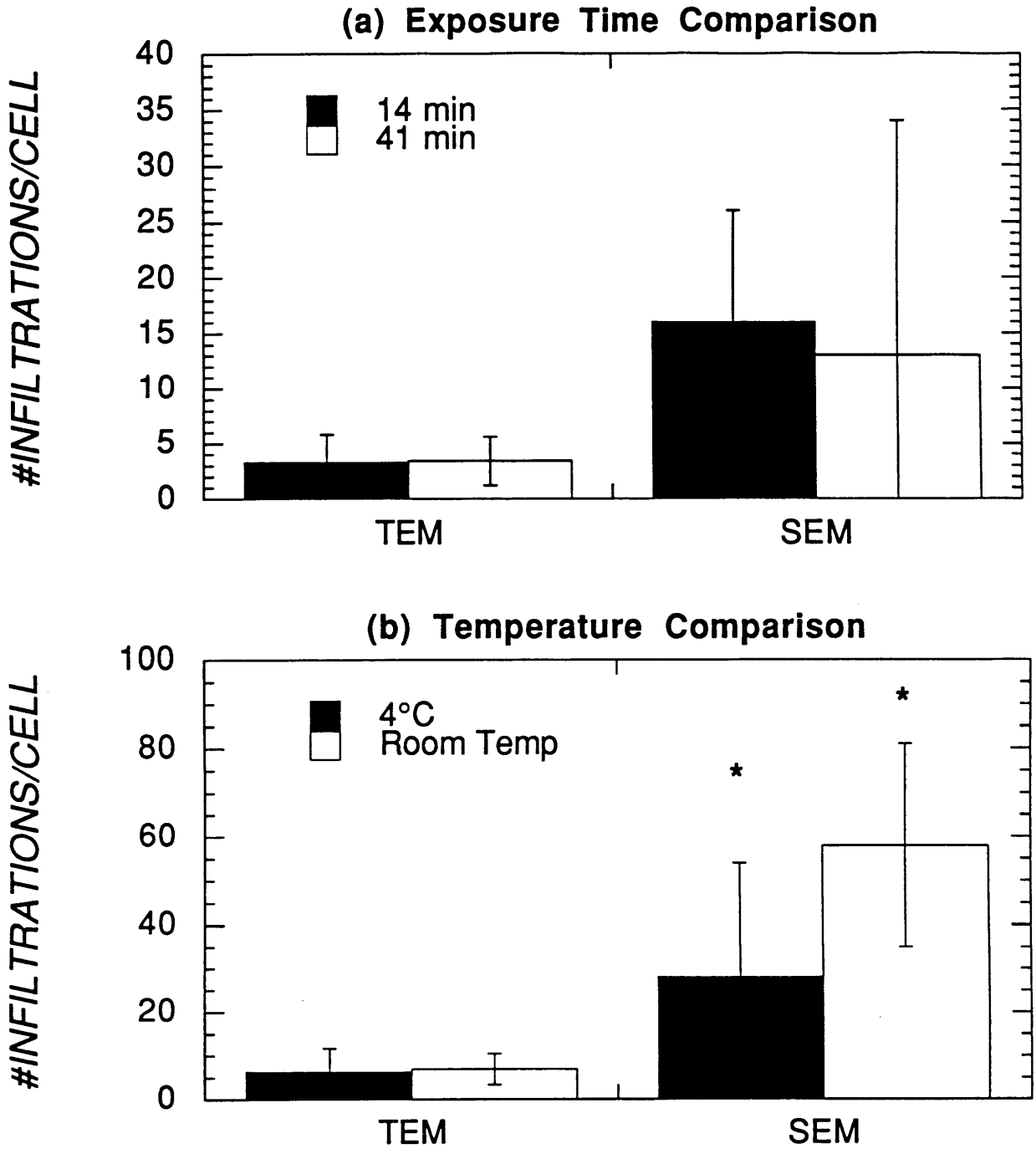

Figure 6.28 Average number of infiltrations per cell for cells with infiltrations for cells pressurized on 0.2 μm PCTE membranes for: (a) two different exposure times (14, min solid bars; 41 min, hollow bars) at a target pressure of 2 mmHg, or (b) cells exposed to two different preparation and handling conditions (4° C, solid bars; room temp, hollow bars) at a target pressure of 5 mmHg. Results are presented as the average number of infiltrations per cell as observed from TEM photomicrographs of individual sections (column 1), or SEM photomicrographs (column 2). Error bars represent one standard deviation, and * denotes difference is statistically significant (p=0.007).

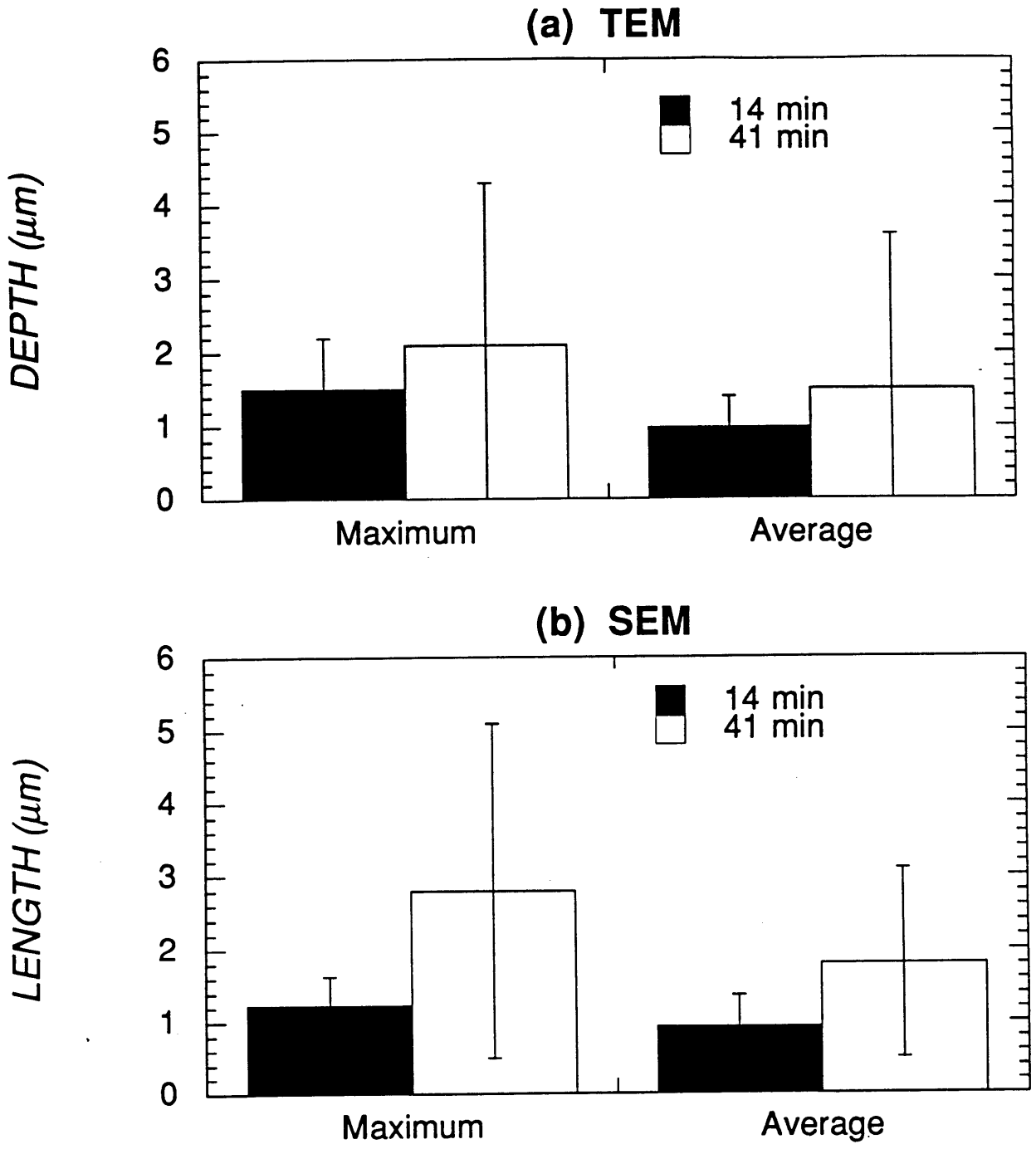

Figure 6.29 Depth and length of infiltrations for cells with infiltrations for cells pressurized on 0.2 μm PCTE membranes for two different exposure times (14, min solid bars; 41 min, hollow bars) at a target pressure of 2 mmHg from TEM photomicrographs (a), or SEM photomicrographs (b). Results are presented as the maximum and average depth or length per cell. Error bars represent one standard deviation.

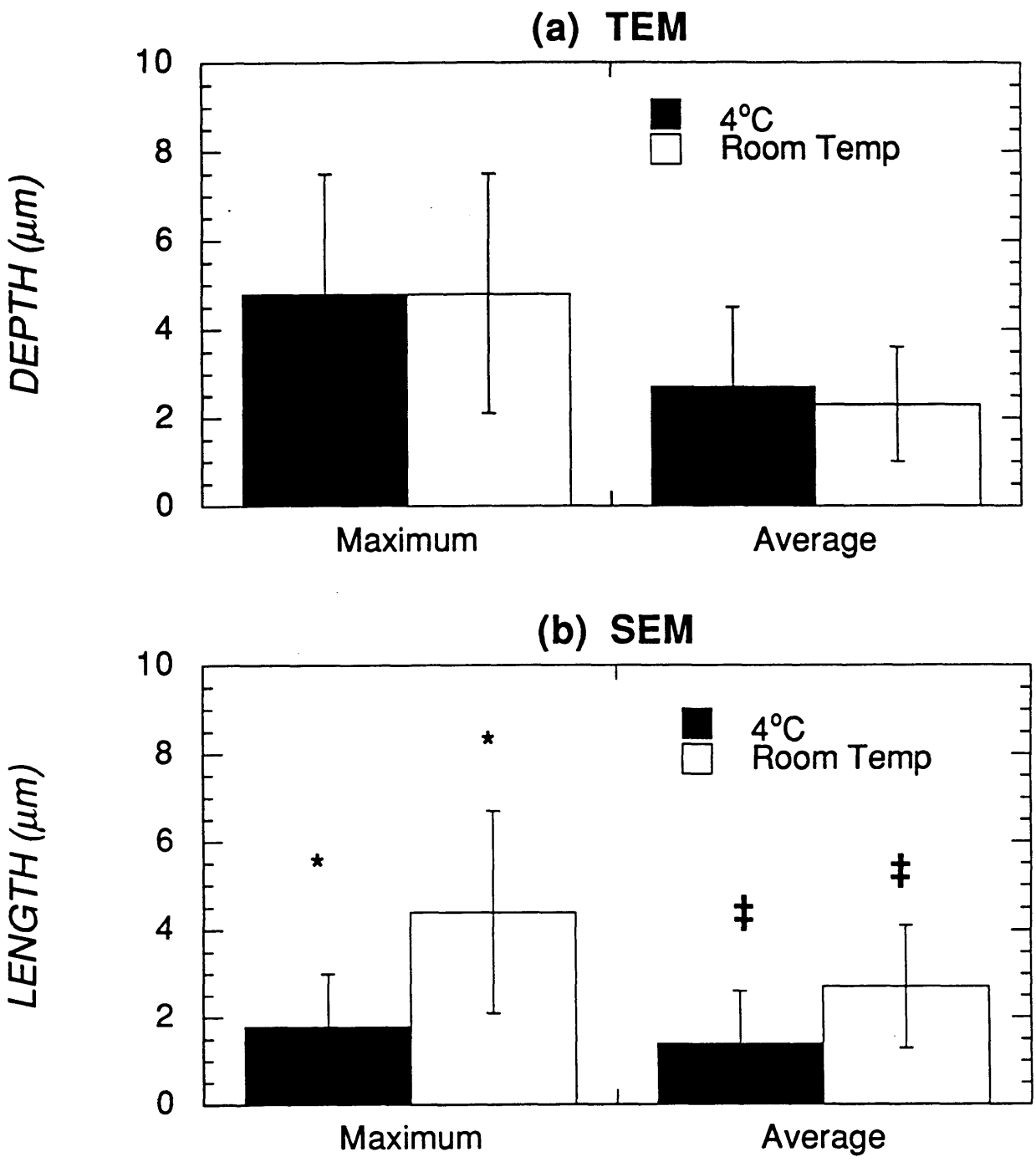

Figure 6.30 Depth and length of infiltrations for cells with infiltrations for cells pressurized on 0.2 μm PCTE membranes at a target pressure of 5 mmHg after preparation and handling at 4° C or room temperature from: (a) TEM photomicrographs, or (b) SEM photomicrographs. Results are presented as the maximum and average depth or length per cell. Error bars represent one standard deviation. and symbols above the bars denote a difference that is statistically significant (*: p=0.003, ‡: p=0.03).

average pressure) using the standard protocol. The target pressure chosen for experiments to test the effect of cell handling and preparation was 5 mmHg, and the actual average pressure was 4.8 mmHg for each.

Figures 6.25 and 6.26 present the results of the on-scope chacterization of cells, analogous to the results shown previously in figure 6.15, for experiments comparing exposure times (figure 6.25) and temperature (figure 6.26) by both TEM and SEM observations. The degree of infiltration was found to be identical for both exposure times as determined by TEM (figure 6.25 (a)), while SEM observations indicated a small (10 %) decrease in the percentage of cells with visible infiltration, and a modest shift in the distribution favoring longer infiltrations for the longer exposure time. Both TEM and SEM observations indicated that cells processed at room temperature instead of 4° C had an increased tendency to infiltrate membranes, and SEM observations show a substantial increase in the proportion of infiltrations longer than 1 μm for cells processed at room temperature.

Results characterizing cellular morphology analogous to the results presented previously in figure 6.16, are summarized in figure 6.27 for experiments to compare exposure times (a) and processing temperature (b). The results indicate that morphology was not significantly affected by increased exposure time or temperature history at the pressure conditions tested.

The average number of infiltrations per cell was not significantly affected by exposure time (figure 6.28 (a)); however, cells which were handled at room temperature had over twice as many infiltrations per cell as cells processed at 4° C as measured from SEM photomicrographs (statistically significant difference, $p=0.007$)(figure 6.28 (a)). This difference was not apparent in TEM photomicrographs (figure 6.28 (b)).

Cells exposed to pressure for 41 min versus 14 min at 2 mmHg pressure displayed

longer infiltrations on average (about twice as long from SEM measurements), but none of the differences was statistically significant ($p>0.05$) (figure 6.29). Analogous results are shown in figure 6.30 for experiments comparing the effect of temperature history. The results are similar to those comparing the number of infiltrations per cell shown in figure 6.28 (b). Again, by TEM, no differences are apparent, but SEM measurements indicate that both the maximum and average infiltration length per cell was approximately twice that for cells processed at room temperature versus 4° C (both differences statistically significant: $p=0.003$ for maximum, and $p=0.03$ for average length per cell.

6.5 Discussion

Our results conclusively showed that HL-60 leukemic leukocytes are able to infiltrate membranes with pore diameters as small as 0.1 μm when filtered onto membranes of well defined pore size under the influence of positive hydrostatic pressure. Results were less conclusive for experiments with 0.05 μm diameter pores, and this pore size may be small enough to restrict the entry of cell infiltrations. Results for both 0.2 and 0.1 μm pore diameter membranes indicated a sharp drop in the degree and extent of infiltration at filtration pressures between 5 to 20 mm Hg for 0.1 μm, and 2 to 5 mm Hg for 0.2 μm membranes. For load pressures higher than these, the fraction of cells in the populations which displayed evidence of infiltration was relatively constant at about 60 to 90 % of the total observed. The degree of infiltration was well correlated to the surface morphology of the cells as observed by SEM, with cells from samples which had a high fraction of cells with infiltrations also having a high fraction of cells with a smooth morphology, and cells from samples which had a low fraction of cells with infiltrations having higher fractions of cells with a ruffled or villous morphology. Measurements of infiltration dimensions from SEM and TEM

photomicrographs suggested that the cells displayed considerable heterogeneity, both from cell to cell within the population, and also possibly from location to location on the same cell. The number of infiltrations per cell and the average infiltration lengths for cells increases sharply over the same critical range of pressure (5 to 20 mmHg and 2 to 5 mmHg for 0.1 and 0.2 μm membranes respectively) observed for changes in the fraction of cells infiltrated and changes in surface morphology. The stress-strain behavior of the cell populations shown in figure 6.24 indicates that the observed strains for cells with infiltrations were very large (*L/Rp* from 10 to 50) over the entire range of stress tested, much larger than that previously observed for red blood cells being deformed into PCTE membrane pores (Brailsford et al., 1977; Missirilis and Brain, 1979; Reinhart et al., 1987) or neutrophil elastic response to similar stresses in micropipet experiments (Chien et al., 1984).

The experimental protocol employed was designed primarily to determine the tendency of cells to infiltrate into membrane pores as a function of pressure and pore size (eg. data from figure 6.15). There are several potential artifacts which must be considered in the interpretation of detailed dimensional measurements and, to some degree, determination of the fraction of cells in a population which infiltrated membrane pores. A complicating factor in the interpretation of TEM images is the presence of a small fraction of overlapping pores on the surface of PCTE membranes. Overlapping pores are of irregular geometry and will have larger effective radii than single pores. A typical cell, as observed by TEM, had a contact area of about 7 μm in diameter. From the data in table 6.1, this cell contact area would cover about 150 holes, 32 of which would overlap to some extent for 0.2 μm diameter membranes, or about 165 holes, 15 of which would overlap for 0.1 μm diameter membranes, or about 300 holes, 9 of which would overlap for 0.05 μm diameter membranes. Because, with TEM images, the relationship of the position and orientation of the section slice with respect to the

infiltration being observed is not precisely known without analyzing a very large number of serial sections for each sample, the precise maximum diameter of any given infiltration is unknown, and, therefore, it is not possible to tell with certainty if a given infiltration results from overlapping pores. However, since the incidence angles of pores are randomly distributed from -34° to 34° with respect to a direction normal to the surface (Osmonics manufacturing specifications) and the pore sizes are very small compared to the membrane thickness, most overlapping pores will diverge into single pores before penetrating very deeply. For example, even for a very conservative estimate considering incidence angles only varying in two dimensions instead of three, fewer than 1% of the holes under a typical cell on 0.2 μm membranes will be overlapping pores with any degree of overlap persisting to a maximum depth of 1 μm below the membrane surface. This fraction will be even less for smaller pore size membranes and deeper overlap depths. In addition, measurements and observations made with SEM are not subject to this complication. With the SEM, the entire infiltration is visible, and only single infiltrations with diameters from 75 to 150 % of the nominal pore diameter were considered (infiltrations falling in this size range constituted the vast majority of observed infiltrations (> 90%)) . Since conclusions based on TEM and SEM were similar for most of the observations in this study, we do not believe that pore overlap was a major complicating factor in the study.

Another potential complication is that the methods used to prepare cells for electron microscopy may have led to an overestimation of the fraction of cells with infiltrations and possibly the average length and depth of infiltrations because cells without infiltrations or with few or short infiltrations may have been preferentially dislodged during the dehydration and sample preparation steps. SEM observations are subject to greater interpretational difficulties compared to TEM when judging whether a feature is an infiltration or a pre-

existing feature for low pressure conditions where the cell morphology is villous; therefore, for conditions where cell morphology is primarily villous, TEM is more definitive in judging whether infiltrations are present on sample sections. In addition, SEM observations may underestimate the fraction of cells with infiltrations and the number and length of infiltrations compared to TEM observations because of the fragility of the infiltrations. Infiltrations which appeared to have broken off from cells were commonly observed on SEM samples. TEM will also show any infiltrations which have pinched off and are no longer connected to the cell contact area but are still within the pores of the PCTE membrane, whereas these infiltrations will be washed away during the dissolution of the PCTE membrane in SEM sample preparation. Normally, one would expect to see more infiltrations per cell and a higher fraction of cells with infiltrations by SEM than TEM since the entire contact area is visible. Since this was not always the case, we conclude that a loss of the infiltrations observed by TEM was occurring to some extent during SEM sample preparation.

The presence of artifactual matter of unknown composition under the contact areas of many cells filtered onto 0.05 μm pore diameter membranes at high pressures (100 to 200 mmHg) made the determination of infiltration difficult. TEM and SEM results were not in close agreement, with SEM observations indicating a greater fraction of cells with short (< 1μm) infiltration-like objects on the contact areas than observed with TEM (see figure 6.15 (a)). However, the objects counted as infiltrations for these conditions did not appear similar in appearance to infiltrations observed with 0.1 and 0.2 μm pore diameter membranes (compare figure 6.14 (a) with figures 6.11 and 6.12), and it is uncertain if these objects were true infiltrations or simply morphological artifacts in the contact areas of these cells.

An important distinction must also be made when considering infiltration density per cell and dimensional measurements of infiltration size between the mean behavior of a

population of heterogeneous cells as opposed to the mechanical properties of a single cell type. Changes in measured properties could be largely accounted for by changes in the distributions of cells with particular mechanical properties retained on the samples. For example, cells observed at low pressure conditions may be significantly enriched in the number of the most deformable cells in the population. Measurements made from SEM photomicrographs are more reliable than those made from TEM photomicrographs because the entire feature is visible, and not just the portion which passes through the section plane as observed by TEM. However, there are significant sources of artifact with SEM measurements as well. As mentioned previously, infiltrations may break off leading to an underestimation of the number per cell and the average length. In addition, overlapping and entanglement of infiltrations leads to a limited fraction of the total number being suitable for inclusion in the detailed measurements of infiltration dimensions. Because longer infiltrations, and large numbers of infiltrations per cell intensify this problem, shorter infiltrations, and infiltrations present on cells with relatively fewer infiltrations per cell are preferentially included in the analysis, especially for conditions yielding a high degree of infiltration (i.e.. high pressures). For example the average fraction of the total number of infiltrations observed on each *cell* which were suitable for detailed measurement ranged from 10% to 100% with an overall average of about 45% of the infiltrations on each cell measured. However, because cells with many infiltrations tended to have more overlapping and entangled infiltrations, a smaller fraction of the total on such cells tended to be included in detailed measurements. As a result, the number of infiltrations included in detailed measurements as a fraction of the total number of *infiltrations* observed on all photographed cells was only about 26%. Finally, correction for irregular contact area orientation, as described in the results section, based on the assumption of a circular contact area will create inaccuracy for cells where this

assumption is not valid; however, errors due to this source should be more or less randomly distributed across the entire range of test conditions. For these reasons, results based on the number and dimensions of infiltrations should be compared relatively between conditions, and not be treated as quantitatively exact for a given condition.

Laplace's law given by equation 1 will tend to underpredict the critical pressure required to deform cells into pores whose radius is not large enough to ignore the effects of bending resistance. Zhelev et al. developed a model which accurately predicts the critical pressure required to aspirate neutrophil membranes into pipets with internal diameter as small as 0.48 μm (Zhelev et al., 1994a). The authors found that the bending rigidity of the membrane-associated cortex significantly increased the pressure required to aspirate cell membranes over that predicted by the law of Laplace. In their model, it is assumed that the membrane-cortex is a thin layer having a smaller thickness than the pipet radius. The apparent cortical tension and bending modulus are treated as free energies per unit area of the membrane-cortex. The development is only rigorously valid for the small initial displacement of the cell membrane into the pipet, and, therefore, is intended to be used in predicting the critical pressure for initial cell entry. The cortical tension, which is assumed to be constant, and the bending resistance are the two sources of mechanical free energy per unit area, and the dependence of the aspiration pressure on the pipet radius is determined by equating the change in free energy for a small change in projection length inside the pipet to the work done by the pressure difference. The critical pressure difference was found to be

$$\Delta P_{crit} = f_0\left(\frac{R_{cell}}{R_p'}, \frac{r}{R_p'}\right) \cdot \frac{k_c}{R_p'^3} + f_1\left(\frac{R_{cell}}{R_p'}, \frac{r}{R_p'}\right) \cdot \frac{T}{R_p'} \tag{10}$$

where T is the cortical tension, k_c is the bending modulus of the membrane-cortex, and the

functional coefficients f_0 and f_1 are defined in the appendix and are functions of the radius of the cell R_{cell}, the radius of the pore minus half the thickness of the membrane-cortex R_p', and the radius of curvature of the small torus region where the cell bends into the pore r (see figure 6.A.1). Using a cortical tension of 0.024 mN/m the authors were able to fit their aspiration data with values of k_c ranging from 1 to 2 × 10^{-18} J for a cortex with a thickness from 0.1 μm down to an infinitely small thickness (0 μm). Table 6.5 presents the predictions for the critical pressures required to enable cells (with mechanical properties similar to neutrophils) to enter the pores of the membranes in this study as calculated by the law of Laplace (column 2), the model of Zhelev et al. for an intact membrane-cortex (column 3), and by the same model for aspiration of a lipid bilayer only (column 4). In order to give a low reasonable estimate of the critical pressure, cortical tension T was assumed to be 0.024 mN/m, the bending modulus for the membrane-cortex used was 1 × 10^{-18} J, the cell diameter outside the pore was 10 μm, and the bending modulus for the phospholipid bilayer used was 0.6 × 10^{-19} J, the lowest value measured for 1-stearoyl-2-oleoyl-*sn*-glycero-3-phosphocholine (SOPC) using a micropipet technique (Zhelev et al., 1994b). To determine a minimum estimate, the thickness of the membrane-cortex was assumed to be zero and the r was chosen so that ΔP_{crit} was minimized for each pore size.

Table 6.5 *Predicted Critical Pressures to Form Infiltrations Into PCTE Membrane Pores*

	ΔP_{crit} (mmHg)		
Pore Internal Diameter (μm)	**Law of Laplace**	**Zhelev et al., 1994a Membrane-Cortex**	**Zhelev et al., 1994a Membrane Only**
0.2	3.5	53	2.8
0.1	7.1	390	23
0.05	14	3,600	190

It is clear from table 6.5 that the model developed to predict critical pressures for aspiration of the membrane-cortex complex of neutrophils into small pipets suggests that formation of infiltrations should not occur at the pressures tested. Recall that our results indicate that the critical pressure range for formation of infiltrations was from 2 to 5 mmHg for 0.2 μm membranes, 5 to 20 mmHg for 0.1 μm membranes. The evidence for infiltrations into 0.05 μm membranes was mixed, with results suggesting that it may not occur at all, or only at the highest pressures tested (100 to 200 mmHg). Table 6.5 suggests that even aspiration of an unsupported lipid bilayer is likely only for the low bending modulus assumed in these calculations.

The exact mechanism of infiltration that was observed at our test pressures is unknown. Several possibilities arise. Cell lysis could be occurring with cytoplasmic contents leaking into the membrane pores. This possibility, however, is unlikely for several reasons. First, the maximum induced tensions in the membrane are at least an order of magnitude lower than those found to be necessary for cell lysis (about 10 mN/m (Shao et al., 1996)). The maximum tension in the cell membrane is created by the force resulting from the applied pressure difference

$$F_{max} = \Delta P \pi R_p^2 \tag{11}$$

and the maximum axial tension created in the membrane can be estimated by (Waugh and Hochmuth, 1987)

$$T_{max} \approx \frac{F_{max}}{2\pi R_p} \tag{12}$$

From equations 11 and 12, the maximum tension applied to the cell for any of the test conditions tested is about 0.3 mN/m. In addition, in both TEM and SEM photomicrographs

cells appear to be intact, and without morphological evidence of cell lysis or gross membrane damage. Also, if the infiltrations were not contained by an intact membrane, the cytoplasmic material would likely be washed directly through the membrane, and the structure of the infiltrations should not have been preserved during dissolution of the membrane during SEM sample preparation.

It is also unlikely that infiltration of the membranes represented a process of active motility on the part of the cells. All experiments were performed in Ca^{++} and Mg^{++} free media, and there was no evidence of pseudopod formation from electron micrograph images. Previous studies in our laboratory have also shown that infiltration is not inhibited by cytochalasin-D or metabolic inhibition with a combination of 2-deoxy-D-glucose and sodium azide (chapter 5).

The fact that most of the infiltrations we observed were not self-supporting after fixation, but instead collapsed onto the contact area of the cell after the PCTE membrane was removed during SEM sample preparation, suggests that infiltrations may not have a supporting F-actin structure. Disruption of the cytoskeleton supporting the membrane could account for a reduction in pressure necessary for infiltration into a pore since the cytoskeletal cortex provides the greatest resistance to cell membrane deformation (compare columns 3 and four in table 6.5). Sufficient forces applied to a cell membrane have previously been observed to disrupt the supporting actin filaments. These forces are typically less than those required to cause cell lysis. When a force of sufficient magnitude to disrupt the supporting cytoskeleton is applied to a cell membrane, filamentous actin depolymerizes, and the cell membrane/cortex undergoes rapid, plastic deformation forming a membrane tether. For example, membrane tethers have been formed from neutrophils by axial pulling forces applied to the membrane (Shao et al., 1996), and also during membrane aspiration into small pipets

with sufficient suction pressures (Zhelev et al., 1995). Zhelev et al. observed that when cells were aspirated into pipets of internal diameter of 0.8 μm with suction pressures of 600 to 900 Pa, the aspirated portions of the cells had a tendency to "neck off" and form long tethers. From equations 11 and 12, this indicates that the critical applied tension in the cortex for plastic deformation is on the order of 0.12 to 0.18 mN/m. A value of 0.12 mN/m would yield critical pressures of 72 mmHg, 36 mmHg, and 18 mmHg, for 0.05, 0.1, and 0.2 μm pore diameter membranes respectively. These values are only a factor of 2 to 4 higher than the critical range of pressures observed to cause infiltration for 0.1 and 0.2 μm pore diameter membranes in this study indicating that this mechanism may be a plausible explanation for the formation and/or elongation of infiltrations. It is also possible that the relatively long exposure times employed in our study could enhance the tendency toward plastic deformation (Chien et al., 1978; Zhelev et al., 1995). Recently, Shao et al., (Shao et al., 1996) directly measured the minimum axial force, applied at a molecular point attachment, required to pull a membrane tether from neutrophils and found it to be 45 pN. This corresponds to minimum critical pressures of 172 mmHg, 43 mmHg, and 11 mmHg, for 0.05, 0.1, and 0.2 μm pore diameter membranes respectively. Again, these values are only a factor of 2 to 3 higher than the critical range of pressures observed to cause infiltration for 0.1 and 0.2 μm pore diameter membranes in this study, much closer to our experimentally observed values than those predicted for infiltration of an intact membrane-cortex (table 6.5).

As mentioned before, TEM observations of cells with infiltrations for conditions of relatively low applied pressure often suggested that pre-formed surface features may enter a pore, as a result of fluid mechanical drag forces associated with fluid flowing into pores, as a first step in the infiltration process (see figures 6.9 and 6.10). These observations may indicate a mechanism by which a portion of membrane-cortex, such as a microvilli, initially

enters a pore without the necessity of a large external force required to overcome bending stiffness. As the pore becomes sealed, the applied mechanical force on the membrane of the surface feature in the pore (equation 11) would create a tension in the attached microfilaments. Subsequent elongation may then occur as a result of plastic deformation of the cytoskeleton undergoing extended periods of stress and strain, or by a passive reorientation of the microfilament system in the direction of the infiltration (Kolega, 1986). A similar phenomenon, involving the formation of long membrane features in the direction of an applied force, has been observed previously for cell outgrowths formed by forces applied to the plasma membranes of mouse embryo fibroblasts and L cells generated by an alternating current electric field (Popov and Margolis, 1988). For forces applied to the membrane equivalent to an aspiration pressure of 7.5 mmHg, the authors observed the formation of long protrusions (up to 15 μm) which were as thin as 0.1 μm in diameter and which contained aligned microfilaments inside the protrusions. The cell outgrowths observed in their experiments looked very similar in appearance to our infiltrations as observed by SEM. They also observed that erythrocytes similarly treated did not produce membrane protrusions, and they speculated that pre-formed membrane features, such as microvilli, were necessary for the formation of long protrusions. Significantly, surface features, such as microvilli,on cells used in the present study were typically on the order of 0.1 to 0.2 μm in diameter, larger than the 0.05 μm pore size where there was no convincing evidence of infiltration into pores.

It is also possible that cell contact with the PCTE membrane under conditions of elevated hydrostatic pressure may cause cytoskeletal rearrangements in the cell as a response to mechanical stress. The flattening, and smoothing out, of the cell in the region of contact with the PCTE membrane even for cells without infiltrations may be indicative of such changes. It has been observed previously that physical stress such as hypotonic osmotic

shock will cause a dramatic decrease in cytoskeletal F-actin in HL-60, and that this in turn causes the cells to display a more folded/villous morphology, similar to our observations for cells with low degrees of infiltration, than is typical for resting cells (Hallows et al., 1996). In addition, the spatial distribution of F-actin in the cortical area of normal, resting HL-60, as observed by fluorescent staining and microscopy has been observed to be heterogeneously distributed with occasional "hot spots," and regions with more diffuse staining (Hallows et al., 1996). Such observations suggest the possibility of significant local heterogeneity in the support of the lipid membrane by the cytoskeletal cortex on the scale of the very small pore sizes used in the present investigation. Whatever the specific mechanism, we believe that the state of cytoskeletal organization is an important factor in cell infiltration. Previous studies in our laboratory have shown that HL-60 infiltration into porous membranes can be almost entirely prevented by pre-fixing the cells with glutaraldehyde before filtration (chapter 5).

To summarize, it appears unlikely based on previous observations with small diameter micropipets, that infiltration of an intact membrane/cytoskeletal support network is occurring. It seems more likely that cytoskeletal disruption of some sort is occurring either before infiltration, or after the aspiration of pre-formed surface features. Alternatively, cytoskeletal support of the plasma membrane could be heterogeneous enough at the scale of the studied pore sizes to permit deformation of unsupported membrane. We observed no direct evidence of tether formation by TEM or SEM. Overwhelmingly, infiltration diameters, as observed by SEM, were largely uniform, and close to the average pore size of the PCTE membrane from which they were removed. TEM photomicrographs of infiltrations with 0.1 and 0.2 μm membranes showed that infiltrations were filled with cytosol and frequently contained ribosomes, and granular material consistent with cross-sections of filamentous actin. They also appeared to be surrounded by an intact membrane. Although we saw no evidence of

"necking" of the infiltrations, or regions with very small diameters indicative of a tether, it is possible that tethers eventually pinch off to form unconnected balls of cytoplasm when resistance to flow and area expansion becomes large enough. The phenomenon of pinching off of small globules by micropipet aspiration has been observed previously for red blood cells (Evans, 1973). Alternatively, the thin tethers may simply be too fragile to survive intact the PCTE membrane removal step during SEM sample preparation. This could, in part, partially explain why average infiltration lengths measured by SEM were less than the average depths measured by TEM.

The stress versus strain behavior of the cell populations shown in figure 6.24 is distinctly non-linear over the entire range of applied stresses and displays a plateau over a range of stress which correlates well with an increase in a smooth morphology of the cells. The response observed over the 0 to 0.05 dynes/cm stress range, which was more linear with a greater slope, may reflect some increase in resistance to expansion with increasing surface area, or may simply indicate that steady state and maximum elongation was not completely attained for the lower stress conditions. To add some support to the latter speculation, we found that increasing the time of exposure to pressure before fixation from 14 min to 41 min for cells on 0.2 μm membranes exposed to the lowest non-zero pressure where infiltrations occurred (about 2 mmHg) resulted in a 50 to 90 % increase in the average length of infiltrations which; however, was not statistically significant at $p = 0.05$.

The total surface area accounted for by infiltrations for a particular condition can be approximated knowing the average infiltration length, diameter and number of infiltrations per cell. The area per infiltration, assuming that the geometry is well approximated by a cylinder with a hemispherical cap is

$$Area/Infiltration = 2\pi RpL \tag{13}$$

where Rp is the average infiltration radius, and L is the average infiltration length as defined in the results section. Multiplication of the area/infiltration by the average number of infiltrations per cell will yield the total surface area accounted for by infiltrations. This value can then be compared to the surface area of a sphere of typical cellular dimensions to determine the amount of excess surface area that is represented by the infiltrations. Typical average values from SEM measurements for infiltration length, diameter, and number per cell for conditions in the high pressure plateau regions of figures 6.22 and 6.23, where the morphology of most cells has become smooth, indicate that infiltration area represents about a 15 % excess of surface area for 0.1 μm membrane samples and about a 10 % excess for 0.2 μm membrane samples for a 10 μm diameter cell. These values are much lower than the 80 - 90 % excess surface area typically reported for neutrophils (Chien et al., 1984; Chien et al., 1987; Schmid-Schönbein, 1990). This discrepancy may be due to an intrinsic difference between the amount of excess surface area for HL-60 cells compared to neutrophils, but is also, most likely, due in part to infiltrations pinching off and/or forming vesicles during pressurization, and breaking off during SEM sample preparation. TEM photomicrographs in figures 6.6 and 6.9 clearly show small vesicles (observed up to 2 μm in diameter) being formed by infiltrations which completely traverse the PCTE membrane. These vesicles were never observed in samples prepared for SEM.

The temperature at which the cells were prepared and stored prior to the experiments had a significant effect on cell infiltration phenomena. Preparing and storing cells at room temperature instead of 4 °C significantly increased the average number of infiltrations per cell and infiltration length as determined from SEM measurements, but had no significant effect

on the fraction of cells with infiltrations, observed cellular morphology, or measurements based on TEM observations. The reasons for these observations are unclear, but may point to a lower fraction of infiltrations pinching off during pressurization for cells not previously exposed to the cold, perhaps due to a higher degree of membrane fluidity, or decreased cytoplasmic viscosity, leading to better preservation of infiltrations during SEM sample preparation. Alternatively, exposure to 4 °C for white blood cells such as cultured lymphocytes, has been observed to reduce the number of microvilli per cell and increase the average diameter of each microvilli (Lin et al., 1973). If aspiration of pre-formed surface features such as microvilli was an important mechanism by which infiltration was occurring, one would expect cells with more microvilli small enough to easily enter pores to display more infiltrations per cell. This was exactly what we observed for cells not exposed to cold conditions prior to experiments compared to cells handled and stored at 4 °C.

In conclusion, we have demonstrated that current theory for leukocyte deformation into small pipets did not accurately describe the deformation of HL-60 leukemic leukocytes into small pores during filtration with positive hydrostatic pressure. While the mechanism of infiltration is unclear, it may be due to aspiration of pre-formed cell surface features with high degrees of membrane curvature with subsequent elongation due to disruption or redistribution of the cytoskeletal support network by pressure-induced stress on the features. Alternatively, infiltration of unsupported plasma membrane may be occurring in regions of the cell-PCTE membrane contact area where the cortical structure has been disrupted by mechanical stresses and/or cell-material interactions, or at locations where there is heterogeneity in cytoskeletal attachment to the plasma membrane on the scale of the pore sizes studied. We found no convincing evidence of infiltration of cells into the smallest pore size studied (0.05 μm diameter). This pore size was smaller than the diameter of typical surface features on the

cells. In the future, a similar study using a more well studied, homogeneous, cell type such as neutrophils, would be helpful to determine the mechanism of cellular infiltration, as would parallel studies looking at the state of cytoskeletal organization, in cells and infiltrations, for cells deforming into holes whose size is similar to the dimensions of the cell cortex.

6.6 Acknowledgements

Scanning electron microscopy was performed in the EM facility of the Center for Materials Science and Engineering at MIT, a Materials Science and Engineering Center supported by the National Science Foundation under grant number DMR 9400334. Special thanks to Dr. David C. Bell, and Mr. Michael Frongillo for assistance with sample coating and microscopy. Transmission electron microscopy was performed in the Biomedical Electron Microscopy Laboratory at MIT. The JEOL 122 EX II was purchased through an NIH multi-user instrumentation program, BRS Shared Instrumentation Grant number S10 RR05734-01. Special thanks to Ms. Patricia Reilly for assistance with sample preparation and microscopy.

6.7 Appendix: Definition of Functional Coefficients in Small Pore Deformation Model

In this appendix, we define the functional coefficients, f_0 and f_1, in equation 10 taken from Zhelev et al., 1994a. The simplified model of cell geometry used is shown in figure 6.A.1. The cell is divided into three regions. The first region consists of the spherically shaped projection inside the pipet. The second region is the curved portion of the cell surface at the pipet orifice, which the authors approximate as a segment of a torus. The third region is the spherically shaped part of the cell outside the pipet. The cortical tension is defined as an energy per unit area

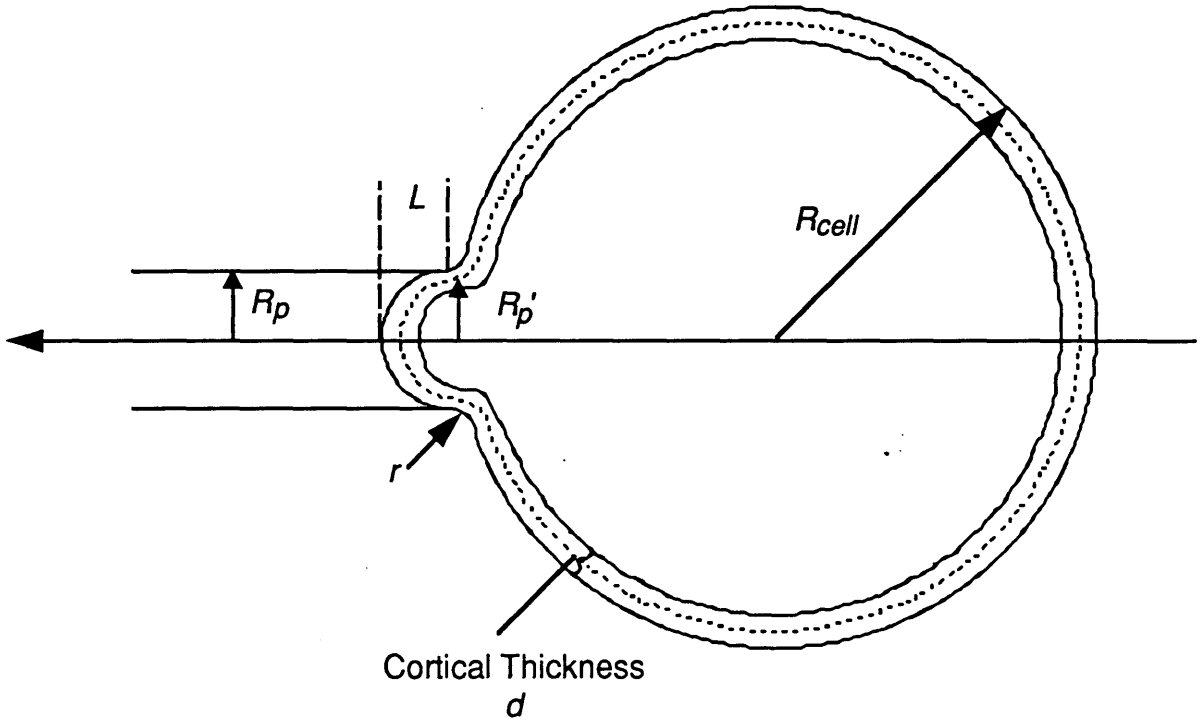

Figure 6.A.1 Geometry of a cell entering a small, cylindrical pipet.

$$g_c = T \tag{A1}$$

and a bending energy per unit area is introduced which is similar to that for lipid bilayers (Helfrich, 1973)

$$g_b = \frac{k_c}{2}(c_1 + c_2)^2 \tag{A2}$$

where k_c is the apparent bending modulus and c_1 and c_2 are the two principle curvatures. The relationship between the cortical tension and the bending resistance of the membrane and the applied forces is obtained by equating the free energy change during small cell deformations to the work done by the applied forces. The mechanical free energy of the cell membrane is calculated from equations A1 and A2 considering the simplified geometry of each of the three regions of the cell. The change in the total mechanical free energy will be the sum of the free energy changes for each region during a small deformation (dL). The expression that the authors derive for the total change in free energy is

$$\begin{aligned} dG_{total} = {} & 2\pi T\left(R_p' + r - \frac{R_p'(R_p' + rC_{vt})}{R_{cell}}\right) \cdot dL \\ & + \pi k_c\left(\frac{1}{r}\left(1 + \frac{r}{R_p'}\right)^2\left(1 + \frac{2r}{R_p'}\right)^{\frac{1}{2}} - \frac{4R_p'C_{ww}(R_p' + rC_{vt})}{R_{out}{}^3(2 + C_{vs})}\right) \cdot dL \end{aligned} \tag{A3}$$

where

$$C_{vt} = 1 + \left(\frac{R_p' + r}{R_p'}\right) + \left(\frac{R_p' + r}{R_p'}\right)^2$$

$$C_{vs} = \frac{2 - ((R_p' + r)/R_{cell})^2}{(1 - ((R_p' + r)/R_{cell})^2)^{\frac{1}{2}}}$$

and

$$C_{ww} = \frac{((R_p' + r)/R_{cell})^2}{(1 - ((R_p' + r)/R_{cell})^2)^{\frac{1}{2}}}$$

The displacement of the cell, dL, is assumed to be a result of the work done by the applied pressure:

$$dW_{total} = \pi R_p'^2 \Delta P \cdot dL \tag{A4}$$

Equating A3 and A4 yields the expression for ΔP_{crit} given in equation 10

$$\Delta P_{crit} = f_0\left(\frac{R_{cell}}{R_p'}, \frac{r}{R_p'}\right) \cdot \frac{k_c}{R_p'^3} + f_1\left(\frac{R_{cell}}{R_p'}, \frac{r}{R_p'}\right) \cdot \frac{T}{R_p'}$$

where

$$f_0\left(\frac{R_{cell}}{R_p'}, \frac{r}{R_p'}\right) = \frac{1}{(r/R_p')}\left(1 + \frac{r}{R_p'}\right)^2\left(1 + \frac{2r}{R_p'}\right)^{\frac{1}{2}} - \frac{4C_{ww}(1 + (r/R_p')C_{vs})}{(R_{cell}/R_p')^3(2 + C_{vs})}$$

*(In the authors' original, there is an apparent algebra error and the denominator of the second term is missing the $(R_{cell}/R_p')^3$ term. The authors apparently only made this error in presenting the equation in their appendix since the numerical results that they generate with the model are consistent with the form of f_0 shown above, but not the form given in their appendix.)

and f_1 is given by

$$f_1\left(\frac{R_{cell}}{R_p'}, \frac{r}{R_p'}\right) = 2\left(1 + \frac{r}{R_p'} - \frac{(1 + (r/R_p')C_{vt})}{R_{cell}/R_p'}\right)$$

6.8 References

Baker, R. F. 1981. Membrane deformability of metabolically depleted human red cells. *Blood Cells.* 7:551-558.

Brailsford, J. D., R. A. Korpman, and B. S. Bull. 1977. The aspiration of red cell membrane into small holes: new data. *Blood Cells.* 3:25-38.

Bray, D., J. Heath, and D. Moss. 1986. The membrane-associated "cortex" of animal cells: its structure and mechanical properties. *Journal of Cell Science Supplement.* 4:71-88.

Chien, S., K.-L. P. Sung, R. Skalak, S. Usami, and A. Tözeren. 1978. Theoretical and experimental studies on viscoelastic properties of erythrocyte membrane. *Biophysical Journal.* 24:463-487.

Chien, S., G. W. Schmid-Schönbein, K.-L. P. Sung, E. A. Schmalzer, and R. Skalak. 1984. Viscoelastic properties of leukocytes. In White Cell Mechanics: Basic Science and Clinical Aspects. Alan R. Liss, Inc., New York. 19-51.

Chien, S., K.-L. P. Sung, G. W. Schmid-Schönbein, R. Skalak, E. A. Schmalzer, and S. Usami. 1987. Rheology of leukocytes. *Annals of the New York Academy of Sciences.* 516:333-347.

Collins, S. J., R. C. Gallo, and R. E. Gallagher. 1977. Continuous growth and differentiation of human myeloid lukaemic cells in suspension culture. *Nature.* 270:347-349.

Dong, C., R. Skalak, K-L. P. Sung, G. W. Schmid-Schönbein, and S. Chien. 1988. Passive deformation analysis of human leukocytes. *Journal of Biomechanical Engineering.* 110:27-36.

Esaguy, N., A. P. Aguas, and M. T. Silva. 1989. High-resolution localization of lactofeffin in human neutrophils: labling of secondary granules and cell heterogenity. *Journal of Leukocyte Biology.* 46:51-62.

Evans, E. A. 1973. New membrane concept applied to the analysis of fluid shear- and micropipette-deformed red blood cells. *Biophysical Journal.* 13:941-954.

Evans, E. A., and R. Skalak. 1980. Mechanics and thermodynamics of biomembranes. CRC Press Inc., Boca Raton, FL.

Evans, E. A., and B. Kukan. 1984. Passive material behavior of granulocytes based on large deformation and recovery after deformation tests. *Blood.* 64:1028-1035.

Evans, E. A., and A. Yeung. 1989. Apparent viscosity and cortical tension of blood granulocytes determined by micropipet aspiration. *Biophysical Journal.* 56:151-160.

Hallows, K. R., and R. S. Frank. 1992. Changes in mechanical properties with DMSO-induced differentiation of HL-60 cells. *Biorheology.* 29:295-309.

Hallows, K. R., F.-Y. Law, C. H. Packman, and P. A. Knauf. 1996. Changes in cytoskeletal actin content, F-actin distribution, and surface morphology during HL-60 cell volume regulation. *Journal of Cellular Physiology*. 167:60-71.

Helfrich, W. 1973. Elastic properties of lipid bilayers: theory and possible experiments. *Zeitschrift fur Naturforschung*. 28c:693-703.

Hochmuth, R. M., H. P. Ting-Beall, B. B. Beaty, D. Needham, and R. Tran-Son-Tay. 1993. Viscosity of passive human neutrophils undergoing small deformations. *Biophysical Journal*. 64:1596-1601.

Kolega, J. 1986. Effects of mechanical tension on protrusive activity and microfilament and intermediate filament organization in an epidermal epithelium moving in culture. *Journal of Cell Biology*. 102:1400-1411.

Lin, P. S., D. F. H. Wallach, and S. Tsai. Temperature-induced variations in the surface topology of cultured lymphocytes are revealed by scanning electron micrscopy. *Proceedings of the National Academy of Sciences USA*. 70:2492-2496.

Mandrusov, E., A. Houng, E. Klein, and E. F. Leonard. Membrane-based cell affinity chromatography to retrieve viable cells. *Biotechnology Progress*. 11:208-213.

Missirlis, Y. F., and M. C. Brain. 1979. An improved method for method for studying the elastic properties of erythrocyte membranes. *Blood*. 54:1069-1079.

Needham, D., and R. M. Hochmuth. 1992. A sensitive measure of surface stress in the resting neutrophil. *Biophysical Journal*. 61:1664-1670.

Nordon, R. E., D. N. Haylock, L. Gaudry, and K. Schindlhelm. 1996. Hollow-fiber affinity cell separation for CD34+ cell enrichment. *Cytometry*. 24:340-347.

Nordon, R. E., and K. Schindhelm. 1997. Design of hollow fiber moduled for uniform shear elution affinity cell separation. *Artificial Organs*. 21:107-115.

Popov, S.V., and L.B. Margolis. 1988. Formation of cell outgrowths by external force: a model study. *Journal of Cell Science*. 90:379-389.

Reinhart, W. H., A. Chabanel, M. Vayo, and S. Chien. 1987. Evaluation of a filter aspiration technique to determine membrane deformability. *Journal of Laboratory and Clinical Medicine*. 110:483-494.

Reynolds, E. S. 1963. The use of lead nitrate at high pH as an electron opaque stain in electron microscopy. *Journal of Cell Biology*. 17:208.

Saul, A., G. Lamont, W. H. Sawyer, and C. Kidson. 1984. Decreased membrane deformability in melanesian ovalocytes from Papua New Guinea. *The Journal of Cell Biology*. 98:1348-1354.

Schmid-Schönbein, G. W. 1990. Leukocyte biophysics. *Cell Biophysics*. 17:107-135.

Shao, J.-Y., and R. M. Hochmuth. 1996. Micropipette suction for measuring piconewton forces of adhesion and tether formation from neutrophil membranes. *Biophysical Journal*. 71:2892-2901.

Ting-Beall, H. P., D. Needham, and R. M. Hochmuth. 1993. Volume and osmotic properties of human neutrophils. *Blood*. 81:2774-2780.

Tsai, M. A., R. S. Frank, and R. E. Waugh. 1993. Passive mechanical behavior of human neutrophils: power-law fluid. *Biophysical Journal*. 65:2078-2088.

Tsai, M. A., R. S. Frank, and R. E. Waugh. 1994. Passive mechanical behavior of human neutrophils: effect of cytochalasin B. *Biophysical Journal*. 66:2166-2172.

Tsai, M.A., R. E. Waugh, and P. C. Keng. 1996. Cell cycle-dependence of HL-60 cell deformability. *Biophysical Journal*. 70:2023-2929.

Waugh, R. E., and R. M. Hochmuth. 1987. Mechanical equilibrium of thick, hollow, liquid membrane cylinders. *Biophysical Journal.* 52:391-400.

Yeung, A., and E. Evans. 1989. Cortical shell-liquid core model for passive flow of liquid-like sherical cells into micropipets. *Biophysical Journal.* 56:139-149.

Zhelev, D. V., D. Needham, and R. M. Hochmuth. 1994a. Role of the membrane cortex in neutrophil deformation in small pipets. *Biophysical Journal.* 67:696-705.

Zhelev, D. V., D. Needham, and R. M. Hochmuth. 1994b. A novel micropipet method for measuring the bending modulus of vesicle membranes. *Biophysical Journal.* 67:720-727.

Zhelev, D. V., and R. M. Hochmuth. 1995. Mechanically stimulated cytoskeleton rearrangement and cortical contraction in human neutrophils. *Biophysical Journal.* 68:2004-2014.